



Investigating Ground and Excited State Properties of Complex Organic/Inorganic Interfaces With Ab-Initio Calculations

Andreas Windischbacher

Doctoral thesis

Institute of Physics
University of Graz

Supervisor: Dr. Peter Puschnig

October 2023

I'm an alien, I'm a legal alien
I'm a chemist doing physics.
based on lyrics by Sting

Abstract

A diverse field of research ranging from photovoltaics to heterogeneous catalysis is based on the understanding of thin films of organic molecules adsorbed at metal surfaces. Within the present work, we investigate the electronic properties of such interfaces utilizing quantum mechanical simulations. Our main experimental reference is photoemission spectroscopy, the simulation of which becomes a recurring topic throughout this thesis.

The first part of the thesis comprises our investigation of two members of the acene family, hexacene and heptacene, and their interaction with the coinage metal surfaces Ag(110) and Cu(110). Simulations of the molecule-metal interfaces within density functional theory reveal strong charge transfer from the substrates to the molecular layers. In addition, we find that the amount of transferred charge is determined by the adsorption configuration. Decoupling the molecules from the Cu-surface by oxygen passivation, we discuss how intermolecular pi-pi interactions display in photoemission spectroscopy and connect the intensity distribution in experimental data to the alignment of the acenes on the surface.

In the second part, we focus on the electronic and geometric properties of metal-organic complexes belonging to the class of Ni-tetrapyrroles. To improve the description of the oxidation and spin state of the central Ni atom, we employ a Hubbard correction to our density functional theory calculations in the form of the GGA+U approach. For Ni-phthalocyanine, we find that interaction with a Cu(100) surface induces an axial displacement of the Ni ion from its coordination pocket, which, in turn, changes the spin state of the metal centre. At the hand of a Ni-tetraphenylporphyrin interface, we demonstrate how the adsorbate's electron configuration can be tuned by adsorption of external gas ligands. For instance, a redox-like interaction between nitrogen dioxide and the Ni centre leads to the formation of a stable, paramagnetic complex at room temperature. Furthermore, we propose the disproportionation of nitric oxide at the interface and elaborate on the possible role of the Ni centre in the reaction mechanism. Besides the properties of the central metal atom, we also briefly address the interface-specific geometries of the carbon backbone of porphyrins. In specific, momentum-resolved photoemission data is able to shed light on their rich conformational landscape.

The third and final part of the thesis is concerned with the simulation of time-resolved photoemission experiments to shed light on the excited states of extended molecular systems. In our calculations, we describe the excited states with linear-response time-dependent density functional theory as well as within the many-body perturbation framework of the Bethe-Salpeter equation. As a first step, we assess the sensitivity of the predicted photoemission spectrum towards different levels of theory for the underlying excited state calculation. Then, we apply our approach to a practical example of a fullerene multilayer film. By comparing experimental data with our theoretical results, we examine the photoemission signals of four excitonic states, one of which is a charge transfer state specific to fullerene aggregates.

Kurzzusammenfassung

Das Hauptaugenmerk dieser Arbeit liegt auf der quantenmechanischen Simulation von Grenzflächen zwischen organischen Molekülen und Metalloberflächen sowie dem Verständnis ihrer elektronischen Eigenschaften. Ein wiederkehrendes Leitmotiv ist dabei der Vergleich von experimentellen und berechneten Photoemissionsspektren.

Der Hauptteil der Arbeit gliedert sich in drei Teile: Der erste Teil behandelt die Wechselwirkung zwischen zwei Vertretern aus der Reihe der Acene, Hexacene und Heptacene, mit Silber und Kupfer (110)-Oberflächen. Die Simulationen basierend auf der Dichtefunktionaltheorie zeigen einen ausgeprägten Ladungstransfer von den Metallsubstraten zu den Molekülen. Die Menge der übertragenen Ladung wird dabei nicht nur vom jeweiligen Acene-Metall System bestimmt, sondern auch von der Adsorptionsgeometrie. Passiviert man die Kupfer-Oberfläche mit Sauerstoff, lässt sich die Wechselwirkung zwischen Molekül und Substrat unterbinden. Dies erlaubt uns, die intermolekularen Wechselwirkungen und deren Auswirkungen auf die beobachteten Photoemissionsintensitäten zu untersuchen. Im Besonderen stellen wir eine Verbindung zwischen der experimentellen Intensitätsverteilung und der Anordnung der Acene auf der Oberfläche her.

Im zweiten Teil der Arbeit wenden wir uns metallorganischen Komplexen zu. Im Fokus stehen hier Nickeltetrapyrrol-Verbindungen auf Oberflächen. Um den Oxidations- und Spinzustand des zentralen Nickelatoms besser zu beschreiben, verwenden wir eine Hubbard-Korrektur zur Dichtefunktionaltheorie im Rahmen der GGA+U Methode. Wir beobachten, dass die Wechselwirkung mit einer Kupfer (100)-Oberfläche das Nickelatom eines Ni-Phthalocyaninkomplexes aus seiner Koordinationsumgebung in Richtung Substrat zieht. Dadurch ändert sich der Spinzustand des Metallatoms. Anhand einer adsorbierten Ni-Tetraphenylporphyrin Monolage zeigen wir weiters, wie sich der Spinzustand auch durch Interaktion mit externen Gas Liganden manipulieren lässt. Hervorzuheben ist beispielsweise Stickstoffdioxid, das durch eine redox-artige Wechselwirkung mit dem Ni-Zentrum einen stabilen, paramagnetischen Komplex bildet. Im Gegensatz dazu scheint Stickstoffmonoxid zu zerfallen, wenn man es der gleichen Grenzfläche aussetzt. Wir diskutieren eine mögliche Rolle des Ni-Zentrums in dieser Reaktion. Die Wechselwirkungen in Molekül-Metall Systemen beeinflussen aber nicht nur das Metallatom der Komplexe, sondern auch die Geometrie des Tetrapyrrol-Liganden. Die auftretenden Konformationen des Kohlenstoff-Gerüsts lassen sich mit winkelaufgelösten Photoemissionsmessungen unterscheiden.

Im Zentrum des dritten und gleichzeitig letzten Akts steht die theoretische Beschreibung von zeitaufgelöster Photoemissionsspektroskopie, mit dem Ziel, Informationen über angeregte Zustände von organischen Molekülen zu gewinnen. In unseren Rechnungen beschreiben wir angeregte Zustände entweder mit der Casida-Gleichung im Rahmen der zeitabhängigen Dichtefunktionaltheorie oder mittels des störungstheoretischen Ansatzes der Bethe-Salpeter Gleichung. Zunächst vergleichen wir den Einfluss unterschiedlicher Näherungsverfahren zur Berechnung der angeregten Zustände auf die vorhergesagten Photoemissionsspektren. Danach analysieren wir die zeitaufgelösten Daten eines Films aus Buckminster-Fulleren Molekülen. Mit Hilfe unserer Simulationen gelingt uns die Identifikation der vier experimentell beobachteten, angeregten Zustände.

Acknowledgements

Ecco, at this point, I want to honour all those people who have contributed in one way or the other to this thesis.

First and foremost, I would like to express my deepest gratitude to **Peter Puschnig**, who had the courage to take me under his wings four years ago. I could not have wished for a better mentor. Thank you for giving me the freedom to take many different scientific turns and gently guiding me when I have taken a wrong turn again. In addition, this endeavour would not have been possible without the steady assistance of **Georg Koller**. Thank you for many, fruitful discussions about science, but especially thank you also for those about somewhat less scientific topics. A special thank you, of course, to **Guido Fratesi** for taking the time to referee my thesis.

I want to thank all my colleagues from the Theoretical Solid State Physics group, who have shared part of my journey. It has been an honour and a privilege to have walked with giants. In particular, special thanks go to **Christian Kern**, not only for all of his physical explanations, but also for his continuous technical support regarding computation software. Furthermore, I want to explicitly mention **Dominik Brandstetter** and **Masoud Hamidi**, who have always brought joy and laughter into the grey everyday life. Without question, an invaluable contribution to this thesis has been made by our experimental colleagues from the Surface Science group, where I have had the pleasure of working with **Martin Sterrer**, **Mike Ramsey**, **Larissa Egger**, **Thomas Boné**, **Florian Schwarz** and **Max Niederreiter**. Their expertise forms the foundation of this thesis. Additionally, I very much enjoyed nice collaborations and numerous stimulating discussions with **Heiko Peisert** and **Marie-Sophie Sättele/Wagner** from Tübingen, as well as **Vitaliy Feyer**, **Iulia Cojocariu** and **Daniel Baranowski** from Trieste. I am grateful to our collaborators from Göttingen, especially **Matthijs Jansen** and **Wiebke Bennecke** for patiently explaining time-resolved pump-probe photoemission to me. Many thanks also to **Xavier Blase** and **Gabriele D'Avino** for introducing me to many-body theory and sharing their Fiesta code with us. Last but not least, I am greatly indebted to our colleagues from Dortmund, namely **Henning Sturmeit**, **David M. Janas** with his astonishing passion for science and **Giovanni Zamborlini**, who has always provided advice and motivation when needed.

Besides work, there has also been time for less serious activities over the past years, which should not go unnoticed. I have shared many happy memories with all the members of the **NanoGraz soccer team** under the leadership of **Robert Nuster**, for which I am sincerely grateful. They have been responsible for keeping my motivation high and my breath short. I thank **Peter Hartmann** for unravelling the mysteries of quantum mechanics and introducing me to the universal Oswald-Lamprecht theory. Going down this rabbit hole together has made life much funnier and easier. I also want to mention the four most extraordinary people, **#TheEtherKing (Thomas Pickl)**, **#QueenNici (Nicole Fohn)**, **#Happy (Markus Rechl)** and **#Kohli (Christoph Kohlfürst)**, without whom I would not have been able to get through this final chapter of my educational career. There will always be a special place in my heart for our fellowship bound by chemical romance.

Finally, I want to thank my family for countless hours of emotional support along this journey and bearing all my little quirks. There are not enough words in the world to express my gratitude and love.

Contents

1	OVERVIEW	1
2	GOING BEYOND PENTACENE	5
2.1	THEORETICAL BACKGROUND	6
2.1.1	INTRODUCTION TO DFT	6
2.1.2	INTRODUCTION TO POT	10
2.2	LONGER ACENES ON COINAGE METALS	14
2.2.1	INTRODUCTION	14
2.2.2	RESULTS AND DISCUSSION	15
2.3	INTERMOLECULAR DISPERSION OF HEPTACENE	26
2.3.1	INTRODUCTION	26
2.3.2	RESULTS AND DISCUSSION	27
2.4	CONCLUDING REMARKS	36
3	CONTROLLING SPIN AT INTERFACES	39
3.1	THEORETICAL BACKGROUND	40
3.1.1	SHORTCOMINGS OF DFT	40
3.1.2	THE HUBBARD CORRECTION	42
3.2	SPIN STATES IN A NiPC LAYER	45
3.2.1	INTRODUCTION	45
3.2.2	RESULT AND DISCUSSION	46
3.3	ADSORPTION OF SMALL GASES AT NiTPP	54
3.3.1	INTRODUCTION	54
3.3.2	RESULTS AND DISCUSSION	55
3.4	APPLICATION IN HETEROGENEOUS CATALYSIS	73
3.4.1	INTRODUCTION	73
3.4.2	RESULTS AND DISCUSSION	74
3.5	DETECTING CONFORMATIONAL CHANGES WITH ARPES	81
3.5.1	INTRODUCTION	81
3.5.2	RESULTS AND DISCUSSION	82
3.6	CONCLUDING REMARKS	87
4	PHOTOEMISSION EXCITON TOMOGRAPHY	89
4.1	THEORETICAL BACKGROUND	90
4.1.1	INTRODUCTION TO TDDFT	90
4.1.2	INTRODUCTION TO GW AND BSE	92
4.1.3	INTRODUCTION TO EXPOT	97
4.2	BENCHMARKING EXPOT	100
4.2.1	INTRODUCTION	100
4.2.2	RESULTS AND DISCUSSION	101
4.3	EXCITED STATES IN C₆₀ AGGREGATES	108

4.3.1	INTRODUCTION	108
4.3.2	RESULTS AND DISCUSSION	109
4.4	CONCLUDING REMARKS	123
5	OUTLOOK	125
6	LIST OF PUBLICATIONS	127
7	METHOD SECTION	129
	LONGER ACENES ON COINAGE METALS (CHAPTER 2.2)	129
	INTERMOLECULAR DISPERSION OF HEPTACENE (CHAPTER 2.3)	130
	SPIN STATES IN A NIPc LAYER (CHAPTER 3.2)	130
	ADSORPTION OF SMALL GASES AT NITPP (CHAPTER 3.3)	131
	APPLICATION IN HETEROGENEOUS CATALYSIS (CHAPTER 3.4)	131
	DETECTING CONFORMATIONAL CHANGES WITH ARPES (CHAPTER 3.5)	132
	BENCHMARKING EXPOT (CHAPTER 4.2)	132
	EXCITED STATES IN C ₆₀ AGGREGATES (CHAPTER 4.3)	133
8	APPENDIX	135
	GOING BEYOND PENTACENE	135
	CONTROLLING SPIN AT INTERFACES	138
9	BIBLIOGRAPHY	147

I Overview

Since the groundbreaking development of the fundamental theory of quantum mechanics, its outcomes, obtained by numerical computations, have enabled us to understand our world on levels far beyond our eyes could grasp at the size of molecules, atoms, and electrons. The theoretical efforts also benefited experimental progress, as a thorough understanding of even the smallest parts in the system is a fundamental aspect in the design of new materials. One such ever growing field of research is covered by the loose term of *organic electronics*. It summarizes a broad range of electronic devices from transistors to diodes or solar cells [1–7], which are not solely based on the classic, inorganic components but also incorporate organic molecules. Besides the intrinsic properties of the molecule, the performance of such devices is largely determined by the interface between molecules and metal contacts – a component of the device, which therefore has gotten increased attention [8–11]. However, the interaction between organic molecules and inorganic surfaces is not only interesting from a physical point of view. Finding its way into chemistry, controlling the interface of molecules and surfaces opened the door to new reactions for heterogenous catalysis and chemical sensors [12–15]. It is this large variety of applications that nowadays drives researchers to study the interplay between organic building blocks and solid surfaces, at which point, theoretical calculations provide insight into the processes on an atomistic level. Employing quantum mechanical simulations, in this thesis, I hope to contribute my share to the understanding of the electronic structure of molecular interfaces.

We will start our journey into surface science by studying the molecular class of acenes. As depicted in Figure 1.1., acenes consist of several benzene rings fused in a linear chain. Deposited onto metal surfaces, they have especially gained attention in the search for organic semiconductors, leading so far that one family member, pentacene (5 benzene rings), eventually became one of the most studied molecules in the field [16,17]. Further increasing the aromatic system is allegedly accompanied by properties favourable for (opto)-electronic devices such as increasing carrier mobility and a decreasing band gap [18–23]. However, going beyond pentacene in the series of acenes has so far been limited by the difficult experimental handling of longer molecules due to their high reactivity [24–28]. Only recently, it has been able to overcome this difficulty and to achieve a controlled growth of longer acenes on surfaces. The first chapter of this thesis is dedicated to the characterization of such newly formed acene-interfaces. In particular, we study monolayer films of hexacene (6 rings) and heptacene (7 rings) on metal surfaces of copper and silver [29–32]. At the hand of the two acene representatives, we introduce density functional theory calculations of extended systems and get to know parameters, which are frequently analysed in such projects. Among others, we meet photoemission orbital tomography as one of the go-to surface science techniques to unravel the energy level alignment of the frontier molecular orbitals. Furthermore, we address several ways how photoemission spectroscopy can assist in the investigation and characterization of new acene-interfaces.

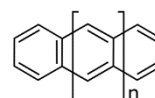


Figure 1.1: General structural formula for linear acenes with $n+2$ benzene moieties.

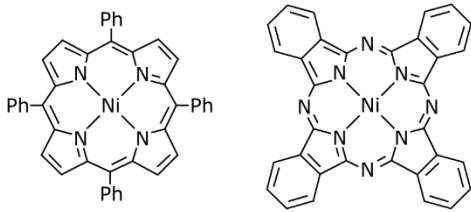


Figure 1.2: Structural formula for Nickel tetraphenylporphyrin (NiTPP, right) and for Nickel phthalocyanine (NiPc, left).

While the interaction between acenes and surfaces is rather straightforward due to their simple hydrocarbon structure, the second chapter deals with more complex systems – quite literally – by considering metal-organic complexes. In this broad class of molecular compounds, organic ligands coordinate a metal ion [33]. For extended systems, this offers the possibility to not only influence the interface properties *via* an organic molecule but, simultaneously, exploit the well-known spin and oxidation state versatility of transition metal ions. The promising fields of research resulting from the control and manipulation of spin states on a surface include spintronics or heterogeneous catalysis [34–36]. Out of the almost infinite pool of organic ligands, we focus on the molecular class of tetrapyrroles, where four pyrroles are connected in a ring-like structure, in the centre of which a metal can sit. Tetrapyrroles are perhaps better known from their most important representatives, the porphyrins, which even have been termed “*The Pigments of Life*” [37] due to their abundance in nature. The porphyrin of interest in this thesis is tetraphenylporphyrin shown to the left of Figure 1.2. As a second tetrapyrrole, we have chosen a molecule from the group of phthalocyanines sketched to the right of Figure 1.2. While phthalocyanines cannot be found in nature, they are easy to synthesise and are closely related to porphyrins – in fact, they could chemically go by the name tetrabenzotetraazaporphyrin. In general, the coordination pocket of a tetrapyrrole is able to incorporate various metal ions. Our main interest in this thesis is directed towards the possible spin and oxidation states of Nickel (Ni). Chelated by the dianionic ligand, Ni initially adopts a (+2) oxidation state, Ni(II). The square-planar environment is responsible for a non-magnetic distribution of the metal’s 8 valence electrons in its d-states. Even though Ni-tetrapyrrole complexes exhibit no initial spin, we will demonstrate how this electronic property can be tuned in contact with a surface [38] or by external stimuli [39–41]. In order to correctly describe the spin states at the interface, we have to extend our framework of density functional theory with the so-called Hubbard correction, which proves to be essential to account for experimental observations.

The first two chapters are mainly concerned with the understanding of ground state properties of specific molecular classes, predominantly, with the help of photoemission spectroscopy. In the final chapter, we take one step further and enter the realm of excited states. We are inspired by the emerging interest in *time-resolved* photoemission spectroscopy, which has resulted from the combination of photoemission spectroscopy with femtosecond lasers. The short laser pulses allow to optically excite and monitor the behaviour of excited states over time with photoemission. Angle-resolved detection of the photoemission aims to find characteristic fingerprints of the excited states in momentum space [42,43]. Recently, a new formalism termed “exPOT” has been developed to intuitively interpret such photoemission data [44]. The method is based on the simulation of the optical absorption spectrum of the molecule connecting the photoemission signal to the calculated excited state wave functions. In this chapter, we intend to test the applicability of the exPOT approach. For this reason, we first learn about two methods to calculate excited states of molecules, namely, linear response time-dependent density functional theory and the many-body perturbation framework of the

Bethe-Salpeter equation. After evaluating exPOT at the hands of three test cases, we present the first application of the new formalism to a real-life system. In our analysis, we discuss the absorption spectrum of the fullerene molecule C_{60} (structure in Figure 1.3) in a multilayer and interpret the relaxation of its excited states as measured with time-resolved photoemission [45].

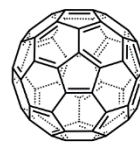
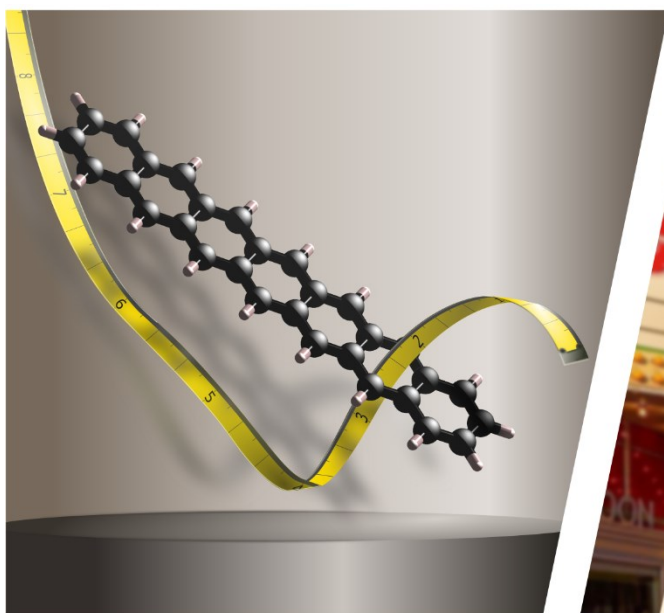


Figure 1.3: Structural formula of the three-dimensional buckminsterfullerene C_{60} .

Following this broad outline, the thesis is basically structured into the three parts mentioned above. Each of these three chapters starts with a general introduction into the theory, on which the chapter is focused. Afterwards, the main body of each chapter is formed by the respective publications, which cover the results of my research work. Most of the publications emerged from an interplay between several surface science approaches, the results of which all deserve to be treated explicitly. However, since this would go beyond the scope of this thesis, I discuss specifically my computational contribution. Consequently, this means that I do not simply reprint the published version of the manuscripts but have adapted text and figures and incorporated supplementary, computational results helpful over the course of the projects. Apart from some occasions, where discussion of measured data has proven necessary for the understanding of the text, further experimental details can be found in the respective publications. At the end of each chapter, I summarize, what we have learned on the way. Finally, we will end with a brief outline of ideas and future projects, which could benefit from this thesis.

Take-home message (THM): Throughout this thesis, the most memorable findings of each section will be summarized in such blue boxes to help the reader extract essential information.

2 Going Beyond Pentacene



Does Length matter?



Summary: Numerous studies have unravelled the thin film properties of the prototypical semiconductor pentacene. In contrast, higher homologues of pentacene have only recently been synthesized and brought onto surfaces for the first time. In this chapter, we investigate the electronic structures of ordered monolayer films of hexacene and heptacene on coinage metals. To obtain information about the interfaces, we mainly utilize photoemission orbital tomography – an approach, where we compare experimental and simulated photoemission data. In this way, we characterize the chemisorptive nature of the metal-molecule interaction on the pure metal surfaces (Ag and Cu). Decoupling the acenes electronically from the surface by passivation with oxygen, we also focus on *intermolecular* interactions and their impact on the photoemission spectra of the molecular monolayers. The results are summarized in the following four publications:

- [M.S. Sättele et al., J. Phys. Chem. C \(2022\)](#) (Hexacene on Ag and Cu)
- [M.S. Sättele et al., J. Phys. Chem. C \(2021\)](#) (Heptacene on Ag)
- [T.G. Boné et al., J. Phys. Chem. C \(2021\)](#) (Heptacene on Cu)
- [T.G. Boné et al., J. Phys.: Condens. Matter \(2023\)](#) (Heptacene on passivated Cu)

2.1 Theoretical Background

2.1.1 Introduction to DFT

For any thesis attempting to simulate molecular properties on an atomistic scale, it is almost inevitable to start with one of the most famous equations in physics and chemistry: the Schrödinger equation. Its main concept builds on the many-body wave function $\psi(\{\mathbf{x}\})$ with the set $\{\mathbf{x}\}$ including the coordinates of all particles forming the system. In the idea of quantum mechanics, this entity fully describes the state of an isolated quantum system and encodes any physical property of this state. For instance, all possible, stationary energy states E of the system are given by the eigenvalues of the Hamilton operator H . The non-relativistic and time-independent form of this equation, which we will be mostly concerned with in this chapter, is given in Equ. 2.1.

$$H\psi = E\psi \quad \text{Equ. 2.1}$$

In the case of molecules, the Hamiltonian considers all contributions to the energy of the interacting electron-nuclei system. Namely, this includes the kinetic energies T_n and T_e of both types of particles, the atomic nuclei and the electrons respectively, the nuclei-nuclei interaction V_{nn} , the electron-nuclei interaction V_{en} and the electron-electron interaction V_{ee} as in Equ. 2.2. Considering N electrons and M nuclei at positions \mathbf{r}_i and \mathbf{R}_i respectively, the operator may be written in its full form as Equ. 2.4. Note that here as for the rest of this derivation we adopt atomic units where $e = m_e = \hbar = \frac{1}{4\pi\epsilon_0} = 1$.

$$H = T_n + T_e + V_{nn} + V_{en} + V_{ee} \quad \text{Equ. 2.2}$$

$$H = -\frac{1}{2} \sum_I^M \frac{1}{M_I} \nabla_I^2 - \frac{1}{2} \sum_i^N \nabla_i^2 + \frac{1}{2} \sum_I^M \sum_{J \neq I}^M \frac{Z_I Z_J}{|\mathbf{R}_I - \mathbf{R}_J|} - \sum_I^N \sum_I^M \frac{Z_I}{|\mathbf{r}_i - \mathbf{R}_I|} + \frac{1}{2} \sum_i^N \sum_{j \neq i}^N \frac{1}{|\mathbf{r}_i - \mathbf{r}_j|} \quad \text{Equ. 2.3}$$

The increasing complexity of this expression for many-body systems is easily apprehensible. The problem is usually approached in a first step by utilizing the well-known Born-Oppenheimer approximation. It is based on the different masses of the atomic nuclei and the electrons, assuming the latter to move considerably faster than the nuclei. With the positions of the nuclei effectively staying fixed, the Hamiltonian can be reduced to its electronic part, where the repulsion V_{nn} between the atomic nuclei becomes merely a constant term and their kinetic energy T_n can be neglected. However, even in this simplified form, we would still have to treat $3N$ coordinates of the many-body wave function when applying the operator – a task, which is virtually impossible. Among other theoretical approaches, the problem became tractable on a large scale with the development of density functional theory (DFT). In the following, I will summarize only the most basic concepts of DFT, in-depth explanations of which fill numerous books and reviews [46–52].

The main idea of density functional theory is to replace the multi-coordinate dependency in the many-body Schrödinger equation with an object, the electron density $n(\mathbf{r})$, which only depends on three spatial coordinates. In two seminal theorems, Hohenberg and Kohn have

formulated that this is indeed possible and that the total energy E_{tot} of an interacting many-electron system can be obtained from Equ. 2.4 as

$$E_{tot} = \int V_{ext}(\mathbf{r})n(\mathbf{r}) d\mathbf{r} + F_{HK}[n] \quad \text{Equ. 2.4}$$

Here, V_{ext} is an external potential usually attributed with the attractive Coulomb potential of the nuclei V_{en} , which is a *unique* functional of the electron density up to an additive constant (*existence theorem*). $F_{HK}[n]$ is a functional independent of the specific V_{ext} of the system, i.e., universally valid, and composed of the kinetic energy $T_e[n]$ and the electron-electron interaction $V_{ee}[n]$. Then, one can show that following Rayleigh-Ritz's minimal principle to find the ground state energy by minimizing E_{tot} with respect to $n(\mathbf{r})$ automatically leads to the ground state electron density (*variational theorem*).

Their realization further meant that also the full Hamiltonian and the many-body wave function are uniquely determined by the electron density and, as a consequence, knowing the density is sufficient to obtain all properties of interest. However, to put the formalism to a test at real systems, we so far, unfortunately, lack an expression for the universal functional F_{HK} on how to treat kinetic energy and electron-electron interaction in terms of the density. Kohn and Sham proposed a practicable solution to this problem by introducing a fictitious auxiliary system. This auxiliary system is composed of non-interacting electrons, which, by construction, yield the exact same electron density as in the interacting real system. Borrowing from Hartree-Fock theory, the many-electron wavefunction of this new system can then be constructed as a single Slater determinant from the single-electron wave functions φ , which are better known to us as the electronic orbitals.

In Kohn-Sham's approach, the kinetic energy $T_s[n]$ equals the sum over the energies of the non-interacting electrons and can be expressed in terms of their orbitals φ as Equ. 2.5.

$$T_s[n] = -\frac{1}{2} \sum_j \langle \varphi_j | \nabla^2 | \varphi_j \rangle \quad \text{Equ. 2.5}$$

Furthermore, since the fictitious system is originally assumed non-interacting, we reintroduce electron-electron interaction with the classical self-repulsion of the electron density $E_H[n]$ (Equ. 2.6).

$$E_H[n] = \frac{1}{2} \int \int \frac{n(\mathbf{r})n(\mathbf{r}')}{|\mathbf{r} - \mathbf{r}'|} d\mathbf{r}d\mathbf{r}' \quad \text{Equ. 2.6}$$

Finally, we rely on a last contribution $E_{xc}[n]$, termed the exchange-correlation energy, to account for all remaining differences between the original and the Kohn-Sham auxiliary system. Namely, this includes non-classical electron-electron interactions not covered by our electrostatic term and the difference between the kinetic energy of the real system and the non-interacting one. Combining these three energies T_s , E_H and E_{xc} , Kohn and Sham arrived at the universal functional in Equ. 2.7

$$F_{KS}[n] = T_s[n] + E_H[n] + E_{xc}[n] \quad \text{Equ. 2.7}$$

and proved that together with Equ. 2.4, their auxiliary system is able to yield the exact electron ground state of the original system.

With Equ. 2.7 and the external potential V_{ext} , we can further formulate single-electron Schrödinger equations for the non-interacting electrons of our auxiliary system moving in an effective potential V_{KS} (Equ. 2.8). The Kohn-Sham potential V_{KS} takes the form of Equ. 2.9, where V_H and V_{xc} are the functional derivatives of the respective energy terms in Equ. 2.7.

$$\left(-\frac{\nabla^2}{2} + V_{KS}(\mathbf{r})\right)\varphi_j(\mathbf{r}) = \varepsilon_j\varphi_j(\mathbf{r}) \quad \text{Equ. 2.8}$$

$$V_{KS}(\mathbf{r}) = V_{ext}(\mathbf{r}) + V_H[n](\mathbf{r}) + V_{xc}[n](\mathbf{r}) \quad \text{Equ. 2.9}$$

The eigenvectors of these Schrödinger equations are the aforementioned single-particle wave functions φ , the Kohn-Sham orbitals, with which we construct the electron density via Equ. 2.10. Recall that as long as V_{KS} , or equivalently the energy functionals in F_{KS} , are chosen appropriately, this density is designed to represent the true ground state density of the real system.

$$n(\mathbf{r}) = \sum_{j=1}^{occ.} |\varphi_j(\mathbf{r})|^2 \quad \text{Equ. 2.10}$$

The Kohn-Sham energies ε are the eigenvalues belonging to φ . Janak proved that they further relate to the total energy as the derivate of the energy with respect to the fractional occupation f_j of orbital j (Equ. 2.11). Although strictly speaking, in the ground state, his theorem only holds for adding or removing charge to the frontier orbitals.

$$\varepsilon_j = \frac{\delta E_{tot}}{\delta f_j} \quad \text{Equ. 2.11}$$

It should be emphasized that we have introduced the single-electron wave functions φ as objects of a non-interacting auxiliary system. Hence, *a priori*, neither φ nor ε should have physical origin with respect to the real system. Nonetheless, utilizing Equ. 2.11, it can be shown that the energy of the highest occupied orbital, and only this energy, can be interpreted and is indeed the ionization potential of the system.

Up to this point, we have outlined the framework of DFT, which links the ground state density to the ground state total energy and, first and foremost, is theoretically exact. Note, however, that we have not yet stated the explicit dependency of the exchange-correlation functional on the density. This is simply because the exact expression is not known – feeling like a *déjà vu*. For DFT to actually work in practical applications, $E_{xc}[n]$ currently needs to be approximated. Over the years, increasingly elaborate schemes have been suggested on how to approach this approximation, which we want to briefly mention. The simplest one is the local density approximation (LDA) and has already been introduced in the work of Kohn and Sham. In essence, it assumes that at each point \mathbf{r} of the real system with density $n(\mathbf{r})$, the xc -contribution corresponds to the xc -energy of a homogeneous electron gas $\varepsilon_{xc}^{hom}(n(\mathbf{r}))$ with the same density (Equ. 2.12).

$$E_{xc}^{LDA}[n] = \int n(\mathbf{r}) \varepsilon_{xc}^{hom}(n(\mathbf{r})) d\mathbf{r} \quad \text{Equ. 2.12}$$

Evaluating the homogeneous electron gas, the energy contribution ϵ_{xc}^{hom} per particle is split linearly into an exchange and a correlation term. While the exchange contribution can be derived analytically e.g., from Hartree-Fock theory, the correlation energy is typically obtained from a function fitted to numerical Monte Carlo simulations over a range of densities. By construction, LDA works well for systems with an almost uniform electron distribution, i.e., where the electron density varies only slowly in space such as in metals. On the opposite, LDA should be expected to fail for molecules with much stronger spatial variations of the density in density. For the latter systems, agreement between LDA calculations and experiments often stem from fortuitous error cancelation rather than from physical reasons.

A first improvement to account for varying electron densities is considering not only the density but also its gradient in the expression of the exchange-correlation functional. Such approaches have become known as generalized gradient approximations (GGA) and take the general form of Equ. 2.13.

$$E_{xc}^{GGA}[n] = \int f(n(\mathbf{r}), |\nabla n(\mathbf{r})|) n(\mathbf{r}) d\mathbf{r} \quad \text{Equ. 2.13}$$

Opposed to LDA, where exchange and correlation are uniquely defined, there is no unique way to create a dependency on the two parameters, $n(\mathbf{r})$ and $\nabla n(\mathbf{r})$. One such relation has been proposed by Perdew, Burke and Ernzerhof (PBE) and, since then, has become the most widely used GGA functional in solid state physics. This thesis being no exception, we have also treated our periodic systems mainly within PBE-GGA [53].

While it can be tedious to derive density functionals for the exchange-correlation contribution, Hartree-Fock theory readily offers an exact expression for, at least, the exchange energy in many-electron systems. This orbital-dependent term is given by Equ. 2.14

$$E_x^{HF} = -\frac{1}{2} \sum_{i,j=1}^N \int \int \frac{\varphi_i^*(\mathbf{r})\varphi_j^*(\mathbf{r}')\varphi_j(\mathbf{r})\varphi_i(\mathbf{r}')}{|\mathbf{r} - \mathbf{r}'|} d\mathbf{r}d\mathbf{r}' \quad \text{Equ. 2.14}$$

for the interaction between orbital i and j . As we have anyway introduced KS orbitals, Equ. 2.14 can also be incorporated into DFT. It was argued that, in conjunction with the density-dependent correlation energy, a linear combination of exact orbital- and approximate density-dependent exchange (E_x^{HF} and E_x^{app} , respectively) should be applied. Hence, in the simplest form, a scaling parameter α determines the weight of each contribution leading to the so-called global hybrid functionals for exchange-correlation (Equ. 2.15) [54,55].

$$E_{xc}^{hyb}[n] = \alpha E_x^{HF}[\{\varphi_i\}] + (1 - \alpha)E_x^{app}[n] + E_c^{app}[n] \quad \text{Equ. 2.15}$$

More sophisticated approaches include range-separated hybrid (RSH) functionals, where the description of exchange is additionally split spatially into a short-range (SR) and long-range (LR) contribution. In the two regions, the weights α and β control E_x^{HF} and E_x^{app} [56–58].

$$E_{xc}^{RSH}[n] = \alpha E_x^{HF,SR}(\gamma) + (1 - \alpha)E_x^{app,SR}(\gamma) + (\alpha + \beta)E_x^{HF,SR}(\gamma) + (1 - \alpha - \beta)E_x^{app,LR}(\gamma) + E_c^{app} \quad \text{Equ. 2.16}$$

The parameter γ , in inverse length scale, essentially defines the spatial range at which the functional switches between both behaviours.

Having focused on improving the exchange term, our approximate solutions to treat correlation are not ideal either. In fact, by applying the LDA or GGA (semi)locally for the

density at each point \mathbf{r} , we miss a possible influence of a perturbation in another region \mathbf{r}' on the potential at \mathbf{r} . Such non-local charge fluctuations arise from spontaneous polarizations in the system and may act over large distances in space. They are termed *van der Waals-* or *dispersion*-interactions. Exchange-correlation functionals have been developed, which specifically capture this long-range electron correlation, however, they are merely mentioned incidentally in this thesis. Instead, we predominantly employ a dispersion correction, which evaluates the dispersion energy atom-pairwise as in Equ. 2.17 [59,60].

$$E_{c,disp} = - \sum_{A \neq B} f_{damp}(R_{AB}) \frac{C_{AB}}{R_{AB}^n} \quad \text{Equ. 2.17}$$

For each atom-pair ($A - B$) with a distance R_{AB} between them, the coefficient C_{AB} specifies the effective interaction strength. In the end, the correction energy is added to the total energy.

2.1.2 Introduction to POT

Besides density functional theory, a recurring topic in this thesis will be the interpretation of photoemission spectroscopy data utilizing the so-called photoemission orbital tomography (POT) approach. It is, therefore, worthwhile to introduce this technique, both, from an experimental as well as a theoretical point of view.

Our understanding of photoemission centres around Einstein's award-winning explanation of some experiments first conducted two decades earlier by Hertz. When a material is excited with light of sufficient energy, electrons will be emitted from the material. The kinetic energy E_{kin} such an electron can possess, is determined by the energy of the incident light ω and the energy E_{Bind} needed to remove the electron from the sample (Equ. 2.18).

$$E_{kin} = \omega - E_{Bind} \quad \text{Equ. 2.18}$$

In this description, electromagnetic light is seen as quantized packages, the photons, and the energy of each package is dependent on the frequency of the light according to Planck's formula. Following Equ. 2.18, *photoelectrons* can be generated as soon as the energy of a photon package is large enough to overcome the electron's binding energy. Conversely, the kinetic energy of a liberated electron contains information about the energy of its initial state in the material. By collecting the whole range of kinetic energies generated by a photon energy, we can map the distribution of electronic levels in the sample under investigation.

However, counting electrons as a function of kinetic energy is not the only information that can be gained from photoemission. For 2D-periodic systems, symmetry arguments suggest that the electron's momenta parallel to the surface have to be conserved during the emission process. Assuming an electron leaves the surface under the azimuthal angle ϕ and the polar angle θ with respect to a reference plane, its parallel momentum components p_x and p_y , or equivalently k_x and k_y in momentum space, are determined by Equ. 2.19 and Equ. 2.20.

$$p_x = k_x = \sqrt{2E_{kin}} \sin \theta \cos \phi \quad \text{Equ. 2.19}$$

$$p_y = k_y = \sqrt{2E_{kin}} \sin \theta \sin \phi \quad \text{Equ. 2.20}$$

Thus, by measuring the photoemission intensity in an angle-resolved manner, that is, as a function of ϕ and θ , we may not only link the *energy* of the electron before and after

photoemission but also its *momentum*. The resulting 3-dimensional data set, $I(E_{kin}, k_x, k_y)$, happens to be a distinct fingerprint for each electronic state and is the basis of angle-resolved photoemission spectroscopy (ARPES) experiments.

At this point, we will not get into instrumental details how the experimental data is actually collected. Instead, we turn towards a more theoretical description of the photoemission process. For this purpose, we closely follow the quantum mechanical explanations by M.Dauth et al. [61], which we will later also revisit in chapter 4.1.3. We start with the general expression of Fermi's golden rule, which states the transition probability $W_{i \rightarrow f}$ between an initial state Ψ_i and a final state Ψ_f as

$$W_{i \rightarrow f} \propto |\langle \Psi_f | H_{int} | \Psi_i \rangle|^2 \times \delta(\omega + E_i - E_f) \quad \text{Equ. 2.21}$$

where H_{int} describes a periodic perturbation with frequency ω responsible for the transition between an initial state with energy E_i and a final state with energy E_f . The term $\delta(E)$ ensures energy conservation during this process. Specifically in the case of photoemission spectroscopy, this perturbation is described by the electromagnetic field of a photon interacting with an N -electron system and exciting it from its initial state Ψ_i^N to the final Ψ_f^N . The electromagnetic field is characterized by the vector potential \mathbf{A} and is assumed to be constant in space. For photon wavelengths in the ultraviolet regime acting on molecules that are roughly two orders of magnitude shorter than the photon's wavelength. Thus, this assumption is reasonable and corresponds to the so-called "dipole approximation", in which the originally space-dependent vector potential is reduced to the lowest-order term of its multipole expansion. With the perturbing potential transforming the original momentum operator \mathbf{P} to $(\mathbf{P} - \frac{e}{c}\mathbf{A})$, H_{int} can ultimately be simplified to yield Equ. 2.22. Note that in the evaluation of the operator expression, the term quadratic in \mathbf{A} is neglected as it is considered to be small.

$$W_{i \rightarrow f} \propto |\langle \Psi_f^N | \mathbf{A} \cdot \mathbf{P} | \Psi_i^N \rangle|^2 \times \delta(\omega + E_i^N - E_f^N) \quad \text{Equ. 2.22}$$

In the context of photoemission, Equ. 2.22 is known as the one-step-model of photoemission, which we aim to understand further. Let us start by analysing the energy conservation during the process. At the start of the experiment, the investigated system is presumed to be in its electronic ground state, the energy of which is given by the expectation value of the N electron Hamiltonian with the ground state wave function $\Psi_{i,0}^N$, i.e.,

$$E_i^N = E_{i,0}^N \quad \text{Equ. 2.23}$$

For the final state Ψ_f^N , we utilize the so-called "sudden approximation", which describes the photoemission as an instantaneous change to the system. Without correlation between the outgoing photoelectron and the remaining system, the wavefunction of the final state can be factorized into the free electron γ_k and a $(N - 1)$ electron term, where a hole remains in the j -th electronic level (Equ. 2.24). Note that the operator \mathcal{A} in Equ. 2.24 simply ensures the correct anti-symmetrisation of $\Psi_{f,j}^N$ to satisfy Pauli's principle. As a consequence of the product ansatz and the associated separation of variables, the energy belonging to Ψ_f^N can be split into the sum

over the two independent contributions, i.e., the kinetic energy of the detached electron E_{kin} and the energy of the j -th ionized $(N - 1)$ system.

$$\Psi_f^N = \mathcal{A} \Psi_{f,j}^{N-1} \gamma_k \quad \text{Equ. 2.24}$$

$$E_f^N = E_{f,j}^{N-1} + E_{kin} \quad \text{Equ. 2.25}$$

With the help of Equ. 2.23 and Equ. 2.25, we rewrite the energy conservation of Equ. 2.22 to predict the measurable kinetic energy of a photoemitted electron. Equ. 2.26 shows the dependency of E_{kin} on the photoemission probe energy, the energy of the initial ground state and the energy of the ionized final state. Assuming a solely vertical process during photoemission, we may neglect electronic and nuclear relaxation. Then, the energy difference between the N and $(N - 1)$ -electron system corresponds to the ionization potential ε_j of the j -th state, from which the electron was removed, and we arrive at an expression very similar to our beginning statement in Equ. 2.18. As will be encountered throughout this thesis, the framework of POT is commonly applied to extended molecular films. For periodic systems, the ionization energy ε_j in Equ. 2.26 can equivalently be expressed by the work function WF and the binding energy of the j -th molecular level E_B^j with respect to the Fermi-level.

$$E_{kin} = \omega + (E_{i,0}^N - E_{f,j}^{N-1}) = \omega - \varepsilon_j = \omega - (E_B^j + WF) \quad \text{Equ. 2.26}$$

After clarifying the energy conservation term, in a next step, we have to evaluate the transition matrix element of Equ. 2.22. For the final state, we assume the product ansatz of Equ. 2.24. In addition, we limit the perturbation to act only on the liberated electron and neglect terms describing indirect effects such as Auger transitions. After some algebra [61], the matrix element can finally be written as Equ. 2.27, where for convenience, we have split the integration over the set of all electronic coordinates of the full system into the contribution of the emitted electron r_N and the remaining set $\{\mathbf{x} \setminus \mathbf{r}_N\}$. This mathematical gimmick reveals an expression for the overlap of the many-electron initial state $\Psi_{i,0}^N$ with the final state $\Psi_{f,j}^{N-1*}$, which is known as the Dyson orbital $D_j(\mathbf{r}_N)$ (Equ. 2.28).

$$\langle \Psi_{f,j}^N | \mathbf{A} \cdot \mathbf{P} | \Psi_{i,0}^N \rangle = \int \gamma_k^*(\mathbf{r}_N) \mathbf{A} \cdot \mathbf{P} \left[\sqrt{N} \int \Psi_{f,j}^{N-1*}(\{\mathbf{x} \setminus \mathbf{r}_N\}) \Psi_{i,0}^N(\{\mathbf{x}\}) d\{\mathbf{x} \setminus \mathbf{r}_N\} \right] d\mathbf{r}_N \quad \text{Equ. 2.27}$$

$$D_j(\mathbf{r}_N) = \sqrt{N} \int \Psi_{f,j}^{N-1*}(\{\mathbf{x} \setminus \mathbf{r}_N\}) \Psi_{i,0}^N(\{\mathbf{x}\}) d\{\mathbf{x} \setminus \mathbf{r}_N\} \quad \text{Equ. 2.28}$$

Employing the construct of the Dyson orbital reduces the dependency of the matrix element from N -electron coordinates to the single coordinate \mathbf{r}_N of the outgoing electron.

$$\langle \Psi_{f,j}^N | \mathbf{A} \cdot \mathbf{P} | \Psi_{i,0}^N \rangle = \int \gamma_k^*(\mathbf{r}_N) \mathbf{A} \cdot \mathbf{P} D_j(\mathbf{r}_N) d\mathbf{r}_N \quad \text{Equ. 2.29}$$

However, to arrive at a conceivable interpretation of the integral in Equ. 2.29, we have to make an additional assumption about the final state of the released photoelectron γ_k . In line with the ‘‘sudden approximation’’, the electron is emitted immediately into the vacuum region and does not feel the potential of the remaining $(N - 1)$ system. The state of such a free electron can be characterized by a plane wave (Equ. 2.30).

$$\gamma_k = e^{i\mathbf{k}\mathbf{r}} \quad \text{Equ. 2.30}$$

Utilizing Equ. 2.30 in Equ. 2.29 and applying the momentum operator reveals the integrand to be simply the Fourier transform of the Dyson orbital D_j , converting it from the real-space electronic coordinate \mathbf{r}_N to momentum space \mathbf{k} . Following Fermi's golden rule, the photoemission intensity in momentum space then relates to the absolute square of Fourier transform modulated by the light-polarization factor $|\mathbf{A} \cdot \mathbf{k}|^2$.

$$I(k) \propto |\mathbf{A} \cdot \mathbf{k}|^2 |\mathcal{F}[D_j](\mathbf{k})|^2 \times \delta(\omega - E_{kin} - \varepsilon_j) \quad \text{Equ. 2.31}$$

The \mathbf{k} -resolved intensity pattern is, thus, mainly determined by the structure of the Fourier-transformed Dyson orbital, which is evaluated along all momentum vectors \mathbf{k} with a certain length. Visualizing a 3-dimensional representation of the Dyson orbital, vectors of equal length correspond to a (hemi)spherical cut through its Fourier transform. The radius of the sphere $|\mathbf{k}|$ is set by the kinetic energy, at which the photoelectron is detected. Combining the dispersion relation of a free electron with Equ. 2.26, the cut is taken according to Equ. 2.32 for all \mathbf{k} -vectors with

$$|\mathbf{k}| = \sqrt{2(\omega - \varepsilon_j)} \quad \text{Equ. 2.32}$$

While Dyson orbitals are the formally correct construct to describe photoemission, they are usually approximated with molecular orbitals in practical application and also throughout this thesis. Molecular orbitals of isolated systems or equivalently molecular bands of extended structures can be readily obtained from quantum mechanical calculations and have proven to be a reliable reference for the interpretation of photoemission experiments [61]. Ultimately, the combination of angle-resolved photoemission data with feasible quantum mechanical predictions forms the heart of photoemission orbital tomography.

2.2 Longer Acenes on Coinage Metals

2.2.1 Introduction

The acene family is perhaps most prominently represented by its five-ring member, pentacene, in the search for organic semiconductors [16,17]. Marked as a potential target for electronic devices, the molecule has been intensively studied and is still considered as a prototypical example for this field of research. Derivatives of pentacene, but also its shorter brother tetracene, are often linked to keywords such as organic light-emitting diodes, thin-film transistors, or photovoltaic cells [18,62–68].

Despite the rumoured range of applications in surface science, acenes longer than pentacene are scarcely deposited on metal substrates. In contrast to their smaller homologues, extensive use in experimental studies is limited by the molecules' instability toward light and oxygen [24–26,69,70]. Bypassing intricate working conditions, on-surface syntheses starting from stable precursors nonetheless provided access to acenes up to dodecacene and, thereby, revealed first insights into the behaviour of higher acenes on surfaces [71–78]. However, such strategies are mainly restricted to submonolayer coverages, where electronic properties are investigated on a single molecule level by scanning tunnelling microscopy (STM) or atomic force microscopy (AFM) [71,72,74,77,79].

For applications in opto-electronic devices, it is often preferred to know the arrangement and electronic structure of full monolayer films. The longest acene, for which controlled film formation on a surface was achieved, is hexacene [80,81], albeit the corresponding studies were conducted on non-interacting substrates. The interaction of aromatic molecules with possible contacts like the coinage metal surfaces of copper and silver presumably leads to a distinct change in the electronic structure due to charge transfer and chemisorption [82–85]. To get more detailed insight into higher acenes on coinage metals, we aim to provide a profound analysis of their geometric and electronic properties.

Article Information and Author Contribution

Our investigations have resulted in three publications, which are reviewed together in the following section. The acene thin films are generally characterized in ref. [29] and [30] employing a variety of surface-sensitive techniques. Here, my calculations complement data measured by my experimental colleagues **Marie S. Wagner** (former **Sättele**) and **Larissa Egger**. I was involved in discussion and interpretation of the results and provided the theoretical analysis, including text and Figures, for the manuscripts. More specifically focusing on charge transfer at an interface, the article of ref. [31] can be regarded as a successful example of computer assisted experiment design and represents my main contribution to this project. Based on my simulations of the interface, **Thomas G. Boné** kindly set up and conducted the corresponding experiments, which I then analysed. Putting calculated and measured data together, I have been responsible for designing the Figures and writing the first draft of the manuscript.

Hexacene on Cu(110) and Ag(110): Influence of the Substrate on Molecular Orientation and Interfacial Charge Transfer

Marie S. Sättele, Andreas Windischbacher, Katharina Greulich, Larissa Egger, Anja Haags, Hans Kirschner, Ruslan Ovsyannikov, Erika Giangrisostomi, Alexander Gottwald, Mathias Richter, Serguei Soubatch, F. Stefan Tautz, Michael G. Ramsey, Peter Puschnig, Georg Koller, Holger F. Bettinger, Thomas Chassé, and Heiko Peisert*

Cite This: *J. Phys. Chem. C* 2022, 126, 5036–5045

Read Online

This is an open access article published under a Creative Commons Attribution (CC BY) License, which permits unrestricted use, distribution and reproduction in any medium, provided the author and source are cited.



ACS
AUTHORCHOICE

Going beyond Pentacene: Photoemission Tomography of a Heptacene Monolayer on Ag(110)

Marie S. Sättele, Andreas Windischbacher, Larissa Egger, Anja Haags, Philipp Hurdax, Hans Kirschner, Alexander Gottwald, Mathias Richter, François C. Bocquet, Serguei Soubatch, F. Stefan Tautz, Holger F. Bettinger, Heiko Peisert, Thomas Chassé, Michael G. Ramsey, Peter Puschnig, and Georg Koller*

Cite This: *J. Phys. Chem. C* 2021, 125, 2918–2925

Read Online

Demonstrating the Impact of the Adsorbate Orientation on the Charge Transfer at Organic–Metal Interfaces

Thomas Georg Boné,[†] Andreas Windischbacher,[†] Marie S. Sättele, Katharina Greulich, Larissa Egger, Thomas Jauk, Florian Lackner, Holger F. Bettinger, Heiko Peisert, Thomas Chassé, Michael G. Ramsey, Martin Sterrer, Georg Koller, and Peter Puschnig*

Figure 2.1: Headers of the three articles [29–31] including all contributing authors. All studies were published in the Journal of Physical Chemistry C.

2.2.2 Results and Discussion

Investigated Systems

We expand the series of acenes towards the two next higher homologous of pentacene, i.e.: hexacene (6A) and heptacene (7A). Both molecules were deposited each onto a Cu(110) and a Ag(110) surface by evaporation. While this is without problems in the case of hexacene, for heptacene, due to its increased instability, the deposition is achieved *via* a precursor molecule. Heating of the precursor leads to a transformation into the acene *via* thermally induced cycloreversion.

The (110) surface of *fcc*-metals is characterized by close-packed metal atom rows in the $[1\bar{1}0]$ crystal direction. Analysis of LEED and STM images suggests that the molecules predominantly arrange along those rows on *both* surfaces. By doing so, 6A and 7A follow the path of smaller acenes on Cu(110), which are all found facing the $[1\bar{1}0]$ direction [85,86]. However, for Ag(110), our observation for the longer acenes is in contrast to previous studies,

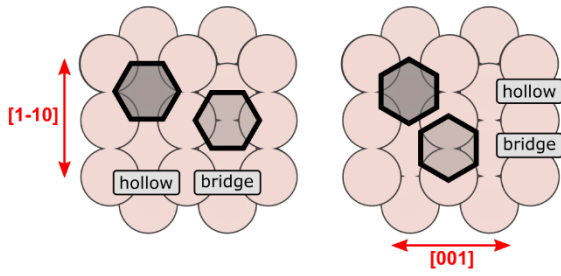


Figure 2.2: Schematic sketch illustrating possible adsorption sites for acenes on (110) surfaces. The long molecular axis might be oriented along the $[1\bar{1}0]$ (left) or the $[001]$ direction.

In addition to the adsorption site, we vary the molecular arrangement on the surface. Beside the experimentally determined unit cells for a full monolayer, we consider cells of differing coverage (small, medium and full coverage) and relative alignment of the molecules (parallel and shifted to each other). In total, we study 20 adsorption configurations for each interface, the epitaxial matrices and molecular coverages of which are listed in the Appendix (Table 8.1).

The adsorption energies of all optimized structures are summarized in Figure 2.3a in the left panels for Ag(110) and in the right panels for Cu(110). In the case of Ag(110), all adsorption configurations of either 6A or 7A are in the same energetic range (within 0.2 eV). As the width of a benzene-ring (2.45 Å) does not match a specific surface unit cell distance of Ag (Ag: 2.89 x 4.05 Å), each configuration along $[001]$ or $[1\bar{1}0]$ consists of benzene moieties above “bridge” and “hollow” sites (e.g.: Figure 2.3b left). The interplay of different interactions of the carbon backbone with the substrate, i.e.: favourable and unfavourable ones, results in a shallow energy landscape. For both acenes, 6A and 7A, there is one configuration each along $[001]$ and $[1\bar{1}0]$ competing for the most favoured structure in an energetic range of about 0.05 eV. Thus, based on our calculations, we are not able to unambiguously confirm the experimental observation, where a $[1\bar{1}0]$ alignment is favoured over the $[001]$ orientation. Instead, we would rather expect mixed domains. We suspect two possible reasons for this

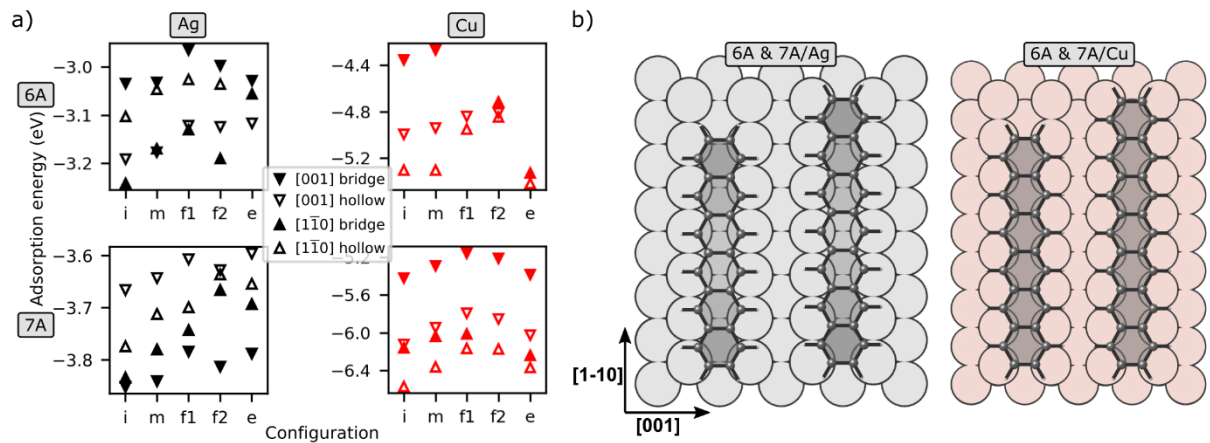


Figure 2.3: a) Adsorption energies of 6A and 7A on Ag(110) and Cu(110) for unit cells with different size and relative alignment of the molecules calculated with PBE-D3. The configurations are denoted as: i=small coverage, m=medium coverage, f1=full coverage with parallel order, f2=full coverage with shift between molecules, e=experimental unit cell b) Model of the acenes oriented along the $[1\bar{1}0]$ direction as determined from experiment.

discrepancy. First, we have to consider the accuracy of the theoretical approximations in our approach. For instance, we describe van der Waals interactions by Grimme’s D3 dispersion correction, which may introduce errors in the same order of magnitude as the observed energy differences between [001] and $[1\bar{1}0]$ configurations. Indeed, it has recently been argued that many-body dispersion effects have to be accounted for to accurately describe the adsorption of acenes on some coinage metal surfaces [89,90]. Unfortunately, we were not able to converge these kinds of calculations. Secondly, the experimental observation of ordered layers with a single molecular orientation despite comparably small energetic differences between the adsorption structures could also indicate kinetic effects during the film growth. Processes such as adsorption at step edges or kinks of the Ag substrate, or diffusion barriers on terraces and across step edges may play a role in the film formation. Indeed, in a later section, we will find further indications for the importance of the preparation conditions. It would certainly be interesting to shed light on all these influences with a high accuracy computational approach, however, this is not the scope of the present work.

On the Cu-surface, we see a clearly preferred adsorption geometry irrespective of the chosen unit cell at the “hollow” position along the $[1\bar{1}0]$ direction, which is energetically favoured to a [001] alignment by at least 0.3 eV. The preferred orientation is in good agreement with experiments and is likely due to the high commensurability of acenes and Cu. In fact, the surface unit cell distance of Cu along the $[1\bar{1}0]$ -direction (Cu: 2.56 Å) matches with the width of a benzene-ring (2.45 Å). Therefore, each benzene moiety occupies nearly the same surface site, e.g., “hollow” (see Figure 2.3b right), and the molecule is easily able to maximize the interaction with the substrate as we will further demonstrate below.

THM: Analysing the adsorption energies of different configurations of hexacene and heptacene on Ag(110), we cannot conclude on a clearly preferred adsorption orientation. In contrast on Cu(110), the commensurability between acenes and surface unit cell favours arrangements along the metal rows in the $[1\bar{1}0]$ direction.

Finally, comparing the two metal surfaces, Ag to Cu, we note the high adsorption energies on the Cu-surfaces compared to their Ag counterparts. In concordance with Cu being more reactive, this is a sign for increased interaction with the surface. Including the smaller homologues, tetracene and pentacene, in our calculations, we find the trend of the adsorption energies given in Figure 2.4. Under the assumption of chemisorption, it is accepted that the energies should scale linear with the size of the acene [91–95], adding for each ring four-times the bond energy of a C-metal bond to the energy of the next smaller aromatic unit. Comparing the straight lines fitted to our calculated energies (dashed in Figure 2.4), we find the assumption valid in both cases, Ag and

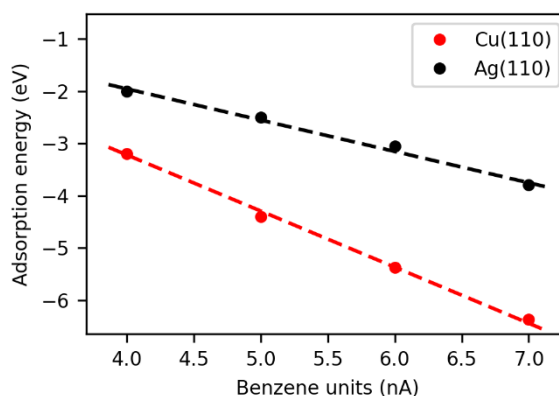


Figure 2.4: Adsorption energies of benzene and different acenes (4A, 5A, 6A, 7A) on coinage metals (Ag and Cu) in the most favourable configurations as obtained with PBE-D3. Dashed lines is a linear fit to the calculated adsorption energies approximate the linear behaviour of chemisorption,

Cu. This would also be in line with the adsorption distances found in our simulations. The molecules approach the surfaces significantly closer (Ag: $\sim 2.7\text{\AA}$; Cu: $\sim 2.2\text{\AA}$) than the estimated limit for physisorption given as the sum of the van der Waals radii of the metals and the molecule (on Ag: 3.42\AA ; on Cu: 3.1\AA).

ARPES

To get a better understanding of the interactions at the interfaces, we turn to photoemission experiments. Connecting the idea of frontier molecular orbitals to experimental photoemission signals, POT has become an established technique to explain the energy alignment of adsorbate-systems. For our acenes, we introduce the approach at the example of 7A in Figure 2.5. Here, the five orbitals HOMO-2 to LUMO+1 calculated for the gas phase molecule are displayed together with their corresponding simulated photoemission intensity distribution. Each orbital is attributed with a unique pattern in momentum space, which can be compared to measured momentum maps. By recording a stack of photoemission data over different binding energies, the energetic position of the orbitals in the valence region can, thus, be mapped (Figure 2.5 right). In the final step, the assignment is confirmed by comparison with calculations for the most stable adsorption structures from the previous section.

The results of our evaluation are summarized in Figure 2.6. Full analysis of the data sets for 6A and 7A on Ag and Cu can be found in the Appendix (Figure 8.1). To complete the picture, we also included the energy levels of tetracene and pentacene from previous investigations [85,86]. Most importantly, compared to the smaller acenes, POT reveals an increased charge transfer upon adsorption of 6A and 7A on both surfaces. In the case of Ag(110), signatures of the LUMO can be found below the Fermi-energy. On Cu, even the LUMO+1 gets occupied by electron transfer from the substrate. This finding is fully supported by our computational models, where we see equally strong charge rearrangements for the respective interfaces.

The complex redistribution of electrons at the interfaces contributes to a change of surface dipoles, which we can quantify *via* photoemission spectroscopy as a modification to the work function of the sample. The measured changes with respect to clean Ag(110) ($WF_{\text{exp}} = 4.35\text{ eV}$) and Cu(110) ($WF_{\text{exp}} = 4.43\text{ eV}$) upon adsorption of the molecules are summarized in Table 2.1. We find little difference between the two acenes. For both, 6A and 7A, the work function change on Ag (-0.2 eV) is significantly smaller than on Cu (-0.8 eV). The calculated electronic properties of our optimized structures reproduce the experimental results nicely.

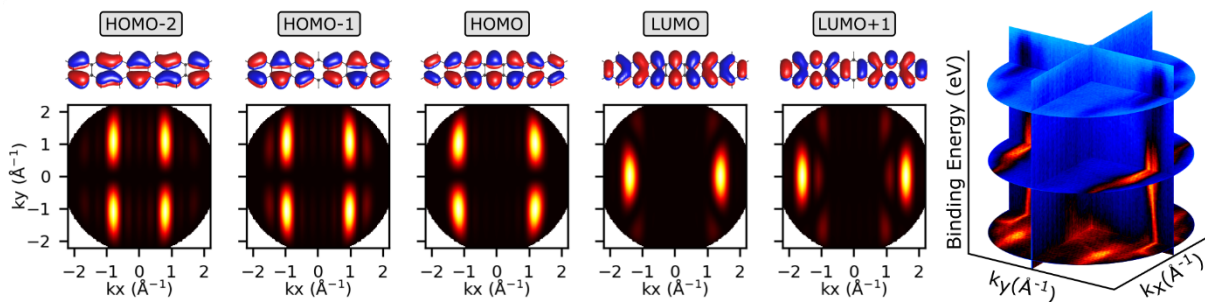


Figure 2.5: Real space images of the frontier π -orbitals of an isolated 7A molecule obtained with B3LYP-D3 and corresponding simulated photoemission momentum maps. On the right, the three-dimensional experimental data set is illustrated with the angle resolved photoemission intensity as a function of binding energy.

With the help of our simulations, we can rationalize these experimental results in more detail. For our analysis, we assume that the surface dipole is influenced by three major components. On the one hand, the approaching molecules push the electron tail of the metal surface back to the surface, leading to a reduction of the work function of the substrate, i.e.: Pauli repulsion, push-back effect (e.g. refs [9,96]). On the other hand, electron transfer from the metal to the molecular layer leads to a surface dipole pointing in the opposite direction and, hence, increases the work function. Finally, changes in the molecular structure induced by the adsorption may result in an intrinsic dipole of the molecule that also contributes to the overall work function change [11].

Starting with the latter effect, we estimate it as the vacuum potential step of a freestanding monolayer of the molecule in its already distorted geometry. On both substrates, our initially planar acenes bend toward the surface, albeit to a different extent, being responsible for a *reduction* of the work function of about -0.12 eV on Ag and -0.35 eV on Cu. Note, how for the Ag-surface, the bend amounts already to almost the complete change of the work function, while for Cu, the influence of the other factors must become more important.

Following our previous POT analysis, the observed charge transfer from the substrates to the molecules will certainly counteract the bending effect. For our model systems, the number of electrons in the acenes after adsorption are obtained via Bader charge analysis [97]. The excess charge of about 1 electron (Ag) and 2 electrons (Cu) qualitatively represents the experimentally found occupation of the LUMO on Ag and, additionally, of the LUMO+1 on Cu. At the same time, it would suggest an *increase* of the work function, which is, at first glance, contrary to what we measure.

The overall *decrease* of the work function can be understood if the effect of the charge transfer is balanced by the push-back effect. On Cu(110), the dipole caused by charge transfer must effectively be overcompensated by an opposite, very large dipole arising from push-back. We can rationalize this observation with the close distance of the molecules to the Cu-surface ($\sim 2.2\text{\AA}$). On Ag(110), the interaction with the substrate is weaker. Remember that on this surface, the total change in work function would already be covered by bending of the molecule. Thus, the adsorption height of $\sim 2.7\text{\AA}$ apparently induces just enough Pauli repulsion to equalize the charge transfer effect.

THM: Photoemission spectroscopy reveals charge transfer from the metal substrates to the acene molecules. The Ag(110)-surface provides electrons to occupy the LUMO of hexacene and heptacene. The interaction on Cu(110) is stronger, filling not only the LUMO but also the LUMO+1.

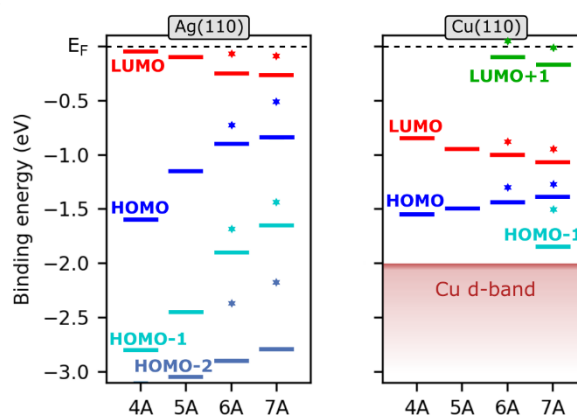


Figure 2.6: Experimental energy alignment of the frontier molecular orbitals of different acenes (4A [86], 5A [85], 6A, 7A) at the valence region on Ag (left) and Cu (right) determined from POT analysis (bars). Data for 4A and 5A was taken from literature. The DFT calculated values (PBE-D3) are marked by the star shaped symbols.

Table 2.1: Comparison between experimentally determined and calculated (PBE-D3) work function changes for the adsorption of 6A and 7A on the Ag and Cu surface. Charge transfer from the substrate to the acenes is quantified by Bader charge analysis as the excess charge after adsorption. Brackets give the highest molecular orbital seen in POT. The adsorption distance is given as the mean distance of the carbon backbone to the surface of our optimized structures.

	Ag(110)		Cu(110)	
	6A	7A	6A	7A
Exp. change [eV]	-0.2	-0.15	-0.8	-0.83
Calc. change [eV]	-0.16	-0.11	-0.88	-0.91
Charge transfer [e-] (exp)	0.70 (LUMO)	0.92 (LUMO)	1.51 (LUMO+1)	1.89 (LUMO+1)
Ad.-distance [Å]	2.67	2.66	2.17	2.14

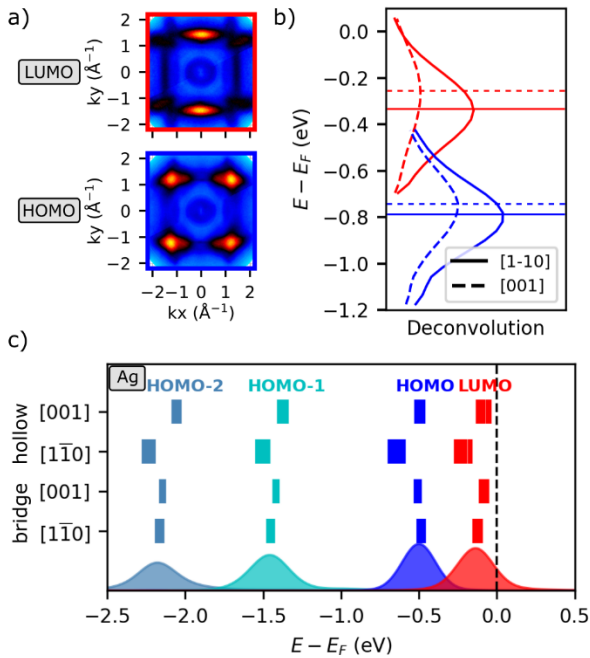


Figure 2.7: a) Experimental momentum maps attributed to the LUMO (top) and HOMO (bottom) of a 7A monolayer deposited on a cold Ag(110) surface. b) Energy dependent deconvolution of the experimental data set using gas phase orbitals with perpendicular orientation. c) Density of states projected onto the molecular orbitals for four different adsorption configurations sampling the overlayer structures of Figure 2.3. Boxes mark the binding energy range of the respective orbital contributions. The spectrum at the bottom corresponds to the “bridge [110]” configuration in the experimental unit cell. All data calculated with PBE-D3.

(bottom) of the molecule. Comparing with the simulations in Figure 2.5, the experimental intensity distribution cannot be explained by a single molecular orientation. Instead, the square pattern of the LUMO or the star shaped feature in the HOMO region reveals the existence of indeed two perpendicular 7A molecules, i.e.: along both crystal directions.

Fitting the measured momentum maps of several binding energies against the simulations [98] results in the deconvolution curves in Figure 2.7b, where we see the HOMO and LUMO peaks appearing for the [110] and [001] direction. The different heights of the peaks reflect the different occupations along the directions in agreement with STM. Interestingly, the maxima

So far, we have treated the systems, as they would be unambiguously described by a single adsorption geometry. Since the calculated adsorption energies of different acene configurations in particular on Ag(110) are close in energy, it is reasonable to expect mixed arrangements on the surface. Especially without providing additional energy to the systems, i.e.: without annealing, the molecules should be able to rest in local minima along both crystal directions, [110] and [001]. Such a situation might be inferred from STM images, where occasionally regions of 6A or 7A along [001] on Ag(110) can be found, besides the aforementioned predominant orientation of [110]. STM, however, displays only local arrangements. More conclusive arguments come from ARPES measurements, which collect data averaged over a larger crystal area. Measured momentum maps for the 7A/Ag interface are shown in Figure 2.7a. The k -values of the emission features uniquely associate the maps to the LUMO (top) and HOMO

of the peaks are shifted by 0.05 eV and 0.1 eV for the HOMO and LUMO, respectively, indicating slightly different electronic properties for both adsorption geometries. Our DFT calculations of different 7A/Ag configurations fully confirm this finding. Projecting the density of states onto the molecular orbitals, we equally observe a variation of the binding energies of the frontier orbitals (Figure 2.7c). Note that our computational analysis includes several molecular coverages, and the interpretation is independent of the unit cell size.

For Cu, the calculated adsorption energies more clearly favour the alignment of the acenes along the $[1\bar{1}0]$ rows. However, our DFT calculations suggest that films with a perpendicular arrangement of molecules could be of particular interest. Analysing the calculated electronic properties of 7A/Cu (Figure 2.8a top, equivalently also 6A), a possible occupation of the LUMO+1 strongly depends on the adsorption configuration of the molecules, which in turn would reflect in the binding energy at which the corresponding ARPES momentum maps could be observed in experiment. Except for the most stable configuration, i.e., the “hollow” configuration along $[1\bar{1}0]$, the LUMO+1 is empty, while the HOMO and LUMO levels shift to about 0.5 eV lower binding energies.

By modifying the growth conditions, specifically by cooling the substrate with liquid nitrogen during the evaporation, we are able to produce films in which a substantial fraction of heptacene molecules orient *perpendicular* to the most favourable $[1\bar{1}0]$ row direction, i.e., along $[001]$. The characteristic emission signatures of the momentum maps allow us to disentangle the contributions from the two molecular species, either oriented parallel or perpendicular to the Cu rows. As demonstrated in the bottom part of Figure 2.8a, deconvolution of the experimental data stack nicely recovers the theoretical predictions, resulting in the observed significant shift of the energy levels and the orientation dependent filling of the LUMO+1.

To highlight the importance of the chosen preparation conditions, Figure 2.8b compares measurements for a sample with a cooled (top) and a heated (bottom) substrate during deposition of the molecules. For the comparison, we have chosen a binding energy of 0.67 eV

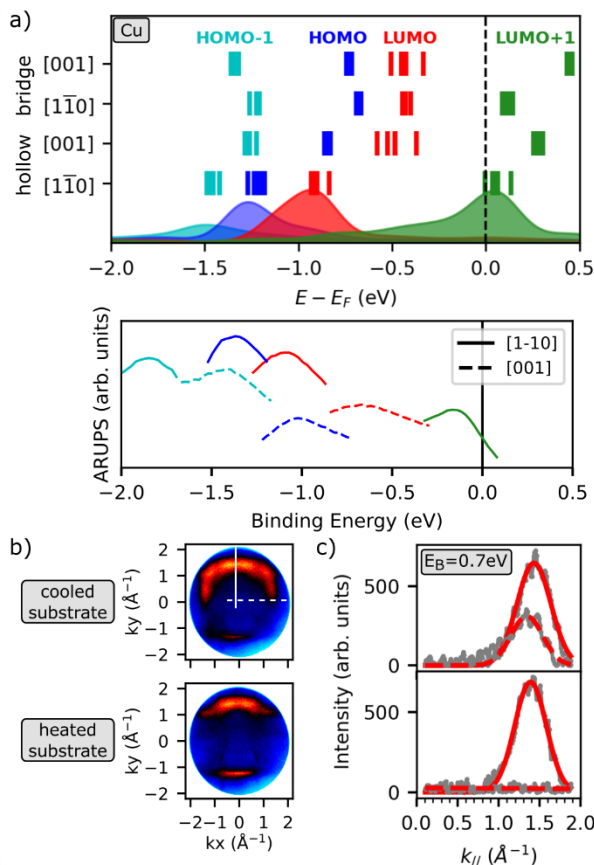


Figure 2.8: a) (top) Density of states of 7A/Cu projected onto the molecular orbitals for four different adsorption configurations sampling the overlayer structures of Figure 2.3. Boxes mark the binding energy range of the respective orbital contributions. The spectrum at the bottom corresponds to the “hollow $[1\bar{1}0]$ ” configuration in the experimental unit cell. All data calculated with PBE-D3. (bottom) Energy dependent deconvolution of the experimental data set using gas phase orbitals with perpendicular orientation. b) Experimental momentum maps of a 7A monolayer prepared on a cold and a hot Cu-surface (same binding energy $E_B=0.67$ eV) c) Line scans along the white lines in b) corresponding to the $[1\bar{1}0]$ (solid line) and the $[001]$ (dashed line) direction. Experimental data points (grey) are fitted with Gaussian curves.

as, at this energy, the LUMO's emissions of molecules along both directions are visible. For the heated sample, almost no emissions along [001] are visible, while with decreasing substrate temperature, emissions along the [001] direction can be recognized. The same conclusion can be inferred from Figure 2.8c, which shows the intensity profiles obtained from linescans along both k-directions (white lines in Figure 2.8b). The peak connected to the minority [001] alignment of heptacene (dashed lines) clearly increases with decreasing temperature, while the majority alignment with heptacene parallel to $[1\bar{1}0]$ prevails. As a side note, it should be mentioned that on repeating the experiment with another Cu crystal, we find the same qualitative trend with temperature, but the ratio between majority and minority orientations deviates slightly. This suggests that in addition to the substrate temperature, peculiarities of the used Cu crystal, e.g., the density of step edges and/or kinks, are also important parameters governing the growth of heptacene on Cu(110).

THM: Acenes on metal(110) surfaces exhibit a different energy level alignment depending if the molecules orient along the $[110]$ or $[001]$ crystal direction. This is particularly evident for 7A on Cu(110), where charge transfer from the surface fills either only the LUMO (along $[001]$) or both, the LUMO and LUMO+1 (along $[110]$).

Albeit in the previous examples, the momentum patterns of two perpendicular species are easily distinguished, POT has proven on several occasions to have high sensitivity to the alignment of the molecules with respect to the crystal directions [99–101]. Considering the symmetry of our (110)-surfaces, the technique should be able to detect rotations in the range of $\pm 10^\circ$, which visibly change the simulated intensity distribution (Figure 2.9a). When depositing a monolayer of 6A (or equivalently 7A [87]) on a hot Ag-substrate, i.e.: avoiding perpendicular orientations, STM images show a predominant alignment of the acenes rotated by $\pm 7^\circ$ off the $[1\bar{1}0]$ direction (right of Figure 2.9b). Comparing measured momentum maps for the films (left of Figure 2.9b) to simulated maps, we observe no indication of such a rotation, but instead, a better agreement with molecules oriented directly along the $[1\bar{1}0]$ rows. The contrasting findings are not necessarily an experimental artefact or a shortcoming of POT. In

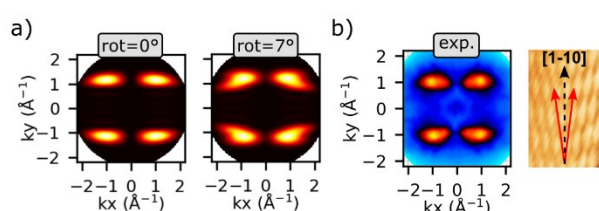


Figure 2.9: a) Simulated HOMO momentum map of isolated 6A calculated with B3LYP applying 2-fold symmetry of the Ag-surface. The long molecular axis is oriented directly along a main crystal direction (left) and slightly rotated to it (right). b) Experimental momentum map of 6A/Ag(110) attributed to the HOMO (left). STM image of a full monolayer 6A/Ag, red arrows indicate the molecular axis with respect to the $[1\bar{1}0]$ direction.

fact for tetracene, it was found, that the rotation of the molecules varies within a small coverage window and is induced when changing the dosage somewhere between 0.8 and a full monolayer [102]. As the films for STM and ARPES measurements were prepared independently in different chambers with different equipment it is plausible that the measurements also correspond to two slightly different monolayer coverages, witnessing the rotational change close to a full monolayer.

Beside energy alignment and geometric structure, POT is also able to contribute to the understanding of the chemical nature of our acene-interfaces. As mentioned in the beginning, the deposition of 7A starts from a precursor molecule. First suggested by Einholz et al. [103], the heating of a mixture of diheptacenes, i.e.: heptacene-dimers coupled at a benzene-unit (see Figure 2.10a), should result in the sublimation of 7A following a cycloreversion reaction. If the C-C bond breaking were not completely successful, we would expect to observe a photoemission distribution such as simulated for the HOMO of an isolated dimer in Figure 2.10b. The momentum map of diheptacene is rich in features, characterized by four major lobes at very low k_y -values and additional minor lobes in the outer rim. In essence, since the C-C bridges break the extended π -conjugated system of each 7A moiety, the split of features originates from the small π subsystems bent to either side. However, no such pattern is observed in the experimental momentum map of 7A in Figure 2.10c exemplary shown for the HOMO region of a monolayer on Cu (nor in the experimental maps of any other molecular emissions). Instead, the k -positions of the photoemission lobes nicely agree with those of a simulated momentum map of a single 7A HOMO (Figure 2.10d). As POT is an area-averaging technique, we measure the accumulated photoemission response of an ensemble of molecules on a macroscopic scale and thereby can confirm the formation of 7A molecules or, using a chemical term, a high reaction yield. The quality of the experimental momentum map, thus, demonstrates the chemical purity of the synthesized 7A.

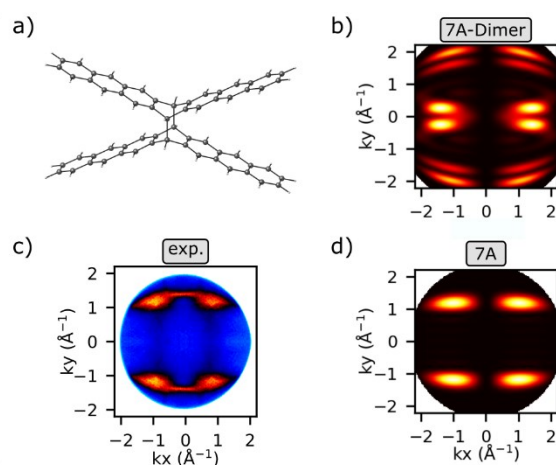


Figure 2.10: a) Structure of the precursor, diheptacene (heptacene-dimer). b) Simulated momentum map of the HOMO emission of a single diheptacene molecule. c) Experimental momentum map attributed to the HOMO emission, (exemplary 7A/Cu). d) Simulated momentum map of the HOMO emission of a single 7A molecule. Calculations in the gas phase with B3LYP-D3.

THM: Since especially longer acenes are difficult to synthesize, formation of acene-interfaces sometimes involves precursor molecules. ARPES provides a possibility to monitor the conversion from a precursor molecule to the actual acene and investigate subtleties during the monolayer growth.

XPS

In the previous section, we investigated the significant charge transfer between the metal substrates and the acenes. By measuring X-ray photoemission spectroscopy (XPS), we demonstrate the effect of this metal-molecule interaction on the core electrons of the molecule. To introduce the C 1s spectra of acenes, we first discuss the spectrum of a multilayer thick film of 6A and 7A as reference samples without influence of the surface (Figure 2.11a top). While the experimental spectra display only one broad peak, calculations suggest that they are in fact composed of three carbon species with different chemical environments. The calculated core level binding energies for 7A are exemplary included in Figure 2.11a as coloured bars following the colour scheme of the carbon atoms in Figure 2.11b. The assignment for 6A is analogue. Aromatic carbons bonded only to other carbons (C-C, orange) appear at the highest binding

energy. The terminal C-H bonded atoms (yellow) are next in line, while the inner C-H (green) are at lowest binding energies. Their relative energetic ordering is in perfect agreement with combined experimental and theoretical data of pentacene [104]. Using these three components in their stoichiometric ratio (10:8:8 for 6A and 12:8:10 for 7A), the C 1s spectra can be well described.

The monolayer spectra in Figure 2.11a (middle and bottom) are distinctly different from those of the thick films, as intensity develops especially at the low-binding energy side. Noteworthy however, on the same surface, the spectra of 6A and 7A exhibit similar shapes, which we attribute to the similar ways both acenes interact with the substrates (compare also energy alignment Figure 2.6).

For our monolayers on Ag(110), the whole XPS spectrum shifts to lower binding energies compared to the bulk originating from the described charge transfer from the metal to the acenes. Final state screening effects in photoemission at the interface to metal substrates may additionally cause a lowering of binding energies (e.g., refs. [105,106]). However, not only an overall shift of the C 1s binding energy is observed in Figure 2.11a, but also a change of the peak shape that could be caused by a relative shift of the different components. Assuming a local charge transfer to certain carbon atoms at the interface, an energetic shift of the respective component toward a lower binding energy would be expected. Recall that on Ag(110), the LUMO of both, 6A and 7A, gets filled. The electron density of the LUMO is mainly located at the inner C-H (green) with less contributions on the terminal C-H (yellow, compare Figure 2.11b). Indeed, we observe a stronger shift for these components leading to the visible shoulder of the spectrum at lower binding energies.

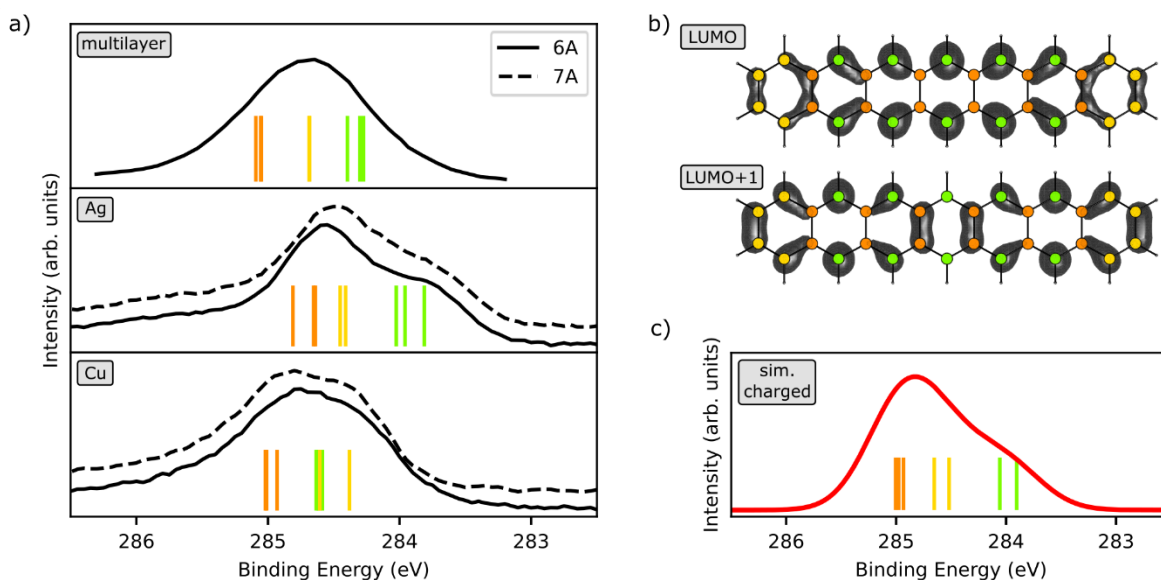


Figure 2.11: a) Experimental C 1s spectra of an hexacene multilayer, and monolayers of 6A and 7A on Ag(110) and Cu(110). Bars mark calculated binding energies, rigidly shifted by 0.8 eV for better comparison with experiment. b) Electron density of the LUMO and LUMO+1 obtained from a B3LYP-D3 calculation. Carbon atoms are coloured according to their chemical environment: C-C (orange), terminal C-H (yellow), inner C-H (green) c) Simulated XPS spectrum of a singly charged 6A molecule. Binding energies are rigidly shifted for comparison with panel a). All calculated values are obtained from the Δ KS approach in GPAW (PBE-D3).

To further substantiate our findings, we perform an additional calculation, where we simulated the C 1s spectrum of a singly charged acene species in the gas phase. As seen in Figure 2.11c, we nicely recover the relative positions of the three carbon species. The simulation without a substrate reaffirms our interpretation that the kink in the emission spectra is not dependent on the surface environment but a direct consequence of the additional charge in the LUMO.

On Cu(110), the electron transfer from the metal into 6A and 7A is even more pronounced, and so the LUMO+1 becomes gradually filled. The higher binding energy of the C 1s spectrum compared to that of 6A on Ag(110) is most likely caused by the different energy level alignment at the interface (pinning at the LUMO+1). We also note that the inner and terminal C–H atoms now appear at the same binding energy according to the calculations. In general, we attribute this to the stronger chemisorptive nature of the adsorption on Cu. However, contrasting to Ag, it cannot solely be rationalized by the filling of another orbital, since the increase in electron density would affect both C-H species alike (Figure 2.11b). Instead, we point to the aforementioned commensurability between the acenes and the Cu-surface unit cell, where both atom species are located at the same position along the Cu rows. Apparently, the strong C-Cu bond dominates the chemical environment over the relative position within the acene, making the different C-H more similar.

This hypothesis is difficult to confirm theoretically, but we have attempted to disentangle the influence of charge and chemical environment by utilizing the adsorption site dependent amount of charge transfer. Here, we shift the molecule by half a unit cell along $[1\bar{1}0]$ from the preferred “hollow” to the “bridge” position. Due to the commensurability, the C-Hs of each benzene unit again feel an equal chemical environment and, moreover, are located at approximately the same distance to the Cu-surface ($\sim 2.3\text{\AA}$) as before. However, compared to the “hollow” configuration, the LUMO+1 is not filled anymore (see Figure 2.12 left). Thus, if charge transfer would be the dominant parameter, we would naively expect a spectrum like on Ag. Instead, the simulated Cu-“bridge” XPS spectrum (Figure 2.12 right) exhibits the same characteristics as the Cu-“hollow” spectrum (bottom in Figure 2.11a) with all C-H species close in binding energy. This would support our assumption that despite being differently charged systems, the short distance to the surface is an important effect for the explanation of the acene spectra on Cu.

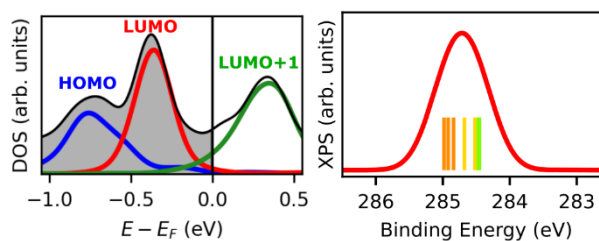


Figure 2.12: (left) Density of states of 7A/Cu in the “[$1\bar{1}0$] bridge” configuration projected onto the total molecule (grey) and the molecular orbitals calculated with PBE+D3. Note that the LUMO+1 is not filled. (right) Simulated XPS spectrum of this species obtained with the Δ KS approach in GPAW. Binding energies are shifted for comparison with Figure 2.11.

THM: The interaction between surface and molecule does not only affect the frontier orbitals but also the core levels of the acenes. On Ag, the charge transfer is responsible for a visible shoulder in their C 1s XPS spectra, which we rationalize by a local increase of electron density at specific carbon atoms. The even stronger interaction on Cu leads to a more uniform chemical environment of the carbon atoms.

2.3 Intermolecular Dispersion of Heptacene

2.3.1 Introduction

As we have seen in our characterization so far, the assembly of higher acenes on coinage metals is largely dominated by the interaction of the molecule with the substrate. Thus, it is also difficult to extract and elaborate on electronic properties intrinsic to the molecular monolayer. Information on molecule-molecule interaction may be gained by studying thicker films, where the influence of the substrate is weakened. The molecular arrangement in the crystalline material, however, does not necessarily represent the geometry of the first wetting layer. Sticking to the monolayer regime, passivating the substrate *via* oxygen has proven an effective way to electronically decouple the adsorbed molecules [107]. Conveniently, the passivation layer also serves as a patterned template for the growth of the molecular structures [81,108–110].

In the context of organic semiconductors, a molecular property of interest is the dispersion of the molecular bands as a measure how effectively charges are transported through the material. The strength of the dispersion depends on the *intermolecular* interaction, which in turn is related to the overlap between orbitals of adjacent molecular units. Therefore, it comes without surprise that the dispersion varies with the structural arrangement, i.e.: the relative alignment between the molecules [111,112]. Conversely, measured band dispersion should encode information about the structure, from which it originates. A fingerprint of dispersing molecular bands in momentum space is provided by ARPES [113,114]. Utilizing such experiments, we want to investigate the connection between band dispersion and molecular alignment in monolayers of acenes.

Article Information and Author Contribution

In the following, I summarize the computational work of the article [32] extended by additional thoughts to the topic. The analysis is based upon measurements of **Thomas G. Boné**. In the course of the project, I set up all calculations, discussed my simulations with our experimental partners and converted the calculated data into Figures for the manuscript.

OPEN ACCESS
IOP Publishing

J. Phys.: Condens. Matter 35 (2023) 475003 (8pp)

Journal of Physics: Condensed Matter

<https://doi.org/10.1088/1361-648X/acf105>

Orientation, electronic decoupling and band dispersion of heptacene on modified and nanopatterned copper surfaces

Thomas Boné^{1,4}, Andreas Windischbacher^{1,4}, Lukas Scheucher¹,
Francesco Presel¹, Paul Schnabl¹, Marie S Wagner^{2,3}, Holger F Bettinger³,
Heiko Peisert², Thomas Chassé², Peter Puschnig¹, Michael G Ramsey¹,
Martin Sterrer^{1,*} and Georg Koller^{1,*}

Figure 2.13: Header of the article [32] including all contributing authors. The study was published in the Journal of Physics: Condensed Matter.

2.3.2 Results and Discussion

Investigated System

To form an interface that sufficiently decouples the adsorbates from the substrate, a Cu(110) surface was oxidized covering it with a passivating Cu(110)-(2x1)-O layer. The oxygen reconstruction adds O-Cu rows along the [001] crystal direction, at which elongated molecules preferably orientate [81,108–110]. Building upon previous studies on pentacene [108] and hexacene [81], we investigate the behaviour of the longest acene accessible to us, heptacene (7A). Like its smaller relatives, STM images show the alignment of 7A monolayers along the troughs of the O-Cu rows.

Utilizing photoemission spectroscopy, we gain insight into the electronic structure at the interface. The experimental valence band spectrum reveals two peaks below the Fermi level (binding energy of -0.7 and -1.7 eV), which are attributed to emissions from molecular orbitals. The angle resolved intensity distribution of the highest occupied level at -0.7 eV is shown in Figure 2.14a (top). While the emission pattern, at first glance, reminds of the momentum fingerprint of the 7A LUMO discussed in the previous section, it appears at a k -value (1.2 \AA^{-1}) characteristic for the HOMO. The unusual shape of the feature can be explained by assuming that the molecules do not lie flat, i.e., with their aromatic planes parallel to the surface, such as for pure coinage metals, but adopt a tilted geometry sketched in Figure 2.14b. Simulating momentum maps of molecules with varying tilt angles and accounting for the mirror symmetry on the surface, we find best agreement with the experimental data for an angle of 37° . The determined adsorption structure for 7A is in line in with measurements for 5A and 6A, which all show indications of a molecular tilt in the range of 30° [81,108].

Periodic calculations of the full interface further support our interpretations. Relaxation of the system favours tilted molecules rotated by 35° within the O-Cu rows, agreeing with experiments. Subsequent analysis of the electronic properties confirms the passivating nature of the O-Cu surface. In the molecular orbital projected density of states (Figure 2.14c), the highest occupied level is the original HOMO of the molecule, while the charge transfer from the Cu to the 7A is suppressed. Note that for the passivated Cu surface out of all investigated surfaces in this thesis, the experimentally observed and theoretically predicted binding energies differ the most, e.g.: for the HOMO $E_B(\text{exp}) = -0.7 \text{ eV}$ vs. $E_B(\text{calc}) = -0.1 \text{ eV}$. Such a deviation in the energy alignment of already the frontier orbitals often hints towards general shortcomings in the theoretical description of the system. As the

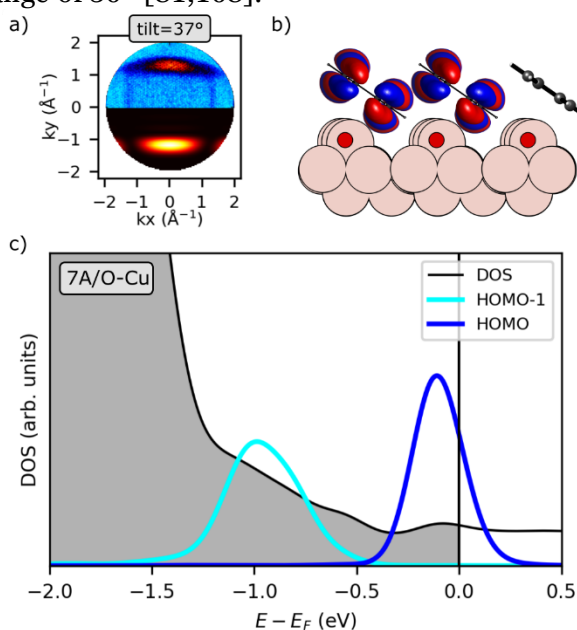


Figure 2.14: a) Experimental momentum map of 7A on passivated Cu (top) compared to simulated HOMO map of isolated 7A tilted around the long molecular axis by 37° . b) Model of the adsorption geometry on the surface, where the molecules lie tilted along the O-Cu rows. Isosurfaces of orbitals illustrate how the close intermolecular spacing facilitates π - π interaction. c) Density of states of the 7A/O-Cu interface projected onto the HOMO and HOMO-1 of the molecule obtained with PBE-D3.

weak interaction between 7A and O-Cu is likely to be dominated by dispersion, we have reoptimized the interface with the van der Waals functional optPBE-vdW [115], which, however, did not change our finding. Furthermore, we computed the density of states at the level of hybrid functionals (HSE06 [116]) mitigating the self-interaction error of semi-local GGA. This step has shown to improve the orbital energies of adsorbate systems [85,117,118] and also in the present case, it considerably improves the HOMO binding energy, $E_B(\text{calc}) = -0.4$ eV, however a significant deviation remains. As a possible reason we suggest that especially with the physisorptive interaction at the O-Cu surface, screening effects, which are not covered in DFT, may become important.

To complete our characterization of 7A/O-Cu, we turn to the work function of the samples as a parameter characteristic for the interface. Determined from photoemission spectroscopy, the work function drastically decreases when depositing a molecular monolayer of 7A ($\Delta\Phi = -0.64$ eV, listed in Table 2.2). Since we claim that the molecules are electronically decoupled from the surface, this result is perhaps counterintuitive, in particular, as we have associated an equally large change in the work function with strong charge rearrangements in the previous chapter. However, our calculations of the system likewise reproduce the large decrease. With no charge transfer anchoring the molecules to the surface, we attribute the change fully to the Pauli pushback effect. Here, the effective repulsion of the electron tail out of the substrate should depend on the adsorption distance of the monolayer. Despite the decoupling, the tilted arrangement between the corrugated O-Cu rows allows 7A to approach similarly close as on, for example, the Ag surface ($\sim 2.8\text{\AA}$).

Table 2.2: Experimental work function and relative change of the passivated Cu-surface and after deposition of a 7A monolayer compared to the absolute work function and relative change for the corresponding simulations with PBE-D3.

	Exp. WF [eV]	Sim. WF [eV]
Clean Cu(110)-(2x1)-O	4.82	4.91
7A monolayer	4.18	4.14
Change	-0.64	-0.77

THM: On Cu-surfaces passivated with oxygen, heptacene adopts a tilted geometry within the O-Cu rows along the [001] crystal direction. We observe no charge transfer from the substrate to the molecule, what we label as “electronically decoupled”.

Intermolecular Dispersion

The close intermolecular spacing enforced by the Cu-O rows, along with the associated tilting of the aromatic planes, enables strong interaction between neighbouring molecules. As a consequence of the overlapping of frontier π -orbitals, the former discrete molecular levels now form dispersive energy bands. The momentum dependent binding energy of these bands can be observed in our experimental ARPES data. As the band structure will only be observable in k-space regions where there is significant photoemission cross-section, the experimental band maps (E vs. k) for the HOMO and HOMO-1 are obtained by slicing through the measured stack of momentum maps at the respective intensity maxima of $k = 1.2 \text{\AA}^{-1}$ (HOMO) and $k = 1.0 \text{\AA}^{-1}$ (HOMO-1) (left of Figure 2.15a). Directly mimicking the experimental approach, we have calculated a stack of momentum maps for our 7A/O-Cu model system and cut along the mentioned k-values resulting in simulated band maps for both orbitals (right of Figure

2.15a). Correcting the binding energy in the simulation by a constant shift of 0.6 eV, we find good agreement between experiment and theory. The HOMO derived band shows a small dispersion (0.3 eV) in a fuzzy shape, whereas the more distinct “V”-shape of the HOMO-1 band extends beyond 0.5 eV. The comparison suggests that although the energy alignment at the interface is not captured correctly, we are able to model the *intermolecular* interactions.

With the help of our calculations, we can further rationalize the extent and intensity pattern of the dispersion on a molecular level. Firstly, the strength of the dispersion originates from the degree of π -overlap between orbitals of neighbouring 7A molecules. The sketch in Figure 2.15b illustrates the arrangement of 7A on the O-Cu surface suggested by STM results. Figure 2.15c, then, shows the consequences of the lateral shift for the frontier orbitals. For the HOMO, the given displacement leads to an unfavourable intersection of nodes and maxima in the electron density resulting in comparably small transfer integrals, hence in a weak interaction and consequently in small dispersion. In contrast, for the HOMO-1 of two adjacent molecules, maxima overlapping with maxima facilitate interaction, i.e.: stronger dispersion. Secondly regarding the shape of the signature, as already mentioned, the observation of any dispersion in ARPES experiments depends on the availability of an appreciable photoemission cross section and, therefore, is effectively determined by the momentum map of the respective orbital. Figure 2.15d displays the symmetrized dispersion relations, i.e.: energy as a function of k , calculated for a freestanding layer of 7A, superimposed with the momentum maps of the HOMO and HOMO-1. The white dashed line represents the cut for the band maps. In case of the HOMO-1, this cut goes through clear “hills” of high and “valleys” of low energy regions responsible for the “V” feature. On the other hand, in the region of the HOMO, the energy variation is smaller in agreement with what we observe in the experimental data. It is important to note, however, that the symmetrized energy dispersion in Figure 2.15d can only

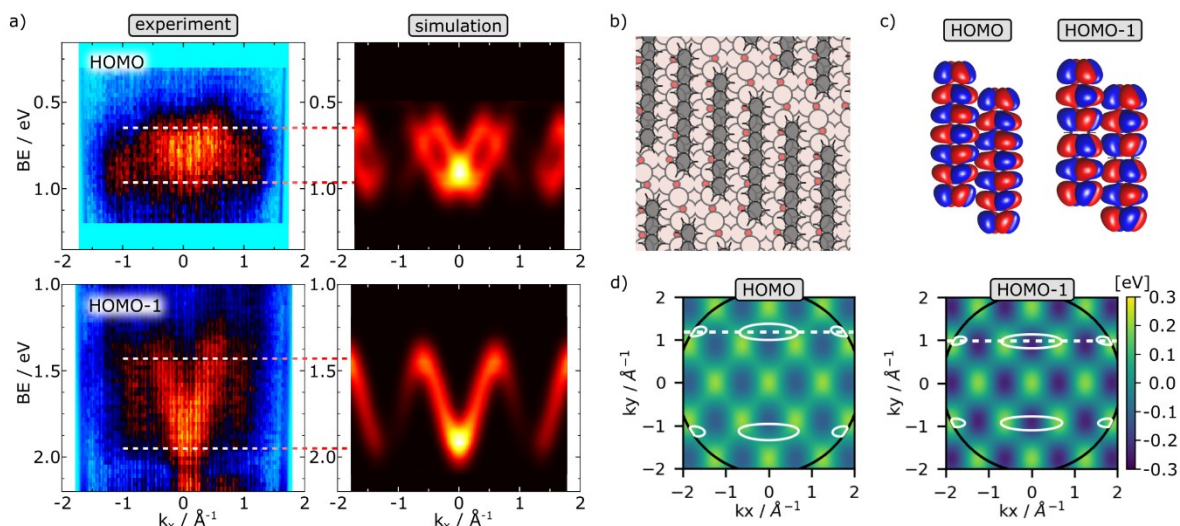


Figure 2.15: a) Experimental and theoretical band maps of the HOMO and HOMO-1 bands at $k=1.2\text{\AA}^{-1}$ and $k=1.0\text{\AA}^{-1}$, respectively. Simulated maps are obtained from a freestanding monolayer, the binding energies are shifted for comparison with experiment. b) Structural model of the 7A/O-Cu surface suggested from the STM results. This arrangement was used in the simulations. c) Isosurfaces of the HOMO and HOMO-1 orbitals of 7A with the lateral shift between neighbouring molecules from STM. d) 2-dimensional representation of the symmetrized energy dispersion of the HOMO and HOMO-1. White dashed lines show the cut of the band map, solid lines are an isosurface of the calculated momentum map of the respective orbital of a tilted 7A. All calculations are with PBE-D3.

serve as an approximative illustration of the effects due to intermolecular interactions. Precise information about the energetic substructure of the ARPES pattern, for instance in case of the HOMO, is lost. Ultimately, the shape of the dispersion can be traced back to the size of the unit cell as will be discussed in the next section.

THM: The specific geometry of 7A on the O-Cu surface facilitates interaction between neighbouring molecules giving rise to intermolecular band dispersion. ARPES band maps can visualize this dispersion, the shape and strength of which we can satisfactorily reproduce by simulating a freestanding monolayer.

Dependence on the Molecular Arrangement

For the previous comparison, adopting the experimental arrangement of 7A is crucial to satisfactorily model the measured dispersion. In the following, we want to elaborate how changes in the alignment of the molecules impact our predictions. Again, we will focus on the two quantities, which mostly determine the appearance of the band map, namely the strength and the shape of the dispersion features. In this context, it is also important to note that we do not examine only a single band but especially the differences of these quantities between the frontier orbitals HOMO and HOMO-1. As often in computational studies, such relative comparisons are more robust.

For our discussion, we have chosen three arrangements with different lateral shifts of the tilted molecules, which are summarized in Figure 2.16. They represent three prototypical cases for the overlap of adjacent π -orbitals. To break free of the commensurability constraint of the full surface calculations, we model freestanding monolayers. As introduced above, the overlap determines the strength of interaction between neighbouring 7A molecules. In a parallel order without any shift (shift 0, top), regions of electron density of both, the HOMO and HOMO-1, will simply interact with the same regions on the next molecules. Consequently, the interaction between the orbitals can be maximized and we observe the largest possible dispersion. In contrast, shifting the next acene by two benzene units (4.9 Å, middle) positions the regions of high electron density of one HOMO-1 exactly at *nodes* of the next orbital. The dispersion for the HOMO-1 diminishes, while it stays strong for the HOMO, as portrayed by the different contrasts of the 2-dimensional dispersion map and the extent of the simulated ARPES features. The reverse situation can be induced by shifting 7A by 2.75 benzene units (6.8 Å, bottom), where now the HOMOs interact unfavourably.

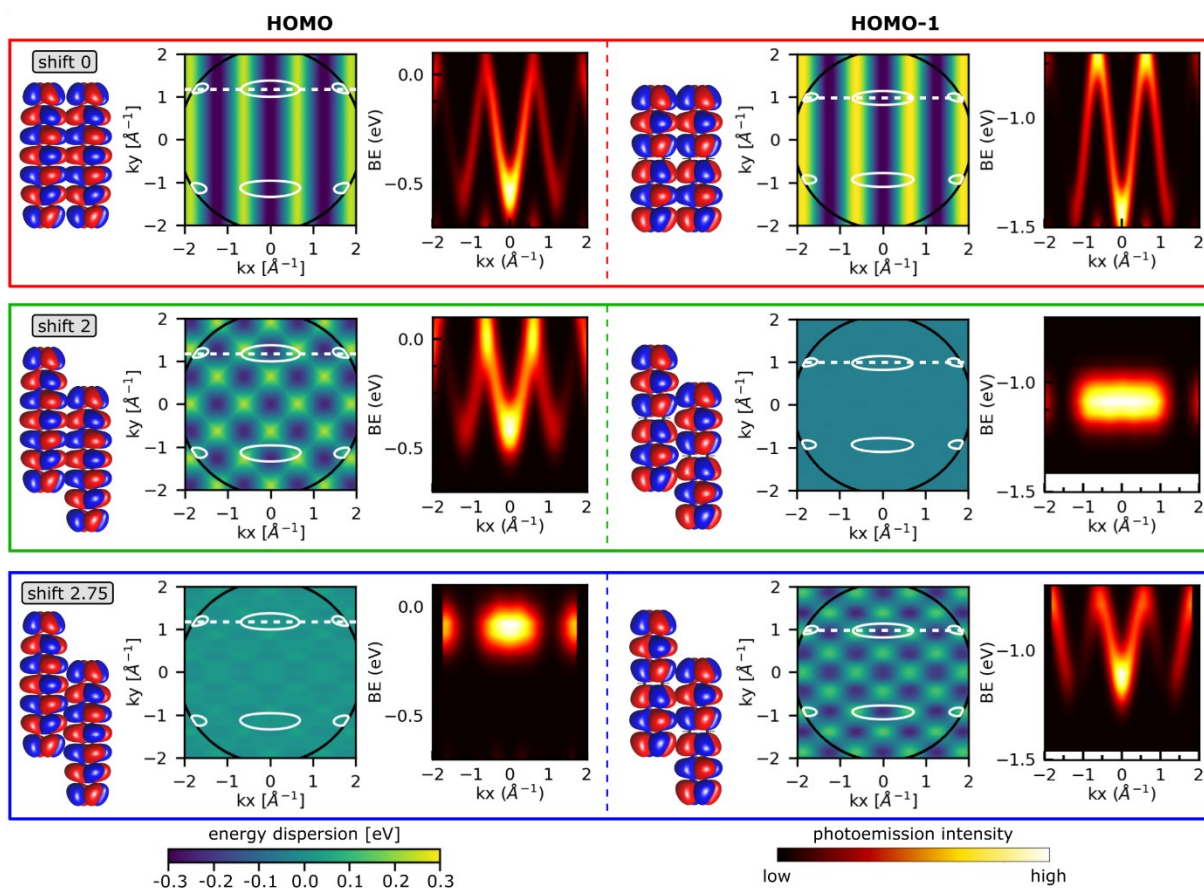


Figure 2.16: Simulated dispersion of HOMO and HOMO-1 derived bands for a free-standing layer of 37° tilted 7A molecules with different lateral shifts (in units of benzene rings). Each panel contains the isosurface of the two orbitals in the respective arrangement, the calculated 2-dimensional energy dispersion, and the photoemission band map (E vs. k) at the maximum of the ARPES feature applying the 2-fold symmetry of the surface. All data calculated with PBE-D3.

Understanding the basic origin of the dispersion, we will now touch upon the parameters, which determine its shape. The overlap of orbitals is not only dependent on nodes and maxima, but also on the relative phase between interacting lobes. Lobes with different phase will result in a state of lower binding energy (more unfavourable) than interactions of the same phase. In the context of periodically extended molecular systems, we can visualize the possible states resulting from favourable and unfavourable interaction in momentum space as energy dispersion. An example of such a 2D representation (E vs. k) for a 7A arrangement is given in Figure 2.17a, where lower binding energies are coloured yellow and higher binding energies blue. In the present example, the molecules are shifted such that lobes with different phases overlap between the HOMOs of neighbouring molecules, i.e., we find unfavourable interaction at the Gamma point. Due to the symmetry of the substrate, there will also be a mirror domain present on the surface.

THM: Analysing molecular dispersion in ARPES experiments, we focus on two major parameters. The dispersion *strength* is determined by the overlap between orbitals of adjacent molecules. The dispersion *shape* is determined by the relative phase shift of those orbitals.

Let us now consider the informative value of dispersion in ARPES experiments in more detail. We will first evaluate the shape of the dispersion features in ARPES band maps specifically for our 7A interface. Superimposing the two dispersion patterns of Figure 2.17a is sketched in Figure 2.17b, where the filled and unfilled points represent the “hills” and “valleys” of higher and low binding energy. The symmetrisation due to the mirror domains has little influence on ARPES band maps around $k = 0 \text{ \AA}^{-1}$. Repeating the reciprocal unit cell to larger k -values will gradually change the dispersion pattern and substructures in the ARPES band map will appear. We can see this, for instance, for the HOMO in the experimental arrangement back in Figure 2.15a. However, we also note, that realistically such predicted substructures will often be lost within the broadening of experimental data. Repeating the unit cells further will result at some point in a reciprocal distance, q_p , where the edges of the two mirror domains cross and corresponding maxima meet. This distance in momentum space can be expressed by the angle α , and the reciprocal lattice vector b_2 (Equ. 2.33). In real space, α and b_2 are determined by the lateral shift of adjacent molecules and the distance between them. The latter, we assume to be fixed by the pattern of the O-Cu rows. To observe a distinct feature without substructure, the k -value of the measured band map cut, k_{feature} , must be an integer multiply of q_p (Equ. 2.34).

$$q_p = \tan \alpha \cdot \frac{b_2}{2} \quad \text{Equ. 2.33}$$

$$k_{\text{feature}} = n \cdot q_p \quad \text{Equ. 2.34}$$

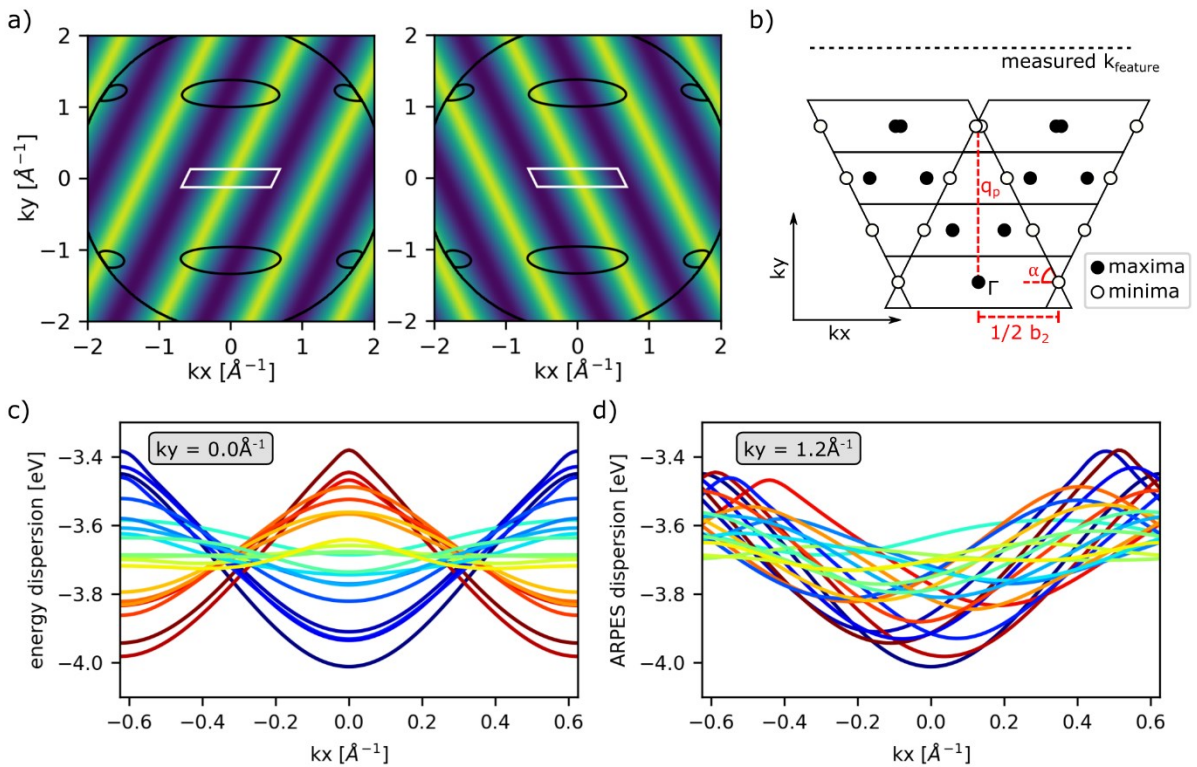


Figure 2.17: a) 2-dimensional energy dispersion maps for 7A in a shifted arrangement showing the two possible symmetries on the O-Cu surface. Reciprocal unit cell is highlighted in white. b) Sketch of superimposing both symmetry orientations. Filled and unfilled points represent the energetic “hills” and “valleys” of the dispersion. c) Dispersion relation of the HOMO of freestanding 7A monolayers with different lateral shifts evaluated around the Gamma point of the first Brillouin zone along a cut of $k_y = 0.0 \text{ \AA}^{-1}$. Colour code follows the gradual transition from favourable (lower energy, blue) to unfavourable (higher energy, red) π - π overlap at Gamma. d) Dispersion relation now evaluated at the k -value with ARPES intensity of the HOMO ($k_y = 1.2 \text{ \AA}^{-1}$). Colour code same as in c).

To illustrate the impact of Equ. 2.34, we have extended our investigation to a variety of molecular shifts and monitored the dispersion around the Gamma-point as well as at the k-value with ARPES intensity. The data is shown exemplary for the HOMO in Figure 2.17c ($k_x = k_y = 0 \text{ \AA}^{-1}$) and Figure 2.17d ($k_x = 0 \text{ \AA}^{-1}, k_y = 1.2 \text{ \AA}^{-1}$), but the finding is equally true for the HOMO-1 ($k_y = 1.0 \text{ \AA}^{-1}$). Note that the colour code does not correspond to the molecular shifts but follows the gradual transition from favourable (lower energy, blue) to unfavourable (higher energy, red) π - π overlap at the Gamma-point (A connection between colour code and shifts can be made from Figure 2.18a). As seen in Figure 2.17c around the Gamma point, the chosen shifts cover the full range of possible dispersion in the unit cell, i.e., arrangements with varying π -interactions. Thus, in ARPES band maps, we would expect to also find varying shapes of “V” and “ Λ ” by simply cutting along $k = 0 \text{ \AA}^{-1}$. However, recall that the ARPES feature of the HOMO does not show intensity around the Gamma point. Instead, it is most interesting to note, that recovering the dispersion relation from the first Brillouin-zone at the *actual* k-position of the ARPES feature is rather an exception than a rule (cut at $k_y = 1.2 \text{ \AA}^{-1}$ in Figure 2.17d). There is a general tendency for a “V” shape in the predicted ARPES pattern rather independent of the molecular arrangement. We can rationalize this by employing Equ. 2.33 and Equ. 2.34 as will be demonstrated here exemplary for the molecular arrangement with the most unfavourable π -interaction between neighbouring HOMOs (dark red “ Λ ” dispersion curve in Figure 2.17c).

This structure corresponds to a molecular shift of 1.25 benzene units, or equivalently the angle $\alpha = 59^\circ$, with the reciprocal lattice distance $b_2 = 1.3 \text{ \AA}^{-1}$. We compare the resulting, critical distance q_p to the k-value with ARPES intensity of the HOMO ($k_{feature} = 1.2 \text{ \AA}^{-1}$) and find that the latter is almost an integer multiply of q_p ($n = 1.1$). Thus, our example represents the stylized case depicted in Figure 2.17b, corresponding to a change of the dispersion shape: Even though the π -interaction gives rise to a “ Λ ” shaped dispersion around the Gamma point, the dispersion recorded at the k-value of the HOMO would show the opposing “V” shape. For the remaining molecular arrangements, we can argue in a similar way. Additionally, for shifts, where a “ Λ ” shape could indeed emerge, the predicted dispersion strength is in the range of experimental resolution probably making actual observation difficult. For illustration of this statement, the simulated symmetrized ARPES dispersion of

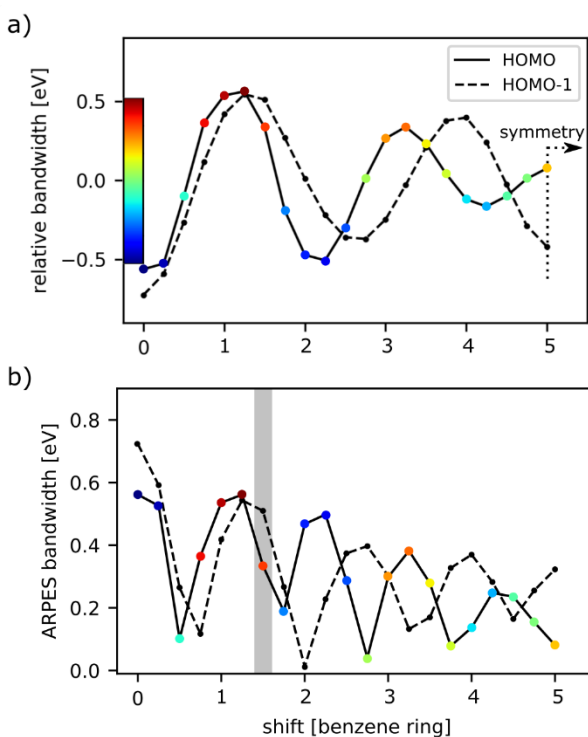


Figure 2.18: a) Energy dispersion (band width) of the HOMO and HOMO-1 derived bands in the first Brillouin zone as a function of the lateral shift in the 7A layer. Energy of each shift at the edge of the Brillouin zone relative to the energy at the Gamma-point. Colour code references Figure 2.17. b) Energy dispersion (band width) of the simulated ARPES band maps of the HOMO and HOMO-1 as a function of the lateral shift in the 7A layer. The grey region marks the shift agreeing with STM, which was used to simulate the experimental data.

all molecular arrangements can be found in the Appendix (Figure 8.2).

While the shape of the band map is more uniform than expected, the energetic width of the dispersion feature can still serve as an informative parameter for our 7A monolayer investigation. Figure 2.18a summarizes the relative bandwidths of the energy dispersions around the Gamma point for both orbitals, the HOMO and HOMO-1. The relative values are obtained by taking the energy differences between peak maxima and minima (peak-to-peak amplitude) of the same arrangements as in Figure 2.17c. The colour bar in Figure 2.18a directly links the bandwidths to the respective dispersion curves in Figure 2.17. A negative relative bandwidth corresponds to lower energy at Gamma, i.e., favourable π - π overlap of the orbitals (blue in Figure 2.17). As a comparison, Figure 2.18b shows the bandwidth taken from simulated ARPES maps for the HOMO (at $k_y = 1.2 \text{ \AA}^{-1}$) and the HOMO-1 (at $k_y = 1.0 \text{ \AA}^{-1}$). Note that we want to focus especially on the general ARPES dispersion width, i.e., the absolute peak-to-peak amplitude. Due to the different nodal structure of the two orbitals, their dispersion strengths modulate with different frequencies. As a consequence, each molecular shift exhibits a unique pair of (HOMO, HOMO-1) widths. In other words, each shift should be determined by the ARPES dispersion strengths of its orbitals. In a perfectly ordered monolayer, comparing the dispersion of different molecular orbitals should allow the characterization of the arrangements of the molecules. The grey area in Figure 2.18b marks the shift of our 7A/O-Cu monolayer determined from the experimental POT analysis discussed above and confirmed by STM.

THM: We have investigated the connection between the molecular arrangement and the predicted dispersion in ARPES experiments for heptacene on passivated Cu. The dispersion *shape* is only weakly dependent on the arrangement in the monolayer. For most molecular shifts, we find the same “V” shape. The dispersion *strength* is a more informative value. In particular, an n-tuple of dispersion strengths obtained from n different molecular orbitals is characteristic for a specific arrangement.

Finally, it should be noted that calculations of the electronic structure of a molecular monolayer on the O-Cu substrate show no appreciable difference to that of a free-standing monolayer (compare example in Figure 2.19). This also demonstrates that, although the specific surface reconstruction mediates the π - π overlap between adjacent orbitals in the first place, the dispersion of the bands is solely governed by intermolecular interactions.

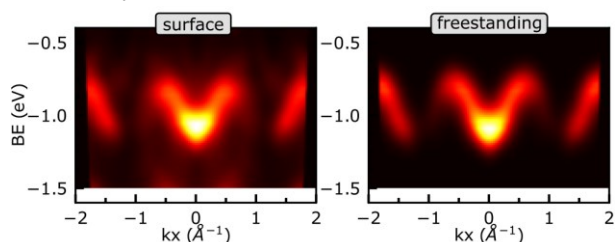


Figure 2.19: Simulated ARPES band map of the HOMO-1 obtained from a full on-surface calculation as well as a freestanding monolayer (both PBE-D3).

Stripe Phase

An interesting property of the O-Cu surface is the possibility to tune the reconstruction pattern *via* the oxygen pressure during manufacturing. Depending on the amount of oxygen, the surface is covered in differently thick stripes of alternating clean Cu and passivated Cu. Combining our understanding of the electronic properties of acenes on the clean coinage metal and on the fully oxygen-passivated substrate, we have investigated a monolayer of 7A on a

stripe phase of equally large stripes. Here, the width of the Cu-regions along the $[1\bar{1}0]$ direction is exactly large enough to host one row of 7A molecules. Indeed, STM images after deposition suggest that on the clean Cu stripes, the acenes orientate in the favoured $[1\bar{1}0]$ position (see chapter 2.2), while on the passivated stripes the molecules arrange along the $[001]$ O-Cu rows (see chapter 2.3). In addition, POT analysis confirms that on each area, the molecules retain their corresponding electronic properties, which we have elucidated previously, i.e.: strong charge transfer occupying up to the LUMO+1 on clean Cu and electronic decoupling from the substrate with no charge transfer on passivated Cu.

THM: On nanopatterned surfaces with alternating stripes of clean Cu *and* passivated Cu, charged and uncharged heptacene molecules coexist on the same surface.

2.4 Concluding Remarks

Longer Acenes on Coinage Metals

We have started our investigation on acenes by studying the electronic properties of hexacene and heptacene on the coinage metal surfaces Ag(110) and Cu(110). Utilizing POT, we give insight into their frontier molecular energy levels revealing strong charge transfer from the surfaces to the monolayers. While the LUMO of the acenes gets occupied on Ag, also the LUMO+1 is at least partially filled in the case of Cu(110). Furthermore, we demonstrate how the electronic properties of the molecules can be tuned with suitable growth conditions. Controlling the temperature of the substrates during deposition, the molecules can move along their shallow potential energy landscape occupying different adsorption configurations. Especially on Cu, varying the adsorption geometry results in drastic consequences for the energy alignment, ultimately deciding about a potential charge transfer into the LUMO+1. Finally, the strong influence of geometric and electronic effects for the different metal surfaces is also reflected in the peak shapes of the C 1s XPS spectra, leading to different energetic shifts of non-equivalent carbon atoms.

Even though for each substrate, both members of the acene family behave very similar, our results present hexacene and heptacene in a much different state than usually found in noble gas matrices or current on-surface synthesized arrangements. We, further, interpret the significant net charge transfer in the present systems as stabilization of the labile acenes and thereby hope to initiate more in-depth studies about the reaction behaviour of these formerly unapproachable molecules.

Intermolecular Dispersion of Heptacene

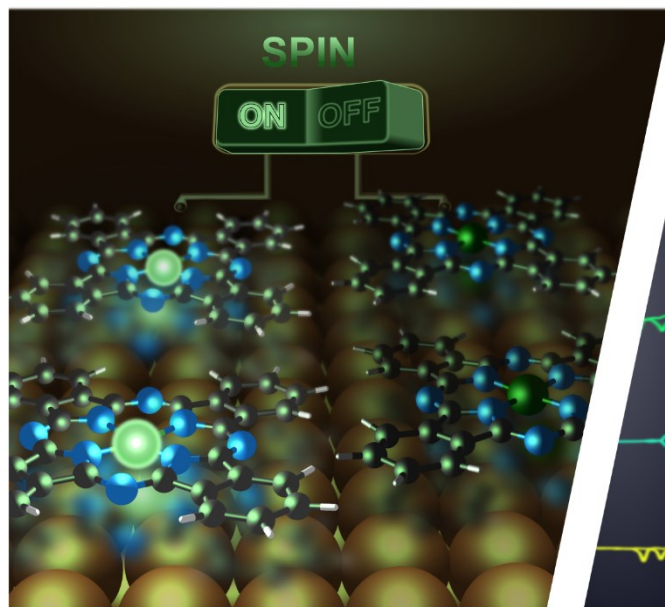
In a next step, we have studied the behaviour of 7A molecules on a Cu(110)-p(2x1)-O reconstructed surface. The oxygen passivation decouples the acenes from the Cu substrate and introduces O-Cu rows, in which the molecules adopt a tilted geometry. The rotation induces strong π - π interaction between adjacent molecules and gives rise to π band dispersion observable in ARPES experiments.

Given that the intermolecular interaction outweighs the molecule-substrate interaction, it is sufficient for the case of decoupled surfaces to model a freestanding monolayer. By doing so, we were able to discuss the connection between the dispersion in ARPES band maps and the molecular arrangement in more detail. Notably, the experimental dispersion pattern is not necessarily equal to what might be expected for a specific arrangement simply based on π -overlap of the molecule's orbitals as photoemission intensity is usually measured beyond the first Brillouin zone. More importantly, by analysing band dispersion stemming from *different* molecular orbitals, the relative alignment of the molecules can be assessed and compared to STM.

Furthermore, the O-Cu surface offers a platform to manipulate the extent of the passivation in a controlled way. Forming alternating Cu and O-Cu stripes, the acene molecules arrange in completely different electronic environments leading to neighbouring arrays of neutral and charged species. We propose that the amount of charge transfer might be governed by the size of the stripes. At low oxygen pressure, large regions of pristine Cu prevail, on which 7A has enough space to orientate along the favoured $[1\bar{1}0]$ Cu-rows getting doubly charged. In

contrast, at high doses of oxygen, the stripes of pure Cu will be smaller than the length of 7A, forcing the molecule to adsorb perpendicular to the $[1\bar{1}0]$ Cu-rows. In such a configuration, 7A would only be singly charged. Thus as a next step, adjusting the size of the stripes could connect the O-Cu-stripe phase with the direction dependent charge transfer of 7A on Cu.

3 Controlling Spin at Interfaces



A Hitchhiker's Guide to Ni-Tetrapyrrole Chemistry



Summary: For surface scientists, tetrapyrrole compounds are an appealing class of metal-organic molecules. They form stable complexes with a wide variety of transition metals and, thus, allow for the incorporation of tuneable electronic properties in the long-range order of extended systems. This chapter specifically centres around the simulation of Nickel containing phthalocyanines and porphyrins adsorbed on metal substrates. Our calculations employ the DFT+U approach especially focusing on the description of the oxidation and spin state of the central metal atom. We address the interaction of the molecules with the surfaces as well as with additional gaseous ligands and explore the potential to integrate these interfaces in molecular spin-switches or heterogeneous catalysis. Furthermore, we investigate the influence of the chemical nature of the metal centre on the geometry of the organic backbone. The results are summarized in the following five publications:

- [I. Cojocariu et al., Adv. Sci. \(2023\)](#) (NiPc on Cu)
- [A. Windischbacher et al., Inorg. Chim. Acta \(2023\)](#) (NiTPP-complexes)
- [H.M. Sturmeit et al., Small \(2021\)](#) (Adsorption of NO₂ to NiTPP)
- [M. Stredansky et al., Angew. Chem. \(2022\)](#) (Adsorption of NO to NiTPP)
- [D.M. Janas et al., Inorg. Chim. Acta \(2023\)](#) (Conformation of porphyrins)

3.1 Theoretical Background

3.1.1 Shortcomings of DFT

Before focusing on the next target system of this thesis, we will continue with discussing some basic properties of density functional theory. In principle, DFT provides an exact framework to predict ground state properties and, so far, we have applied the theory extensively to describe the interfaces between basic hydrocarbon molecules and metal surfaces. However, the approximations enabling the computational practicability of DFT introduce errors to the theory, which we should be aware of, especially when moving to more complicated systems. In the following, we want to give an overview on the shortcomings of density functional theory regarding the interpretation of orbital energies and their consequences in practical applications. For this purpose, we will mainly follow the explanations of Kronik and Kümmel in their review on the topic [119].

In DFT, a serious amount of trouble is related to spurious electron interactions, which complicate the comparison of simulations with experimental data. Let us start by considering a single electron system. Without electron-electron interaction, the energy of such a system can only consist of the kinetic energy of the electron and the influence of an external potential. Consequently, the many-electron contributions to the energy functional, the Hartree term E_H and the exchange-correlation E_{xc} , have to cancel each other for any one-electron density n_{1e} . The relation in Equ. 3.1 holds true for the exact functional, however, not in the framework of practicable approximations like LDA or GGA.

$$E_H[n_{1e}] + E_{xc}[n_{1e}] = 0 \quad \text{Equ. 3.1}$$

The error that arises is known as the one-electron self-interaction error and can intuitively be visualized from the expression of the Hartree potential (Equ. 3.2). Here, the electron feels the *whole* density and, hence, also itself.

$$V_H = \int d\mathbf{r}' \frac{n_{1e}(\mathbf{r}')}{|\mathbf{r} - \mathbf{r}'|} \quad \text{Equ. 3.2}$$

As our KS orbitals, which we intend to interpret, are effectively constructed as one-electron densities, they are likewise prone to this error. In particular, the self-interaction introduces an orbital-dependent shift of the energy levels. In conjunction with the distance dependency in Equ. 3.2, especially molecular orbitals with a strongly *localized* character, i.e., where the single electron picture prevails, are affected. They are destabilized in an effort to minimize the electron-electron repulsion. Conversely, the system favours *delocalization*. For systems, in which both types of orbitals occur, the self-interaction error can ultimately lead to a wrong ordering of the orbital eigenvalues [117,118,120,121].

Moving from the single electron picture to the system as a whole is accompanied by what is sometimes referred to as the many-electron self-interaction error [122]. Albeit difficult to distinguish from the one-electron self-interaction error, this name usually signifies the infamous “band gap problem” of DFT. To illustrate the problem, we start by introducing a true property of the exact functional in Equ. 3.3. When Perdew et al. [123] generalized the energy functional to densities with non-integer particle numbers, they noted that the total energy of

any fractionally occupied system can be obtained by a linear interpolation between the total energies of its integer electron neighbours.

$$E(N + q) = (1 - q)E(N) + qE(N + 1) \quad \text{Equ. 3.3}$$

From the condition in Equ. 3.3 follows, that the function of the total energy dependent on the electron number q connects the energies of any N and $(N + 1)$ electron system in a straight line. Hence, the exact functional leads to an expected piecewise linear behaviour of the total energy as sketched in Figure 3.1.

As the slope of any linear segment is constant between two integer electron numbers, we may evaluate the quantity for the change of one full electron. For the removal of one electron, the slope of the energy functional between the $(N - 1)$ and N electron system simply equals the difference of their energies $E(N - 1)$ and $E(N)$. This difference is nothing else than the definition of the ionization potential IP . Analogously for adding an electron, we find the slope to be the difference between $E(N)$ and $E(N + 1)$, which

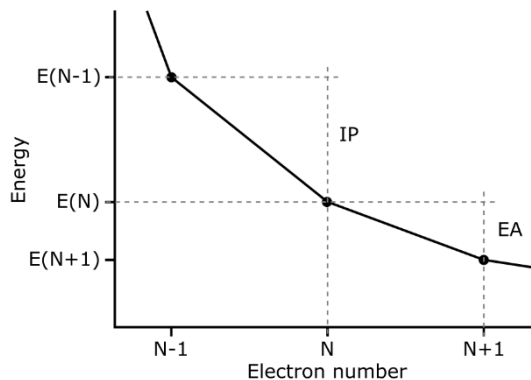


Figure 3.1: Sketch of the total energy as a piecewise linear function of non-integer electron numbers. Definition of the ionization potential (IP) and electron affinity (EA) is indicated.

corresponds to the electron affinity EA . For all systems with a band gap, i.e., where the ionization potential is larger than the electron affinity, it follows that the slopes left and right of the N electron system must be different. Mathematically speaking, even though the energy functional is continuous, the derivative of the curve at point N must have a discontinuity. By analysing the contributions to the KS potential, it was concluded that this abrupt change at integer points stems from the exchange-correlation potential and the constant compensating for the jump was termed exchange-correlation derivative discontinuity Δ_{xc} .

Recalling Janak's theorem (chapter 2.1.1), the derivative of the total energy with respect to the occupation of an orbital equals the orbital's eigenenergy. Thus, combining the theorem with the arguments discussed above, Equ. 3.3 implies that the slope between $(N - 1)$ and (N) , i.e., the ionization potential, corresponds to the energy of the highest occupied KS orbital ε_H . The expression is given in Equ. 3.4, where we take the slope at point N approaching it from below by an infinitesimal occupation change δ . Although the Janak theorem is formally only valid for the highest occupied orbital, the energy of the lowest *unoccupied* orbital ε_L can be related to the slope of the (N) to $(N + 1)$ segment, i.e., the electron affinity, by Equ. 3.5. Here, we take the slope to the right of point N , but have to correct it for the aforementioned derivative discontinuity.

$$\varepsilon_H(N - \delta) = -IP \quad \text{Equ. 3.4}$$

$$\varepsilon_L(N + \delta) + \Delta_{xc} = -EA \quad \text{Equ. 3.5}$$

Comparing Equ. 3.4 and Equ. 3.5, we see that the fundamental gap, i.e., the difference between ionization potential and electron affinity of a system, must differ from the gap between the frontier KS eigenenergies by the derivative discontinuity Δ_{xc} .

$$IP - EA = \varepsilon_L - \varepsilon_H + \Delta_{xc} \quad \text{Equ. 3.6}$$

Unfortunately, early approximations to the KS potential like semi-local LDA or GGA functionals neither respect the piecewise linearity of the total energy nor the exchange-correlation derivative discontinuity. As a consequence, interpreting the respective orbital energies as experimental excitation energies often leads to poor results.

3.1.2 The Hubbard Correction

The pitfall of “self-interaction” can be partly avoided by the use of hybrid functionals (see chapter 2.1.1). The explicit orbital-dependent treatment of exchange instead of a dependence on the whole electron density prevents interaction of the electron with itself and has also been shown to improve piecewise linearity. However, despite the development of several advanced techniques, hybrid functionals are used cautiously in surface science due to the computational cost of such calculations. For the simulation of extended systems, it is much more applicable to add correction terms on top of LDA or GGA and thereby enhance the physical behaviour of these “low-cost” functionals. A common approach is the so-called “+ U ” method, which we outline below. A more detailed discussion on the topic can be found in recent reviews [124–126].

The general DFT+ U scheme is based upon the explicit treatment of a subset of electrons with an additional model Hamiltonian [127], which describes their electron-electron interaction within a Hubbard model. The remaining valence electrons are treated by standard DFT. To obtain the total energy functional E_{DFT+U} , the usual DFT energy E_{DFT} of the system is simply extended by the Hubbard energy E_{Hub} . A term E_{dc} then compensates for double counting the energy contribution of the chosen electron set in DFT and the Hubbard correction (Equ. 3.7).

$$E_{DFT+U} = E_{DFT} + E_{Hub} - E_{dc} \quad \text{Equ. 3.7}$$

In its most complete formulation, the double-counting term explicitly corrects for the Coulomb energy U and the exchange energy J of the subset of electrons [128]. In the following, we will introduce the simplified variant of the DFT+ U formalism proposed by Dudarev et al. [129], which is mainly employed in this thesis. Its derivation combines the Hubbard model and double-counting term so that the correction to the electron interaction can be characterized by a single parameter \tilde{U} , which relates to the Coulomb energy U and the exchange energy J via Equ. 3.8. It can be thought of as the *effective* energy barrier to fill an orbital with a second electron. Once chosen, the Hubbard parameter acts on all atoms a of a specific atom species correcting the electrons in the subshell with quantum numbers nl . The Hubbard functional added to the pure DFT energy functional is given in Equ. 3.9. Note that expression Equ. 3.9 is evaluated for each spin channel separately, but the spin index σ was omitted to avoid crowding superscripts.

$$\tilde{U} = U - J \quad \text{Equ. 3.8}$$

$$E_{DFT+U} = E_{DFT} + \frac{U_{nl}^a}{2} \sum_a \sum_{nl} Tr[\mathbf{s}_{nl}^a - \mathbf{s}_{nl}^a \mathbf{s}_{nl}^a] \quad \text{Equ. 3.9}$$

Here, \mathbf{s}_{nl}^a corresponds to the occupancy matrix. Its matrix elements are obtained by projecting the molecular KS orbitals φ_j onto localized atomic states ϕ_m^a giving the element with indices m and m' as in Equ. 3.10. In practice, ϕ_m^a is represented by a spherical harmonic belonging to the set of m functions with angular momentum l . The projection is additionally weighted by the occupation f_j of φ_j according to a smearing function, e.g., a Fermi-Dirac distribution.

$$s_{mm'}^a = \sum_j f_j \langle \varphi_j | \phi_{m'}^a \rangle \langle \phi_m^a | \varphi_j \rangle \quad \text{Equ. 3.10}$$

The eigenvalues of the occupancy matrix can be interpreted as the occupations of the localized orbitals, where 1 corresponds to a fully occupied and 0 to a completely unoccupied level. The sum over the eigenvalues correspond to the number of electrons, which are distributed in the subshell nl of either spin channel.

To illustrate the consequences of the Hubbard correction for quantum chemical simulations, it might be helpful to analyse its contribution to the KS potential. For a *diagonalized* occupation matrix, i.e., where the matrix elements s_m^a equal the occupation eigenvalues, the Hubbard potential can be derived from the energy functional in Equ. 3.9 as

$$V_U = \frac{U_{nl}^a}{2} \sum_{a,m} (1 - 2s_m^a) |\phi_m^a\rangle \langle \phi_m^a| \quad \text{Equ. 3.11}$$

To start the interpretation, it should be recalled that the U-term only affects electrons of atom species a in the subshell nl . The interaction within the remaining system stays untouched. With this in mind, for orbitals with a less than half-filled occupation ($s_m^a < \frac{1}{2}$), the Hubbard potential will be positive, i.e., *repulsive*. Figuratively speaking, electrons get discouraged to localize in this particular state. Considering Equ. 3.10, there might be two possible reasons for such a situation. First, the occupation f_j of the underlying molecular orbital is initially small, which would translate to the orbital being above the Fermi-level and, hence, unoccupied. Second, the projection $\langle \varphi_j | \phi_m^a \rangle \langle \phi_m^a | \varphi_j \rangle$ of the j -th molecular orbital onto the m -th localized state shows little atomic character. The second case corresponds to strongly delocalized – sometimes called hybridized – orbitals. On the contrary, occupied molecular orbitals with strong contribution of one atomic state will give a larger occupation number ($s_m^a > \frac{1}{2}$). As a consequence, the Hubbard potential will be *attractive*, and electrons are more likely to localize on this site. Evaluating the effect of the augmented KS-potential on the energies of the molecular orbitals, the Hubbard correction stabilizes occupied, localized orbitals and penalties both, delocalized and unoccupied orbitals. From a chemist's perspective, the degree of localization is usually high for non- or anti-bonding states and low for bonding ones, meaning while the first are lowered in energy within DFT+U, the latter are shifted upwards compared to pure DFT.

With regard to the total energy in Equ. 3.9, a system will strive to reduce the penalty on the energy inflicted by the Hubbard-correction and, thus, to minimize the trace of the matrix expression $\mathbf{s}_{nl}^a - \mathbf{s}_{nl}^a \mathbf{s}_{nl}^a$. Employing linear algebra, it can be shown that the trace minimizes

when the occupancy matrix s_{nl}^a becomes idempotent, i.e., if $s_{nl}^a = s_{nl}^a s_{nl}^a$ applies. A special property of such an idempotent matrix is that its eigenvalues are either 0 or 1. Interpreting this in context of the occupancy matrix s_{nl}^a means that the calculation drives towards either completely occupying or emptying the localized orbitals considered in the U-correction.

By propagating the localization of electrons, the DFT+U approach directly counteracts the self-interaction error. At the same time, the correction often changes the orbital level placement and, when affecting the frontier orbitals, adjusts the band gap. A molecular compound class, which fits the scope of application of DFT+U, are metalorganics. Especially the d-orbitals of the chelated metal are imagined in chemistry as rather localized orbitals and profit from the Hubbard correction. In determining the degree of hybridization between the subsystems, a vital aspect of modelling metal-organic complexes is the correct energy alignment between ligand and metal-d orbitals.

3.2 Spin States in a NiPc Layer

3.2.1 Introduction

Being able to incorporate various metal ions, the tetrapyrrole moiety is famously attributed with the ability to host ions with different spin and oxidation states. When extended to well-ordered surfaces, this property becomes appealing for sensing, heterogeneous catalysis, or molecular spintronic devices [12,34–36].

In the context of interfaces, variable spin states of the central metal can be introduced either as an intrinsic property of the metalorganic complex, i.e., the coordination environment of the organic backbone induces the spin, or as a consequence of a *post-synthetic* interaction, i.e., interaction with other molecules after formation of the interface [130–134]. Both times, research strives to find external stimuli such as light, pressure, temperature or electric current to transition between different electron configurations on the potential energy surface. Preferably, such a spin change should be switchable and capable to be executed under ambient conditions. In this regard, utilizing metalorganics, for which two spin states are already inherently close in energy, presents a rather challenging task on a surface. Often, the strong interaction with the substrate locks the complex in a specific magnetic moment and, in that way, deactivates the spin switching functionality.

It is also for this reason, why there are only few realizations of intrinsic spin-complexes as periodic arrays [130,134,135], even though, for example metal-phthalocyanines, are frequently associated with magnetic interfaces [35]. Our aim is to further fill this gap with an investigation of Ni-Phthalocyanine (NiPc) on a Cu-surface, where we demonstrate a purely surface mediated bistability of magnetic and non-magnetic molecules in a monolayer.

Article Information and Author Contribution

The following summary covers the computational work included in the article [38] and is extended by complementary data analysis. The corresponding experiments of this project were mainly conducted by **Iulia Cojocariu**. I was responsible for the computational modelling of the system. In coordination with the experiments, I set up the calculations, analysed the data and discussed the results with our experimental partners. They drafted the first version of the manuscript, for which I then provided text and figures for the theoretical part.

RESEARCH ARTICLE

 Check for updates

ADVANCED
SCIENCE

www.advancedscience.com

Surface-Mediated Spin Locking and Thermal Unlocking in a 2D Molecular Array

Iulia Cojocariu, Andreas Windischbacher, Daniel Baranowski, Matteo Jugovac, Rodrigo Cezar de Campos Ferreira, Jiří Doležal, Martin Švec, Jorge Manuel Zamalloa-Serrano, Massimo Tormen, Luca Schio, Luca Floreano, Jan Dreiser, Peter Puschnig, Vitaliy Feyzer,* and Claus M. Schneider*

Figure 3.2: Header of the article [38] including all contributing authors. The study was published in Advanced Science.

3.2.2 Result and Discussion

Investigated System

We start the computational characterization of NiPc on the Cu(100) surface with a broad screening for the most favoured adsorption geometry of the system. Our search includes the three most common adsorption sites of the (100) lattice, *i.e.* “top”, “bridge” and “hollow”, on top of which the Ni center of the molecule is placed. Additionally, the starting structures consider various azimuthal rotations of the molecule with respect to the crystal directions. Optimization of the systems leads to the relative energetic ordering listed in Table 3.1. The azimuthal rotation is given as the angle between the N-Ni-N axis of NiPc and the main crystal direction [011].

Table 3.1: Relative energies and molecule-surface distances of NiPc adsorbing at different adsorption sites and rotated by various angles in reference to the main crystal direction [011].

Adsorption site (rotation)	Relative energy [eV]	Ni-surface distance [Å]	Macrocycle-surface distance [Å]
Top (0°)	0.87	2.91	2.96
Top (30°)	1.01*	3.10*	3.00*
Top (45°)	0.11	2.81	2.58
Bridge (0°)	0.58	2.79	2.71
Bridge (30°)	0.66*	2.82*	2.72*
Bridge (45°)	0.56	2.87	2.77
Hollow (0°)	0.15	2.78	2.51
Hollow (30°)	0.00	2.33	2.34
Hollow (45°)	0.90	3.00	3.01

*These values correspond to structures, which were relaxed on loose convergence settings (forces below 0.05 eV/Å). Tightening the convergence criteria to 0.01 eV/Å revealed that these adsorption configurations are not local minima, but lie on a flat plateau region of the potential energy surface. With further optimization, Top (30°) transitioned into Top (45°) and Bridge (30°) relaxed to Hollow (30°).

As will be described in more detail in a later section, the molecular arrangement at the interface is dominated by the interaction between the organic macrocycle and the surface. NiPc favours configurations where the benzene ring of the isoindole units lies above a “hollow” site of the Cu lattice (Top(45°), Hollow(0°), Hollow(30°)), which allows for best hybridization between molecule and surface and, correspondingly, for the shortest adsorption distance (cf. Table 3.1). Among these candidates, the Ni on a hollow site with the molecule rotated by 30° (shown in Figure 3.3a) seems to be most favourable, as the molecule is positioned almost perfectly flat on the surface.

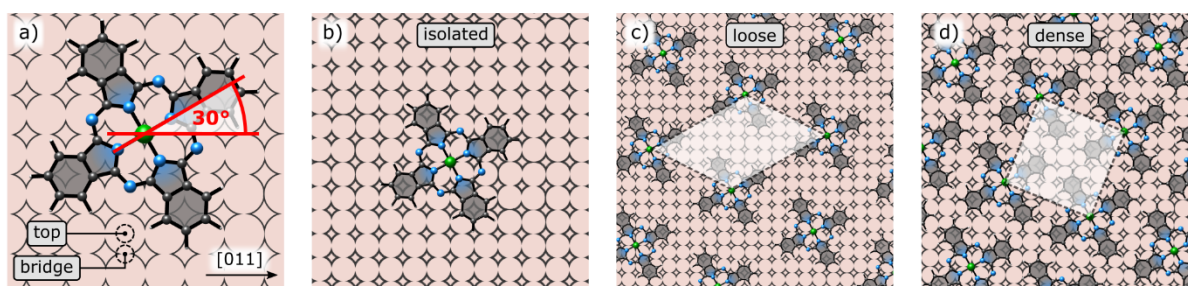


Figure 3.3: a) Most favourable adsorption configuration of NiPc on a Cu(100) surface. The molecule is adsorbed at the “hollow”-site and rotated 30° to the [011] crystal direction. The sites “top” and “bridge” of Table 3.1 are marked as well. b-d) Unit cells simulating the increasing coverages in experiment going from an isolated molecule to a full monolayer.

THM: The interaction between Ni-Phthalocyanine and a Cu(100) surface is maximized when the molecule adsorbs with the Ni at a “hollow” site and the N-Ni-N axis is oriented 30° to the main crystal direction [011].

STM images confirm the theoretically predicted rotation of the molecule with respect to the main crystal directions. For this configuration, we constructed three unit cells of different size in accordance with the experimental study, thereby varying the molecular coverage of the monolayer. The three coverages are shown in Figure 3.3b-d and are represented from left to right by the epitaxial matrices: isolated $\begin{pmatrix} 8 & 0 \\ 0 & 8 \end{pmatrix}$, loose $\begin{pmatrix} 7 & -1 \\ 3 & 6 \end{pmatrix}$, dense $\begin{pmatrix} 5 & -2 \\ 2 & 5 \end{pmatrix}$ with an increasing molecular density of 0.25, 0.35 and 0.55 molecules/(nm)².

Spin of Metal Centre

Chelated in the square-planar environment of the phthalocyanine’s coordination pocket, the Ni-centre adopts a diamagnetic (+2) oxidation state. The electrons of the metal occupy the d-states in a d⁸ configuration with an empty d_{x²-y²} orbital as shown on the left of Figure 3.4. Such an electronic configuration is inferred from gas phase calculations and expected for NiPc. This is, however, not the only spin solution that can be found for the “Hollow (30°)” adsorption site. Due to the close distance between molecule and surface, charge can be transferred from Cu to the molecular layer filling the Ni d_{x²-y²} with a single electron (see Figure 3.4a right). As a result, a spin is induced on the molecule and the chelated Ni changes to a Ni(I) d⁹ configuration. Our calculations, thus, suggest two local minima for the same adsorption site, which differ in the spin of the system (spin and no-spin). This prediction is confirmed experimentally by XPS measurements, where two peaks arise in the Ni spectrum matching the binding energy of a Ni d⁸ and d⁹ species.

For an isolated molecule on the surface, the spin on the Ni provides an additional energy gain of 0.08 eV. Upon increasing the coverage to a loose packing, the d⁹ state is still favoured by 0.07 eV. Finally, the stability of Ni(I) is reduced to 0.01 eV, when the molecules are adsorbed in a closely packed arrangement. Assuming the molecular states follow a Boltzmann distribution [136] in thermodynamic equilibrium at room temperature (Equ. 3.12),

$$N_{(no-spin)}/N_{spin} = e^{(\Delta E/k_B T)} \quad \text{Equ. 3.12}$$

the calculated energy difference, ΔE , between the spin and no-spin configuration suggests the spin-polarized species to be predominantly found at low coverage (population ratio of 96:4% and 94:6% for *isolated* and *loose*, respectively). In a saturated monolayer, both Ni states should exist almost equally on the surface (ratio 60:40%). Indeed, a similar trend can be observed in coverage dependent XPS experiments. Evaluating the areas of the two photoemission lines with increasing molecular packing, the Ni(I) species is more abundant than Ni(II) in the less dense layer, while in saturated coverage almost equal numbers of molecules adopt both spin configurations.

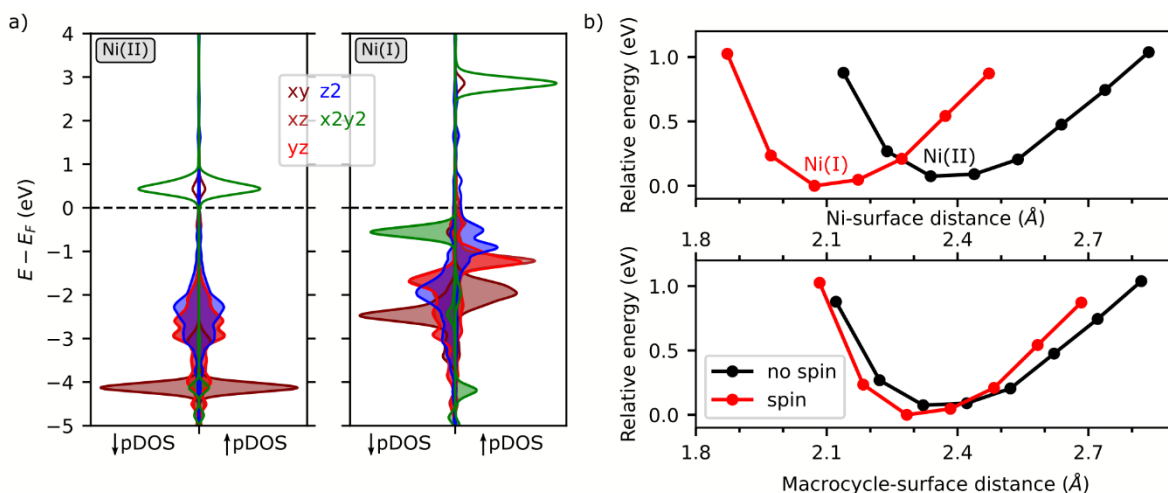


Figure 3.4: a) Density of states projected onto the Ni d-states for the non-magnetic and magnetic Ni species. Energies are in reference to the Fermi-energy shown as dashed line. b) Potential energy scan for both NiPc complexes obtained by varying the adsorption height of the two molecules. Energies are relative to the energetically lowest structure. All calculations utilize PBE+U-D3 ($\tilde{U}=3$ eV).

In this regard, it should be stressed that the occurrence of a *spin* species is closely connected to the utilization of DFT+U. In the present study, we have chosen an effective Hubbard parameter of 3 eV. Note that *ab initio* calculation of \tilde{U} for isolated NiPc suggest a much higher value ($\tilde{U} = 8$ eV [137,138]), however, due to the screening of surrounding electrons, \tilde{U} can be expected to decrease on surfaces compared to the pure gas phase. Without the Hubbard correction, it was not possible to optimize a stable minimum of Ni(I)Pc on Cu. Instead, estimating from single point calculations, pure PBE favours the *diamagnetic* Ni(II) state by 0.05 eV.

THM: Employing DFT+U, we find that the surface stabilizes two, almost isoenergetic spin states of the central Ni atom – a diamagnetic Ni(II) and a paramagnetic Ni(I). To accept the additional electron for a d9 configuration, the Ni atom moves out of the tetrapyrrole environment towards the surface.

Apart from the energetic difference of the spin states, our findings are robust with respect to the NiPc coverage. A detailed analysis of the molecular properties now follows exemplary only for the loose arrangement. For the central Ni atom, changing its spin has in particular geometric consequences. The interaction with the Cu substrate pulls the Ni out of the molecular plane towards the surface (from 2.33 Å to 2.07 Å), while the molecular macrocycle is locked at approximately the same height (~ 2.3 Å). Figure 3.4b shows a scan of the potential energies of the two species as a function of the molecule-surface distance, i.e.: obtained by gradually adjusting the adsorption height of the molecules. In first approximation, we thereby estimate the transition between the two stable spin states during deposition. Once Ni(II)Pc approaches a certain height above the surface, the energetic barrier towards the distorted Ni(I) structure mainly concerns the Ni leaving its coordination pocket.

Charge Transfer to Macrocycle

The almost identical heights of the macrocycle for both adsorption configurations already indicates a strong interaction, binding the carbon backbone to the Cu substrate. Charge density difference analysis indeed reveals a charge transfer from the surface to the molecules. Independent of the spin on the Ni, regions associated with the degenerate LUMO and LUMO+1 of the molecule get populated upon adsorption (compare Figure 3.5a for Ni(I) and Figure 3.5b for Ni(II)). Projecting the density of states of the total system onto the molecular orbitals of NiPc further supports our finding. Illustrated in Figure 3.6a, on the surface, the formerly unoccupied states LUMO/+1 shift below the Fermi level. The charge transfer is accompanied by a large decrease in the work function from 4.6 eV for the pristine Cu-surface to 3.9 eV for the molecular monolayer. In this regard, it might be interesting to note that the work function change is not uniform for both spin-species. Instead, our calculations suggest that the work function for a film with Ni(I) is 0.05 eV larger than for the Ni(II) species. In other words, the additional electron transfer to form the spin-polarized Ni(I)Pc effectively increases the work function. This could be a further explanation why we observe both spin-species on the surface as such local work function increases during film growth might prevent neighbouring molecules to adopt the Ni(I) state as well.

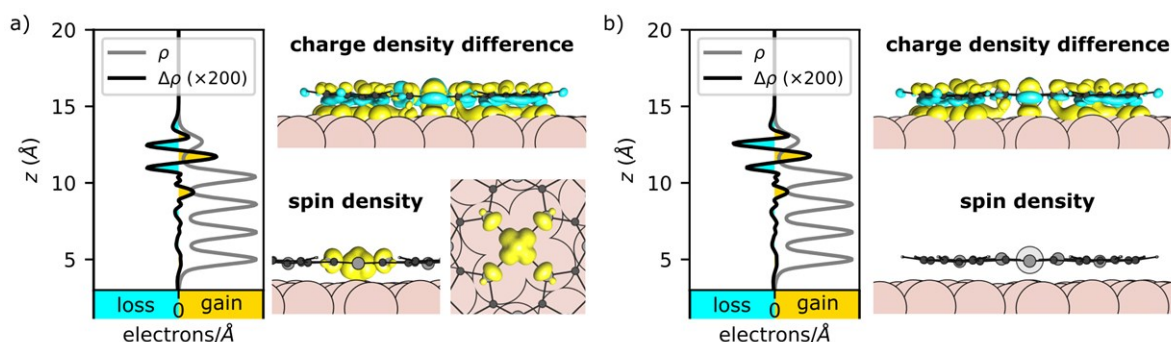


Figure 3.5: Charge density difference analysis and spin density for the complex hosting Ni(I) (panel a) and Ni(II) (panel b) as obtained with PBE+U-D3.

Experimental insight into the energy level alignment of the frontier orbitals is provided by photoemission spectroscopy. The valence band spectra acquired for NiPc/Cu show the presence of three peaks located at binding energies of 0.2, 1.0 and 1.6 eV. Employing the approach of photoemission orbital tomography (POT), the angle resolved momentum maps at these binding energies are compared to simulations obtained from the interface (top panel Figure 3.6b). Note that due to intense bands of the substrate at low k -values, the simulated intensities inside a circle of radius = 0.09 \AA^{-1} have been suppressed for better contrast. Also note that the 4-fold symmetry of the substrate and the concomitant presence of rotational domains has been taken into account in the simulated momentum maps. The peak at highest binding energy (1.6 eV) can be attributed to emissions from the HOMO, while the peak just below the Fermi level ($EB = 0.2 \text{ eV}$) belongs to the LUMO/+1 of NiPc. Averaging over a large area within the molecular assembly, the sharp photoemission features suggest one specific orientation of the molecules on the substrate, consequently confirming the 30° rotation of the N-Ni-N axis to the main crystal direction [011] seen in STM images.

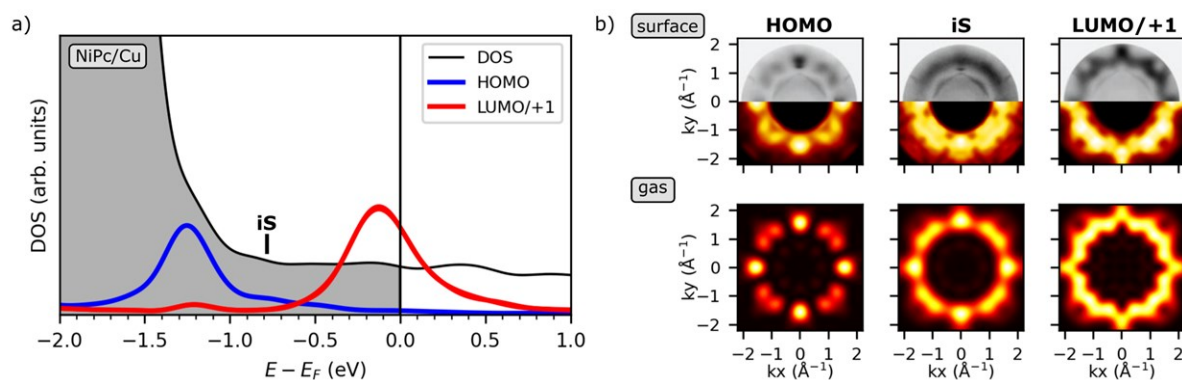


Figure 3.6: a) Density of states of the NiPc/Cu interface projected onto the HOMO, LUMO and LUMO+1 of the molecule. The intermediate state found in photoemission experiments is denoted “iS”. b) Comparison of experimental momentum maps (top) to simulated maps of the periodic interface (middle, PBE+U-D3) and in the gas phase (bottom, B3LYP-D3). Note that for the periodic interface, the simulated intensities inside a circle (radius = 0.09\AA^{-1}) have been cut to suppress intense substrate features at low k -values and increase contrast.

As we cannot straightforwardly associate the third feature arising at 1 eV with a molecular orbital, we label it tentatively as an intermediate state (iS). Searching through the corresponding energy range in the simulated momentum maps, we find indeed an intensity pattern originating from both spin species that fits the experimental maps. In order to understand the origin of the peak on a molecular level, we utilize simulated maps of NiPc in the gas phase (Figure 3.6 bottom panel). While a suitable emission pattern cannot be found for the gas phase molecule, the intensity distribution of the iS can indeed be reproduced by a superposition of HOMO and LUMO emissions. In contrast to energetically localized states in a gas phase molecule, a consequence of the strong interaction of the molecule with the substrate is a broadening of the electron density between the HOMO and LUMO states. The resulting overlap between both orbitals gives rise to the observed ARPES map, which is, therefore, a true interface feature.

THM: Strong charge transfer from Cu(100) to the tetrapyrrole backbone anchors the macrocycle on the surface regardless of the spin state of the Ni. Photoemission orbital tomography suggests the occupation of the degenerate LUMO and LUMO+1 molecular levels.

Annealing

Next, we investigate the thermal stability of the Ni(I) configuration observed in the pristine NiPc layer. According to measured data the *spin* configuration is stable up to relatively elevated temperatures. Only upon annealing to 575 K, spin sensitive methods like XMCD and NEXAFS detect no signal related to the Ni d^9 species any more suggesting full conversion to a Ni(II). Simultaneously in photoemission spectroscopy, both molecular features associated with HOMO and LUMO are shifted by 0.2 eV toward the metal Fermi level and the intermediate state vanishes. This points towards a decreased molecule-substrate interaction going to a more decoupled molecular system after annealing.

We can mimic the experimental findings by artificially increasing the adsorption height of NiPc. As inferred from the potential energy scan (Figure 3.4b), above a Ni-surface distance of 2.3\AA , the distorted spin-polarized species quickly becomes unfavourable and transitions into the planar molecule without spin. Lifting the molecule further from the surface not only

changes the spin but then also affects the interaction of the macrocycle with the surface. As the molecule is moved upwards, the charge transfer, or in other words, the molecule-surface hybridization at the interface is gradually suppressed. The influence on the frontier orbitals is illustrated in Figure 3.7 by the density of states projected onto the atoms of the macrocycle. Our calculations indicate that already an upward shift of the macrocycle backbone by $\geq 0.5 \text{ \AA}$ leads to a downshift of -0.2 eV of the HOMO and LUMO levels in good agreement with the experimental observations. Furthermore, the intermediate state, which is seen as a clear peak in the projected density of states of the optimized interface, diminishes by increasing the molecule-surface distance.

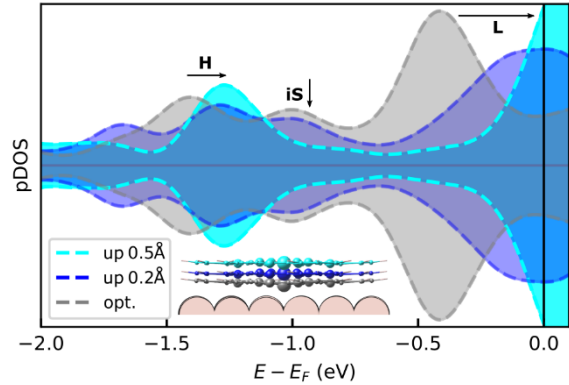


Figure 3.7: Density of states projected onto the atoms of the macrocycle for different molecule-substrate distances. The inset sketches the artificial shift of the molecule from its optimized position upwards.

Supporting our above statements, increasing the adsorption height in the simulations also nicely reproduces the relative changes in the work function of the samples. The observed trend points towards the qualitatively different interactions before and after annealing. First, the work function decreases compared to clean Cu(100) due to the strong interaction of NiPc with the surface ($\sim -0.7 \text{ eV}$). By annealing, this interaction is reduced (or even completely broken), thereby increasing the work function ($\sim +0.1 \text{ eV}$), which we recover in our simulations by lifting the molecule away from the surface.

Table 3.2: Experimental work function and relative change of the clean Cu-surface, after deposition of NiPc and after annealing to 575K compared to the absolute work function and relative change for the corresponding simulations with PBE+U-D3.

Experiment	WF [eV]	Change [eV]	Simulation	WF [eV]	Change [eV]
clean Cu(100)	4.70		clean Cu(100)	4.56	
NiPc monolayer	4.00	-0.7	opt. NiPc	3.87	-0.69
annealed	4.10	+0.1	dist. $\geq 0.4 \text{ \AA}$	3.95	+0.08

Complementary to the NEXAFS and POT experiments, we have performed X-ray photoemission spectroscopy (XPS) to study the effect of annealing on the core levels of NiPc. As the frontier orbitals of NiPc, which are involved in the switchable substrate-molecule interaction, are mainly localized on the carbon macrocycle, we expect the largest influence on the C 1s spectra. To establish the main peaks in our NiPc C 1s analysis, we start with the experimental data of NiPc on an oxygen-passivated Cu surface as a reference system (Figure 3.8a). Similar to the investigation of heptacene in chapter 2.3, we find that the molecule behaves gas-phase-like and is electronically decoupled from the surface. The experimental spectrum consists of two dominant peaks, which can be attributed to emissions from carbons bound to other carbons (284.6 eV) and to nitrogen (286.0 eV), respectively. The small peak at 287.8 eV has previously been identified as a $\pi \rightarrow \pi^*$ satellite [139–141]. In accordance with the stoichiometric ratio of C-C and C-N in NiPc (24:8), we obtain a ratio of the experimental peak intensities of 3:1. The electronic decoupling from the surface further allows us to compare the

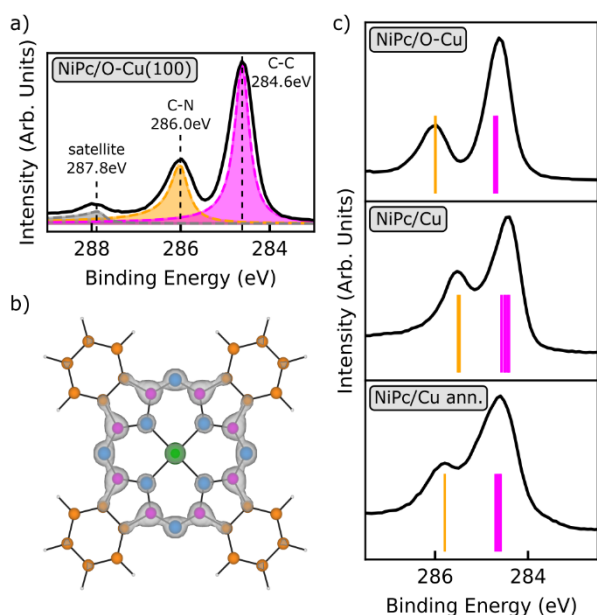


Figure 3.8: a) C 1s XPS of NiPc/O-Cu(100) with experimental peak fits. b) Calculated electron density summed over LUMO and LUMO+1. c) Experimental C 1s spectra of NiPc on passivated Cu and deposited on bare Cu before and after annealing; lines mark the calculated energies using the $\Delta K-S$ approach; absolute values are shifted for comparison with experiment.

experimental spectra to C 1s core-energies of the gas phase molecule calculated with the $\Delta K-S$ approach. Here, we find excellent agreement in the relative peak positions between experiment and theory, thus, supporting our assignment (Figure 3.8c top, the absolute calculated values are shifted for comparison).

Going from the non-interacting passivated to the above discussed, pure Cu surface, the as-deposited NiPc receives charge from the substrate. According to our calculations, the additional occupation of the LUMOs increases especially the electron density at the C-N component (seen in Figure 3.8b). Assuming such a local charge transfer would also imply a shift of the respective C 1s component toward lower binding energies. Indeed, we see a decrease of the peak distance in the experimental XPS spectrum from 1.37 eV (O-Cu) to 1.10 eV (Cu) (Figure 3.8c middle). This relative shift between the two C components is nicely reproduced in the XPS simulation for the NiPc/Cu interface, where the relative peak distance of 1.30 eV for the molecule in the gas phase reduces to 1.02 eV on the Cu-surface.

Upon annealing, the experimental XPS spectrum broadens, and the two main peaks move further apart again (1.19 eV). We can explain these findings by the decrease of the electron density in the LUMO, pointing toward a reduced charge transfer between the NiPc and the surface. Artificially lifting the molecule upwards from its optimized adsorption height yields a similar relative shift in the simulated XPS spectrum (1.15 eV) as was found in measured data (Figure 3.8c bottom). Thus, the comparison between XPS experiments and theory additionally supports our idea of a change in interaction between molecule and substrate upon annealing.

In our simulations, increasing the molecule-surface distance is necessary to reduce the calculated charge transfer and, consequently, affect properties such as the work function or the C1s XPS spectra. However, it should also be mentioned that above temperatures of 575 K, STM images show the occasional formation of new supramolecular structures with estimated distances between adjacent molecules smaller than van der Waals radii. Similar high temperatures (close to 575 K) have been reported for on-surface reactions in metal porphyrin molecules on metal substrates [142,143]. While we cannot unambiguously identify the processes taking place upon heating, our combined experimental and theoretical approach most importantly provides strong evidence that annealing breaks the molecule-surface interaction.

THM: Upon annealing, experiments suggest a *reduced* interaction of NiPc with the surface. In our calculation, we are able to mimic this situation by deliberately moving the molecule away from the substrate, thereby, recovering the experimental energy level alignment, work function change and XPS spectrum. Hence, it is reasonable to believe that the interaction is indeed reduced after the heating, albeit the underlying mechanism remains to be solved.

3.3 Adsorption of Small Gases at NiTPP

3.3.1 Introduction

Besides moving on an intrinsically shallow energy landscape as the metal complex in the previous example, an alternative means of switching the spin state of the Ni atom may be external stimuli leading to actively modifying the ligand field around the metal centre [133,144,145]. Such modifications may include conformational changes in the molecule or the adsorption of axial ligands. Especially the latter method is frequently exploited in natural processes, which utilize the molecular structure of porphyrins – the biological pendant to the synthetic phthalocyanines and the second important group of tetrapyrroles. The most prominent example of a ligand induced spin-change is the adsorption of oxygen to the haem-group to transport the life sustaining gas in the bloodstream [146–148]. Stimulated by its success in nature, the adsorption of small gases to porphyrins has also repeatedly attracted attention in the playground of surface science [149–155].

While various experimental techniques can give insight into the electronic and magnetic changes induced by the additional ligand, thorough understanding on a molecular level comes from comparison with theoretical simulations. Here, density functional theory (DFT) is almost exclusively the method of choice from the theoretician's toolbox. Its practical implementation, however, relies on several approximations, which in turn may limit the informative value of the calculation. At the moment, modelling surface chemistry is realistically feasible within the generalized gradient approximation (GGA). This level of prediction suffers from well-known and fiercely discussed problems [119,156–159], nonetheless, it allows accurate insights into the electronic structure of porphyrins for extended molecular layers [160–163]. On the opposite, the adsorption of small molecules at porphyrin interfaces has also been successfully modelled by applying a cluster approach, where the surface is replaced by a cluster of metal atoms, or at the extreme, by a single atom [164,165]. Missing the effect of periodic replica comes at the advantage of allowing for a higher-level theory, e.g.: in the form of hybrid functionals, for the description of a rather localized property such as oxidation and spin state of the central metal atom. On the other hand, neglecting intermolecular interaction or simplifying the molecule-substrate interactions may as well lead to a poor description of the electronic structure when compared to actual experiments.

Either way, careful analysis within the limitations of the method is needed to obtain reliable interpretations. Therefore in this section, we first aim to deepen our understanding of actual and spurious interactions that may arise when investigating porphyrin-interfaces and, in particular, molecular switches before evaluating experimental data.

Article Information and Author Contribution

The following section summarizes our search for a ligand induced spin-switch interface. The investigation eventually culminated in two publications, in which I was involved. The article [41] represents my main contribution, as it specifically covers the theoretical aspects and complexity of modelling periodic spin-interfaces. Beside the calculations, I have created the underlying concept of the manuscript and written the first draft. In [39], a molecular spin-switch has been realized in close collaboration with especially **Henning M. Sturmeit** and **Giovanni Zamborlini**, who conceptualized the study and conducted the experiments. We

discussed the results together and I contributed the computational part – including text and figures – of the manuscript, as well as revised it.

Inorganica Chimica Acta 558 (2023) 121719



Contents lists available at ScienceDirect

Inorganica Chimica Acta

journal homepage: www.elsevier.com/locate/ica



Computational study on the adsorption of small molecules to surface-supported Ni-porphyrins

Andreas Windischbacher^a, Peter Puschnig^{a,*}



RESEARCH ARTICLE

Check for updates

small

www.small-journal.com

Room-Temperature On-Spin-Switching and Tuning in a Porphyrin-Based Multifunctional Interface

Henning Maximilian Sturmeit, Iulia Cojocariu, Andreas Windischbacher, Peter Puschnig, Cinthia Piamonteze, Matteo Jugovac, Alessandro Sala, Cristina Africh, Giovanni Comelli, Albano Cossaro, Alberto Verdini, Luca Floreano, Matus Stredansky, Erik Vesselli, Chantal Hohner, Miroslav Kettner, Jörg Libuda, Claus Michael Schneider, Giovanni Zamborlini,* Mirko Cinchetti, and Vitaliy Feyrer

Figure 3.9: Headers of both articles [39,41] including all contributing authors. The computational study was published in *Inorganica Chimica Acta*, the experimental work in *Small*.

3.3.2 Results and Discussion

Adsorbents (NiTPP)

Our investigation centres around the metal-organic complex Ni-tetraphenylporphyrin (NiTPP), which we will study in three different environments. First, to introduce the electronic properties of NiTPP, we present gas phase simulations. Here, we can also explain the adsorption behaviour of additional ligands in the form of chemically intuitive metal-ligand interactions. Building the bridge to surface science, we then focus on two different surfaces, which control the oxidation state of the Ni centre, since the electron density at the Ni should reflect the way how additional ligands adsorb at the metal atom. So as the second system, we have chosen NiTPP on an oxygen-passivated Cu(100) surface with a (2x2)R45 reconstruction (O-Cu, Figure 3.10a). In a previous study, on O-Cu, the Ni-complex was found to be decoupled from the surface, essentially retaining its gas phase behavior [107] and chelating a low spin Ni(d⁸) (cf. Figure 3.10c). Our third system consists of a monolayer NiTPP adsorbed on a pure Cu(100) surface (Figure 3.10b). Previous studies on this system have shown a strong charge

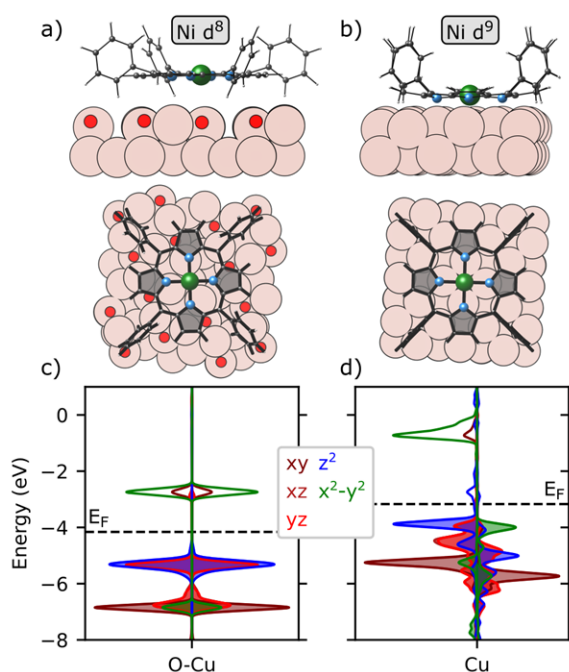


Figure 3.10 Side and top views of the adsorption structure of NiTPP on oxygen-passivated Cu(100) (a) and clean Cu(100) (b), respectively. Panel (c) and (d) display the density of states projected onto the Ni d-states for both systems. The energy is in reference to the vacuum energy, the dashed lines mark the Fermi energy E_F .

transfer from the substrate to the NiTPP, resulting in a strongly distorted adsorption geometry [142,166]. Simultaneously, the diamagnetic Ni(2+) is reduced to a paramagnetic Ni(d⁹) species (cf. Figure 3.10d).

Usually, the interaction of the metal centre with its surrounding ligands can be understood as a redistribution of electrons between the involved species. Assuming that mainly valence electrons contribute to bond formation, the ligands are then classified according to the ability of their frontier orbitals to donate/accept electrons to/from the d-orbitals of the metal. The strength of this interaction is governed by the energy level alignment and symmetry of the interaction partners. To better understand the classification of our adsorbate gases, we will first describe their highest occupied and lowest unoccupied molecular orbitals (HOMO and LUMO, cf. Figure 3.11). For the bonding, we will adopt the common notation of sigma and pi-orbitals depending if a nodal plane passes through the bonded nuclei (π) or not (σ).

As ligands, we have chosen six small gases (CH₄, H₂O, NH₃, CO, NO and NO₂), which are typically associated with different coordination behaviour in organo-metallic chemistry. At this point, it may be helpful to revisit the bonding concepts of coordination complexes before we look into their properties at the above-mentioned hybrid interfaces.

Adsorbates (Small Gases)

As ligands, we have chosen six small gases (CH₄, H₂O, NH₃, CO, NO and NO₂), which are typically associated with different coordination behaviour in organo-metallic chemistry. At this point, it may be helpful to revisit the bonding concepts of coordination complexes before we look into their properties at the above-mentioned hybrid interfaces. Usually, the interaction of the metal centre with its surrounding ligands can be understood as a redistribution of electrons between the involved species. Assuming that mainly valence electrons contribute to bond

THM: Adsorption on a pure and a passivated Cu-surface controls the oxidation and spin state of Ni-tetraphenylporphyrine interfaces forming molecular monolayers with a Ni(I) and a Ni(II) species, respectively. We will investigate the consequences of both initial spin states for the adsorption of external ligands.

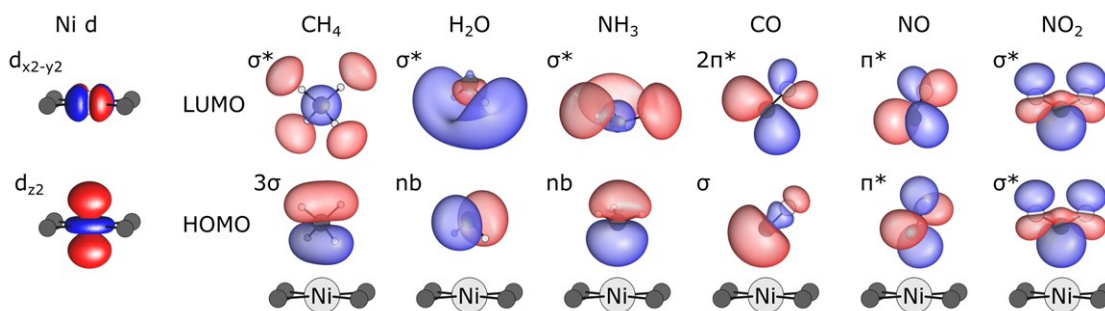


Figure 3.11: Highest occupied and lowest unoccupied d-orbital of the Ni-complex as well as molecular orbitals of the adsorbate gases, as obtained from gas phase calculations using the B3LYP functional.

Methan (CH₄)

The frontier orbitals of CH₄ are described as linear combinations of the carbon 2s and 2p valence orbitals with the hydrogen 1s. The resulting molecular orbitals are of sigma-character, where the HOMO is notably three-fold degenerate. With all valence electrons shared over the four single bonds and in the absence of a lone pair, the saturated molecule does usually not take part in coordination. CH₄, therefore, acts as a non-interacting reference gas in our investigation.

Water (H₂O)

The highest four valence electrons of H₂O are easily mistaken as two equivalent lone pairs located at the oxygen. These lone pairs, however, turn out to be not energetically degenerate. Due to symmetry arguments during the combination of atomic orbitals, the HOMO of H₂O corresponds mainly to the non-bonding O 2p-orbital perpendicular to the molecular plane. Coordinating via the oxygen, H₂O can then be termed as a weak pi-donor. This classification is variable also depending on the coordination geometry and the energy alignment with the metal d-orbitals.

Ammonia (NH₃)

In the case of NH₃, chemical intuition and theory match much better than for H₂O. The lone pair at the nitrogen, which is expected to interact with the chelated transition metal within the porphyrin macrocycle, has strong N 2p-character and points away from the H-cone. Any ligand-interaction of the non-bonding HOMO can only be of sigma-type.

Carbon Monoxide (CO)

Despite its simple diatomic structure, CO is an interesting ligand in coordination chemistry. While consisting of contributions from both atoms, the HOMO is strongly polarised towards the carbon. In first approximation, it can be thought of as the C lone pair, which forms a sigma-bond to orbitals on the metal. The versatility of the gas, however, stems from its doubly degenerate LUMO. Depending on the metal, suitable d-states may transfer electrons into one of the two anti-bonding pi-orbitals in what is usually referred to as “backdonation”, thus providing additional stability to the complex.

Nitric Oxide (NO)

The molecular orbital diagram of NO is similar to CO. Only, an additional electron is now localized in one of the anti-bonding pi-orbitals making it a SOMO. Being a radical allows for ambiguous coordination concepts. In complexes, where NO provides the single electron as well as its N lone pair for the interaction with the metal, the ligand often behaves analogously to CO

as an electron donor and acceptor. Such complexes are characterized by a linear coordination geometry. On the other hand, if solely the radical electron participates in the bonding, the donor properties mostly prevail, and the NO ligand is bent.

Nitrogen Dioxide (NO₂)

Similar to NO, NO₂ is also a radical with its single electron mainly located at the nitrogen. However, due to its polarized resonance structures, NO₂ can either coordinate via the electron withdrawing nitrogen or one of the lone pairs at the more electronegative oxygen, depending on the complex. With the highest electron affinity of our gases, it is also the best oxidizing agent in our investigation.

Isolated Metal-Ligand Complexes

Having the basic properties of our adsorbates in mind, we start our discussion by comparing the symmetry and energy of their molecular orbitals to those of the NiTPP complex. To give an overview of the energetic situation, Figure 3.12 shows the energies of the Ni d-states and of the frontier orbitals of the adsorbates in reference to the vacuum energy, i.e.: following Janak's theorem providing a measure of the ionization potential (HOMO) and electron affinity (LUMO) of the molecules. The symmetry of the involved orbitals can be inferred from Figure 3.11. Upon axial adsorption at the square planar coordinated Ni centre, possible orbitals for interaction involve mainly the Ni d_{z²} and d_{x²-y²} levels. Note that contributions from the degenerate d_{xz} and d_{yz} can be found at the same energy slightly below the d_{z²} in our calculations (see Figure 3.12 for gas phase and Figure 3.10 for periodic systems). However, these electrons are already involved in pi-bonding delocalized over the whole macrocycle, making them more unlikely to be shared with an additional ligand.

From the relative energy alignment between Ni d-states and gas orbitals of the *separate* subsystems, we estimate potential charge rearrangements occurring upon adsorption. Whenever ligand-metal orbitals are close in energy, they could impact our search for molecular spin switches in two major ways. First, the interaction with the ligand may alter the splitting of the Ni d-states, so that local rearrangements at the Ni flip its spin without affecting its oxidation state. Second, electron density may shift between ligand and metal centre, inducing a change in the oxidation state and consequently also the spin state of the chelated Ni. On the other hand, orbitals, which are energetically well separated are more unlikely to interact and influence the spin in the system. In the following section, we elaborate how the comparison in Figure 3.12 provides a first estimate about the expected spin behaviour in our surface-systems. Then, we test the established concepts by analysing the calculated electronic properties of the *full* adsorbate-complexes, which are summarized in Table 3.3. A detailed description of all molecular orbital diagrams, charge density differences and spin densities used in our characterization can be found in the Appendix (Figure 8.5 to Figure 8.10).

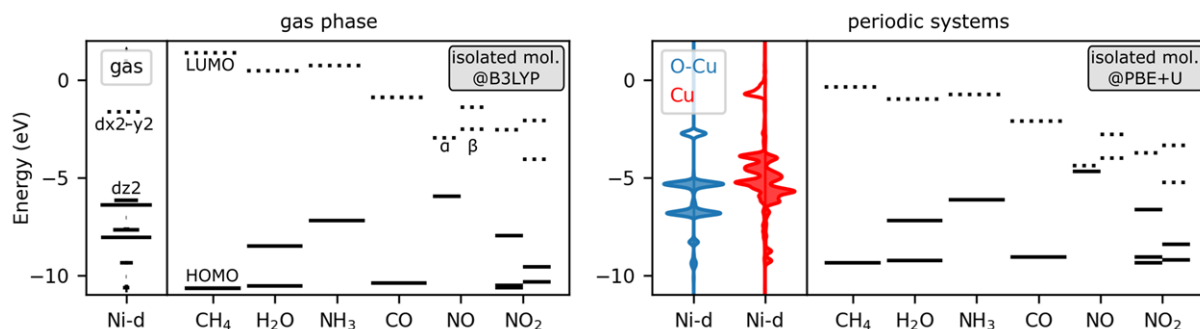


Figure 3.12: Orbital energies of the separate subsystems (NiTPP and ligand molecules) before formation of a complex. Occupied orbitals are displayed as filled, solid lines, unoccupied orbitals as blank, dotted lines. For open shell systems, both spin channels are shown as α and β . Gas phase values are calculated with B3LYP-D3. The periodic calculations (Cu and O-Cu) are at the PBE+U-D3 level of theory and their DOS aligned relative to the vacuum energy.

We first analyse the gas phase calculations (Figure 3.12 left), where the comparably smaller size of the system allows for a higher level of theoretical description (hybrid-functional B3LYP). Considering the molecular orbitals before formation of a complex, CH₄ should indeed take the role as the most weakly interacting ligand. Its HOMO and LUMO are energetically well separated from the Ni-d states. For H₂O, even though its HOMO-LUMO gap is reduced compared to CH₄, (i.e. the ionization potential *decreases* and simultaneously electron affinity *increases*), we find a similar picture. In both cases, analyses of the full CH₄ and H₂O-complexes reassure their non-interacting nature with regard to their spin-switch capabilities. The Ni-complex remains in its low spin d⁸ configuration feeling little influence from the additional ligand.

Proceeding with NH₃, the ligand-metal interaction is expected to increase significantly. This is because the HOMO of the gas adsorbate and the filled Ni d_{z²} lie within the same energy range and, furthermore, exhibit similar symmetry. Both factors facilitate the overlap between the ligand and metal orbital and due to the involved levels being occupied, (Pauli) repulsion between their electrons. This unfavourable repulsion is avoided by promoting an electron from the Ni d_{z²} to the empty Ni d_{x²-y²}, effectively decreasing the splitting of the Ni-d states (which is sometimes referred to as weak field behaviour of NH₃ [33]). Indeed, our calculations reveal a clear preference for a high-spin Ni d⁸ in the gas phase, which is favoured by 0.17 eV over the low-spin species. Note that the change of spin state is also accompanied by a change in the overall molecular geometry of the porphyrin macrocycle. Different to the distorted geometry of a low spin species, high-spin Ni prefers a flattened core (for geometry of high-spin Ni, see Appendix Figure 8.7 and compare Ref.[167]).

In contrast, the frontier orbitals of CO are placed well apart from the Ni-d states. Thus, CO again fulfils our description of a non-interacting case and leaves the Ni in its original singlet d⁸ configuration.

Regarding the radical species, NO behaves similar to NH₃ as our calculation places its SOMO close in energy to the Ni d_{z²}. In a tilted adsorption geometry, the pi*-orbital of NO overlaps with the Ni d_{z²} lifting an electron from Ni d_{z²} to d_{x²-y²}. For the second time, our gas phase calculation suggests a spin switch to a high-spin Ni(d⁸) species.

On the other hand, judging from the relative energy alignment, NO₂ should show no influence on the spin state of Ni. Indeed, as there are no particular charge rearrangements, the gas phase structure belongs to a Ni d⁸.

THM: At an isolated Ni(II)TPP complex, the gases NH₃ and NO induce a spin-flip from a low-spin d⁸ Ni(II) to a high-spin d⁸ Ni(II).

Table 3.3: Spin state of Ni in the full NiTPP-ligand complex (S=singlet, D=doublet, T=triplet). Adsorbate-complexes which switch spin state upon adsorption of gas are highlighted bold.

	NiTPP	CH ₄	H ₂ O	NH ₃	CO	NO	NO ₂
Gas (B3LYP)	Ni(2+), d ⁸ S	S	S	Ni(2+), d⁸ T	S	Ni(2+), d⁸ T	S
O-Cu (PBE+U)	Ni(2+), d ⁸ S	S	S	Ni(2+), d⁸ T	S	Ni(2+), d⁸ T *	S
Cu (PBE+U)	Ni(1+), d ⁹ D	D	D	Ni(2+), d⁸ T	D	Ni(2+), d⁸ T	Ni(2+), d⁸ T

*The spin state of the NO-complex on O-Cu strongly depends on the level of theory, for explanation see main text.

From Isolated Molecules to Surfaces

As a lot of spin-switch investigations focus on extended interface-systems, it is desirable to transfer the concepts explained above for the isolated NiTPP to the surface realm. Such a link seems rather straightforward for NiTPP on passivated Cu, where the molecule is commonly considered to behave gas-like [107] and where, intuitively, bonding concepts analogous to the isolated molecule should apply.

While it is a widely accepted standard to treat the electronic structure of isolated molecules at least on a hybrid-functional level, large periodic systems are currently most of times still described at the GGA level. Therefore, when comparing results for gas phase calculations with those from extended, adsorbed layers, one also has to take the differences in theory into account. We highlight two of them, which become important in investigations like ours. First, the GGA functional leads to smaller HOMO-LUMO gaps of all species compared to the above-described hybrid functional calculations [168,169]. Tackling this problem on a periodic scale

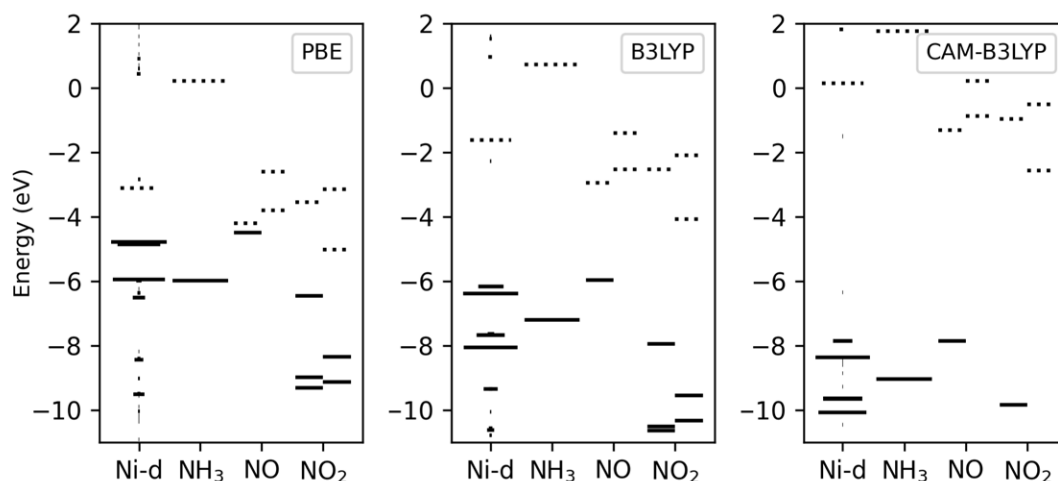


Figure 3.13: Orbital energies of the separate subsystems (NiTPP and ligand molecules) before formation of a complex calculated at three different levels of theory (PBE, B3LYP, CAM-B3LYP). Occupied orbitals are displayed as filled, solid lines, unoccupied orbitals as blank, dotted lines. For open shell systems, both spin channels are shown.

is subject of current investigations on periodic embedding schemes, which are beyond the scope of this work [170–174]. Second, it leads to a different energetic ordering of specifically the NiTPP states [166]. We can partially counteract the latter problem by treating the Ni d-states with an effective Hubbard-U correction. Before delving into the extended systems, we want to showcase the effect of both drawbacks on the adsorption of our ligands at the hand of the isolated molecules. Our discussion focuses on the three ligands NH₃, NO and NO₂.

To illustrate how an increasing opening of the HOMO-LUMO gaps of our components impacts the interpretation of our simulations, we have chosen three functionals with increasing exact exchange going from a GGA-functional (PBE) to a standard (B3LYP) and long-range separated hybrid-functional (CAM-B3LYP [58]). For each method, Figure 3.13 shows the energetic positions of the Ni d-states and the frontier orbitals of the ligands for the *separated* subsystems. The electronic structure of the Ni *after* adsorption is then summarized in Figure 3.14.

For NH₃, the orbital energies of its HOMO and of the Ni d_{z²} align increasingly better with higher theory. Thus, to minimize repulsion with the NH₃ HOMO, electron density moves from the Ni d_{z²} orbital to the d_{x²-y²} facilitating the spin-flip of the Ni centre. This reflects in the interesting result that the hybrid-functionals favour a high-spin Ni (by 0.17~eV (B3LYP) and 0.25~eV (CAM-B3LYP)) as opposed to PBE, where the alignment between the respective orbitals provides no need for a spin-flip of the Ni (see Figure 3.14 left). There instead, the low-spin Ni is predicted to be lower in energy by 0.34~eV. In other words, the wrongful level alignment of pure GGA underestimates the repulsion between the occupied orbitals.

In the case of NO, all three functionals position the SOMO of the molecule equally close to the Ni d_{z²} to suggest a high-spin Ni d⁸ species similar to NH₃. Indeed for the hybrid-functionals, we find a flip of the Ni d⁸ from low-spin to high-spin, which leads to a very loosely bound NO (E_{ad} = -0.07 eV(B3LYP) and -0.04 eV(CAM-B3LYP)). At the PBE level, however, the Ni remains in its initial d⁸ configuration (see Figure 3.14 middle). The difference is caused by the nearly degenerate frontier orbitals of NO in the GGA calculation. To minimize the interaction with the metal, the lone electron of NO occupies the pi* orbital with smallest overlap. Instead of a spin change at the Ni, electron density is redistributed with less effort between the two pi* orbitals. The energy gap error, thus, enables a spurious electronic rearrangement within the ligand.

At last, for NO₂, increasing theory decreases the electron affinity of NO₂, i.e.: its potential to uptake electrons. Analysis of the PBE calculation shows the SUMO of NO₂ lying below the Ni

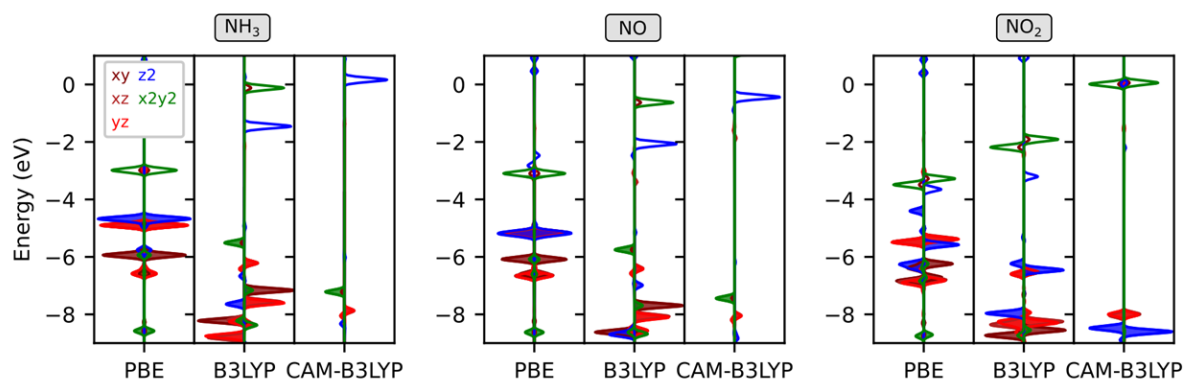


Figure 3.14: Density of states projected onto the Ni d-states for the NH₃, NO and NO₂-complex calculated at three different levels of theory (PBE, B3LYP, CAM-B3LYP) in the gas phase. Molecular levels artificially broadened for better visualization.

d_{z^2} and receiving electrons from the Ni (Figure 3.14). As the prediction of any partial reduction towards Ni d7 is dependent on the relative energy level alignment, the redox-reaction gets less with hybrid-functionals.

As a concluding remark, the most drastic influence on the overall properties is certainly encountered when moving from GGA to hybrid functionals, i.e.: including exact exchange in our calculations. The range separated description of exchange-correlation may then lead to better experimental agreement (albeit unproven due to the lack of data) but does not change our interpretation on a fundamental level.

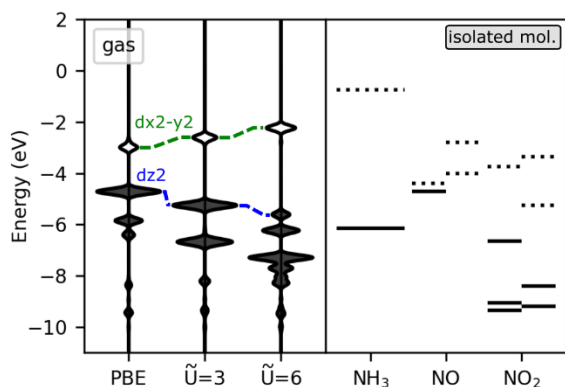


Figure 3.15: (left) Ni d-states of isolated NiTPP calculated with PBE+U-D3 for a \tilde{U} value of 0, 3 and 6 eV. (right) Orbital energies of the frontier molecular orbitals of the isolated gas ligands NH₃, NO and NO₂. Occupied orbitals are displayed as filled, solid lines, unoccupied orbitals as blank, dotted lines. For open shell systems, both spin channels are shown.

In an effort to mimic the electronic structure of NiTPP obtained with hybrid functionals, we employ a Hubbard correction scheme to the Ni d-states. Improving the on-site correlation of the d-orbitals in this way, the correction in particular affects their energetic positions. In Figure 3.15 (left), we demonstrate the gradual adjustment of the Ni d-orbitals when increasing the effective Hubbard parameter from 0 to 6 eV (0 eV corresponding to a standard PBE calculation in the gas phase). Note how the band gap between d_{z^2} and $d_{x^2-y^2}$ as well as the ordering of the d-states progressively resembles the B3LYP calculation as the occupied

(unoccupied) states shift to lower (higher) energy indicated by the dashed lines.

To evaluate the Hubbard correction not only with regard to pure NiTPP but to the adsorption of our ligands, Figure 3.15 (right) reminds of ionization potentials and electron affinities of the gases. Applying DFT+U on top of a PBE calculation, the appropriate energies correspond to the PBE obtained values. Analysis of the *full* adsorbate complexes depending on \tilde{U} is summarized in Figure 3.16. Here, the colour scheme illustrates the transition between different spin and oxidation states of the Ni centre due to changing energy alignments with the ligands. As a measure for the interaction strength, Figure 3.16 also shows the progression of the adsorption energy and the distance between Ni and ligand. A detailed discussion of these properties follows in a later section.

As aforementioned, the description of $\text{NH}_3\text{-NiTPP}$ with uncorrected PBE places the electronic levels of the gas and the metal-organic complex too far apart for an interaction. Accordingly, the metal centre is in its initial d^8 low-spin configuration with a weakly bound NH_3 at the van der Waals distance above it. Increasing \tilde{U} lowers the energy of the Ni d_{z^2} towards the NH_3 HOMO until with $\tilde{U} = 6$ eV both orbitals lie almost degenerate. During the scan, the approaching of the two occupied levels induces a high spin Ni d^8 accompanied by strong stabilization. Noteworthy, an effective Hubbard correction between 3 and 4 eV predicts electronic properties in best agreement with those from hybrid functionals ($E_{\text{ad}} = -0.5$ eV).

The Hubbard correction is helpful, whenever our prediction is dependent on the energy level alignment between both, the Ni and the ligand. If the adsorption behaviour is dominated solely by the energy gap of the ligand such as in the special case of NO, a simple shift of the Ni states has smaller effects. For this gas, neither PBE nor PBE+U is able to predict the correct spin behaviour of a high-spin Ni d^8 . Nonetheless, NO can serve as a theoretical example illustrating the opposing trend to NH_3 . When the U-parameter is increased, the Ni d_{z^2} shifts further apart from the NO HOMO. Since the tendency for interaction gets thereby reduced, the gas gets less attracted to the metal-complex, e.g.: as seen in the significant reduction of the Ni-ligand bond length by about 1 Å.

So far for NH_3 and NO, the DFT+U approach triggered either the on- or off-switching of a metal-ligand interaction compared to DFT. For NO_2 , we can observe how different flavours even within the same level of theory may lead to contrasting interpretations. The pure PBE alignment predicts the electron affinity of NO_2 to be high enough to partially receive electrons from the Ni d_{z^2} (d^7 character). In contrast, with a sufficiently strong Hubbard correction, the Ni d_{z^2} is positioned closer to the HOMO of NO_2 and repulsion of the occupied orbitals promotes an electron to the $d_{x^2-y^2}$ (d^8 high spin). The transition between the two interaction mechanisms can easily be induced by adjusting the U parameter in the calculations. At the turning point between the interactions, the adsorption energy and coordination bond exhibit a kink in their graphs, i.e.: an extremum. In the range of our scan, this structure exhibits the least interaction between NO_2 and NiTPP and best resembles the hybrid functional calculations.

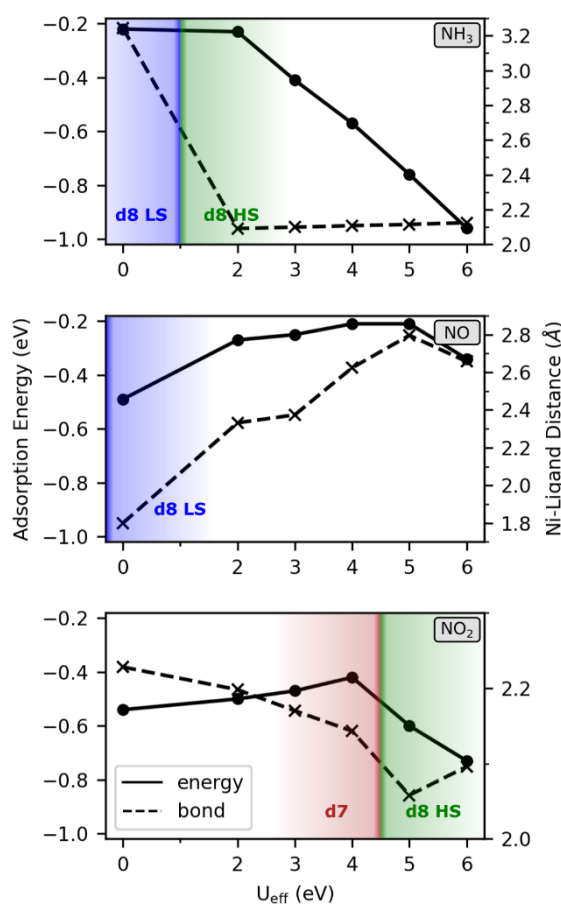


Figure 3.16: Analysis of the full metal-ligand complexes employing PBE+U-D3 with varying \tilde{U} . adsorption energy (left axis) and Ni-Ligand distance (right axis), LS=low spin, HS=high spin

From Figure 3.15 we have learned, that validating the electronic structure of NiTPP against higher-level calculations would suggest effective Hubbard parameters of about 6 eV. Perhaps unexpected, such a comparison does not automatically guarantee the correct description of the adsorbate complex. Indeed, in the search of an appropriate \tilde{U} for adsorption studies, the decisive parameter is not the agreement of the absolute orbital energies of the d-states, but the relative energetic position to the frontier orbitals of the ligands. For the present investigation, we, thus, recommend an \tilde{U} between 3 and 4 eV.

THM: In the calculation of metal complexes, the alignment between the energy levels of the chelated metal centre and a ligand is an important parameter determining the metal-ligand interaction. The band-gap problem in (semi)local functionals such as PBE is one source of error leading to false predictions about those interactions. For cases, where a wrong estimation of the metal's states is the main problem, DFT+U provides the possibility to nonetheless obtain reliable results. However, we should also be aware that solely correcting the energies of the metal's states does not automatically guarantee a correct description of the metal-ligand interaction.

Representative for the non-interacting ligands, Table 3.4 compares the adsorption energies of the isolated complexes across our set of methods. As expected, for our non-interacting molecules CH₄, H₂O and CO, there is no specific dependence on the functional, when climbing the rungs of Jacob's ladder (PBE, PBE+U, B3LYP, CAM-B3LYP).

Table 3.4: Adsorption energies for non-interacting ligands calculated in the gas phase at four levels of theory: PBE, PBE+U ($U = 3$ eV), B3LYP and CAM-B3LYP.

E_{ad}	CH ₄	H ₂ O	CO
PBE	-0.21	-0.40	-0.22
PBE+U	-0.18	-0.28	-0.21
B3LYP	-0.18	-0.37	-0.18
CAM-B3LYP	-0.18	-0.40	-0.17

O-Cu Surface

In light of the demonstrated shortcomings of our GGA calculations, we turn to the description of a monolayer NiTPP on passivated Cu. Remember, that for this interface, the electronically decoupled NiTPP complex should preserve its gas phase properties. Based on the discussion in the previous section, we have chosen to model it with a Hubbard correction for the Ni d-states of 3 eV, a value, which is also commonly used for pyrrolic systems in literature. [152,175–180]. Indeed, readjusting the d-states of NiTPP on the passivated surface resulted in a similar molecular orbital ordering as in the gas phase B3LYP calculations. In the comparison of the *separate* subsystems (as in Figure 3.12 right), this correction clearly only impacts the periodic NiTPP adlayer. Electron affinity and ionization potential of the adsorbate gases remain at to the conventional GGA (PBE) values.

As expected, the *full* periodic calculations on the passivated surface predict the same electronic behaviour as in the gas phase (cf. Table 3.3 and previous section). Namely, the three ligands, CH₄, H₂O and CO, take the role of non-interacting ligands also in the full periodic simulations. We observe no major redistribution of electrons and, consequently, the initial spin

state of the Ni, i.e.: d^8 , is unaltered upon ligand adsorption. For NH_3 , NO and NO_2 , the discussion with all its caveats largely corresponds to the previous section and is only briefly reviewed here.

Applying an \tilde{U} of 3 eV, NH_3 -NiTPP on passivated Cu mimics our gas phase calculations. The energy level alignment suggests that electron density moves from the Ni d_{z^2} orbital to the $d_{x^2-y^2}$ to minimize repulsion with the NH_3 HOMO. Consistently, the *high-spin* Ni d^8 state is stabilized by 0.18 eV compared to the low-spin state (close to the 0.18-0.25 eV stabilization from hybrid functionals).

On the other hand, the electronic behaviour of the nitrogen oxides on the passivated surface cannot be completely reproduced by PBE+U. For NO , the energetically close, occupied orbitals (Ni d_{z^2} and SOMO of NO) should promote an electron from the Ni d_{z^2} to $d_{x^2-y^2}$. This is however not the case in the periodic calculation. Instead, on the passivated surface, our calculation finds Ni in its initial *low-spin* d^8 configuration. In the charge density difference (Appendix Figure 8.9), we see the electron density being redistributed between the two nearly degenerate π^* orbitals, which prevents the spin-flip of the Ni.

Upon adsorption of NO_2 , our analysis of the periodic calculation shows partial charge transfer from Ni to NO_2 , which is facilitated by the symmetry of the NO_2 SUMO. Employing the GGA functional for the periodic surface mainly decreases the electron affinity of NO_2 to such an extent that its LUMO comes to lie close in energy to the Ni d_{z^2} . Choosing an \tilde{U} of 3 eV, the implied redox reaction is already weakened compared to pure PBE but still significantly stronger than in the case of hybrid functionals.

THM: Ni(II)TPP on a passivated Cu-surface behaves just as the gas phase molecule, even though, shortcomings in standard DFT may suggest otherwise and can cause misleading interpretations in some cases.

Cu-Surface

Our third system is the periodic array of NiTPP on a pure Cu-surface. Here, the monolayer NiTPP receives electrons from the substrate already upon deposition on the surface. Without the impact of additional ligands, partial filling of the Ni d_{z^2} has changed the initial spin configuration of the system to a Ni d^9 doublet [166]. While the $d_{x^2-y^2}$ does not possess the right symmetry to overlap with one of our gas candidates, the major impact of the charge transfer can be seen in the energetic readjustment of the d-states. The d-orbitals of the now electron rich Ni shift to higher energies, i.e., their ionization potential decreases. As a general consequence, the Ni can be expected to more likely donate one of its electrons.

Nonetheless, the energetic distance between Ni states and frontier orbitals of CH_4 and H_2O remains large. Thus, also for the case of the pure Cu-surface, there is no indication for interaction (cf. Figure 3.12). Very similar for CO on the metallic substrate, NiTPP seems to remain in its initial d^9 configuration. Interestingly, the charge density difference (Appendix Figure 8.8) still suggests some kind of charge rearrangements. A possible interpretation of its shape utilizes the common π -backbonding characteristics of the CO ligand, where the metal d-states interact with both frontier orbitals. Indeed, we find increased electron density in regions of the LUMO of CO and, at the same time, decreased electron density in the HOMO. It

is however important to note, that the strength of electron donation and back-donation in CO-complexes is an ongoing puzzle in DFT and it is repeatedly discussed that they are wrongly estimated within GGA [157,181].

The case of NH₃ exhibits a surprisingly similar energy alignment as on the gas phase and O-passivated Cu. However, while the HOMO of NH₃ is still close to the d_{z²} orbital, a Ni d⁹ species is not able to perform such a spin switch from low-spin to high-spin to avoid electron repulsion as commonly explained for Ni d⁸. Instead, charge density analysis suggests NH₃ to force electrons back into the substrate at the expense of the initial charge transfer from the Cu-surface to NiTPP (see Appendix Figure 8.7). A similar weakening of the molecule-surface bond has recently been recognized as the "*surface trans-effect*" [164,182].

The nitrogen oxides show a different interaction. On pure Cu, unoccupied orbitals of NO and NO₂ are calculated to have larger electron affinity than the ionization potential of the Ni d_{z²} and, additionally, face the metal atom with favourable symmetry. Thus, both times, the electron-rich Ni is able to perform a redox reaction by reducing the gas ligands and oxidizing the Ni d⁹ to a high spin d⁸. Note however, that we will show in the following, how the necessary approximations in theory again may influence this interpretation.

THM: On the pure Cu-surface, our DFT+U calculations suggest the gases NH₃, NO and NO₂ to change the initial d⁹ configuration of Ni(I)TPP to a d⁸ Ni(II). The excess electron is either transferred back to the surface or to the gas ligand.

Single Point HSE06

For passivated Cu, we have been able to assess the results of our simulations with the help of gas phase reference calculations. Unfortunately, we are unable to draw a similar comparison for NiTPP adsorbed on the pristine Cu-surface, as the interface-specific charge transfer from the substrate to the NiTPP is essential for modelling its electronic properties and cannot simply be reproduced in the gas phase. Instead, we have performed single point calculations of the periodic structures at the level of hybrid-functionals employing HSE06. The d-orbital resolved DOS to the right of Figure 3.17a confirms the desired Ni d⁹ configuration on Cu.

Even without full geometric optimization, the recalculated energy alignment for the *separated* subsystems in Figure 3.17b should allow for an estimate of the interaction in our metal-ligand complexes. Supporting our previous conclusions, the four ligands CH₄, H₂O, NH₃ and CO suggest the same behaviour as analysed for the PBE+U calculations. The electronic structures of their *full* complexes can be found in the Appendix (Figure 8.4).

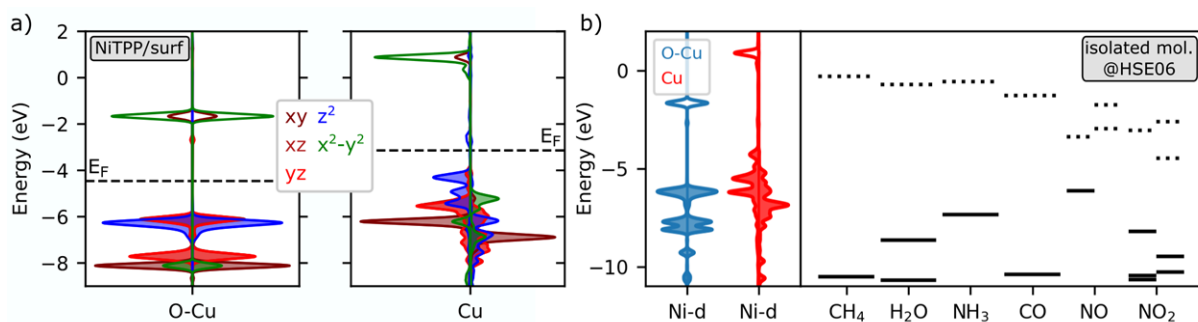


Figure 3.17: a) Density of states projected onto the Ni d-states for NiTPP on passivated Cu and pure Cu-surface. The dashed lines mark the Fermi energy E_F . b) Orbital energies of the separate subsystems (NiTPP and ligand molecules) before formation of a complex. Occupied orbitals are displayed as filled, solid lines, unoccupied orbitals as blank, dotted lines. For open shell systems, both spin channels are shown as α and β . All energies are calculated with single point HSE06 and in reference to the vacuum energy.

For NO, the infamous gap problem comes into play again. Although the HSE06 result is very similar to PBE+U as it equally predicts a spin change at the Ni, its cause has to be evaluated carefully. Remember that PBE+U calculates the ionization potential of the Ni d_{z^2} to be smaller than the electron affinity of NO. Thus, the SUMO of NO becomes partially filled. HSE06, on the other hand, hinders such a redox reaction by decreasing the electron affinity of NO (see orbital diagram on the left of Figure 3.18). Instead, any interaction between metal and ligand involves their occupied orbitals employing a competing orbital-effect similar to the case of NH_3 on Cu. Such an interpretation suggests electron transfer back to the substrate as cause of the spin-flip in the system. Therefore, although the spin of the Ni converts to a high-spin d^8 configuration for both levels of theory, HSE06 suggests a different underlying explanation.

With HSE06 exposing the erroneous PBE+U charge transfer of NO-NiTPP/Cu, doubts could analogously arise for NO_2 on the Cu surface. However, as seen in Figure 3.18 (right), the electron affinity of NO_2 calculated with the hybrid functional is still high enough to receive electrons from the Ni d_{z^2} . Thus, we are confident about the predicted redox reaction between NO_2 and NiTPP on pure Cu.

At this point, we briefly want to touch upon the passivated Cu-surface, for which the Ni d-projected DOS obtained with HSE06 is

also included in Figure 3.17. As we have already verified the results of our PBE+U simulations with the help of gas phase reference calculations, we did not explicitly recalculate the electronic structure of the *full* adsorbate-complexes. However, we may compare the energy level alignment of the *separate* subsystems from the single point periodic calculation (HSE06) in Figure 3.17 to the gas phase optimized energies from B3LYP in Figure 3.12. Evaluating the relative energy positions of the orbitals between both functionals, we find strong similarities. At a Ni d^8 centre, the frontier orbitals of CH_4 , H_2O and CO are energetically out of range to interact with the Ni d_{z^2} . The same goes for NO_2 , where both hybrid functionals raise the electron affinity of the molecule above the d_{z^2} level and prevent the spurious charge transfer suggested within GGA. Opposed to these non-interacting cases, the HOMOs of NH_3 and NO

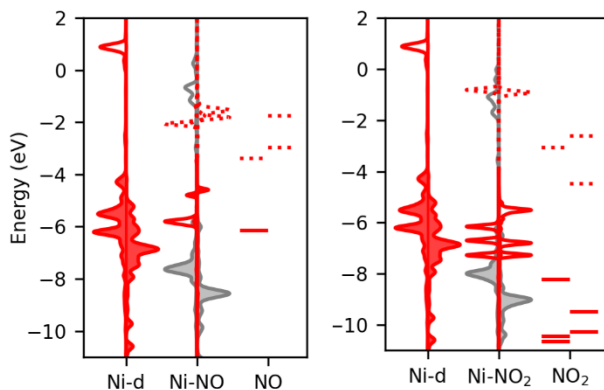


Figure 3.18: Molecular orbital diagrams for the adsorption of NO and NO_2 at NiTPP/Cu as obtained by single point HSE06.

may overlap with the occupied Ni d_{z^2} and, to avoid electron repulsion, promote the flip of Ni d^8 low spin to high spin. The agreement between two methods on the hybrid functional level simulating allegedly different environments strengthens our previous assumption that the passivation decoupled NiTPP can be treated as its gas phase counterpart.

THM: Recalculating the periodic interfaces on a hybrid functional level (HSE06) reaffirms our initial interpretations obtained from DFT+U. Solely for the nitrogen oxide NO the predictions differ, as the hybrid functional prevents the redox reaction between NO and Ni(I)TPP on the Cu-surface.

Interaction Mechanisms

Keeping the theoretical peculiarities in mind, our pool of exemplary gas ligands has so far shown four major interaction mechanisms with the central Ni-atom, that we characterize as a) non-interacting, b) weak-field d -splitting, c) competing *surface-trans* effect and d) redox reaction. The effects of these interactions are illustrated in Figure 3.19 with the help of the charge density difference between before and after the adsorption of the ligand. The first two mechanisms, a) and b), emerged for the Ni(d^8) species common for NiTPP in the gas phase or decoupled from a surface like on passivated Cu. In cases, where the frontier orbitals of the gas and the Ni d -states are distinctly separated, they will not interfere with each other. Consequently, as seen in panel a) at the example of $\text{CH}_4/\text{O-Cu}$, no major charge rearrangements can be observed in the system. On the other hand, occupied levels of the metal (Ni d_{z^2}) and ligand (HOMO) may compete with each other, given a correct symmetry and energy. For instance, for $\text{NH}_3/\text{O-Cu}$ (panel b)), electronic repulsion promotes an electron from the Ni d_{z^2} to the $d_{x^2-y^2}$ leading to a spin-flip of the Ni centre. Fittingly, the charge density difference shows electron density moving from above and below the atom (a region associated with the d_{z^2}) towards its centre.

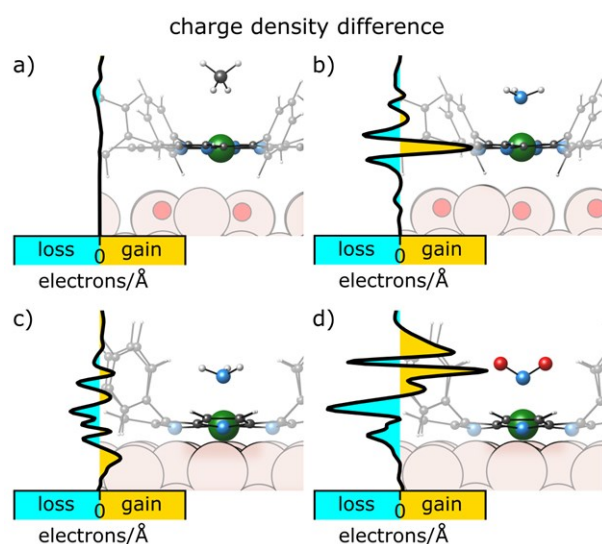


Figure 3.19: Charge density difference showcasing four possible interaction mechanisms of ligands with NiTPP. a) non-interacting (e.g. CH_4 on O-Cu), b) weak field d -splitting (e.g. NH_3 on O-Cu), c) surface *trans*-effect (e.g. NH_3 on Cu), d) redox reaction (e.g. NO_2 on Cu).

With the pure Cu-surface and its Ni(d^9) species, two more concepts characterizing the NiTPP-ligand interaction need to be introduced, illustrated by panels c) and d). Both concepts are covered under the broad term of the *surface trans*-effect, as the adsorbing ligand visibly weakens the Ni-surface bond pulling the chelated metal 0.2 Å away from the surface. However, we find the underlying interaction mechanisms to be of contrasting nature. In example c), competing occupied orbitals of the Ni and the gas ligand result in redistribution of electron density. As the $d_{x^2-y^2}$ is not empty anymore but already holds an electron, the interaction instead weakens the initial charge transfer from the Cu-substrate. Accordingly, this effect leads to

reduced density at the Ni and charge accumulation in the substrate, e.g., in the case of NH_3/Cu . With Ni-ligand and Ni-surface interactions opposing each other, the observed *surface trans*-effect is of antagonistic origin. In contrast in example d), the initial charge transfer, which reduced the Ni to an electron-rich d^9 species, can in turn be exploited to reduce the gas ligand. Charge rearrangements obviously involve both redox partners with an electron from the Ni moving to the ligand as for NO_2/Cu (panel d)). In this case, weakening of the Ni-Cu bond results from a synergistic *surface trans*-effect, as the preceding Ni-Cu interaction makes reduction of the ligand possible in the first place. Either way, both effects on Cu ultimately leave the initial Ni(d^9) in a d^8 high-spin configuration.

Adsorption Energy

Briefly summarizing, our simulations so far have identified three potential candidates (NH_3 , NO and NO_2) to manipulate the spin of our interfaces, although with different underlying mechanisms. To estimate the strength of these interactions, we compute the adsorption energies for the Ni-ligand systems as $E_{\text{ad}} = E_{\text{full}} - E_{\text{NiTPP}} - E_{\text{ligand}}$. Note that in evaluating this expression, we allow for a full geometry optimization for the individual subsystems. The results for all three environments (gas, O-Cu, Cu) are shown in Figure 3.20a.

Similar to our discussion above, we start by comparing the adsorption energies of our gas phase reference simulations (B3LYP) to the ones calculated for the O-Cu system (PBE+U). Overall, we find a surprisingly good agreement, with deviations between different levels of theory being smaller than 0.1 eV for the adsorption energies of CH_4 , H_2O , NH_3 and CO . Only for the nitrogen oxides the predictions differ significantly. This may be expected, as we have demonstrated already above, how for both molecules the electronic properties are sensitive to the chosen theory, i.e.: PBE+U overestimates adsorption due to a spurious interaction from small molecular band gaps. Out of all ligands, NH_3 , for which we have discussed the theory-independent spin-flip, shows the largest stabilization in energy at a Ni d^8 centre.

Switching to pure Cu, the adsorption of the gases gets in general favoured. The strongest change can be seen for the nitrogen oxides. As mentioned in the discussion above, they get stabilized through a redox reaction, which is reflected in their large adsorption energies (0.9 eV for NO and 1.6 eV for NO_2). However, the adsorption energy of NO significantly decreases when the reduction of NO is hindered as a result of choosing another level of theory (compare PBE+U vs. HSE06 in Figure 3.20b, where E_{ad} is reduced from 0.9 eV to 0.6 eV), leaving the interaction strength of NO_2 unmatched among our ligand candidates by about 1 eV.

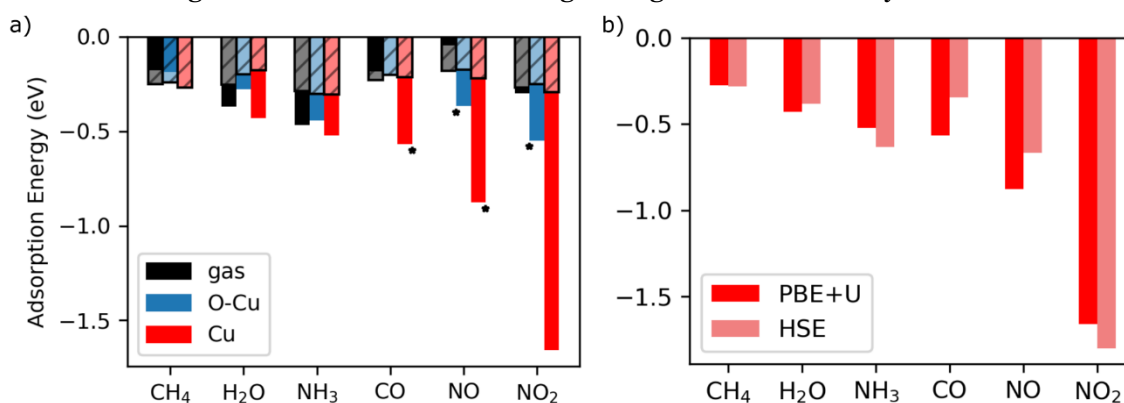


Figure 3.20: a) Adsorption energies in the gas phase (B3LYP-D3) and on both surfaces (PBE+U-D3). Hatched areas mark the contributions from the D3 dispersion correction. Values with a star are prone to theoretical shortcomings explained in the main text. b) Adsorption energies on the pure Cu-surface calculated with PBE+U-D3 and single point HSE06.

The energies of the non-interacting CH₄, H₂O and CO complex can be considered equally low for all environments. Extracting the dispersion contribution from the calculated adsorption energies suggests that van der Waals interactions dominate the ligand-bonding in these complexes. Note only, the significant stabilization of CO on the Cu-surface compared to the Ni d⁸ centres. As seen in the Appendix (Figure 8.8), this goes hand in hand with charge rearrangements similar to pi-backbonding observed for the PBE+U calculation. As pi-backbonding decreases when going from PBE+U to the more sophisticated HSE06 approximation, its adsorption energy aligns with the others and consists mainly of dispersion again.

Bond Length Changes

As spin states and adsorption energies are often challenging to measure, we want to demonstrate the findings of our investigation also with an experimentally more readily accessible parameter. Techniques such as infrared spectroscopy, X-ray standing wave or photoelectron diffraction allow bond lengths, but especially their changes to be observed also for molecular surface layers. In this regard, we have chosen two geometric parameters, which should play a characteristic role in the coordination of a ligand to a metal complex. First, we compare the Ni-ligand distance in Figure 3.21a. With most stable Ni-coordination bonds in the range of 2 Å [183,184](for example, also the distance from the Ni centre to the N of the porphyrin core), distinctly larger bond lengths indicate a reduced interaction. Second, we monitor the bond length changes of the gases before and after adsorption as *dafter* - *dbefore* (Figure 3.21b). Note that due to the symmetries of the gases, we can confine the analysis to a single bond. Redistribution of electron density will result in an increase or decrease of the ligands' bonds depending on the bond order of the involved orbitals.

Gases like CH₄, H₂O or CO, where the bonding is dominated by dispersion in all environments, stay well above 3 Å from NiTPP at the approximated van der Waals radii (3.3 Å for Ni-C and 3.2 Å for Ni-O).

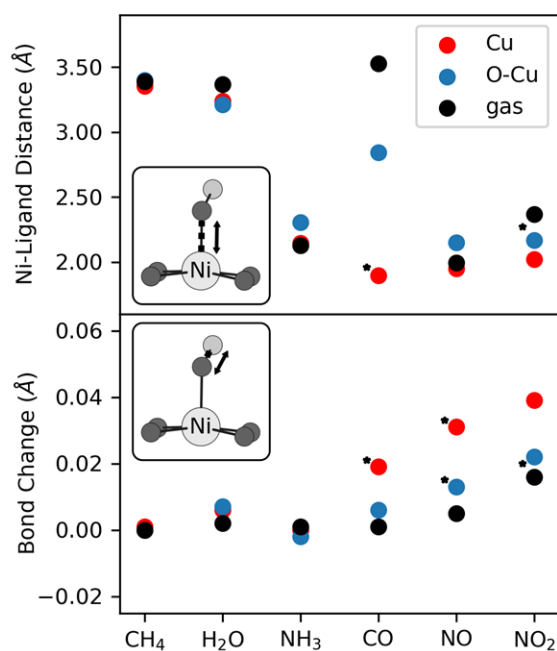


Figure 3.21: Metal-ligand distance in the adsorbate complex and bond length changes of gas molecule before and after adsorption. Values with a star are prone to theoretical shortcomings explained in the main text.

Moreover, the equilibrium geometries of these molecules are undisturbed as their frontier orbitals are not involved in interaction with the NiTPP. Note solely the case of CO at the Cu-interface, which may be discussed in more detail. Here, the predicted bond changes originate from the aforementioned pi-backbonding within the PBE+U simulation, which draws the ligand towards the Ni. Accepting electrons from the CO bonding HOMO, while simultaneously donating into the CO anti-bonding LUMO additionally weakens the C-O bond, i.e.: increases its length. So far, we have found that this pi-backbonding interaction decreases already within a non-self consistent hybrid functional calculation. We suggest that its

effect on the bond lengths would be reduced even further after full optimization of the periodic system on a higher-level theory.

NH₃ sets a contrasting example. In all three systems, the molecule moves significantly closer to the Ni-centre (2 Å) due to the interaction with the metal. Still, changes in the bond lengths of NH₃ cannot be seen, as the suggested repulsion between the occupied Ni d_{z²} and the HOMO of NH₃ involves no actual electron redistribution and, hence, does not change the bond order of the molecule.

The strongest changes in their bond lengths display the nitrogen oxides, which, however, should be evaluated critically. Following our previous discussion, changes for these molecules result either indeed from a redox reaction with the Ni-center (NO₂/Cu) or from spurious charge rearrangements within GGA (NO/Cu, NO/O-Cu, NO₂/O-Cu). Either way, the N-O bonds in the simulations are weakened by the filling of an anti-bonding sigma*-orbital (the LUMO) of the molecule. We will again briefly address these spurious deviations in the bond lengths and consequences of the theory dependency. As shown above, instead of oxidizing the Ni, we predict NO to behave on both surfaces similar to NH₃ with the main interaction being between *occupied* orbitals. Therefore, the same reasoning as for NH₃ should also apply to the bonds of NO. While the molecule interacts closely with the Ni, we would expect negligible changes in its bond lengths - a situation, which is actually recovered in the hybrid functional gas phase calculations. For NO₂, on the other hand, PBE+U seems to generally overestimates its reactivity on the passivated surface, favouring a redox-reaction, which is otherwise suppressed in higher level calculations. This is implied in Figure 3.21 when changing to B3LYP for the isolated complex, as the Ni-NO₂ distance increases and the weakening of the N-O bonds is reduced. Decreasing the electron affinity of the molecule further, e.g.: with range-separated hybrid functionals, finally completely separates NiTPP and NO₂ to their van der Waals radius and the gas approaches its undisturbed geometry.

THM: We have identified three major interaction mechanisms promoting a ligand-induced spin change in NiTPP interfaces. In a simplified picture, two of these mechanisms can be imagined as Pauli repulsion between electrons in competing occupied orbitals. The third and strongest interaction is achieved between a ligand with sufficiently high electron affinity and an electron-rich Ni(I) centre, which is formed by charge transfer on a Cu-surface.

Experimental Evidence

For the strongest interacting ligand, NO₂, a combination of experimental surface science techniques with our calculations has been able to confirm the formation of a stable NO₂-NiTPP complex on the pure Cu-surface [39]. Upon dosing of NO₂ onto a monolayer NiTPP on Cu at room temperature, STM images have suggested the adsorption of the gas at the NiTPP centre, whose formerly dark depression gets replaced by a bright bump. A complementary result is obtained from XPS data of the N 1s core level shell. Besides the four chemically equivalent nitrogen atoms of the macrocycle, a new peak at higher binding energy emerges after exposure to NO₂.

To investigate the magnetic moment of the central Ni atom, spin sensitive near-edge X-ray absorption fine structure (NEXAFS) and X-ray magnetic circular dichroism (XMCD)

measurements have been conducted [39]. Independently, both experiments agree with the simulation that interaction with the NO₂ oxidizes the initial Ni(I) species to a high spin Ni(II).

In contrast, applying the same multi-technique approach to dosage of NO₂ onto NiTPP on a passivated Cu surface, no absorption was detected. This counter experiment, at least, implies that an estimated adsorption energy in the range of -0.5 eV or below is too low to induce stable adsorbate-complexes at room temperature.

3.4 Application in Heterogeneous Catalysis

3.4.1 Introduction

As an extension to the previous section, we now seek to utilize the spin versatility of the NiTPP/Cu interface beyond simple gas adsorption. Inspiration comes again from nature, where metalloporphyrins have a long tradition in catalysing reactions. Their flexible oxidation states have proven valuable to such an extent that they eventually became responsible for major catalytic processes in enzymes [185–187]. After recognition of their importance, investigations have started to mimic these biological compounds and eventually paved the way to an ever-increasing variety of structures in the search for new catalysts [188–191].

In the case of nickel-porphyrins, the most prominent biological example is the coenzyme F430. It assists in methanogenesis, i.e.: the formation of methane by microbes, and thereby contributes up to 70 % of the global methane emissions [185,192]. A key role in the reaction is played by a Ni(I) species and its ability to donate electrons during the catalytic cycle [193,194]. For this enzyme, a biomimetic connection to surface science has recently been made by Zamborlini et al., who emphasized the similarities in the electronic structure between F430 and the above-mentioned NiTPP/Cu system [166]. By reducing the complex F430 porphyrin-unit to its core while at the same time retaining its redox properties, the interface meets all requirements as a suitable candidate in catalytic applications. In the following, we put this hypothesis to a test, albeit not for the production of methane. Instead, we investigate the behaviour upon dosage of NO and a possible activity in the conversion from NO to NO₂.

Article Information and Author Contribution

This computational section can in part be found in [40] and is extended by additional thoughts and explanations. The multi-technique approach to the problem was coordinated by **Erik Vesselli**, who together with **Giovanni Zamborlini** was also responsible for the first draft. Based on preliminary calculations of Peter Puschnig, I intensified the computational analysis of the system and discussed the results with our collaborators. Regarding the manuscript, I have summarized the theoretical investigation, provided the corresponding figures and revised the text.

The image shows the header of a research article. At the top left is the GDCh logo. In the center, it says 'Research Articles'. On the right is the 'Angewandte Chemie International Edition' logo with the website 'www.angewandte.org' and a 'Check for updates' button. Below the logos, there is a 'Surface Chemistry Hot Paper' badge. The article title is 'Disproportionation of Nitric Oxide at a Surface-Bound Nickel Porphyrinoid'. The authors listed are Matus Stredansky, Stefania Moro, Manuel Corva, Henning Sturmeit, Valentin Mischke, David Janas, Iulia Cojocariu, Matteo Jugovac, Albano Cossaro, Alberto Verdini, Luca Floreano, Zhijing Feng, Alessandro Sala, Giovanni Comelli, Andreas Windischbacher, Peter Puschnig, Chantal Hohner, Miroslav Kettner, Jörg Libuda, Mirko Cinchetti, Claus Michael Schneider, Vitaliy Feyrer, Erik Vesselli,* and Giovanni Zamborlini*.

GDCh

Research Articles

Angewandte
International Edition
Chemie
www.angewandte.org

Check for updates

Surface Chemistry Hot Paper

How to cite: *Angew. Chem. Int. Ed.* **2022**, *61*, e202201916
International Edition: doi.org/10.1002/anie.202201916
German Edition: doi.org/10.1002/ange.202201916

Disproportionation of Nitric Oxide at a Surface-Bound Nickel Porphyrinoid

Matus Stredansky, Stefania Moro, Manuel Corva, Henning Sturmeit, Valentin Mischke, David Janas, Iulia Cojocariu, Matteo Jugovac, Albano Cossaro, Alberto Verdini, Luca Floreano, Zhijing Feng, Alessandro Sala, Giovanni Comelli, Andreas Windischbacher, Peter Puschnig, Chantal Hohner, Miroslav Kettner, Jörg Libuda, Mirko Cinchetti, Claus Michael Schneider, Vitaliy Feyrer, Erik Vesselli, and Giovanni Zamborlini**

Figure 3.22: Header of the article [40] including all contributing authors. The study was published in *Angewandte Chemie International Edition*.

3.4.2 Results and Discussion

Investigated Systems

The main focus of this study is a monolayer of NiTPP on a Cu(100) surface, which is exposed to NO. With increasing dosage (above 100 Langmuir NO), experimental methods detect a change in the system. A bright protrusion in STM images suggests the adsorption of a molecule at the chelated Ni. The coordination is confirmed by XPS measurements, where the peak assigned to the initial Ni(I) species is replaced by a feature at higher binding energies typical for oxidation of the metal centre. While previous investigations have interpreted the data straightforwardly as adsorption of NO [166], infrared spectroscopy (IR), which is particularly sensitive to the molecular environment, reveals an unexpected detail about the adsorbate. Although the stretching vibration of terminal NO would be expected above 1600 cm⁻¹ [195], the IR spectra see a resonance rising at 1320 cm⁻¹. Provoked by the difference, we have extended the comparison to other members of the nitrogen family finding that the vibration could be associated with the stretch of an adsorbed NO₂ species [39,196]. As a control experiment, the NiTPP layer is directly exposed to NO₂ and growth of the exact same feature at 1320 cm⁻¹ is readily observed. STM and XPS data for coordinated NO₂ match as well. Therefore, as vibrational and electronic properties are unique for a specific molecule, the experimental techniques actually point towards the adsorption of NO₂ at the NiTPP/Cu(100) layer after exposure to NO. For comparison, we have conducted the same dosing series of NO with Ni(II)TPP on a passivated Cu surface. There, we find no indication for a NO₂ species, suggesting that the Ni(I)TPP on Cu takes part in the NO conversion. Time-resolved experiments suggest that the NO₂ formation rate obeys higher order kinetics. An unintentional reactivity of the Cu(100) substrate or gas contamination could also be excluded by experimental means. Instead, we propose a well-known reaction as possible reason for the appearance of NO₂: the disproportionation of NO according to Rct. Equ. 3.1.



Thermodynamically, the products are clearly favoured in this equilibrium with a gain in Gibbs free energy of about 1 eV at room temperature [197,198]. At high pressure (200 bar in gas cylinders), i.e.: pressuring Le Chatelier's principle, the reaction is one of the alleged causes for NO₂ contamination in NO [199]. At ambient conditions, however, it was found to be kinetically hindered [199]. Therefore, in literature, the conversion of NO is usually discussed together with metal-organic biochemical catalysts [200–204], which stabilize different NO_x intermediates along the stepwise addition of NO to the metal site. Following pathways similar to those suggested, we assume formation of the (NO)₂ dimer (Rct. Equ. 3.2), [205–208] which is then converted to NO₂ and N₂O consuming a third NO (Rct. Equ. 3.3).



Proposed Reaction Pathway

Additional explanation of the experimental results would benefit from a full mechanistic study. However, as many intermediates are expected to be short-lived, hard to access, and difficult to detect experimentally, this was not feasible up to now. At this point, further corroboration comes from theory.

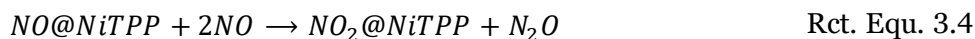
Before we address the proposed NO disproportionation mechanism, it is worthwhile to introduce the dimer species of Rct. Equ. 3.2. It has been noticed early on that two weakly bound NO molecules are difficult to describe theoretically [207,209–212]. Instead of a recombination of the two radicals to form a covalent bond, the unpaired electron of each NO monomer can remain rather localized in one of the two degenerate π^* orbitals of NO. The various possible configurations of the ground state are then best described in a multireference fashion. Working within the framework of single Slater determinants such as DFT, the most favourable electronic configuration is a triplet state. However, due to the insufficient description of the bonding situation, calculated values for bond lengths and formation energies deviate from experimental observables.

Bearing these caveats in mind, we continue by discussing the thermodynamic components of Rct. Equ. 3.2 and Rct. Equ. 3.3. As a start, we analyse the classical, uncatalyzed scenario of the reaction, i.e.: the pure gas reactants without NiTPP. Considering the problematic modelling of the involved nitrogen species, we evaluate the reaction at two different levels of theory, namely with a hybrid functional (B3LYP-D3) and at the GGA level (PBE-D3). Figure 3.23a shows the relative energies of the two steps $(\text{NO})_2 + \text{NO}$ and $\text{NO}_2 + \text{N}_2\text{O}$ in reference to the initial educts of 3NO.

The energetic difference of the first step represents the formation energy, D_0 , of the $(\text{NO})_2$ dimer. For the hybrid functional, the dimer is only slightly more stable than the separated NO monomers ($D_0 = 0.01$ eV). Although not a perfect match, the calculated formation energy is in the same range as experimental data ($D_0 = 0.1$ eV) [206,213–217]. In contrast, over-delocalization in the GGA approximation leads to a spurious stabilization of the $(\text{NO})_2$ species with $D_0 = 0.74$ eV. Our findings confirm previous studies [212], where more advanced description of exchange-correlation in DFT improves agreement with experimental values. Note that $(\text{NO})_2$ can in principle adopt a *cis* or *trans* conformation geometry, both are, however, energetically equal within 0.001 eV.

The Gibbs free energy of the reaction, ΔG_g , serves as a second characteristic parameter comprising the change of enthalpy and entropy during the reaction. According to measured data, ΔG_g is about -1.6 eV for NO disproportionation at 0 K [197,198]. At 0 K, temperature dependent terms become negligible and ΔG_g can be expressed from the enthalpy of formation of the reactants, H_f . Hence in our calculations, ΔG_g (equalling ΔH_f) simply relates to the total energy difference between educts and products. For comparison with the experimental value, we correct our simulation for zero temperature vibrations with experimental frequencies, as we obtain solely the ground state energy of the *static* molecules, $\Delta G_{\text{method}} = \Delta E_{\text{static}} + \Delta E_{\text{ZPE}}$ ($ZPE_{\text{NO}} = 0.12$ eV, $ZPE_{\text{NO}_2} = 0.23$ eV, $ZPE_{\text{N}_2\text{O}} = 0.29$ eV [218–220]). Again, the B3LYP calculated value ($\Delta G_{\text{B3LYP}} = -1.71$ eV) agrees better with measurements than PBE ($\Delta G_{\text{PBE}} = -2.70$ eV). Independent of the method, the total energy is lowered throughout the reaction coordinate, meaning the simulated equilibrium correctly favours NO disproportionation.

Going beyond the gas phase nitrogen oxides in our calculations, we want to elaborate on the possible role of NiTPP in the reaction. Introducing NiTPP into the catalytic cycle, we formulate the partial Rct. Equ. 3.4



for which the thermodynamic energy gain corresponds to $\Delta G_{Ni} = \Delta G_g + (E_{ad,NO_2} - E_{ad,NO})$, where ΔG_g is the free energy of the reaction without NiTPP and E_{ad} is the adsorption energy of the respective gas at NiTPP. Note that, likewise, we can formulate similar reaction equations by introducing NiTPP into the intermediate steps of Rct. Equ. 3.2 and Rct. Equ. 3.3. Compared to the pure gases, the difference of the adsorption energies of the gas adsorbates can be viewed as an additional stabilization energy ΔE_{ad} in the reaction due to adsorption. This is a fortunate connection for our further computational investigation, in which we focus on the influence of periodic NiTPP interfaces. While B3LYP is clearly superior in describing the nitrogen oxides, we are, however, limited to PBE(+U) by the extended size of the interfaces. Moreover, we have already shown in chapter 3.3 how adsorption energies are less prone to different levels of theory, in contrast to the highly method dependent energies of the gas phase NO disproportionation discussed above. Therefore, even though thermodynamic quantities of the original NO conversion may be described insufficiently within GGA, we should, at least, be able to identify the additional stabilization energy ΔE_{ad} , which is provided to the reaction by different NiTPP environments.

Including an isolated NiTPP molecule in our gas-phase calculations shows little impact on the reaction. The additional energy gain due to adsorption at the complex is negligible ($\Delta E_{ad} = 0.1$ eV), for both B3LYP and PBE. Furthermore, the same value is obtained from periodic PBE simulations of NiTPP on an oxygen passivated Cu-surface, where the complex is electronically decoupled from the substrate. Thus, our calculations support the experimental finding that NiTPP in a d^8 configuration does not interfere with NO disproportionation.

For the main candidate of interest, the NiTPP/Cu interface, we explore the configuration and potential energy landscape of the nitrogen oxides starting from various geometries of the adsorbate gases. Optimization of the extended systems leads to the relative energy alignment

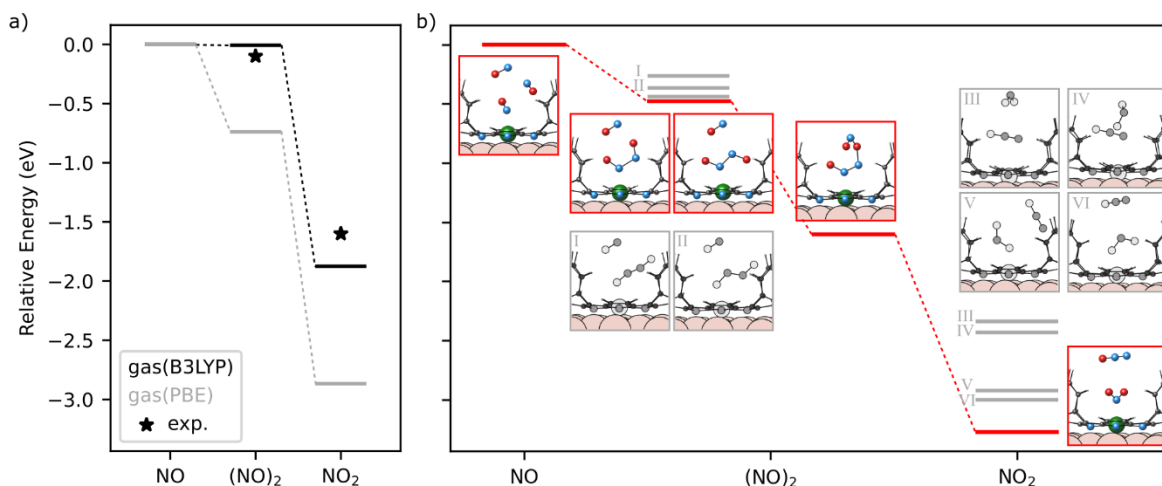


Figure 3.23: a) Relative energies of the reactants $(NO)_2+NO$ and NO_2+N_2O in reference to the educt $3NO$ calculated in the gas phase at two different levels of theory (B3LYP-D3 and PBE-D3). Comparison to experimental values (formation energies of NO-dimer and Gibbs free energy for overall reaction at 0K). b) Stable configurations of the nitrogen oxides adsorbed at the periodic NiTPP/Cu interface along the reaction coordinate of Rct. Equ. 3.4 as obtained by a structure search with PBE-D3. Energetically most favoured geometries of each step are marked red.

in Figure 3.23b. Following Rct. Equ. 3.4, the initial arrangement includes 3 NO molecules as educts. While one is coordinated to the Ni centre, the other two NO molecules are distributed in the gas phase above the surface.

Upon approaching of one NO to the NO-NiTPP complex, a dimer between the two gas molecules, (NO)₂, is formed. The dimer species may be present in its *cis*- or *trans*-configurations with the corresponding isomers close in energy and is preferably coordinated to the Ni *via* one of its nitrogen atoms. On the contrary, insets I and II in Figure 3.23b show coordination *via* an oxygen, which is energetically unfavourable.

The consumption of the final NO completes the reaction. One of the most important abilities of a presumed catalyst is the stabilization of intermediate geometries not accessible to the original pathway. In this context, we have indeed found a stable structure, which illustrates a possible intermediate on this route. In our example, the NO attaches to a *cis*-(NO)₂ at the exposed O. We want to stress, that this structure might not necessarily represent the true step in the actual reaction pathway but should be rather understood as a proof of concept that several intermediates could be formed at the NiTPP/Cu interface. Other reasonable intermediates could also include rearrangements to O-coordinated and four or five-membered metallacycles as in ref. [199], which simply have not been found yet. It should also be mentioned that optimization of corresponding starting geometries resulted in either one of the structures shown in Figure 3.23b. Regardless of the exact mechanistic model, the reaction yields NO₂ and N₂O. Following the pathway of our example, N₂O would initially be left at the metal-organic complex. Insets III-VI in Figure 3.23b, then, show stable structures along the following replacement of N₂O with NO₂ at the Ni centre. Throughout the reaction, the Cu-interface provides an additional energy gain of 0.5 eV due to adsorption of the gases at the NiTPP complex.

Finally, the catalytic cycle may be completed by triggering the release of the NO₂ species *via* external stimuli.

In conclusion, we emphasize again that purely thermodynamic arguments, may it be energy differences or intermediate structures, are not sufficient to pinpoint the catalytic activity of the Ni centre. Ultimately, transition state searches would have to answer, if the stabilized intermediates give indeed access to lower reaction barriers compared to the gas phase. Such calculations were, however, beyond the scope of this work.

THM: Concluding this section, we have found two aspects which speak in favour of the NiTPP/Cu interface as a catalyst. First, the access to multiple coordination configurations may facilitate the transition from educts to products as is characteristic for catalysts. Second, compared to Ni d⁸, adsorption at Ni d⁹ provides an additional thermodynamic driving force (additional $\Delta E_{\text{ad}} = -0.5$ eV) for this part in the catalytic cycle.

Influence of the Cu-surface

To understand the peculiar role of the Ni(I) species on Cu in more detail, we turn to the same concepts and analysis, which we have already established in chapter 3.3. Recall that the electronic properties of NO and NO₂ adsorbed at NiTPP/Cu have also been discussed in chapter 3.3. Instead, in this paragraph, we focus on the intermediate molecular structure (NO)₂ as found by our structure search. Note that the structure search in Figure 3.23, which has also been used in the original publication [40], has been conducted with the simple GGA functional PBE. For consistency with chapter 3.3, the most stable configurations are here recalculated employing the DFT+U approach with an effective Hubbard-correction of 3 eV. These results are the basis for the following discussion. While the absolute values slightly differ, the conclusions are identical to those of the original publication drawn from pure DFT values.

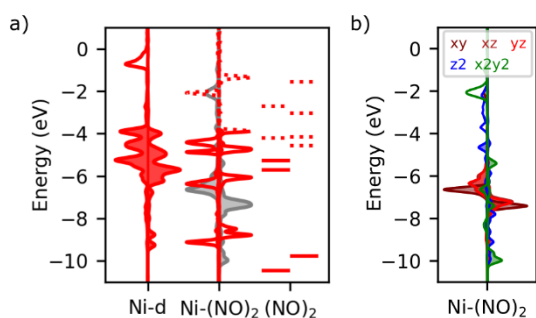


Figure 3.24: a) Molecular orbital diagram for the adsorption of (NO)₂ to NiTPP on the Cu-surface. Occupied orbitals are displayed as filled, solid lines, unoccupied orbitals as blank, dotted lines. For open shell systems, both spin channels are shown. b) Density of states projected on the Ni-d states for the full ligand-metal complex (PBE+U-D3). All data is aligned relative to the vacuum energy.

By comparing the separate subsystems, we find that the unoccupied orbitals of (NO)₂ come to lie lower in energy than the d_{z²} orbital of the NiTPP complex. Consequently, the electron-rich Ni(I) should be able to perform a redox reaction by reducing the gas ligands and oxidizing the Ni d⁹ to a high spin d⁸. Analysing the full adsorbate-system, we find indeed such a charge transfer emptying the Ni d_{z²}, as illustrated by the d-state projected DOS in Figure 3.24b. After the charge transfer, the resulting (NO)₂ anionic ligand species may be better termed as a “hyponitrite”. For comparison, the energy levels in the gas phase and on the passivated Cu-surface can be found in the Appendix (Figure 8.11 and Figure 8.12).

Analysis *via* energy level diagrams also reveals, why the adsorption of N₂O at NiTPP/Cu is energetically unfavourable compared to the adsorption of NO₂ as indicated in our structure search. The frontier orbitals of N₂O are placed well apart from the Ni-d states (see Appendix) and, thus, the gas fulfils our description of a non-interacting ligand. Opposed to NO₂, there are no charge rearrangements between N₂O and the Ni and the molecule stays at the van der Waals distance above the metal centre. Consequently, the side product N₂O should be replaced in any case by the stronger interacting NO₂ in the last step of the reaction.,

To illustrate the mentioned ΔE_{ad} , the adsorption energies of the Ni-ligand complexes in different environments are summarized in Figure 3.25a. On the Cu surface, the increasing electron affinity of the nitrogen oxides also increasingly favours their adsorption. For each intermediate step, adsorption at NiTPP/Cu provides an additional thermodynamic stabilization for the reaction. In contrast, at the isolated NiTPP or on the passivated surface, the mostly dispersion dominated interaction between the gases and the Ni centre results in

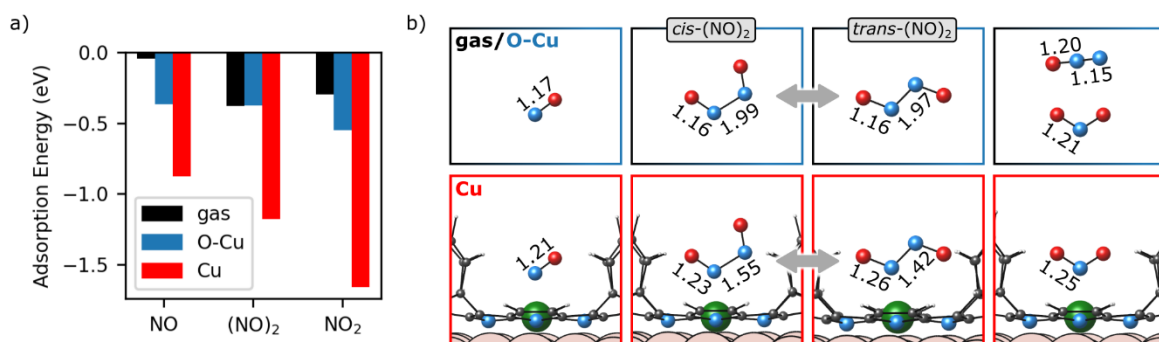


Figure 3.25: a) Adsorption energies of molecules to NiTPP in the gas phase (B3LYP-D3) and on both surfaces (PBE+U-D3). b) Bond length (in Å) of the nitrogen oxide species adsorbed at NiTPP in the gas phase and on the passivated Cu surface (both up) as well as on the pure Cu surface (bottom) optimized with PBE+U-D3.

uniformly low adsorption energies. As a consequence, along the reaction coordinate, the molecules gain little thermodynamic energy by adsorption.

So far, we have focused a lot on thermodynamics, simply because our analysis is limited to ground state calculations. However, the geometric changes in the gases found at the Cu-interface may even shed some light on the kinetic aspect of the reaction without performing a transition state search. Figure 3.25b illustrates the bond lengths of the reactants on the Cu surface in contrast to O-Cu and the isolated gas molecules. First, we want to highlight that differences in the bond lengths between the gas phase and the passivated O-Cu environment are negligible. However, all three presumed stages of the reaction are affected by adsorption to a Ni(I) d^9 species on the pure Cu surface. In case of the educt and product complex, NO and NO₂, the bond length changes in the molecule are moderate and have been summarized previously in Figure 3.21 in chapter 3.3. In the intermediate hyponitrite species, independent of its *cis* or *trans* conformation, interaction with the Ni(I) centre induces severe changes. The LUMO of (NO)₂ is antibonding with respect to the N-O bond of each NO moiety but, instead, is bonding along their N-N connection. Consequently, due to charge transfer into the NO-dimer on the Cu-surface (cf. Figure 3.24) and filling of the unoccupied states, the N-N bond gets strengthened. The quite drastic shortening of the bond in the range of 0.5 Å agrees with previous studies on anionic hyponitrite species [209,221,222]. Such a stabilization of the dimer is not observed in the gas phase or on the passivated surface with only weakly interacting NOs at a N-N distance of 2 Å. Basically, the shortened N-N bond could be interpreted as an already strong deformation from a single bond towards the final multiple bonding in the product N₂O. Therefore, we argue that less activation energy would be needed to form a transitioning state between both species. In literature, a stable hyponitrite intermediate is repeatedly associated with lower transition barriers and, thus, suggested as a first step in NO disproportionation catalysis [202,204,223].

THM: The catalytic activity of Ni(I)TPP in the disproportionation of NO on the Cu-interface might be the stabilization of a (NO)₂ hyponitrite species by charge transfer. The intermediate step in the reaction might lead to pathways with lower activation energy.

At last, we want to briefly mention a second disproportionation reaction of NO in Rct. Equ. 3.5, which could result in the adsorption of NO₂. As a side product, the reaction yields N₂. While we did not consider this pathway explicitly, we want to show that also N₂ would not compete for adsorption at the Ni centre.

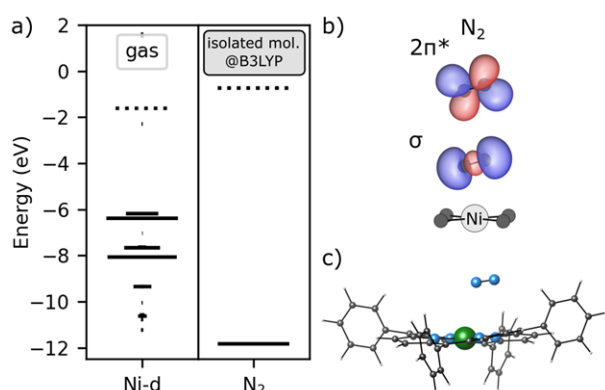
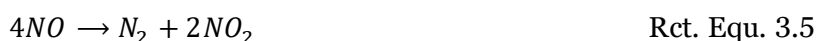


Figure 3.26: a) Orbital energies of the separate subsystems, NiTPP and N₂, before formation of a complex. Occupied orbitals are displayed as filled, solid lines, unoccupied orbitals as blank, dotted lines. b) Highest occupied and lowest unoccupied molecular orbital of N₂. c) Relaxed adsorption geometry of the full complex. All data is obtained in the gas phase with B3LYP-D3.

Figure 3.26a shows the energy levels of the separate subsystems NiTPP and N₂ in the gas phase calculated with B3LYP. The HOMO and LUMO level of N₂ (real space representation in Figure 3.26b) are placed energetically well apart from the Ni d-states. Thus, similar to CH₄ in chapter 3.3, N₂ represents a prototypical non-interacting case for our system. In the fully optimized coordination-complex, the gas stays at the van der Waals distance, 3.3 Å, above the Ni centre (cf. Figure 3.26c). Accordingly, the adsorption energy of -0.22 eV is completely covered by the dispersion correction. Note that we transfer our interpretation of the isolated system to

the on-surface complexes, although we have not explicitly calculated them. Interface induced changes of the Ni d-states unfold in an energy region far from the frontier orbitals of N₂, same as for N₂O. In conclusion, while transition-metal complexes with N₂ do exist [224,225], a coordination to NiTPP is unlikely to be observed.

3.5 Detecting Conformational Changes with ARPES

3.5.1 Introduction

During the investigation of the low and high spin species of Ni(II) in chapter 3.3, we have already encountered a structural peculiarity of porphyrin molecules. Remember that the change in the spin configuration of the central metal atom is reflected by conformational changes in the organic macrocycle. Such distortions of the molecule are, in fact, not rare. Either induced by varying sizes of the metal centre or by steric effects arising from substituents on the macrocycle, metal-porphyrin complexes exhibit a wide range of conformations [226–228]. Their conformational flexibility is also one of the reasons for their versatile use in nature [228]. Besides the ability to alleviate strain in the system, a distortion of the macrocycle can induce changes in the electronic structure ultimately influencing the oxidation potential [229–231], absorption bands [232,233] or excited state lifetimes [234,235].

Findings from biochemical studies refer mainly to geometries in solution or crystallized form and cannot *a priori* be transferred to surface science. Fortunately however, when deposited on surfaces, metal-porphyrins preserve their conformational range [180,236,237]. This was found especially relevant for the adsorption of additional ligands [165,237,238], where molecular distortion could provide another option to tailor the interface for sensing or catalysis. Therefore, to gain better control over the interface, a detailed understanding of the molecular conformation is desirable. Recently, it has been demonstrated that POT should give access to such information, as it is highly sensitive to geometric distortions of aromatic compounds [239]. Our goal is to utilize POT as a tool for the determination of the conformation of porphyrins on surfaces.

Article Information and Author Contribution

In the following, I present the computational analysis of the article [240]. The corresponding experiments have been performed by **David M. Janas** and co-workers. I set up all calculations and produced the computational results and their analysis, which were then compared to the measured data. In addition, I have also contributed to the discussion, writing and revisions of the manuscript.



Metalloporphyrins on oxygen-passivated iron: Conformation and order beyond the first layer

David Maximilian Janas^{a,*}, Andreas Windischbacher^b, Mira Sophie Arndt^a, Michael Gutnikov^a, Lasse Sternemann^a, David Gutnikov^a, Till Willershausen^a, Jonah Elias Nitschke^a, Karl Schiller^a, Daniel Baranowski^c, Vitaliy Feyer^c, Iulia Cojocariu^{c,d}, Khush Dave^e, Peter Puschnig^b, Matija Stupar^a, Stefano Ponzoni^a, Mirko Cinchetti^a, Giovanni Zamborlini^{a,*}

Figure 3.27: Header of the article [240] including all contributing authors. The study was published in *Inorganica Chimica Acta*.

3.5.2 Results and Discussion

Investigated Systems

We apply our conformation analysis to the two complexes nickel and zinc tetraphenylporphyrin (NiTPP and ZnTPP, respectively). We have already seen throughout the thesis, how charge transfer may lock molecules in specific adsorption geometries. However, for the current investigation, it is apparently preferable to grant the macrocycle maximal freedom of deformation, i.e.: the substrate should show minimal interaction with the adsorbed molecules. As oxygen passivation has proven an effective way of decoupling a metal surface from its adsorbates [107], we have chosen an oxygen passivated Fe surface, Fe(100)-p(1x1)O, in the following referred to as O-Fe. Moreover, on this surface, recent STM studies have already started to shed light on the adsorption conformation of NiTPP and ZnTPP monolayers [180,241–243] serving as a reference to our study.

Note that a passivated Cu-surface as in previous chapters would be an equally appropriate choice and, indeed, the same experiments were also conducted on O-Cu. There however, disentangling the experimental data has proven to be challenging and is current work in progress (work by Jonah E. Nitschke). Judging from STM, porphyrin molecules on O-Cu seem to adopt at least two different conformations on the same surface and with no apparent regular order. Consequently, the interpretation of ARPES data is more involved than in the discussion below.

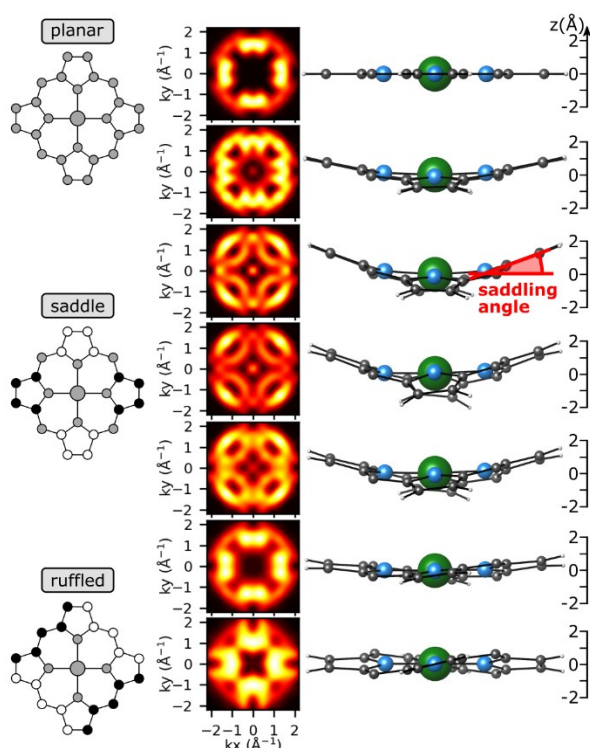


Figure 3.28: (left) 2D-skeletal models of the three main conformations of porphyrins: planar, saddle and ruffled. The grayscale variation indicates the different distortion. (middle) Superposition of HOMO and HOMO-1 momentum maps of seven differently distorted porphyrins calculated in the gas phase with B3LYP-D3. Maps are taken at $E_{\text{kin}}=30$ eV and symmetrised to match 2-fold symmetry. (right) Corresponding structural models, phenyl rings are omitted for clarity.

Effect of Conformation on POT

Before analysing the experimental data of the full interfaces, it is worthwhile to take a deeper look at the rich conformational landscape of porphyrins and its consequences for POT. Simply based on the aromatic core of the molecule, it is chemically intuitive to assume a planar organic backbone. In addition to this geometry, several stable out-of-plane distortions of the molecule have been found [227]. For our study, we focus on three often found conformations for phenyl-substituted porphyrins [244–248], namely planar, saddle and ruffled, which are depicted as skeletal models on the left of Figure 3.28. Note that for the clarity of the presentation, the phenyl moieties are not shown. By interpolating between planar/saddle and saddle/ruffled, we generated two intermediate structures each and end up with in total seven structures gradually illustrating the distortions (right of Figure 3.28).

In order to connect solely the conformational changes to POT, we rely on calculations of single molecules in the gas phase, thereby preventing any influence of intermolecular and molecule-substrate interactions of the extended system. The highest occupied orbitals of each structure, HOMO and HOMO-1, are transformed into k-space. The resulting momentum maps shown in the middle of Figure 3.28 are then calculated as superpositions of the maps for both orbitals, as the corresponding KS energies are nearly degenerate. Note that this is only an accidental degeneracy, as, for example, for the D_{4h} planar geometry they belong to the different symmetry point groups a_{2u} and a_{1u}, respectively. Moreover, the maps are symmetrized respecting the at least 2-fold rotation axis of the structures. Following the evolution of the simulated ARPES features with the conformation reveals striking differences between the structures. While planar and ruffled porphyrins are mainly distinguished by the stronger “U”-like ARPES features of the latter, inducing a saddle shape in the macrocycle shifts the intensity by 45° and towards higher k-values. Remarkably, all seven conformations exhibit distinct intensity patterns. This is a promising starting point for our aim to resolve the porphyrin geometries also on the surface. Note that the above relation between momentum distribution and structure is valid for both, NiTPP and ZnTPP, as their frontier orbitals show almost identical real space distribution on the tetrapyrrolic backbone (as in Figure 3.30a).

THM: Each distortion in the carbon macrocycle of tetrapyrrole compounds produces a unique ARPES fingerprint making different conformations of the molecule distinguishable.

Unravelling NiTPP

As the next step, we want to apply our understanding of the relation between conformation and ARPES intensity distribution to extended systems. We start our investigation with the familiar NiTPP molecule on the passivated surface. As charge transfer is prevented by the passivating layer, the ARPES signal at lowest binding energies is expected to arise from the HOMO and HOMO-1 of the molecule. This signal will be the focus of our computational discussion. Depositing a monolayer NiTPP on O-Fe, the first molecular-induced peak in the experimental valence band spectrum arises at a binding energy of 1.5 eV. The corresponding measured momentum map averaged over all maps in the binding energy range from 1.7 to 1.3 eV is shown to the left of Figure 3.29. To elucidate on the geometric structure, we first put the experimental data up against the simulated maps of molecules in different conformations (planar, saddle and ruffled) and with different azimuthal rotation on the surface. Figure 3.29 shows nine exemplary maps of this scan using geometry 1, 4 and 7 of Figure 3.28. Because experimental ARPES measurements could not resolve different orbital contributions and calculations likewise suggest close

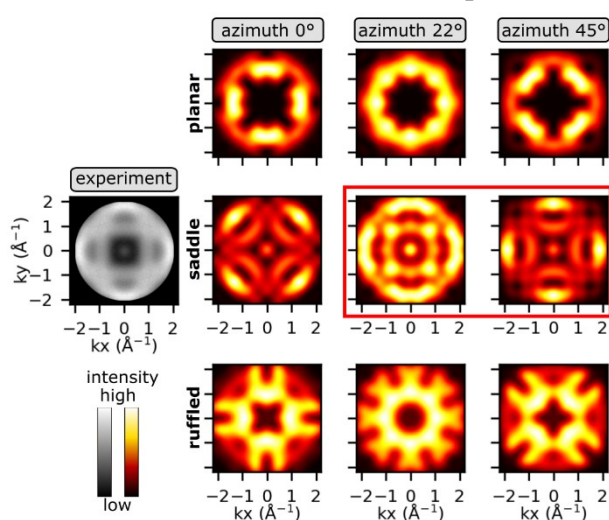


Figure 3.29: Experimental momentum map of degenerate HOMO/HOMO-1 of NiTPP (greyscale, left) compared to simulated maps (right) scanning through different macrocycle conformations and azimuthal rotations of the molecule on the surface.

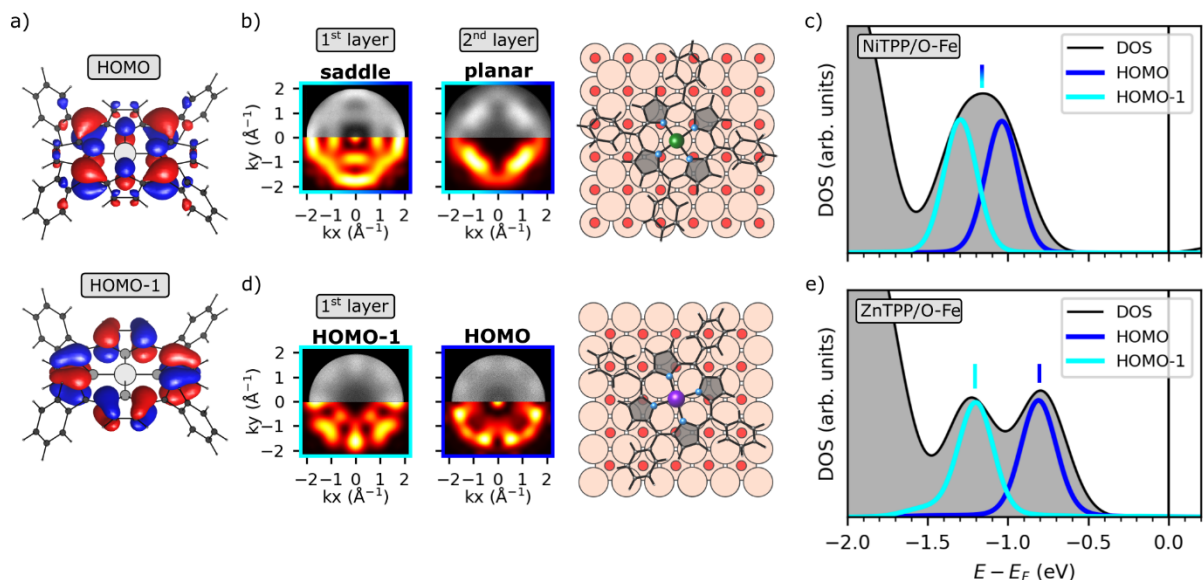


Figure 3.30: a) Real space images of HOMO and HOMO-1 of MTPPs ($M=\text{Ni, Zn}$) calculated with B3LYP-D3. b) Comparison of experimental momentum maps (top grayscale map) of the first and second NiTPP layer to simulated maps (bottom yellow-red coloured map). Structural model of NiTPP on O-Fe in the determined azimuthal orientation. c) Density of states of the NiTPP/O-Fe interface projected onto the total molecule and on the HOMO and HOMO-1 separately (PBE+U-D3). d) Comparison of experimental momentum maps (top) of the first ZnTPP layer to simulated maps (bottom). Structural model of ZnTPP on O-Fe in the determined azimuthal orientation. e) Density of states of the ZnTPP/O-Fe interface projected onto the total molecule and on the HOMO and HOMO-1 separately (PBE+U-D3).

energy levels, we treat the frontier orbitals, HOMO and HOMO-1, in the comparison as degenerate. Considering the D4 symmetry domains on the Fe-O surface, the best agreement with our screening test set, judged by visual inspection, is achieved, when a severe saddling is introduced to the molecules (middle row in Figure 3.29). In particular, prominent features, such as the faint intensity near the map centre and stronger intensity at k -values beyond 1.5 \AA^{-1} , are only reproduced when a saddle-shape of the macrocycle is taken into account. Additionally, the molecular N-Ni-N axis has to be rotated at an angle of 35° to the substrate [001] axis.

Our best fitting simulation is compared to the experimental map of the molecular monolayer in Figure 3.30b (left). A saddle-shaped molecule rotated off the substrate axis is in good agreement with the adsorption geometry determined by the combined STM and DFT study of Fratesi et al. [180]. Assuming their adsorption site atop a Fe-atom, the structure of NiTPP on O-Fe as independently suggested from POT and STM is shown on the right of Figure 3.30b.

A more detailed clarification of the ARPES peak assignment comes from the calculations of the full interface, where we adopt the commensurate $(5 \times 5)R37^\circ$ superstructure found in

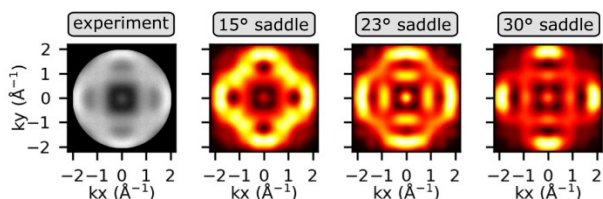


Figure 3.31: Comparison of experimental momentum map of NiTPP to simulated maps from two artificial saddle conformations (15° and 30°) and the structure taken from periodic PBE+U-D3 calculation (23°).

literature [180]. The projection of the density of states of the periodic system onto the orbitals of freestanding NiTPP molecules is shown in Figure 3.30c. The analysis suggests two orbitals within the energy region of the experimental UPS peak, namely indeed the HOMO and HOMO-1, separated by 0.25 eV. Including the experimental broadening of about 0.3 eV (full width at half maximum),

the contributions of both orbitals merge into one peak (grey curve in Figure 3.30c), explaining why they could not be resolved experimentally. Furthermore, we are able to determine from the optimized periodic structure the saddling angle, as defined by the average angle enclosed by the plane of the pyrrole units with the horizontal. In our calculations, NiTPP embodies a saddling of 23° on the surface. We have extracted the optimized molecule from the periodic structure and recalculated its momentum map in the gas phase. Due to the periodically optimized saddling angle, this naturally yields a further improved agreement between the simulated map and the photoemission measurements compared to our previous attempt of scanning through our test set. (see Figure 3.31 including two saddling angles from our test set).

Having clarified the electronic and geometric properties of the interface, we briefly want to showcase the potential of POT as conformation analysis tool by moving beyond a single monolayer coverage. Upon increasing the coverage from 1 ML to 2 ML, the first experimental peak at 1.5 eV shifts towards higher binding energies (1.7 eV). Most notably however, the corresponding momentum map lacks the distortion-related features (cf. top Figure 3.30b). Instead, a comparison with our simulated momentum distributions strongly suggests flat molecules (cf. bottom Figure 3.30b). Thus, it can be assumed that, after completion of the first saturated ML, subsequent NiTPP molecules adsorb in an undistorted, planar configuration. The fact that only molecules with explicit proximity to the Fe-O surface show traces of an altered macrocycle indicates that the saddle-shape is a consequence of the molecule-substrate interaction.

THM: Photoemission orbital tomography confirms that NiTPP adsorbs on passivated Fe in a saddle shape geometry with its N-Ni-N axis rotated by 35° to the substrate [001] axis as inferred from STM. For the second molecular layer, the distinct pattern in ARPES momentum maps suggests that the molecule adopts a planar configuration.

Influence of the Central Metal – ZnTPP

As stated in the introduction, besides the surface, also the size of the central metal atom may influence the conformation of the metal-organic complex. To investigate this effect, we replace the Ni d^8 with the fully closed shell Zn d^{10} inside the porphyrin core. Analogous to NiTPP/O-Fe, we apply POT analysis to a monolayer of ZnTPP on the passivated Fe-surface. Again, the first ARPES signal below the Fermi energy can be observed at a binding energy of 1.5 eV. However, in contrast to NiTPP, the valence band spectrum of ZnTPP exhibits a double peak structure at this energy. Intrigued by the splitting, the experiments were repeated with increased integration time and two momentum maps could be extracted corresponding to the energy range of each peak (top part in Figure 3.30d). By scanning through the range of our conformational structures, we recognize that the two discerned peaks can be ascribed separately to the HOMO and HOMO-1 of ZnTPP. The measured data is reproduced best, when a saddle distortion is induced in the porphyrin and the molecules aligns with the N-Zn-N axis at an angle of 17° to the [100] substrate direction (bottom part Figure 3.30d). Distorted ZnTPP molecules arranging slightly rotated to the substrate axis are in accordance with previous investigations, a structural model of the system is shown to the right of Figure 3.30d. The Zn-centre is placed atop an O-atom as suggested by Fratesi et al. [180].

Adopting the proposed (5x5) unit cell structure [180], we turn to the periodic modelling of the interface. Starting from a distorted geometry, optimization of the ZnTPP on the surface leads to a saddling angle of the aromatic backbone of 17°, which is slightly less than for NiTPP. Extracted momentum maps of the HOMO and HOMO-1 for this particular adsorption conformation in the gas phase are again in excellent agreement with their experimental counterparts, also improving our initial comparison (exemplary for HOMO, top row Figure 3.32). The difference between different saddling angles is however less apparent than in the case of NiTPP. In this regard, we want to briefly mention the importance of photon energy for the analysis, a subject which was highlighted by Hurdax et al. [239]. In ARPES, distortion related features get usually more pronounced with higher photon energy. Due to experimental reasons, momentum maps for ZnTPP were taken at a photon energy of 30 eV ($E_{\text{kin}}=25$ eV), while the data of NiTPP corresponds to a photon energy of 40 eV ($E_{\text{kin}}=35$ eV). Illustrating this

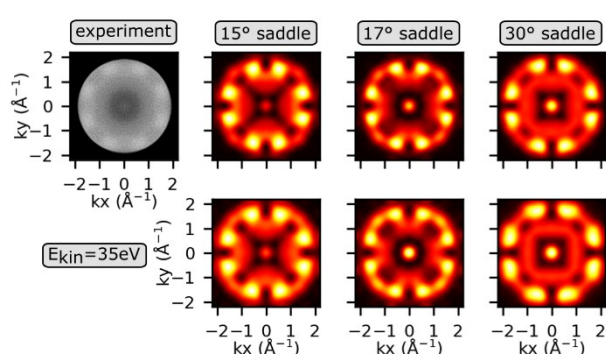


Figure 3.32: (top) Comparison of experimental momentum map of ZnTPP to simulated maps with a kinetic energy of 25eV from two artificial saddle conformations (15° and 30°) and the structure taken from periodic PBE+U-D3 calculation (17°). (bottom) Simulated momentum maps taken at a higher kinetic energy (35eV).

difference, we have simulated momentum distributions for the ZnTPP HOMO at an increased kinetic energy in the bottom row of Figure 3.32. The resulting slight variations in intensity apparently enhance the distinction between conformations of different saddling angles, in our example even within the range of a few degrees saddling. Note that the higher kinetic energy is only one of the reasons for the straightforward connection between structure and maps of NiTPP. The specific azimuthal orientation of NiTPP and its superposing orbital contributions amplify the effect and facilitate the comparison.

THM: In accordance with STM, ARPES momentum maps of ZnTPP on passivated Fe suggest a saddle-shaped molecule, which orientates with its N-Ni-N axis at an angle of 17° to the substrate [001] axis. We theorize that repeating the experiments with varying photon energies may lead to an improved accuracy in the determination of the saddling angle.

Finally, to explain the maybe unexpected appearance of distinct orbital contributions for ZnTPP, Figure 3.30e analyses the molecular orbital projected density of states. The frontier orbitals HOMO and HOMO-1 are found around a binding energy of 1 eV with their energy separation of 0.39 eV almost doubling that of NiTPP. Therefore, contrasting to NiTPP, they can still be distinguished when simulating experimental broadening (grey curve in Figure 3.30e). Comparing the calculated energy positions of NiTPP and ZnTPP (Figure 3.30c with e), the larger splitting originates mainly from a shift of the HOMO towards lower binding energies. Interestingly, the splitting is specifically related to the adsorption conformation and remains when calculating the same geometry in the gas phase. The electronic reason for the increased splitting of ZnTPP compared to NiTPP may be found in the different occupation of the d-levels of the two metals. The additionally filled $d_{x^2-y^2}$ of Zn d^{10} competes mainly with electron density in the HOMO and destabilizes the orbital.

3.6 Concluding Remarks

This chapter has demonstrated the various impacts of a surface on the electronic and geometric properties of Ni-tetrapyrroles. In particular, we have set a focus on the oxidation and spin states of the central Ni-atom.

Spin States in a NiPc Layer

First, at the example of a NiPc/Cu interface, we have investigated the interplay between structural properties and magnetic states of a molecular ad-layer. By utilizing a combination of DFT based calculations and experimental methods, we revealed that interaction with the copper surface may induce an axial displacement of the Ni ion from its coordination pocket, which, in turn, changes the electron configuration of the metal centre. Due to the flexible position of the transition metal, a magnetic Ni d^9 and a non-magnetic Ni d^8 spin state coexist as two stable minima in the pristine layer. At the same time, strong charge transfer from the surface anchors the phthalocyanine macrocycle of both species at a constant height above the surface.

A thermal stimulus ends the magnetic bistability of the system in favour of the non-magnetic Ni d^8 . The spin switching is accompanied by an electronic decoupling of the molecular monolayer from the substrate, which is mimicked in simulations by an artificial increase of the adsorption distance.

Adsorption of Small Gases at NiTPP

While the first study was concerned with solely molecule-substrate interaction, we have, then, allowed additional ligand molecules to interact with our interfaces. Changing to NiTPP instead of NiPc, we have started by reviewing general bonding concepts of metal-organic complexes and their display in quantum-chemical calculations. Then, we combine geometric, electronic and energetic arguments to rationalize how gas adsorption may induce spin-switching of the Ni centre. In the process, we demonstrate how such surface studies have to be assessed critically. Comparing different levels of theory is necessary to distinguish interactions, which can likely be observed in experiment, from those, which are simply related to shortcomings of theoretical approximations. In most cases, correcting the on-site correlation of the Ni d -states with the DFT+U approach has shown to improve the description of the adsorbate complexes.

We apply our concepts to six prototypical external gas ligands. We suggest that for NiTPP arrays adsorbed on a Cu surface, a redox-like interaction between Ni(+1)TPP and a strong π -acceptor such as NO_2 is the most promising approach to induce a spin-switch of the Nickel ion at room temperature. Here, the preceded reduction of the gas-phase like configuration of Ni(2+) to Ni(1+) on the substrate is the crucial step to form a stable spin-switching complex. For application, we want to emphasize that the possibility of measuring the predicted properties naturally correlates with the energetic stability of the complexes. As the adsorption energy of $\text{NO}_2/\text{NiTPP}/\text{Cu}$ is notably high, we have been able to indeed measure the electronic properties of NO_2 at room temperature. Importantly, the experimental data has proven to be consistent with our theoretical predictions.

We further suggest that a spin change should be observable for NH_3 and NO at NiTPP arrays on both clean and O-passivated surfaces. However due to the weaker interaction, experiments should be conducted under cooled conditions.

Application in Heterogeneous Catalysis

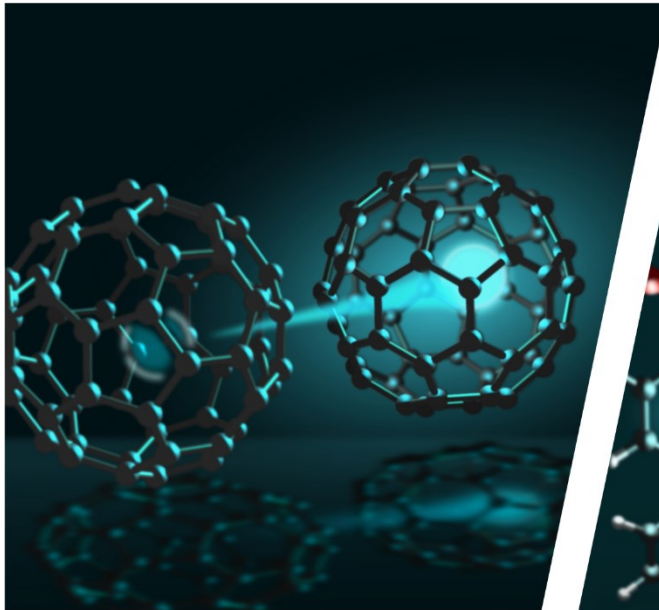
Surprisingly and perhaps contradictory to the previous conclusion, upon exposure of a NiTPP/Cu(100) monolayer to NO , we have found the formation of a stable NO_2 species at the chelated Ni centre. The presence and stability of the ligand was observed by several, independent experimental approaches, which suggests an active role of the NiTPP/Cu interface in the gas conversion. With the support of ab initio simulations, we study an atomistic model of a NO -disproportionation mechanism that is compatible with experimental observations. It is based on the initial step of coordination of one nitric oxide molecule to the Ni(I) reactive site, followed by the intermediate capture of two additional NO molecules, and by the final release of N_2O , which leaves a stable NO_2 molecule at the Ni site. In this process, the electron rich Ni(I) centre again plays an important role as it is able to donate electrons and, thereby, stabilizes intermediate structures on the reaction coordinate. Such a stabilization cannot be found in simulations of the reaction in the gas phase or at a Ni(II)-complex on a passivated surface. Complementing the measured data, we, thus, conclude that the unique environment of the NiTPP/Cu system does not only provide a platform for molecular spin-switches but also for heterogeneous catalysis.

Detecting Conformational Changes with ARPES

Besides the properties of the central metal atom, we have also briefly addressed the interface-specific geometries of the carbon backbone of tetrapyrroles. For this purpose, we have investigated the interfaces formed by ZnTPP and NiTPP monolayers on an oxygen-passivated Fe(100)-p(1x1)O surface by employing photoemission orbital tomography. In both cases, the momentum-resolved data could confirm previously reported conformation and azimuthal alignment of the molecules. On top of that, we have demonstrated how POT can shed light on the rich conformational landscape of porphyrins without relying on the interpretation of STM images. In the case of NiTPP, we observe that molecules in the first layer remain in their strong saddle-shape distorted state while the ones in the second layer show features of a planar structure. On the one hand, this finding highlights the sensitivity of POT to conformational changes. On the other hand, it also indicates that while oxygen passivation is a viable way to decouple the organic molecule from the substrate, the interaction between the chelated ion and the surface is not completely suppressed. For ZnTPP, we were able to unambiguously identify the first double-structured peak as HOMO and HOMO-1, which are visibly separated in energy. Here too, the sensitivity of POT reacts to the saddling of the molecule.

Hence, from measurements performed at a single photon energy, it is possible to probe simultaneously the energy level alignment, the azimuthal orientation, and the adsorption geometry of complex aromatic molecules, such as metal-containing tetraphenyl porphyrins. By changing the photon energy, one may further increase the accuracy of POT for detecting conformation related features in porphyrins and ascertain the degree of distortion.

4 Photoemission Exciton Tomography



To Be, or Not to Be Excited.



Summary: Advances in time-resolved photoemission spectroscopy enable new insights into excited states of extended molecular systems. The interpretation of these powerful but complex experiments strongly benefits from theoretical support. Here, the recently introduced method “exPOT” links the photoemission spectrum of excited states to the intuitive molecular picture of single-orbital excitations. This chapter aims at showing the capabilities and limitations of the approach in practical applications. We employ linear response TD-DFT and the many-body perturbation framework of GW+BSE to calculate the excited states of molecules. In the first part, we compare predicted absorption spectra especially regarding the description of the exciton wavefunctions. As different levels of theory may vary in their composition of the single-particle contributions, we explore to what extent these differences impact the simulated momentum maps of excitons. Second, we investigate the excited state landscape of fullerene in the gas phase and in a periodic multilayer. For the latter system, we actively employ exPOT by comparing with experimental data. The results are summarized in the following two manuscripts:

- [C.S.Kern et al., Phys.Rev.B. \(2023\)](#) (Introduction of method)
- [W.Bennecke et al., arXiv \(2023\)](#) (Application to fullerene films)

4.1 Theoretical Background

4.1.1 Introduction to TDDFT

As applied in the previous chapters, density functional theory has originally been devised to obtain the electronic ground state of a system. In the following, however, our focus will shift to systems, in which the absorption of light excites electrons from their ground state into higher lying levels. To be formally able to describe such excited states, we have to expand our theoretical framework. This section is dedicated to one of the most common approaches to predict the excited state spectra of especially molecular systems: linear response time-dependent DFT. We will review the formalism following the book of Ullrich [249] and refer also to the detailed reviews by Casida [250,251].

In principle, any dynamic light-matter interaction is encoded in the time-dependent Schrödinger equation (Equ. 4.1)

$$i \frac{\partial}{\partial t} \psi(\{\mathbf{x}\}, t) = H(t) \psi(\{\mathbf{x}\}, t) \quad \text{Equ. 4.1}$$

However, as with the time-independent form, it is intricate to solve Equ. 4.1 directly for large systems. Instead, it proved more convenient to treat the interaction with the electromagnetic field as a small time-dependent perturbation H' to the static Hamiltonian H_0 . (Equ. 4.2) and focus only on the change, which is induced by the perturbation to the system. In our case, H' is described by the external field potential δU coupling to any observable in our system.

$$H = H_0 + H' \quad \text{Equ. 4.2}$$

For instance, we may consider the change of the density δn between the start of the perturbation at t' and some time t . The arising difference is called the response of the density to the perturbation. Approximating the change to first order, it is possible to derive the *linear* response of the density in Equ. 4.3 defined by the field potential δU and the density response function χ . For consistency with later sections, we will introduce at this point an index notation to describe the combined space-time coordinates, e.g., $(1) \equiv (\mathbf{r}_1, t_1)$. The response function χ essentially contains the variation of the density at some position \mathbf{r} and time t with respect to an earlier perturbation at \mathbf{r}' and t' (Equ. 4.4). Equivalently, we can understand it as the time-dependent change of the observable “*density*” when the density operator ρ acts on the many-body ground state ψ_0 . In the latter picture, the step function θ ensures that there is only a full response once the perturbation is turned on.

$$\delta n(1) = \int \chi(1,2) \delta U(2) d(2) \quad \text{Equ. 4.3}$$

$$\chi(1,2) = \frac{\delta n(1)}{\delta U(2)} = -i\theta(t - t') \langle \psi_0 | [\rho(1), \rho(2)] | \psi_0 \rangle \quad \text{Equ. 4.4}$$

The next step argues that for our purposes, it is not necessary to actually follow the real time evolution of our system. Instead, Fourier transforming Equ. 4.3 allows us to convert the time-dependent relation into frequency space, where Equ. 4.5 then tells us the frequency-specific response of the system to an electromagnetic field. Or from a more spectroscopic perspective,

we have now gained access to the change of our system when interacting with light of different energy.

$$\delta n(\mathbf{r}, \omega) = \int \chi(\mathbf{r}, \mathbf{r}', \omega) \delta U(\mathbf{r}', \omega) d\mathbf{r}' \quad \text{Equ. 4.5}$$

Evaluating Equ. 4.4 in the frequency domain as well results in the Lehmann representation of the response function (Equ. 4.6) connecting the ground state ψ_0 with the i -th excited state ψ_i via the density operator. The energy needed to transition from the initial system into the new state is given by $\Omega_i = E_i - E_0$.

$$\chi(\mathbf{r}, \mathbf{r}', \omega) = \lim_{\eta \rightarrow 0^+} \sum_i \left\{ \frac{\langle \psi_0 | \rho(\mathbf{r}) | \psi_i \rangle \langle \psi_i | \rho(\mathbf{r}') | \psi_0 \rangle}{\omega - \Omega_i + i\eta} - \frac{\langle \psi_0 | \rho(\mathbf{r}') | \psi_i \rangle \langle \psi_i | \rho(\mathbf{r}) | \psi_0 \rangle}{\omega + \Omega_i + i\eta} \right\} \quad \text{Equ. 4.6}$$

Analysing Equ. 4.6, we note that this formulation of the response function conveniently has poles when the energy ω reaches values of Ω_i . Hence, we have found a suitable mathematical relation, from which we may obtain the excitation energies of a system. Realizing that we can predict optical absorption spectra from Equ. 4.6 is the core idea of linear response theory.

Runge and Gross proved that the time-evolution of a many-body system is uniquely determined by the time-dependent density with a one-to-one correspondence to any time-dependent external potential. Utilizing Runge and Gross's theorem, it can further be shown that the *response* of the density with respect to the potential is a functional of the *ground state* density only. This relation enables the formal bridge between response theory and density functional theory. In analogy to the assumption of Kohn and Sham for ground state DFT, the linear response of our many-electron system can be mapped onto the response of an auxiliary system of non-interacting electrons. The relation between the true density response function χ and the response function of the non-interacting system χ_0 is given in Equ. 4.7. The integrand couples both quantities with the DFT kernel Ξ^{DFT} and accounts for the response of electron-electron interaction via the Coulomb and exchange-correlation potential (Equ. 4.8).

$$\chi(1,2) = \chi_0(1,2) + \int \chi_0(1,3) \Xi^{DFT}(3,4) \chi(4,2) d(3,4) \quad \text{Equ. 4.7}$$

$$\Xi^{DFT}(3,4) = V_H(3) \delta(3,4) + \frac{\delta V_{xc}(3)}{\delta n(4)} \quad \text{Equ. 4.8}$$

While χ is still formally exact to give the excitation energies Ω_i of the true system, χ_0 must be understood as its pendant for the non-interacting case. Similar to Equ. 4.6, the frequency-dependent expression of χ_0 can be reformulated in a Lehmann representation using the single-particle Kohn-Sham orbitals ϕ^{KS} connecting the j -th occupied orbital with the c -th unoccupied orbital (Equ. 4.9). The response function of Equ. 4.9 has poles at the energy difference between the Kohn-Sham eigenenergies ε_j and ε_c and simply gives the excitation energies of single-particle excitations in a non-interacting system.

$$\chi_0(\mathbf{r}, \mathbf{r}', \omega) = \lim_{\eta \rightarrow 0^+} \sum_{j,c} (f_c - f_j) \frac{\phi_j^{KS}(\mathbf{r}) \phi_c^{KS*}(\mathbf{r}) \phi_j^{KS*}(\mathbf{r}') \phi_c^{KS}(\mathbf{r}')}{\omega - (\varepsilon_j - \varepsilon_c) + i\eta} \quad \text{Equ. 4.9}$$

Inserting Equ. 4.7 into Equ. 4.5 together with Equ. 4.8 and Equ. 4.9, Casida first showed in a seminal article [250] how the linear response of the density, $\delta n(\mathbf{r}, \omega)$, can take the shape of

an eigenvalue problem (Equ. 4.10). The eigenenergies of the resulting equation, later known as ‘‘Casida’s equations’’, give the excitation energies Ω_i of the system. The corresponding eigenvectors (X^i, Y^i) describe the excited state wave functions in terms of excitations and de-excitations in the single-particle KS basis. The matrices R^{DFT} and C^{DFT} are the resonant and coupling matrices, respectively, treating the Coulomb and exchange-correlation interactions between the single-particle transitions within Ξ^{DFT} . As the exact DFT kernel is not known anyway, it is worthwhile to evaluate the matrix elements in Equ. 4.10 directly based on one of the common exchange-correlation approximations. This will, furthermore, facilitate the comparison to the Bethe-Salpeter approach in our discussion below. Employing the formalism of a general hybrid functional to describe the exchange-correlation part of the full Ξ^{DFT} , the matrix elements R_{j_c, j'_c}^{DFT} and C_{j_c, j'_c}^{DFT} can be written as Equ. 4.11 and Equ. 4.12. Here, the coefficient c_{HF} gives the amount of exact Hartree-Fock exchange utilized in the construction of the exchange-correlation functional, so that $c_{HF} = 0$ would correspond to pure TDDFT.

$$\begin{pmatrix} R^{DFT} & C^{DFT} \\ -C^{DFT*} & -R^{DFT*} \end{pmatrix} \begin{pmatrix} X^i \\ Y^i \end{pmatrix} = \Omega_i \begin{pmatrix} X^i \\ Y^i \end{pmatrix} \quad \text{Equ. 4.10}$$

$$R_{j_c, j'_c}^{DFT} = \delta_{j, j'} \delta_{c, c'} (\varepsilon_c^{KS} - \varepsilon_{j'}^{KS}) + (j_c | j' c') - c_{HF} (j j' | c c') + (1 - c_{HF}) \Xi_{j_c, j'_c}^{xc} \quad \text{Equ. 4.11}$$

$$C_{j_c, j'_c}^{DFT} = (j_c | c' j') - c_{HF} (j c' | c j') + (1 - c_{HF}) \Xi_{j_c, c' j'}^{xc} \quad \text{Equ. 4.12}$$

Note that for clarity of Equ. 4.11 and Equ. 4.12, we have abbreviated matrix elements of the bare Coulomb potential $v(|\mathbf{r} - \mathbf{r}'|)$ with the notation $(ab|cd)$ and the response due to V_{xc} with the exchange-correlation kernel Ξ^{xc} . The respective double integrals are defined in Equ. 4.13 and Equ. 4.14.

$$\Xi_{j_c, j'_c}^{xc} = \iint \phi_j(\mathbf{r}) \phi_c(\mathbf{r}) \Xi^{xc}(\mathbf{r}, \mathbf{r}') \phi_{j'}(\mathbf{r}') \phi_{c'}(\mathbf{r}') \, d\mathbf{r} d\mathbf{r}' \quad \text{Equ. 4.13}$$

$$(j_c | j' c') = \iint \phi_j(\mathbf{r}) \phi_c(\mathbf{r}) v(|\mathbf{r} - \mathbf{r}'|) \phi_{j'}(\mathbf{r}') \phi_{c'}(\mathbf{r}') \, d\mathbf{r} d\mathbf{r}' \quad \text{Equ. 4.14}$$

4.1.2 Introduction to GW and BSE

In the following, I will briefly introduce an alternative approach to TD-DFT for the simulation of excitation spectra of many-electron systems. I will examine the approach mainly from a practical perspective and leave the derivations of the theory to many excellent reviews on this topic [252–254]. Furthermore, I will follow Blase et al. [254] to connect the formalism to the framework of (TD)DFT, in tone with the rest of this thesis.

As opposed to the density in density functional theory, the main entity, on which many-body perturbation theory builds, is the one-body Green’s function G . In essence, the Green’s function as defined in Equ. 4.15 describes the propagation of an electron added or removed to/from the N -electron system Ψ^N from one position in space-time (\mathbf{r}_1, t_1) to another (\mathbf{r}_2, t_2) . Here, we again use the combined index notation from above. The field operators a and a^\dagger ensure the

removal and addition of the electron, respectively, while T denotes the correct time-ordering of the operator product.

$$G(1,2) = -i\langle\Psi^N|T[a(1)a^\dagger(2)]|\Psi^N\rangle \quad \text{Equ. 4.15}$$

If a^\dagger acts first by creating an electron in (2), G provides the probability to probe this electron later in (1). In contrast, if the electron is first removed from (1) by a , G gives the probability that the remaining electron *hole* can be found later in (2). The energies related to the described processes would then correspond to the electron affinity $EA = E(N) - E(N + 1)$ and the ionization potential $IP = E(N - 1) - E(N)$ of the N -electron system.

The respective energies are indeed also encoded in the Green's function. Explicitly deriving the time-evolution of the field operators in Equ. 4.15 and converting the resulting expression for G into frequency-space leads to Lehmann's representation of the Green's function (Equ. 4.16). Here, g_s are the so-called Lehmann's amplitudes, which we will later associate with quasi-particle wave functions, and ε_s are the electron addition and removal energies. In the notation of Equ. 4.16, energies ε_s smaller than the chemical potential μ correspond to IP s and ε_s larger than μ give EAs .

$$G(\mathbf{r}, \mathbf{r}', \omega) = \sum_s \frac{g_s(\mathbf{r})g_s^*(\mathbf{r}')}{\omega - \varepsilon_s + i\eta \times \text{sgn}(\varepsilon_s - \mu)} \quad \text{Equ. 4.16}$$

By knowing the energy-dependent Green's function, we could determine ε_s as poles of the function. Thus ultimately, it should be our aim to find a computable expression for G .

We start by writing the equation of motion for the one-body Green's function (Equ. 4.17). Assuming the interaction between electrons in the system as a perturbation to a non-interacting system allows us to introduce separated operators. h_0 is the one-body Hamiltonian including the kinetic term of the particle, its interaction with the nuclei and the bare Coulomb interaction. Σ is the self-energy operator accounting for all exchange-correlation effects in the system, thus, formally performing the task of the xc -potential in DFT. However, opposed to many (semi)local descriptions of V_{xc} , specifically note how the self-energy is *non*-local and energy dependent.

$$[\omega - h_0(\mathbf{r})]G(\mathbf{r}, \mathbf{r}', \omega) - \int \Sigma(\mathbf{r}, \mathbf{r}'', \omega)G(\mathbf{r}'', \mathbf{r}', \omega) d\mathbf{r}'' = \delta(\mathbf{r} - \mathbf{r}') \quad \text{Equ. 4.17}$$

With the help of Equ. 4.16, Equ. 4.17 can be rewritten in a more familiar formalism as an eigenvalue equation with respect to the Lehmann's amplitudes g_s (Equ. 4.18). In contrast to the Kohn-Sham equation in Equ. 2.8, this time, the eigenvalues ε_s do indeed represent to the true addition and removal energies of the system.

$$h_0(\mathbf{r})g_s(\mathbf{r}) + \int \Sigma(\mathbf{r}, \mathbf{r}', \varepsilon_s)g_s(\mathbf{r}') d\mathbf{r}' = \varepsilon_s g_s(\mathbf{r}) \quad \text{Equ. 4.18}$$

Up to this point, the Green's function provides an exact framework to obtain occupied and unoccupied electronic energy levels associated with adding and removing electrons from a system. Comparing Equ. 4.16 with Equ. 4.18, we have just reformulated the problem of finding ε_s as poles to the function G into an eigenvalue problem. This comes at the cost that, as usual,

our operator to account for exchange-correlation effects in the system, Σ , is unknown. A definition was proposed by Hedin [255]. Characterizing the auxiliary system of non-interacting particles by the Green's function G_0 , he derived a set of five integro-differential equations listed in Equ. 4.19 to Equ. 4.23. Hedin's equations link the self-energy Σ to the interacting and non-interacting Green's function, the dynamically *screened* Coulomb potential W , the polarizability P and the so-called vertex function Γ .

$$\Sigma(1,2) = i \int G(1,4)W(3,1^+)\Gamma(4,2,3) d(3,4) \quad \text{Equ. 4.19}$$

$$G(1,2) = G_0(1,2) + \int G_0(1,3)\Sigma(3,4)G(4,2) d(3,4) \quad \text{Equ. 4.20}$$

$$W(1,2) = v(1,2) + \int v(4,2)P(3,4)W(1,3) d(3,4) \quad \text{Equ. 4.21}$$

$$P(1,2) = -i \int G(2,3)G(4,2)\Gamma(3,4,1) d(3,4) \quad \text{Equ. 4.22}$$

$$\Gamma(1,2,3) = \delta(1,2)\delta(1,3) + \int \frac{\delta\Sigma(1,2)}{\delta G(4,5)}G(4,6)G(7,5)\Gamma(6,7,3) d(4,5,6,7) \quad \text{Equ. 4.23}$$

He further suggested to neglect the second part of the vertex function in Equ. 4.23, thereby reducing the dependency of the self-energy to G and W (Equ. 4.24) – and giving name to the approximation and method itself.

$$\Sigma^{GW}(1,2) = iG(1,2)W(2,1^+) \quad \text{Equ. 4.24}$$

While in principle, Hedin provided a self-consistent way to evaluate Σ and the GW-formalism reduced the complexity of the problem, we still lack a zeroth order starting point to calculate G . In practice, the similarity between the eigenvalue equation emerging in Green's function theory (Equ. 4.18) and Kohn-Sham DFT (Equ. 2.8) is utilized. By approximating the many-body wave function with a single-Slater determinant, the Lehmann's amplitudes g_s become single-body objects and their respective energies ε_s become the single-particle energies ε_i^{GW} interpretable as electronic states. In a next step, the single-particle KS orbitals φ_i^{KS} and energies ε_i^{KS} are inserted into the reduced Hedin's equations to build an approximation for Σ^{GW} . Finally, the self-energy is treated as a perturbation to the KS exchange-correlation potential V_{xc}^{KS} to correct ε_i^{KS} according to Equ. 4.25 and obtain ε_i^{GW} .

$$\varepsilon_i^{GW} = \varepsilon_i^{KS} + \langle \varphi_i^{KS} | \Sigma^{GW}(\varepsilon_i^{GW}) - V_{xc}^{KS} | \varphi_i^{KS} \rangle \quad \text{Equ. 4.25}$$

The set of equations necessary to formulate Σ^{GW} in terms of KS orbitals are summarized in Equ. 4.26 to Equ. 4.29.

$$\Sigma^{GW}(\mathbf{r}, \mathbf{r}', E) = \frac{i}{2\pi} \int G^{GW}(\mathbf{r}, \mathbf{r}', E + \omega)W^{GW}(\mathbf{r}, \mathbf{r}', \omega') d\omega' \quad \text{Equ. 4.26}$$

$$G^{GW}(\mathbf{r}, \mathbf{r}', E) = \sum_i \frac{\varphi_i^{KS}(\mathbf{r})\varphi_i^{KS*}(\mathbf{r}')}{E - \varepsilon_i^{KS} + i0^+ \times \text{sgn}(\varepsilon_i^{KS} - E_F)} \quad \text{Equ. 4.27}$$

$$W^{GW}(\mathbf{r}, \mathbf{r}', \omega) = v(\mathbf{r}, \mathbf{r}') + \int v(\mathbf{r}, \mathbf{r}_3) P_0^{GW}(\mathbf{r}_3, \mathbf{r}_4, \omega) W^{GW}(\mathbf{r}_4, \mathbf{r}', \omega) d\mathbf{r}_3 d\mathbf{r}_4 \quad \text{Equ. 4.28}$$

$$P_0^{GW}(\mathbf{r}, \mathbf{r}', \omega) = \sum_{i,j} (f_i - f_j) \frac{\varphi_i^{KS*}(\mathbf{r}) \varphi_j^{KS}(\mathbf{r}) \varphi_j^{KS*}(\mathbf{r}') \varphi_i^{KS}(\mathbf{r}')}{\varepsilon_i^{KS} - \varepsilon_j^{KS} - \omega - i0^+ \times \text{sgn}(\varepsilon_i^{KS} - \varepsilon_j^{KS})} \quad \text{Equ. 4.29}$$

Besides information on electron addition or removal, the one-body Green's function also contains information about optical electron excitations. Very similar to response-theory, we may consider the change of the one-body Green's function $G(1, 1')$ with respect to an external, but this time *non*-local perturbing field $U(2, 2')$. This change is expressed in Equ. 4.30 by the famous Bethe-Salpeter equation (BSE) as a two-particle correlation function $L(1, 2; 1', 2')$. L describes the correlated propagation of two particles, namely an electron and a hole, which are simultaneously created and annihilated during the optical excitation process. In analogy to the non-interacting density response function χ_0 , the function L_0 considers only non-interacting electron-hole pairs, the excitation energies of which would simply be given by the difference of their quasi-particle energies ε_i^{GW} . The interacting BSE kernel Ξ^{BSE} connects the free and correlated electron-hole pairs and is given in Equ. 4.31 within the GW approximation.

$$L(1, 2; 1', 2') = L_0(1, 2; 1', 2') + \int L_0(1, 4; 1', 3) \Xi^{BSE}(3, 5; 4, 6) L(6, 2; 5, 2') d(3, 4; 5, 6) \quad \text{Equ. 4.30}$$

$$i\Xi^{BSE}(3, 5; 4, 6) = v(3, 6) \delta(34) \delta(56) - W(3^+, 4) \delta(36) \delta(45) \quad \text{Equ. 4.31}$$

Transforming L from the time-domain into frequency-domain, we find that the correlation function L in dependence of energy has poles at the true excitation energies Ω_i of the system. Obtaining these can again be formulated as an eigenvalue problem (Equ. 4.32), where the eigenenergies give the excitation energies Ω_i . The corresponding eigenvectors (X^i, Y^i) describe the excited state wave functions in terms of excitations and de-excitation processes in the basis of single-particle electron and hole states. The matrices R^{BSE} and C^{BSE} are the resonant and coupling matrices, respectively, treating the Coulomb and *screened* Coulomb interactions between the single-particle transitions stemming from Ξ^{BSE} . Their matrix elements R_{j_c, j'_c}^{BSE} and C_{j_c, j'_c}^{BSE} can be written as Equ. 4.33 and Equ. 4.34.

$$\begin{pmatrix} R^{BSE} & C^{BSE} \\ -C^{BSE*} & -R^{BSE*} \end{pmatrix} \begin{pmatrix} X^i \\ Y^i \end{pmatrix} = \Omega_i \begin{pmatrix} X^i \\ Y^i \end{pmatrix} \quad \text{Equ. 4.32}$$

$$R_{j_c, j'_c}^{BSE} = \delta_{j, j'} \delta_{c, c'} (\varepsilon_c^{GW} - \varepsilon_j^{GW}) + 2(jc | j' c') - W_{j j', cc'} \quad \text{Equ. 4.33}$$

$$C_{j_c, j'_c}^{BSE} = 2(jc | c' j') - W_{j_c, c' j'} \quad \text{Equ. 4.34}$$

In order to make the relation to our description of linear-response TDDFT more apparent, we have again abbreviated expressions with a classical Coulomb dependency as $(ab|cd)$, while W corresponds to the *screened* Coulomb contribution from many-body theory. The full forms of the respective double integrals are given in Equ. 4.35 and Equ. 4.36.

$$W_{j j', cc'} = \iint \phi_j(\mathbf{r}) \phi_{j'}(\mathbf{r}) W(\mathbf{r}, \mathbf{r}') \phi_c(\mathbf{r}') \phi_{c'}(\mathbf{r}') d\mathbf{r} d\mathbf{r}' \quad \text{Equ. 4.35}$$

$$(jc|j'c') = \iint \phi_j(\mathbf{r})\phi_c(\mathbf{r})v(|\mathbf{r}-\mathbf{r}'|)\phi_{j'}(\mathbf{r}')\phi_{c'}(\mathbf{r}')d\mathbf{r}d\mathbf{r}' \quad \text{Equ. 4.36}$$

For completeness, we also give the i -th excited state wave function as spanned by the eigenvectors (X^i, Y^i) with respect to the electron \mathbf{r}_e and hole \mathbf{r}_h coordinate in Equ. 4.37.

$$\psi_i(\mathbf{r}_h, \mathbf{r}_e) = \sum_{j,c} [X_{jc}^i \phi_j^*(\mathbf{r}_h)\phi_c(\mathbf{r}_e) + Y_{jc}^i \phi_j^*(\mathbf{r}_e)\phi_c(\mathbf{r}_h)] \quad \text{Equ. 4.37}$$

Finally, we will utilize our attempt to summarize TD-DFT and GW-BSE in a uniform manner to briefly compare the predictive strength of both methods. In particular, we intend to highlight two factors, which determine the agreement of the respective excitation energies Ω_i with experiment. First, recalling the previous introductions, we notice that in practical applications, we simulate excitations starting from an approximate ground state. As discussed in the previous chapters, in case of DFT, the exchange-correlation functional majorly influences the set of ground state orbitals and energies $\{\varphi^{KS}, \varepsilon^{KS}\}$, which then enter Casida's equation. While GW is formally concerned with the Green's function, the method still builds on DFT orbitals and energies as a starting guess. Preferably, the whole set $\{\varphi^{KS}, \varepsilon^{KS}\}$ would be corrected self-consistently (qsGW) [256], but often solely the energies are considered (evGW). In a first approximation, the energies may even be corrected only once (G₀W₀). Consequently, depending on the chosen correction scheme, the BSE Hamiltonian also suffers from the choice of the underlying DFT description albeit to different extent. As a broad statement, we may summarize that the obtained optical spectra can obviously be only as good as the ground state starting conditions in our simulations.

As the second issue, we want to address the calculation of the excitation energies more specifically. Here, it is helpful to consider a fictitious system of two well separated molecules, the orbitals of which do not overlap spatially. Let us further assume that an excitation involves the transfer of an electron from the occupied orbital j of one molecule to the unoccupied orbital c of the other molecule. As we have set the overlap between j and c to zero, neither the Coulomb $(jc|j'c')$ nor the exchange-correlation response $\Xi_{j_c, j'c'}^{xc}$ contributes to the interaction matrices R^{DFT} and C^{DFT} . Hence, for such an excitation, the excitation energy in (semi)local TD-DFT ($c_{HF} = 0$) simply reduces to the difference between the Kohn-Sham orbital energies $\varepsilon_c^{KS} - \varepsilon_j^{KS}$, i.e., to the single-particle excitation energy of a non-interacting system. Upon relying on approximate exchange-correlation functionals, we apparently suffer from the same erroneous description of the KS gap as already encountered throughout this thesis. The situation is majorly improved by applying hybrid functionals ($c_{HF} > 0$). The Coulomb-like response from exact exchange re-introduces "electrostatic" attraction between excited electrons and remaining holes. For comparison, this interaction is automatically captured by the *screened* Coulomb contribution W within BSE. In other words, BSE has an intrinsic advantage in the treatment of spatially separated electrons and holes.

4.1.3 Introduction to exPOT

Experimentally, the excitation energies of a system are traditionally accessed by optical absorption spectroscopy. However, by combining ARPES with recent progress in ultra-fast laser technology, photoemission spectroscopy has developed into a complementary technique to investigate excited state landscapes. It has become possible to pump and probe the excited states of a system and follow the dynamics of the excitation processes over time. In the following, we want to extend the concept of ground-state photoemission orbital tomography to describe such pump-probe ARPES experiments. This section summarizes the derivations given in greater detail in ref. [44].

In difference to the introduction of POT in chapter 2.1.2, this time, the photoemission spectroscopy does not probe the electronic ground state $\Psi_{i,0}^N$ but an optically excited state $\Psi_{i,m}^N$ of the system. The difference is illustrated in Equ. 4.38, where we have substituted $\Psi_{i,0}^N$ with $\Psi_{i,m}^N$ in the original Fermi's golden rule expression of Equ. 2.22.

$$W_{i \rightarrow f} \propto |\langle \Psi_f^N | \mathbf{A} \cdot \mathbf{P} | \Psi_{i,m}^N \rangle|^2 \times \delta(\omega + E_{i,m}^N - E_f^N) \quad \text{Equ. 4.38}$$

Let us again start by analysing energy conservation during the photoemission process. The initial energy $E_{i,m}^N$ corresponding to the initially m -th excited state $\Psi_{i,m}^N$ is obtained by adding the optical excitation energy Ω_m to the ground state energy $E_{i,0}^N$ (Equ. 4.39). The system after photoemission can be seen equal to the ground state, from which the j -th electron has been emitted $\Psi_{f,j}^{N-1}$. Here we assume that upon optical excitation, a hole is left behind in the j -occupied state of the system and remains unaffected, while the excited electron is photoemitted. Relying again on the sudden approximation, the wavefunction of the photoemission final state is represented by the anti-symmetrized product of this $(N - 1)$ electron state and the free electron γ_k . Consequently, the energy of the final state E_f^N can be written as the sum of the energy of the $(N - 1)$ system $E_{f,j}^{N-1}$ and the kinetic energy E_{kin} of the detached electron.

$$E_{i,m}^N = E_{i,0}^N + \Omega_m \quad \text{Equ. 4.39}$$

$$E_f^N = E_{f,j}^{N-1} + E_{kin} \quad \text{Equ. 4.40}$$

Inserting Equ. 4.39 and Equ. 4.40 to fulfil the energy conservation of Equ. 4.38, the measurable kinetic energy corresponds to

$$E_{kin} = \omega - (E_{f,j}^{N-1} - E_{i,0}^N) + \Omega_m = \omega - \varepsilon_j + \Omega_m \quad \text{Equ. 4.41}$$

where $E_{f,j}^{N-1} - E_{i,0}^N$ represents the j -th vertical ionization potential ε_j of the system. Interpreting Equ. 4.41 in terms of a pump-probe experiment, the kinetic energy of a detected photoelectron is determined by the probe energy ω , the pump energy Ω_m with which the initially excited state is generated and the ionization energy ε_j of the ‘‘hole’’-state that is left behind.

For the evaluation of the matrix element in Equ. 4.38, we resort to the Dyson-orbital description of photoemission, which conveniently introduced the dependency on a single electron coordinate only (Equ. 4.42). Applying it to the initial $\Psi_{i,m}^N$ and final state $\Psi_{f,j}^N$, the

Dyson orbital $D_{j,m}$ in Equ. 4.42 describes the overlap between the m -th N electron excited state and the j -th ionized ($N - 1$) system (see Equ. 4.43).

$$\langle \Psi_{f,j}^N | \mathbf{A} \cdot \mathbf{P} | \Psi_{i,m}^N \rangle = \mathbf{A} \int \gamma_k^*(\mathbf{r}_N) \mathbf{P} D_{j,m}(\mathbf{r}_N) d\mathbf{r}_N \quad \text{Equ. 4.42}$$

$$D_{j,m}(\mathbf{r}_N) = \sqrt{N} \int \Psi_{f,j}^{N-1*}(\{\mathbf{x} \setminus \mathbf{r}_N\}) \Psi_{i,m}^N(\mathbf{x}) d\{\mathbf{x} \setminus \mathbf{r}_N\} \quad \text{Equ. 4.43}$$

In order to derive a more descriptive expression of $D_{j,m}$, we approximate the wavefunction of our system with a single Slater determinant. The ($N - 1$) final state, where the electron has left a hole in the electronic level ϕ_j , can then be written as

$$\Psi_{f,j}^{N-1}(\{\mathbf{x} \setminus \mathbf{r}_N\}) = \frac{1}{\sqrt{(N-1)!}} \begin{vmatrix} \phi_N(\mathbf{r}_1) & \dots & \phi_N(\mathbf{r}_{N-1}) \\ \vdots & \dots & \vdots \\ \phi_{j+1}(\mathbf{r}_1) & \dots & \phi_{j+1}(\mathbf{r}_{N-1}) \\ \phi_{j-1}(\mathbf{r}_1) & \dots & \phi_{j-1}(\mathbf{r}_{N-1}) \\ \vdots & \dots & \vdots \\ \phi_1(\mathbf{r}_1) & \dots & \phi_1(\mathbf{r}_{N-1}) \end{vmatrix} \quad \text{Equ. 4.44}$$

In the spirit of single-reference excited state methods, the initial optically excited state is built from the same basis of occupied and unoccupied orbitals of the ground state as a sum over Slater determinants weighted by the excitation coefficient X_{jc}^m (Equ. 4.45). Each determinant in Equ. 4.45 can equivalently be expressed by utilizing Laplace's cofactor expansion resulting in Equ. 4.46 – a mathematical manipulation, which comes handy for our subsequent derivations. Note that for readability of the present introduction, the excited state is treated within the Tamm-Dancoff approximation, where de-excitation contributions are neglected.

$$\Psi_{i,m}^N(\mathbf{r}_1, \dots, \mathbf{r}_N) = \frac{1}{\sqrt{N!}} \sum_{(jc)} X_{jc}^m \begin{vmatrix} \phi_c(\mathbf{r}_1) & \dots & \phi_c(\mathbf{r}_N) \\ \phi_N(\mathbf{r}_1) & \dots & \phi_N(\mathbf{r}_N) \\ \vdots & \dots & \vdots \\ \phi_{j+1}(\mathbf{r}_1) & \dots & \phi_{j+1}(\mathbf{r}_N) \\ \phi_{j-1}(\mathbf{r}_1) & \dots & \phi_{j-1}(\mathbf{r}_N) \\ \vdots & \dots & \vdots \\ \phi_1(\mathbf{r}_1) & \dots & \phi_1(\mathbf{r}_N) \end{vmatrix} \quad \text{Equ. 4.45}$$

$$\det(\Psi) = (-1)^{1+N} \phi_c(\mathbf{r}_N) \det(\{\Psi \setminus \phi_c\}) + (-1)^{2+N} \phi_N(\mathbf{r}_N) \det(\{\Psi \setminus \phi_N\}) + \dots \quad \text{Equ. 4.46}$$

Combining Equ. 4.44 and Equ. 4.46, we construct the Dyson orbital from Equ. 4.43. Evaluating the product of Slater determinants in the integrand, the overlap integrals between $\det(\Psi_{f,j}^{N-1})$ and $\det(\{\Psi_m^N \setminus \phi_i\})$ vanish in most cases due to the orthogonality of the many body states. In fact, in the multiplication with $\det(\Psi_{f,j}^{N-1})$ only the first terms $\det(\{\Psi \setminus \phi_c\})$ survive from the Laplace expansion, provided that the hole sits in the j -th occupied level. Within our approximations, we arrive for the j -th Dyson orbital at

$$D_{j,m}(\mathbf{r}_N) = \sum_c X_{jc}^m \phi_c(\mathbf{r}_N) \quad \text{Equ. 4.47}$$

Inserting Equ. 4.47 into the expression for the photoemission matrix element and making use of the plane-wave approximation for γ_k introduces again the Fourier transform of the Dyson orbital. Its linearity property allows us to include the Fourier transform into the sum of Equ. 4.47 converting $\phi_c(\mathbf{r}_N)$ to $\mathcal{F}[\phi_c](\mathbf{k})$ (Equ. 4.48). In essence, for a certain exciton m leaving a hole in the j -th occupied state, the pattern of the \mathbf{k} -dependent intensity distribution is determined by a sum over the Fourier transformed, unoccupied levels ϕ_c . The excitation coefficients X_{jc}^m act as weighting factors to these Fourier transforms.

$$I_m(\mathbf{k}) \propto |\mathbf{A} \cdot \mathbf{k}|^2 \sum_j \left| \sum_c X_{jc}^m \mathcal{F}[\phi_c](\mathbf{k}) \right|^2 \times \delta(\omega - E_{kin} - \varepsilon_j + \Omega_m) \quad \text{Equ. 4.48}$$

The mathematical expressions for the \mathbf{k} -resolved momentum distribution and the energy conservation are the two main implications of Equ. 4.48 and the foundation of exPOT. Below, we illustrate their interpretation at the example of four prototypical exciton structures (a-d) schematically depicted in Figure 4.1. For the sake of simplicity, we only consider contributions from four frontier orbitals (HOMO-1, HOMO, LUMO and LUMO+1). In case a, the exciton involves only a single transition from the highest occupied orbital (H) to the lowest unoccupied orbital (L), which is often thought of as the lowest-energy excitation in molecules. Trivially, exPOT predicts a single peak in the photoemission spectrum at a kinetic energy $E_{kin} = \omega - \varepsilon_H + \Omega_a$ depending on the ionization potential of the HOMO, ε_H , and the excitation energy, Ω_a . The corresponding momentum pattern is determined by the Fourier transform of the LUMO.

Cases b to d represent more intricate examples comprising of linear combinations of single particle transitions. In particular, exciton b with the transition energy Ω_b is described by a sum over the two transitions, HOMO-1->LUMO and HOMO->LUMO+1. As a consequence of energy conservation, exPOT now predicts two photoemission peaks corresponding to the ionization levels ε_H and ε_{H-1} . At each peak, the momentum map can be associated with either the LUMO (for ε_{H-1}) or the LUMO+1 (for ε_H) according to the respective electron-hole configuration. For case c, we assume transitions from two different occupied levels (HOMO-1 and HOMO) into the same unoccupied orbital (LUMO). Here, we still expect two photoemission peaks, but this time with an identical intensity distribution pattern. Finally in case d, the excitation leaves only a single hole in the HOMO, however, the electron is distributed in either the LUMO or the LUMO+1. Thus following Figure 4.1, in a single photoemission peak, the momentum map should be proportional to the coherent sum of the unoccupied orbitals weighted by their excitation coefficient X_c .

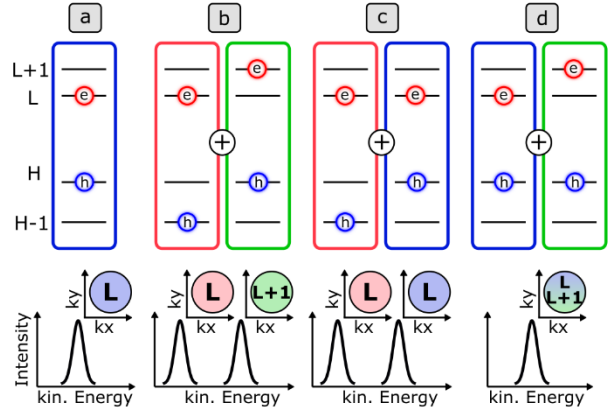


Figure 4.1: Four prototypical exciton structures (a-d) and the corresponding predictions of exPOT. (top) Single particle contributions of an exciton are illustrated as the excited electron (e) in an unoccupied orbital (L) and the left-behind hole (h) in an occupied orbital (H). (bottom) Expected photoemission spectra and momentum maps.

4.2 Benchmarking exPOT

4.2.1 Introduction

Presently, methodical means and computational feasibility divides the simulation of pump-probe photoemission experiments into two theoretical camps. The approach on either side focuses only on one of the two steps involved in the experiment, i.e., either the optical pumping or the photoemission probing process.

On the one hand, as experiments investigate increasingly complex systems, simulations are in demand of a more advanced description of the excited state landscape. A possible approach is the aforementioned extension of photoemission orbital tomography (POT) to excited states as initial state of the photoemission process (exPOT). According to this formalism, the initial state resulting from the optical pump pulse is expressed as natural transition orbital, or to be more precise as a coherent superposition of unoccupied orbitals weighted by their excitation coefficients [44]. All necessary information for the computation is readily available from the transition density matrix – a quantity which can be obtained from high level Casida or BSE calculations. Both frameworks have proven equally successful to describe complex excited states in molecules but also in the solid state [251–253,257]. However, approximating the photoemitted electron as a plane-wave has sparked scientific discourse about the validity of the approach [258].

On the other hand, developments in scattering theory utilizing Green’s functions [259–261] as well as in real-time TDDFT approaches (rt-TDDFT) [262–264] have led to an increased understanding of the photoemission process itself capturing also final state effects of the photoemitted electron. In particular, simulating experiments in real-time, real-space promises to be a useful tool for the interpretation of measured pump-probe data [265–267]. So far, however, its limitation lies in the description of the electronic structure of the initial state as applications to experimentally interesting systems are hardly feasible beyond adiabatic LDA in the real-time TDDFT schemes. The rudimentary inclusion of exchange-correlation may miss important electronic properties of the initially pumped excitation.

Uniting both worlds, e.g.: by implementing an efficient hybrid functional kernel in rt-TDDFT, must ultimately be the goal of future developments, however, is beyond the scope of this work. Instead, the following section wants to highlight the importance of an adequate description of the optically excited states, which are created by pump pulse in tr-ARPES experiments.

Article Information and Author Contribution

Here, I show complementary calculations to the work of **Christian S. Kern** et al. [44], to which I have contributed in several discussions. The computational data presented in the following section provides additional insights to support the theory of “exciton POT” (exPOT) as introduced in our common publication.

Photoemission orbital tomography for excitons in organic moleculesC. S. Kern , A. Windischbacher , and P. Puschnig ^{*}
Institute of Physics, NAWI Graz, University of Graz, 8010 Graz, Austria

Figure 4.2: Header of the article [44] including all contributing authors. The study was published in *Physical Review B*.

4.2.2 Results and Discussion

Investigated Systems

Building upon Equ. 4.48 from chapter 4.1.3, the recently introduced method exPOT predicts the photoemission intensity of pump-probe photoemission experiments solely based on the calculation of optically excited states as obtained from either Casida's equation within linear response TDDFT or from solving the Bethe-Salpeter equation (BSE) in the framework of many-body perturbation theory. In ref.[44], the main implications of Equ. 4.48 were tested against real-time TDDFT – a framework, which directly simulates the photoemission process beyond the plane-wave final state approximation. For this theoretical validation, three molecules have been chosen, TCNQ, porphyrin and PTCDA (structures top of Figure 4.3). While exPOT is in general applicable to any organic molecule, these molecules specifically represent one of the three intricate cases of Figure 4.1b-d. Comparing exPOT with rt-TDDFT, we were able to confirm the two main propositions of Equ. 4.48. First, energy conservation during the photoemission process and, hence, the kinetic energy of the emitted electron, is determined by the hole configurations of the exciton wavefunction. Second, the angle-resolved intensity pattern can be approximated by the Fourier transform of a coherent superposition of unoccupied orbitals weighted by their excitation coefficients.

Due to computational limitations of rt-TDDFT in ref. [44], the comparison of the two theoretical schemes has been realized at an adiabatic LDA level. While this approximation in some cases may lead to convincing agreement with experiment, often due to advantageous error cancellation, recent years have seen the development of more advanced descriptions of excited states. To test the robustness of the exPOT approach beyond LDA, we here compute the optical absorption of our three exemplary molecules employing three different levels of theory. First, calculations within LDA serve as a comparison between the excited state calculations from rt-TDDFT and linear response TDDFT, which is the starting point for our exPOT analysis. Comparing both calculation schemes, we investigate if the two frameworks predict the same excited states, and thus, provide the same starting condition for any pump-probe photoemission simulation. Subsequently, we use linear response TDDFT to compare our LDA results to more advanced descriptions of the electronic structure. So in a second approach, we calculate the molecular excitations with a range-separated hybrid functional (Casida@CAM-B3LYP). Third, we employ many-body perturbation theory (GW+BSE) to obtain the optical properties. As our GW calculations are based on DFT ground states, in the third step, we can apply the many-body correction on top of either the LDA or the CAM-B3LYP ground state denoted as BSE@LDA and BSE@hybrid, respectively. The so obtained absorption

spectra for TCNQ, porphin and PTCDA are summarized in Figure 4.3. Note that for comparison with ref.[44], we show the absorption projected along a specific direction of the transition dipole (y-direction for TCNQ and PTCDA, x-direction for porphin according to the coordination frame defined on top of Figure 4.3). The rt-TDDFT simulation excites the molecules with a “delta-kick” polarized along the respective direction and, thus, probes only excitations with respective contributions to the transition dipole. For each molecule, the exciton with the strongest oscillator strength is marked by a star. The analysis of the LDA results (solid lines, top and middle panel) for these excitons can be found in ref. [44,268] and have been the basis for our initial comparison between rt-TDDFT and exPOT. We will not repeat the comparison, but want to emphasize that both, linear response and rt-TDDFT, agree in their description of the excited states of the three molecules. As a consequence, both methods also lead to the same photoemission intensity distributions predicted for the excited states. Switching to the calculation with a hybrid functional (dashed line, middle panel), we find a strong change in the excitation energies and the magnitude of the predicted transition probabilities. Applying the GW+BSE formalism on top of DFT (bottom panel), then, leads to small corrections in the excitation energies, but the overall spectral shape and the relative intensities of the peaks stay the same compared to the hybrid functional. Interestingly, BSE converges to similar, only slightly shifted results, independent of whether we use LDA or CAM-B3LYP as a starting point. This demonstrates that the many-body corrections appear to be quite insensitive to the underlying DFT approximation. Employing the evGW scheme, we attribute this to the self-consistent correction of the respective initial KS energies to obtain the GW energy levels. Independent of the LDA or CAM-B3LYP starting point, the evGW correction results in similar quasi-particle energies.

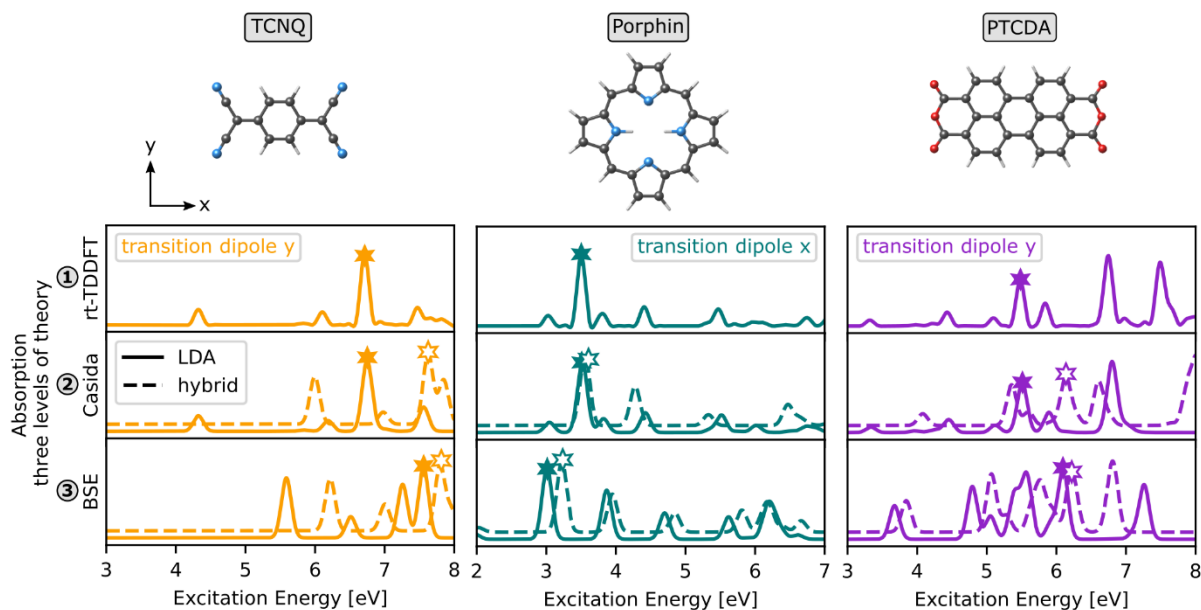


Figure 4.3: (top) Geometries of the three molecules used in our investigation (TCNQ, Porphin and PTCDA). (bottom) Optical absorption spectra of the three molecules projected along a specific direction of the transition dipole in accordance with ref.[44]. The spectra are obtained at three different levels of theory (real-time TDDFT with adiabatic LDA, Casida formalism of linear response TDDFT and GW+BSE). The many-body correction is applied on top of a LDA and hybrid functional (CAM-B3LYP) ground state.

Dependency of exPOT on the Underlying Excited State Description

Within our theoretical means, GW+BSE on top of a CAM-B3LYP ground state is expected to yield the most sophisticated description of the electronic properties of the molecules. On the example of TCNQ, this is indeed confirmed when comparing the calculated quasi-particle energies of the frontier orbitals (HOMO and LUMO) to experimentally determined ionization potential (HOMO) and electron affinity (LUMO). The GW corrected values (IP = 9.3 eV and EA = 3.0 eV) agree well with their experimental gas phase counterparts (IP = 9.6 eV [269] and EA = 3.3 eV [270]). For comparison LDA results in the expectedly large deviation (IP = 7.3 eV and EA = 5.9 eV). Utilizing BSE, we are also able to satisfactorily predict the optical spectrum, where the first excited state with appreciable oscillator strength is placed at 3.2 eV (polarised in x-direction and therefore not shown in Figure 4.3) compared to 3.1-3.2 eV in experiments (only slightly dependent on the solvent environment). LDA underestimates the transition with an energy of 2.8 eV, nonetheless, is still in reasonable agreement presumably due to a fortuitous cancellation of errors.

We now turn to the question, of how the underlying description of the excited state affects the predictions of “exPOT” in terms of kinetic energy spectra and photoemission angular distribution. Figure 4.4 summarizes the exPOT simulation of TCNQ according to Equ. 4.48 building upon the CAM-B3LYP orbitals, GW energies and BSE absorption coefficients. Applying Equ. 4.48, we obtain the k-resolved photoemission intensity distribution over the whole range of calculated excitons. Here, in coordination with the real-time TDDFT simulation of the pump-probe process, we focus our analysis on the specific excitation marked with a star in Figure 4.3 (dashed line, bottom panel). For the region of the transition around 7.8 eV, Figure 4.4a shows the simulated absorption and exPOT spectrum. For the excited state pumped with 7.8 eV, we observe notable photoemission intensity at three different kinetic energies. Recalling the energy conservation term in Equ. 4.48, this finding reflects the multiple hole contributions to the exciton wavefunction. The differences between the kinetic energies relates to the differences between the quasi-particle energies and, therefore, suggests contributions from the HOMO, HOMO-1 and HOMO-2. Furthermore, at each kinetic energy, we extract an ARPES map displaying a different momentum fingerprint (Figure 4.4b). Relating this again to Equ. 4.48, the intensity distribution can be associated with the states of the electron for a specific hole contributing to the exciton wave function. In that way, exPOT disentangles the single-particle contributions of the exciton wave function. We list the contributions of the specific exciton at 7.8 eV of our BSE calculation in Table 4.1. Note that, with the three single-particle contributions all differing in their hole and electron states, TCNQ corresponds to “case b” of the prototypical exciton structures introduced in Figure 4.1

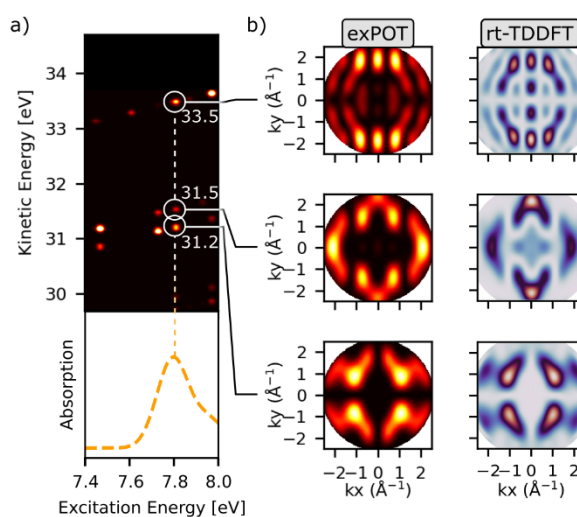


Figure 4.4: a) Photoemission intensity of excited states in TCNQ simulated with the exPOT method based on GW+BSE calculations. b) Simulated momentum maps extracted at the regions indicated in a) compared to maps obtained from real-time TDDFT calculated within LDA.

Table 4.1: Single particle contributions (valence \rightarrow conduction) and their weight for the excited state of TCNQ marked with a star in Figure 4.3 as obtained from LDA and GW+BSE on top of CAM-B3LYP.

BSE@CAM-B3LYP, $E_{\text{ex}}=7.8\text{eV}$		LDA, $E_{\text{ex}}=6.7\text{eV}$	
v \rightarrow c	c^2	v \rightarrow c	c^2
H \rightarrow L+12	0.29	H \rightarrow L+12	0.08
H-1 \rightarrow L+1	0.10	H-1 \rightarrow L+1	0.36
H-2 \rightarrow L+2	0.32	H-2 \rightarrow L+2	0.43

Building the bridge to our analysis in ref.[44], we compare the exPOT momentum maps based on BSE@CAM-B3LYP to maps obtained from rt-TDDFT (Figure 4.4b). Within rt-TDDFT, the photoemission process is mimicked directly without relying on the plane-wave final state approximation of exPOT. This advantage, however, comes currently at the cost of resorting to adiabatic LDA to describe the excited state landscape. In ref.[44], we have already shown that the plane-wave final state is an adequate approximation in the case of the three molecules TCNQ, porphin and PTCDA. There are only marginal differences between maps predicted from rt-TDDFT and exPOT on the same level of LDA. Figure 4.4 now focuses on maps obtained from different methods *and* at different levels of theory for describing the initial excited state, namely, LDA (rt-TDDFT) and BSE@CAM-B3LYP (exPOT).

In rt-TDDFT, we likewise excite the transition marked with a star in Figure 4.3 (top panel). Within the LDA description of the optical absorption, the transition peaks at 6.7 eV. Analogue to our exPOT simulation, we find photoemission intensity at different kinetic energies. The momentum maps corresponding to these energies are displayed to the right of Figure 4.4b and the single-particle contributions of the excitation are given in Table 4.1. Comparing the momentum maps resulting from both simulation approaches, we note strong similarities which may come as a surprise given the largely different excitation energies. In particular, we want to emphasize two observations. First, important for the evaluation of the energy conservation, the three most prominent contributions to the exciton wavefunction are described by the same hole configurations as with BSE. Second, after accounting for the reordering of the energy levels between the calculation methods, also the predicted momentum maps are in good agreement. Thus, the results of both approaches lead us to a similar interpretation. Namely, we can expect to observe momentum maps of distinct character at three kinetic energies corresponding to holes in the HOMO, HOMO-1 and HOMO-2.

At this point, we briefly want to mention another interesting feature of exPOT, which becomes apparent from Figure 4.4a. Focusing on the exciton with smaller excitation energy around 7.5 eV, we find that our BSE calculation suggests a negligible oscillator strength close to zero. It is a so-called dark exciton. Nonetheless, our exPOT formalism based on the whole excitation spectrum provides access also to this exciton predicting its photoemission intensity. While experiments should not be able to directly pump and, subsequently, probe the electronic structure of this specific excited state, signatures of dark excitons may appear following relaxation processes from higher lying excitons during time-resolved ARPES.

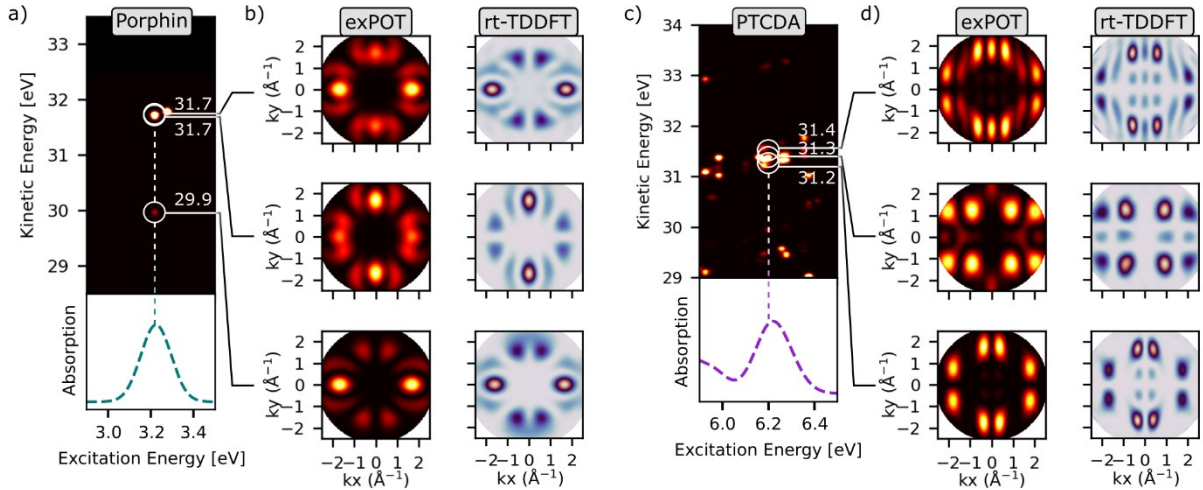


Figure 4.5: a) and c) Photoemission intensity of excited states in porphin and PTCDA, respectively, simulated with the exPOT method based on GW+BSE calculations. b) and d) Simulated momentum maps extracted at the regions indicated in a) and c) compared to maps obtained from real-time TDDFT calculated within LDA.

Next, we analyse the marked excitons of porphyrin and PTCDA in an analogue way to TCNQ. The corresponding photoemission spectra are summarized in Figure 4.5 and the single-particle contributions of the investigated excited states are given in Table 4.2. Starting with the BSE calculation of porphin, we focus on the exciton at 3.2 eV. For the energy region of the transition, Figure 4.5a shows the simulated absorption and exPOT spectrum. In accordance with the most prominent single-particle contributions to this excitation, exPOT predicts notable photoemission intensity at two kinetic energy regions. First, the strongest intensity relates to hole contributions from the nearly degenerate HOMO and HOMO-1 of porphin. Second, at a 2 eV lower kinetic energy, we find intensity stemming from a hole in the HOMO-3. Extracting the exPOT momentum maps at these kinetic energies, we can compare the electronic parts of the involved single-particle transitions (Figure 4.5b). Corresponding to the HOMO, we find intensity patterns characteristic for the LUMO+1, and for the HOMO-1 features of the LUMO. In this regard, it is important to note that, to mimic energy resolution of experimental data, we have evaluated Equ. 4.48 on a coarse kinetic energy mesh (0.05 eV). Consequently, as both hole states are very close in energy, the momentum maps in Figure 4.5b are superpositions of both electronic orbital contributions. This is a result of the *implementation* of exPOT and not of the formalism itself. More importantly, we find the LUMO+1 emission feature again at the kinetic energy of the HOMO-3. Thus, for the excitation of porphin with 3.2 eV, exPOT suggests that the same emission signature (LUMO+1) is observable at two different kinetic energies. Recalling Figure 4.1, we have introduced such a behaviour as “case c”. Our finding is fully confirmed by rt-TDDFT calculations (right of Figure 4.5b and Table 4.2). At the level of LDA, the exciton peaks at 3.5 eV but equally shows single-particle transition from the HOMO-3 *and* HOMO into the LUMO+1. Note that the presented rt-TDDFT ARPES intensities of ref.[44] have been projected onto the respective ground state orbitals to avoid the superposition of energetically close orbitals.

Turning to PTCDA, we study the bright exciton at 6.2 eV and analyse the simulated exPOT spectrum in Figure 4.5c. Out of the multiple intensity peaks for this exciton, we want to specifically highlight photoemission intensity at kinetic energies relating to the HOMO-2, HOMO-3 and HOMO-4. These hole states can be associated with the most predominant single-particle contributions in Table 4.2. The corresponding exPOT momentum maps show distinct

ARPES features (left of Figure 4.5c), which are also recovered in rt-TDDFT calculations (right of Figure 4.5c). In contrast to the previously discussed excitons, the emission patterns cannot be ascribed to a single electron state. For instance, for the hole in the HOMO-3, the electron is majorly distributed between the LUMO+3 *and* the LUMO+2 (cf. Table 4.2). Following Equ. 4.48, the exPOT momentum map can best be described by a coherent sum over the unoccupied orbitals. Consequently, the case of PTCDA demonstrates “case d” in the introduction.

Table 4.2: Single particle contributions (valence \rightarrow conduction) and their weight for the excited states of porphin and PTCDA marked with a star in Figure 4.3 as obtained from LDA and GW+BSE on top of CAM-B3LYP.

Porphin			
BSE@CAM-B3LYP, $E_{\text{ex}}=3.2\text{eV}$		LDA, $E_{\text{ex}}=3.5\text{eV}$	
v \rightarrow c	c^2	v \rightarrow c	c^2
H-1 \rightarrow L	0.50	H-1 \rightarrow L	0.36
H \rightarrow L+1	0.45	H \rightarrow L+1	0.27
H-3 \rightarrow L+1	0.08	H-3 \rightarrow L+1	0.25

PTCDA			
BSE@CAM-B3LYP, $E_{\text{ex}}=6.2\text{eV}$		LDA, $E_{\text{ex}}=5.5\text{eV}$	
v \rightarrow c	c^2	v \rightarrow c	c^2
H-3 \rightarrow L+3	0.57	H-3 \rightarrow L+3	0.40
H-4 \rightarrow L+1	0.08	H-10 \rightarrow L+1	0.12
H-3 \rightarrow L+2	0.07	H-2 \rightarrow L+14	0.11
H-2 \rightarrow L+14	0.06	H-3 \rightarrow L+2	0.03

THM: For the three molecules TCNQ, porphin and PTCDA, we find that, even though the absorption spectrum is calculated at different levels of theory (LDA vs. GW+BSE), simulation of pump-probe photoemission with either real-time TDDFT or the exPOT method give consistent results.

Before concluding this chapter, we want to draw attention to an open question. So far, we have deliberately focused on the excitons with the strongest oscillator strengths in the absorption spectra of our molecules. Perhaps biased by this decision, we have found good agreement between the simulations based on LDA and GW+BSE. However, staying with our working example TCNQ, the previously investigated exciton is not the only allowed excitation with a transition dipole in the y-direction. In fact, at lower energies, we observe two more states, both in the LDA as well as in the BSE calculation (labelled S1 and S2 and marked with a circle and a diamond in Figure 4.6), which we want to briefly investigate in more detail. Their predominant electron-hole contributions are listed in Table 4.3, and the simulated momentum maps of these excitons are shown for both levels of theory at the bottom of Figure 4.6. Different to Figure 4.5, where we have solely concentrated on the pattern of arising emission features, the maps in Figure 4.6 are also compared on an absolute intensity scale. In the framework of exPOT in Equ. 4.48, the intensity of an emission feature majorly depends on the excitation coefficient of the respective single-particle transition and, thus, on the contribution to the exciton wave function as determined by the underlying excited state calculation. Note that the molecular orbitals change their order when going from LDA to GW@CAM-B3LYP and we have corrected the labelling accordingly.

The first optically allowed excited state S1 is predicted at 4.3 eV with LDA and 6.2 eV with BSE@CAM-B3LYP, respectively. At both levels of theory, the strongest contribution to the exciton wave function consists of a transition into the LUMO. Consequently, most of the photoemission intensity is distributed in a momentum map with the characteristic features of the LUMO (maps top row in Figure 4.6). The second strongest contribution is described by completely different single-particle transitions. However, the excitation coefficient of these contributions and, therefore, the intensity of the momentum map is already small – probably too small to be resolved in experiment (maps bottom row in Figure 4.6). Hence, we might argue that, in a hypothetical comparison with experiments, both LDA and BSE would lead to the same interpretation of the measured data.

In the case of the second optically allowed state S2 (6.2 eV in LDA and 7.0 eV in BSE), the differences between the methods become more apparent, although the excited state energies are in better agreement compared to S1. Employing BSE, the momentum map with the highest photoemission intensity displays signatures of the LUMO+1 of TCNQ. In contrast, in LDA, the S2 exciton is dominated by a transition into the LUMO+12, resulting in distinctly different ARPES features (top row in Figure 4.6). Note that, in LDA, we do indeed find the transition into the LUMO+1, however, only as the second strongest single-particle contribution. The corresponding photoemission signal is already comparably weak (bottom row in Figure 4.6). For the absorption peak S2, simulating the photoemission spectrum within LDA and BSE results in different predictions for experiments. While the differences in the description of the optical spectra between LDA and BSE might not be surprising, their influence on the simulated exPOT photoemission spectra should be kept in mind when comparing calculated to measured data.

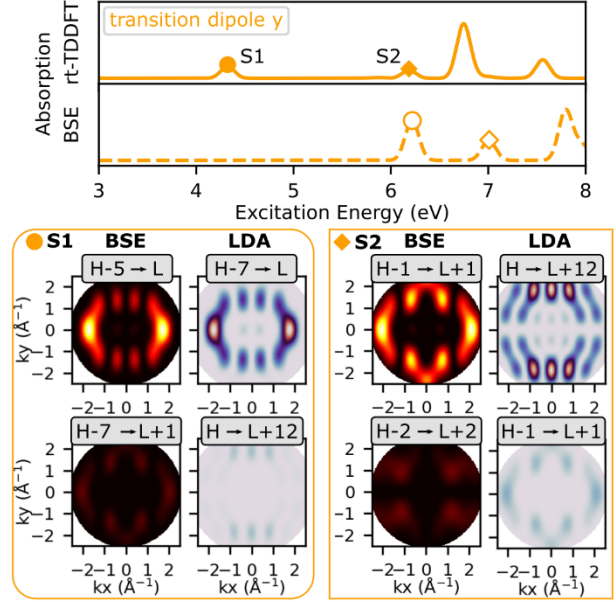


Figure 4.6: (top) Absorption spectrum of TCNQ projected along the y -direction of the transition dipole calculated with LDA and GW+BSE@CAM-B3LYP. The two allowed states with lowest energy are marked with a circle (S1) and a diamond (S2). (bottom) Momentum maps for exciton S1 and S2. For each exciton, maps are shown for the single-particle contributions with the two largest excitation coefficients.

Table 4.3: Single particle contributions (valence \rightarrow conduction) and their weight for the excited states S1 and S2 of TCNQ marked in Figure 4.6 as obtained from LDA and GW+BSE on top of CAM-B3LYP.

BSE@CAM-B3LYP, $E_{\text{ex}}=6.2\text{eV}$		LDA, $E_{\text{ex}}=4.3\text{eV}$	
$v \rightarrow c$	c^2	$v \rightarrow c$	c^2
H-5 \rightarrow L	0.91	H-7 \rightarrow L	0.95
H-7 \rightarrow L+1	0.03	H \rightarrow L+12	0.03
BSE@CAM-B3LYP, $E_{\text{ex}}=7.0\text{eV}$		LDA, $E_{\text{ex}}=6.2\text{eV}$	
$v \rightarrow c$	c^2	$v \rightarrow c$	c^2
H-1 \rightarrow L+1	0.80	H \rightarrow L+12	0.79
H-2 \rightarrow L+2	0.17	H-1 \rightarrow L+1	0.06

4.3 Excited States in C₆₀ Aggregates

4.3.1 Introduction

In the previous section, we have introduced and analysed the exPOT method merely on a theoretical basis. In this section, we take the next natural and attempt a comparison with real-life pump-probe experiments. Organic semiconductors should be a field of research greatly benefiting from such a technique. Over the last years, major experimental and theoretical efforts have been directed towards the realization of optoelectronic devices based on molecular crystals, striving for applications in light emitting diodes or photovoltaics [271–276]. The basis of those investigations is built upon a thorough knowledge of the optical excitations in the organic material. Time-resolved ARPES enables further deepening of this understanding as not only the time evolution of excited states in molecular films can be monitored, but simultaneously the exciton wave function is imaged in momentum space [42,43,277].

In the search for suitable light-active materials, the fullerene molecule (C₆₀) has become a rising star soon after its discovery – perhaps also partly due to its resemblance with a soccer ball. Anyway, the molecule has been recognized with unique electronic properties. Among others, several studies have focused on the absorption of C₆₀ in thin films [278–280], revealing excited states different to the single molecule and, for instance, of great importance for mediating charge separation in organic solar cells [281–283]. These condensed phase phenomena are now slowly unravelled with the help of increasingly evolved computational models [281,284,285]. Contributing to the pool of investigations, our goal is to employ exPOT to a multilayer of C₆₀ and, in the process, introduce a new way how to disentangle the exciton landscape of organic semiconductors.

Article Information and Author Contribution

In the following, I summarize the computational background of the article [45]. The project was conceptualized by **G. S. Matthijs Jansen** and his student **Wiebke Bennecke**, who also conducted the main experiments and drafted the manuscript. I was responsible for the calculations, analysing the computational results and in writing the theoretical section.

Disentangling the multiorbital contributions of excitons by photoemission exciton tomography

Wiebke Bennecke,¹ Andreas Windischbacher,² David Schmitt,¹ Jan Philipp Bange,¹
Ralf Hemm,³ Christian S. Kern,² Gabriele D'Avino,⁴ Xavier Blase,⁴ Daniel
Steil,¹ Sabine Steil,¹ Martin Aeschlimann,³ Benjamin Stadtmüller,^{3,5} Marcel
Reutzler,¹ Peter Puschnig,² G. S. Matthijs Jansen,^{1,*} and Stefan Mathias^{1,6,†}

Figure 4.7: Header of the article [45] including all contributing authors. The manuscript is available on arXiv.

4.3.2 Results and Discussion

Investigated System

As we have discussed in the previous chapter 4.2, the level of theory, on which we base the evaluation of exPOT, may influence the interpretation of the subsequent photoemission simulation. It is, therefore, worthwhile to revisit some basic electronic properties of a single C_{60} molecule [286,287] and assess their dependency on theoretical approximations, before investigating the more complex case of C_{60} multilayer films. Figure 4.8 reviews the orbital energies of a single molecule calculated on different levels of theory. With an increasingly involved description, the energy gap between the occupied and unoccupied levels (HOMO and LUMO) widens from 1.6 eV with LDA and GGA over to 2.9 eV for the hybrid functional PBE0 to a value of 5.1 eV after GW correction. Well known as a test molecule in method comparisons [257,288], the quasi-particle energies of C_{60} within the many-body framework compare nicely to the experimentally determined ionization potential and electron affinity of gas phase C_{60} (marked with a star in Figure 4.8) and its energy gap of 4.9 eV [289]. For our project, we have therefore decided to utilize the good agreement of GW with experiment.

A closer look at the frontier orbitals reveals more details about the molecule (Figure 4.9a). Though simply referred to as HOMO or LUMO (or shorthand H and L, respectively) so far and also in the following discussion, each orbital of C_{60} is, in fact, comprised of several degenerate energy levels. The degree of degeneracy of each orbital is determined by the symmetry of the overall molecule. C_{60} being a highly symmetric 3-dimensional ball exhibits icosahedral symmetry and is described by the symmetry operations of the point group I_h . As a consequence, its orbitals transform according to the irreducible representations, Γ_i , of this point group, each having a respective degree of degeneracy. In particular, the HOMO-2 (irreducible representation h_g) is 5-fold degenerate, the HOMO-1 (g_g) 4-fold, the HOMO (h_u) again 5-fold and the LUMO (t_{1u}) and LUMO+1 (t_{1g}) are both 3-fold degenerate. Moreover, note that the levels of the HOMO-2 and HOMO-1 are closer in energy and hard to distinguish in experiment. Thus, they are often treated as one orbital [290–292], even though they are formally derived from two different irreducible symmetry representations.

Most importantly for our investigation, the above symmetry considerations can help us to get a better insight into the excited state landscape of fullerene. Thus, in the following, we will give a brief excursion about the connection of symmetry and absorption spectra. For an optical transition to be allowed, we have to find a non-zero probability for the transition from a molecular ground state, ψ_g , to an excited state, ψ_e . In quantum mechanics, this transition probability relates to the absolute square of the transition dipole moment d_{eg} given as

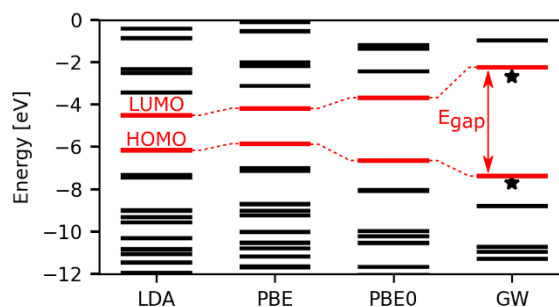


Figure 4.8: Energy levels of a single C_{60} molecule calculated at different levels of DFT (LDA, PBE and PBE0) and after GW correction on top of PBE0. The evolution of the frontier orbitals (HOMO and LUMO) is illustrated in red. The stars mark the experimental ionization potential and electron affinity of C_{60} [289].

$$\mathbf{d}_{eg} = \int \psi_e^* \boldsymbol{\mu} \psi_g \, d\tau \quad \text{Equ. 4.49}$$

where both states are coupled by the electric dipole moment operator, $\boldsymbol{\mu}$, and integrated over the whole space.

Evaluating the symmetry of the mathematical objects in Equ. 4.49, we can deduce, when this integral *has to* vanish [287]. In a nutshell, only integrand functions, which are fully symmetric, i.e.: do not change under the symmetry operations of the molecule's point group, have a chance to equal a value other than zero for \mathbf{d}_{eg} . Employing group theory, the symmetry representation of the object $\psi_e^* \boldsymbol{\mu} \psi_g$ corresponds to the direct product of the irreducible representations of its components, ψ_e , $\boldsymbol{\mu}$, ψ_g . Specifically for C_{60} , the non-degenerate, closed shell electronic ground state, ψ_g , of the molecule has A_g symmetry. The symmetry of any excited state, ψ_e , is given by the direct product of the respective hole and electron states, i.e.: in terms of single-particle excitations $\Gamma_{HOMO-n} \otimes \Gamma_{LUMO+m}$. Lastly, in the icosahedral point group, the electric transition dipole transforms according to the irreducible representation t_{1u} . In the case of C_{60} , the symmetry of the integrand $\psi_e^* \boldsymbol{\mu} \psi_g$ can, thus, be determined with the following expression (Equ. 4.50):

$$\Gamma_{\psi_e} \otimes \Gamma_{\boldsymbol{\mu}} \otimes \Gamma_{\psi_g} = \Gamma_{HOMO-n} \otimes \Gamma_{LUMO+m} \otimes T_{1u} \otimes A_g. \quad \text{Equ. 4.50}$$

As multiplication with the fully symmetric representation A_g does not change the symmetry of the function, Equ. 4.50 effectively reduces to $\Gamma_{HOMO-n} \otimes \Gamma_{LUMO+m} \otimes T_{1u}$. To fulfil our initial

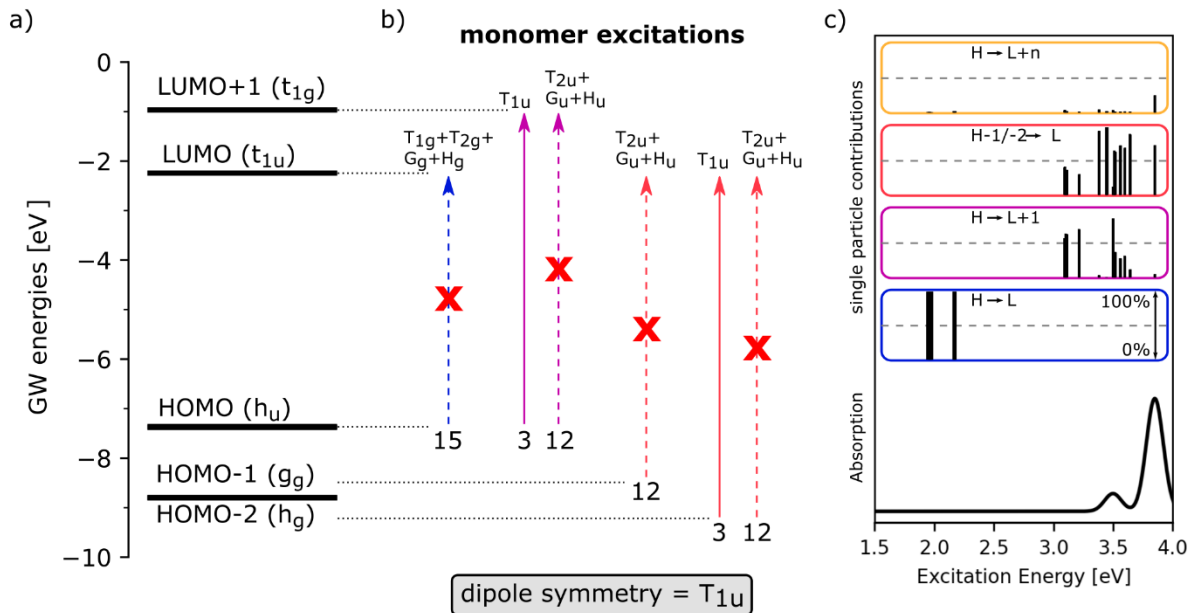


Figure 4.9: a) GW quasi-particle energy levels of a single C_{60} molecule. The frontier orbitals are labelled according to their irreducible symmetry representation of the point group I_h . b) Lowest-energy optical excitations in C_{60} in terms of transitions between the occupied and unoccupied orbitals of a). The irreducible characters and degeneracy of each transition is given. Solid arrows mark symmetry allowed transitions, dashed arrows with red cross mark symmetry forbidden transitions. Note that the arrows from HOMO-1 and HOMO-2 deliberately have different length to distinguish the contributions from the degenerate orbitals. c) Bottom panel displays the absorption spectrum of a single C_{60} molecule calculated with GW+BSE. Panels above show the weight of the single-particle contributions to each exciton wave function grouped into HOMO \rightarrow LUMO, HOMO \rightarrow LUMO+1, HOMO-1/-2 \rightarrow LUMO and HOMO \rightarrow higher lying LUMOs (LUMO+n) transitions.

condition, this direct product must again contain the fully symmetric representation A_g for the integrand $\psi_e \mu \psi_g$ to be non-zero and the transition $H-n \rightarrow L+m$ to be allowed.

Exemplifying Equ. 4.50, the irreducible characters of the lowest-energy optical transitions in a single C_{60} molecule are given in Figure 4.9b together with the predicted degeneracy of the excitons. For instance, following the above symmetry arguments, the HOMO-LUMO transitions, i.e.: all 15 possible ones, are found to be forbidden. In fact, from all possible excited configurations involving the (degenerate) frontier orbitals HOMO-2 to LUMO+1, only three $H \rightarrow L+1$ and three $H-2 \rightarrow L$ transitions satisfy the symmetry conditions and should be observable in absorption spectroscopy.

Putting the group theoretical considerations to a test, Figure 4.9c shows the results of a BSE calculation of a single C_{60} molecule based on our calculated GW energies. The bottom panel displays the absorption spectrum which includes a Gaussian broadening of 0.1 eV. The four framed panels above group the excitons into four categories according to the single-particle energy levels, which contribute to the optical transitions. The first 15 excitons at around 2 eV are indeed described by $H \rightarrow L$ excitations with no oscillator strength. Interestingly, they are further divided into two groups, where five configurations belonging to H_g symmetry can be found at slightly higher excitation energies. Then, 42 excitons follow in the energy range between 3 and 4 eV. In this assembly, three excitations, predominantly described by $H \rightarrow L+1$ contributions are responsible for the small absorption feature at 3.5 eV. The most pronounced absorption feature resulting in the peak at 3.9 eV arises from three excitons, which are a mixture of $H-2 \rightarrow L$ transitions with transitions from the HOMO to higher lying LUMO states. Altogether, we find 57 excitons up to excitation energies of 4 eV, which we can directly associate with the group-theoretical analysis of the transitions in Figure 4.9b.

It is interesting to note that symmetry is also able to make some statements on the strength of the absorption [286,293–295]. Transitions involving orbitals with fewer nodes, i.e., states with smaller angular momentum, will have greater overlap in phase between the wave functions and hence a stronger transition dipole. Applying this statement to C_{60} , the transition $H-2 \rightarrow L$ can be associated with the angular momenta $l = 4$ to $l = 5$ in the point group I_h , while $H \rightarrow L+1$ corresponds to $l = 5$ to $l = 6$. Accordingly, the former transition should show larger oscillator strength – a fact, that we also find in the numerical BSE results.

Comparing our GW+BSE results to other absorption spectra from the literature, we find varying predictions for the two lowest optically-allowed transitions. Depending on the level of theory, the symmetry allowed excitations are either placed at 3.0 and 3.8 eV (CNDOL [296]), 2.8 and 3.5 eV (GGA [284]), 3.3 and 4.2 eV (hybrid functional [281]) or 3.5 and 3.9 eV (screened range separated hybrid functional [285]). Likewise, absorption spectra of the molecule have been measured under different working conditions [284,297–301], providing a range of absorption peaks for validation of the theoretical methods. Depending on the data set, the *first* symmetry allowed transition $H \rightarrow L+1$ has been ascribed to a small shoulder varying between 3 and 3.5 eV. More unanimously, literature agrees on a first well resolved peak at 3.8 eV, attributed to the *second* symmetry-allowed transition $H-2 \rightarrow L$. Furthermore, experimental spectra show an absorption band at 5.0 eV from a $H \rightarrow L+3$ transition, which we have not explicitly discussed here. Comparing these values to our GW+BSE calculation ($H-$

$2 \rightarrow L$ at 3.9 eV and $H \rightarrow L+3$ at 5.1 eV), we are confident that we can correctly capture the optical properties of a single C_{60} molecule in the gas phase.

Optical Properties of C_{60} Aggregates

Building upon our understanding of the optical transitions in an isolated C_{60} molecule, we will next consider excitations in C_{60} aggregates. We start by investigating C_{60} clusters of different intermolecular separation and increasing size. The obtained absorption spectra are summarized in Figure 4.10, where the top panel displays the already discussed spectrum of a single molecule as reference. In a first step and to test the reliability of our computational approach, we compare our reference spectrum to the absorption of an aggregate of two C_{60} molecules (denoted as dimer), in which the two molecules are placed apart by 20\AA . Such a distance is sufficient to prevent interaction between the two C_{60} units and, accordingly, we retain the absorption spectrum of a single molecule. The characterization of the single particle contributions leads to analogous results as the analysis in Figure 4.9c for only one C_{60} molecule, with $H \rightarrow L+1$ and $H-2 \rightarrow L$ transitions being responsible for the two major absorption features.

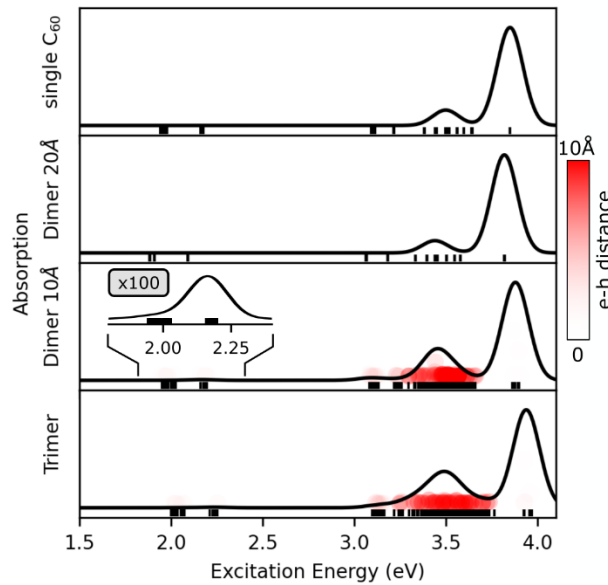


Figure 4.10: Absorption spectra of C_{60} clusters of different size (one, two or three molecules) as obtained from GW+BSE. Inset shows a 100x magnified detail of the dimer absorption spectrum. The black bars mark all calculated excitation energies. The red circles specifically mark the position of charge-transfer excitons, where in an ideal case electron and hole sit separately on two different molecules.

Decreasing the spacing in the C_{60} dimer to the intermolecular distance found in a periodic multilayer (10\AA) notably affects the excited state landscape of our cluster. First, as shown in the inset in Figure 4.10, the close distance between the molecules breaks the perfect icosahedral symmetry of each C_{60} subunit making the $H \rightarrow L$ absorption at 2 eV (and likewise all other symmetry-forbidden transitions) weakly allowed. Furthermore, at an energy region of 3.5 eV, new excitons with predominant $H \rightarrow L$ character arise, which contribute to the absorption spectrum but cannot be found for the single molecule or the well separated dimer (Figure 4.9c). To understand the origin of these new transitions and their dependence on the intermolecular distance, we evaluate the spatial extent of the exciton wavefunctions. For this, we analyse the *hole-averaged*

electron density $\rho_i(\mathbf{r}_e)$ and *electron-averaged* hole density $\rho_i(\mathbf{r}_h)$ as in Equ. 4.51 and Equ. 4.52 to obtain the averaged position of electron and hole in our excitons.

$$\rho_i(\mathbf{r}_e) = \int \psi_i(\mathbf{r}_e, \mathbf{r}_h) \psi_i^*(\mathbf{r}_e, \mathbf{r}_h) d\mathbf{r}_h \quad \text{Equ. 4.51}$$

$$\rho_i(\mathbf{r}_h) = \int \psi_i(\mathbf{r}_e, \mathbf{r}_h) \psi_i^*(\mathbf{r}_e, \mathbf{r}_h) d\mathbf{r}_e \quad \text{Equ. 4.52}$$

In all previously characterized transitions, the electron-hole pair is localized on the same molecule, and we consider them as Frenkel-like excitons. In contrast, for the excitations at

3.5 eV, we find electron and hole to be separated between the dimer's subunits (colour-coded red in Figure 4.10). Since electron and hole are located on two *different* C₆₀ molecules, we label these transitions as charge transfer excitons (CT). Note that the appearance of CT excitons in C₆₀ arrangements (or the modelling thereof) critically depends on the intermolecular distance, as also found in literature [302,303]. It is, therefore, beneficial to adopt this parameter from experiment. Including a third molecule in our aggregate does not visibly change the absorption spectrum according to our analysis, except leading to more excited states in the energy region up to 4 eV.

THM: The formation of charge transfer excitons upon optical excitation is induced by aggregation of C₆₀ molecules.

Ultimately, we seek to simulate the absorption of a C₆₀ multilayer. Thus, a small aggregate model will probably not suffice to capture the nature of such a periodic environment. However, a full periodic modelling of the film on the level of GW+BSE has proven to be computationally too demanding. To overcome this challenge, we decided to mimic the surrounding of a C₆₀ film by a discrete polarizable model (accounting for max. 250 molecules), in which we, then, embed a dimer cluster for our high accuracy calculation. Such an approach has already shown to successfully recover periodic properties on a molecular level [304,305]. However, we are aware that this approximation might miss some effects inherent to a periodic array of C₆₀ molecules such as the full excitonic band structure.

In accordance with experiment, the embedding model is built upon an arrangement found in experimental C₆₀(111)-surfaces, where four molecules adopt a 2x2 super-cell as sketched in Figure 4.11a. In this superstructure, three C₆₀ molecules differing in their azimuthal orientation only by 120° rotations (labelled 1, 2 and 3 in Figure 4.11a) are surrounding a fourth molecule (labelled 4). Note that the alignment in such a superstructure has been inferred from STM [306–310], however, besides the uppermost layer of our film, we have little knowledge about the actual rotational orientation or disorder in the layers beneath. Working at low temperatures (80 K), we assume an epitaxial growth of the (111)-surface of the low-temperature *simple-cubic* phase of C₆₀ on the Cu(111) substrate. Considering the unit cell in Figure 4.11a, we can extract six different dimer clusters involving the four C₆₀ subunits. Scanning over the six different arrangements, we find no influence on the quasi-particle energy levels or the absorption spectrum. Therefore, in the following, we will discuss the impact of the embedding on the electronic properties of a C₆₀ dimer exemplary for a cluster of molecule 1 and 2 (dimer1-2, labelling according to Figure 4.11a).

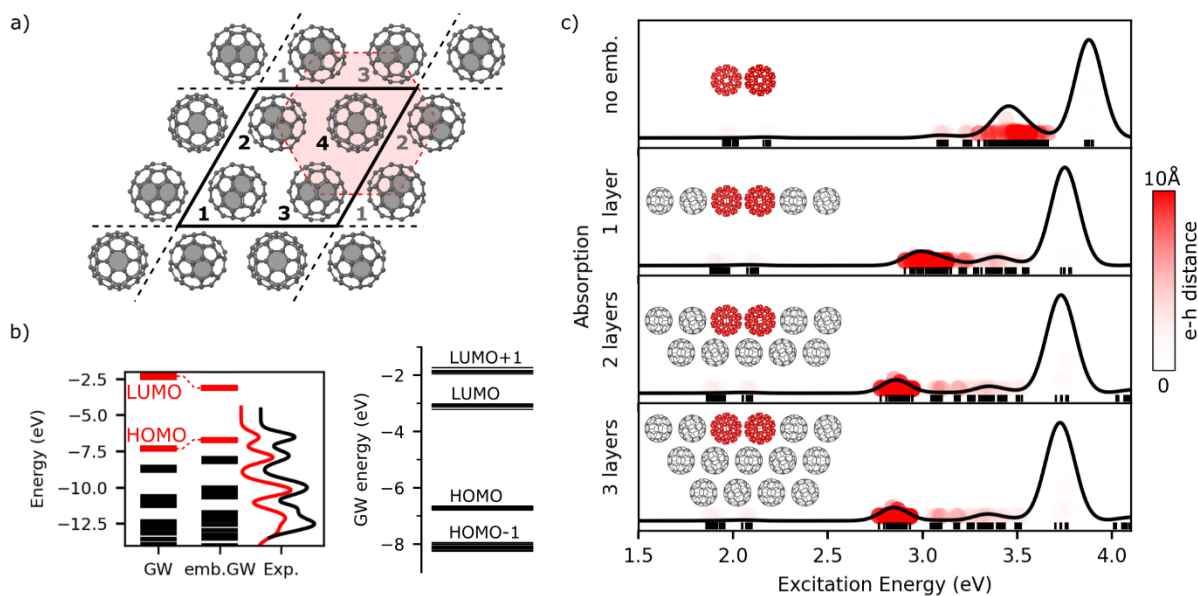


Figure 4.11: a) Unit cell of an experimental C₆₀ multilayer [307,309] consisting of four differently oriented molecules, out of which dimer clusters were extracted for subsequent GW+BSE calculations. Only topmost layer is shown for clarity. b) (left) GW quasi-particle energies of dimer1-2 cluster with and without embedding in a polarizable crystal environment compared to the density of states obtained from photoemission experiments [45] for the multilayer in a). Red curve shows a density of states simulated from GW energies employing a Gaussian broadening of 0.5 eV and a rigid shift of 0.2 eV. (right) Detailed view of the frontier orbitals of an embedded dimer cluster. c) Absorption spectra of a C₆₀ dimer considering an increasing amount of crystal layers in the embedding (systems illustrated by the insets). Red dots in the spectra mark the position of charge-transfer excitons.

At the GW-level, the chosen embedding approach mainly affects the ionization potential and electron affinity of the dimer cluster. As a response to polarization in the crystal environment, it will become easier to remove and add charge to the system, i.e., the ionization potential of the dimer is expected to *decrease*, while its electron affinity *increase*. Indeed, by increasing the number of layers to the C₆₀ film, the HOMO-LUMO gap is reduced by more than 1 eV compared to the isolated dimer (cf. Table 4.4 and illustration to the left of Figure 4.11b). We found that mimicking two layers of the surrounding C₆₀ film in such a way resulted in the convergence of the band gap to within 0.1 eV with a removal energy from the highest valence level of 6.65 eV. This quasi-particle energy is in close agreement with the experimentally determined ionization potential of 6.5 eV [45,291], which is needed to extract an electron from the HOMO of the C₆₀ film. Building upon the GW energies, we have further simulated the density of states of the embedded C₆₀ dimer employing a Gaussian broadening of 0.5 eV (red curve in Figure 4.11b). Comparing this simulation to the density of states as obtained from photoemission experiments [292], we are able to reproduce the experimental findings apart from a small rigid shift of only about 0.2 eV. This gives us confidence in the choice of our embedding environment.

Table 4.4: Ionization potential (IP) and HOMO-LUMO gap (E_{gap}) of a C₆₀ dimer embedded in an increasing amount of layers of the periodic structure as obtained from GW calculations.

Embedding	IP [eV]	E _{gap} [eV]
no	7.21	4.79
1 layer	6.82	3.82
2 layers	6.65	3.43
3 layers	6.61	3.34

A close-up of the calculated energies of the frontier orbitals of the embedded dimer are shown to the right of Figure 4.11b. Note that, here, the finite width of the black bars arises from the multiple energy levels forming bands on the energy axis. Analogous to the single C_{60} molecule we characterize them as HOMO-2 (10 levels), HOMO-1 (8 levels), HOMO (10 levels), LUMO (6 levels), and LUMO+1 (6 levels). Note that we combine HOMO-2 and HOMO-1 in our discussion as HOMO-1/-2, as aforementioned the states of these orbitals are overlapping in energy and are, therefore, not treated separately.

In the optical absorption spectrum in Figure 4.11c, the renormalization of the energy levels upon embedding becomes especially noticeable for excitons associated with a large separation of electron and hole. Modelling an increasing amount of surrounding film layers, these charge-transfer excitations shift by about 0.6 eV from the excitation energy of 3.4 eV in an isolated dimer. In accordance with the convergence of the quasi-particle energies, the excitation energies converge to about 2.8 eV for dimers embedded in 2 or 3 layers of film. For comparison, Frenkel-like excitations are influenced by a maximum of 0.1 eV. Note that the shift to smaller excitation energies should not be mistaken for stronger bound excitons. In the contrary, due to the simultaneous reduction of the band gap, the CT states in the embedded dimer experience a significantly weaker exciton binding energy ($EB = 0.6$ eV) than in the isolated case ($EB = 1.4$ eV). This can be rationalized by the fact that the polarizable environment stabilizes the separation of charge. In conclusion, we have converged ground state as well as excited state properties of a reduced model system to simulate a periodic film.

THM: Embedding of C_{60} clusters in a polarizable environment is essential for the simulation of the excitation spectrum of C_{60} films, especially to predict the excitation energies of charge transfer states. We find that mimicking two layers of surrounding film is sufficient to converge the spectrum.

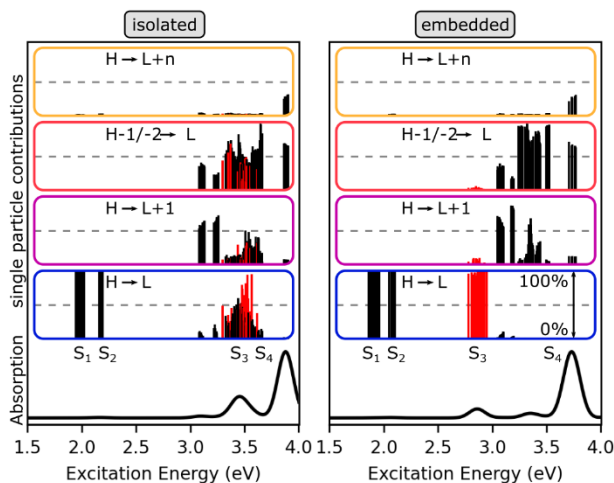


Figure 4.12: Absorption spectrum of an isolated and embedded C_{60} dimer calculated with GW+BSE. S_1 - S_4 denote the four most important exciton bands mentioned in the main text. The panels above the spectra show the weight of the single particle contributions to each exciton wave function grouped into HOMO- \rightarrow LUMO, HOMO- \rightarrow LUMO+1, HOMO-1/-2- \rightarrow LUMO and HOMO- \rightarrow higher lying LUMOs (LUMO+n) transitions. Excitons associated with charge transfer are marked red.

wave function also changes its single particle composition. This is illustrated in Figure 4.12 showing the different contributions for an isolated (left) and embedded (right) dimer cluster. Here, excitations associated with significant charge transfer character are marked red. While in both systems, CT excitons are largely described by transitions from the HOMO to the LUMO ($H \rightarrow L$), they are considerably mixed with excitations from the HOMO-1/HOMO-2 ($H-1/-2 \rightarrow L$) in the isolated dimer. Recall that the energetic level of the hole impacts the energy conservation in Equ. 4.48, and, thus, determines at which kinetic energy we would predict photoemission intensity in a simulated trARPES spectrum. Comparing the contributions in Figure 4.12, we could expect intensity at two different kinetic energies (relating to hole in H and H-1/-2) for the isolated dimer, while simulation of the embedded dimer would only result in one peak (originating from holes in H). These contrasting predictions once again highlight the importance of a critical assessment of the underlying calculations of the optically excited states entering the exPOT formalism.

THM: The embedding approach does not only correct the excitation energies of charge transfer states in C_{60} -films but also the composition of their exciton wave functions. This has direct consequences for the simulation of pump-probe photoemission within the exPOT formalism.

Based on the considerations of the previous sections, we have decided to mimic the experimental C_{60} multilayer as a dimer suitably embedded in two layers of crystalline environment. While so far, the rotation and orientation of the molecular subunits of the dimer with respect to each other had little impact on our findings, we have to recall the sensitivity of ARPES to these parameters. Fortunately, to cover the possible arrangements of the C_{60}

exPOT of C_{60}

Before transitioning to the results of our exPOT simulation, we want to briefly emphasize again the importance of the embedding procedure for the present investigation. As discussed in the introduction, within the quasi-static approximation that is inherent in exPOT's description of the pump-probe photoemission process, the results rely on only two properties of the initial vertical absorption spectrum, namely, the excitation energies and the excitation coefficients, which enter Equ. 4.48 and are important to converge. In the previous section, we have demonstrated how the response of a surrounding environment affects the excitation energies of especially charge transfer excitons. Simultaneous to shifting energetic position, the respective exciton

molecules in the periodic unit cell also in our exPOT comparison, it is sufficient to treat two dimers explicitly. Following the labelling in Figure 4.11a, they consist of the molecules 1-2 and 3-4. Other possible combinations in the crystal (like dimers 1-3, 2-3, 1-4 or 2-4) can be obtained by suitable rotation of either the dimer 1-2 or the dimer 3-4 by 120° . Utilizing the Kohn-Sham orbitals, GW energies and BSE excitation coefficients, we evaluate the photoemission intensity distribution of our excited dimers according to Equ. 4.48. Subsequently, we take the 3-fold rotational symmetry into account and sum over both dimers (Figure 4.13).

At this point, I want to mention an important detail. As a last step to ultimately match experimental data, our predicted maps have to be rotated by 90° . On one hand, in line with many other examples in this thesis, this finding could simply reflect the rotation of the C_{60} molecules on the surface. This interpretation would suggest that our initial starting geometry adapted from STM images from literature [307,309] was not correct. While we have been able to confirm the overall unit cell by LEED measurements, none of our experiments uniquely determines the rotation of the molecules *within* the cell of our multilayer films. On the other hand, I also want to highlight that preliminary real-time TDDFT results for C_{60} suggest the importance of final state effects, which are not included in the plane-wave approximation of exPOT but significantly influence the shape of the ARPES intensity distribution for such three-dimensional molecules [268]. The origin of this 90° rotation discrepancy is currently subject of *ongoing* research. Further experiments as well as comparisons between different methods will hopefully lead to further insights and clarification of the momentum fingerprints of C_{60} .

Keeping this discrepancy in mind, let us continue by discussing the photoemission simulation of the C_{60} film. In accordance with the experimental setup, we consider a probe energy of $h\nu = 26.5$ eV. Furthermore, we include an inner potential to correct for the photoemission intensity variation of 3D molecules along the moment vector component perpendicular to the surface (further details will be discussed below). Note that Equ. 4.48 is given within the Tamm-Dancoff approximation but can in general be extended to include also de-excitation terms. Although our present calculations treat the full BSE Hamiltonian to obtain the absorption spectrum, we found the de-excitation contributions to be marginal (below 0.05%) without affecting Equ. 4.48 and our interpretation.

Finally, application of Equ. 4.48 to the embedded dimer models provides us with a 4D data set of simulated photoemission intensity as a function of the excitation energy Ω , the kinetic energy E_{kin} , and the momentum components (k_x and k_y). We visualize the calculated 4D data $I(\Omega, E_{kin}, k_x, k_y)$ by integrating the intensity of each exPOT momentum map over all k_x and k_y , thereby, reducing it to the 2D data $I(\Omega, E_{kin})$ shown in Figure 4.14a. The intensity distribution reflects what we have already been able to infer from the analysis in Figure 4.12. We find

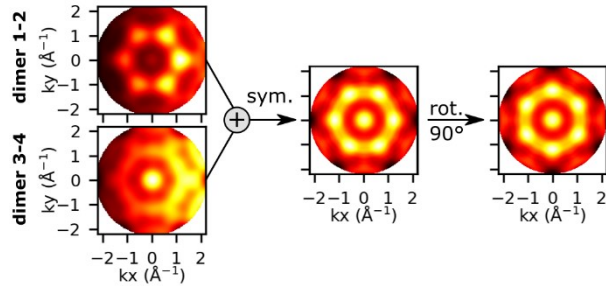


Figure 4.13: Scheme to illustrate the generation of the simulated momentum maps. Maps are obtained for each dimer, which are then added and symmetrized according to the 3-fold symmetry of the crystal. The final maps have to be rotated by 90° to match with experiment.

distinct peaks for the lowest-lying excitons of the initially symmetry forbidden $H \rightarrow L$ transitions (labelled S1 and S2) as well as for the CT excitons of the absorption band S3. Above 3 eV, multiple hole states contribute to the excitation configurations giving rise to the double-line feature with an energy difference of $E(H) - E(H-1/-2)$ between the two kinetic energies. Note that in contrast to the CT excitons, the theoretical description of the Frenkel-like excitons between 3 and 4 eV with hole contribution from the HOMO and the HOMO-1 does not depend on the cluster size or the embedding and, thus in every case, predicts the intensity splitting at two kinetic energies.

Since the optically dark excitons S1 and S2 cannot be excited, the first experimentally accessible exciton band belongs to the aforementioned charge transfer states S3. They can be excited by a light pulse of 2.9 eV. Analysing the measured pump-probe photoemission data, we observe an exciton cascade similar to previous experiments [292]. At first, direct excitation of the exciton S3 feature leads to a photoemission signal at a kinetic energy of 22.8 eV. After some time, additional photoemission intensity builds up at $E_{\text{kin}} = 22.0$ eV and 21.7 eV. We assign the measured data with the help of our calculated photoemission spectrum in Figure 4.14. In our simulation, the band S3 likewise gives rise to a peak at a kinetic energy of 22.8 eV. In addition, the almost dark states S2 and S1 would contribute to a kinetic energy at 22.0 eV and 21.8 eV, thus, fitting nicely to the measurements. From the agreement between experiment and theory, we interpret the cascade after initial excitation of S3 as relaxation to the lower-lying excitons S2 and then S1. Taking momentum maps at the three energies (S1, S2 and S3) may provide further information. We compare the experimental and calculated maps in Figure 4.14b. In all experimental maps, highest intensity is found at a k -radius of 1.5 \AA^{-1} and distributed into six lobes forming the corners of a hexagon. Furthermore, comparing the experimental map of S3

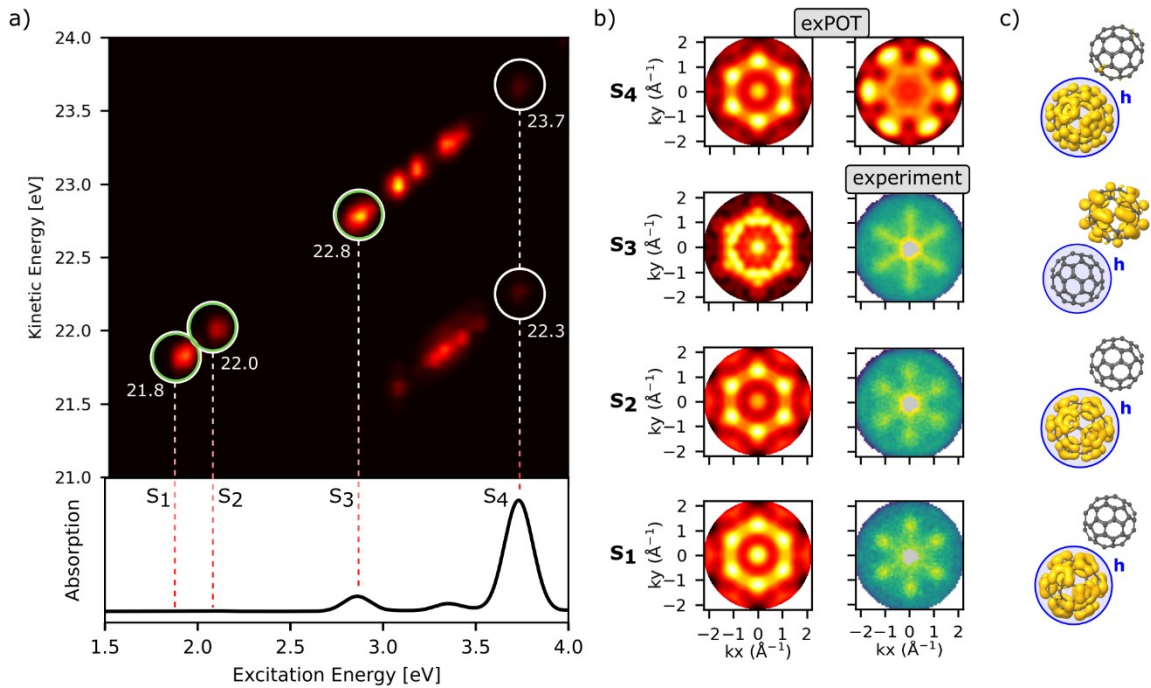


Figure 4.14: a) Photoemission intensity of excited states in a C_{60} multilayer simulated with the exPOT method assuming a probe energy of 26.5 eV based upon GW+BSE calculations assuming an inner potential of 12.5 eV. The periodic film was mimicked within a cluster approach as superposition of two embedded dimers. Four specific intensity regions of the ARPES spectrum (S_1 - S_4) are linked to exciton bands of the absorption spectrum in the panel below. b) Momentum maps extracted in the regions of the four exciton bands. For the excited state S_4 , we predict intensity distribution at two different kinetic energies. The simulated maps of S_1 - S_3 are compared to experimental data. c) Isosurfaces of the integrated electron probability density (yellow) for fixed hole positions on the bottom-left molecular subunit (blue circle) of a dimer.

to the maps at lower kinetic energy, we recognize a slightly more star shaped pattern instead of six separate lobes. In our simulated maps for the S1, S2 and S3 band, we see intensity at a similar k -value (1.4 \AA^{-1}) also distributed in the six corners of a hexagon. For the maps stemming from S1 and S2, the agreement to experiment is convincing. In the case of S3, the simulated momentum map is consistent with the experimental observation that its emission pattern differs significantly from those of S1 and S2, although we can only partially reproduce the experimental star-shape in our simulation. A straightforward reason for the different shape between the three excited states would lie in the different nature of the excitons, i.e.: charge transfer (S3) versus Frenkel-like (S1 and S2). We have illustrated the excitonic nature in Figure 4.14c by computing the averaged electron density (yellow) of each state for hole positions fixed on one C_{60} molecule (blue circle). This visualisation of the BSE data graphically shows the different spatial extent of S1, S2 and S3, which we have already addressed previously. While electron and hole are located on the same molecule for state S1 and S2, the excited electron has transitioned to the neighbouring C_{60} in the case of S3. Note that, as mentioned in the beginning of this section, the 3-dimensional structure of the molecule in conjunction with our approximative description of the photoemission process may also contribute to the difference between experiment and theory.

Even though our simulation suggests numerous other excitons with an excitation energy between 3 and 4 eV, collecting a photoemission signal for these transitions turned out to be not possible in experiment. This may be partly due to the small oscillator strengths, which theory predicts for their initial excitation, resulting in too few excited electrons to be probed efficiently.

In contrast, due to its strong optical oscillator strength, the absorption band S4 should be ideally suited to access in a pump-probe experiment. Moreover, extracting momentum maps out of our simulated data set at the kinetic energies corresponding to the hole in the HOMO ($E_{\text{kin}} = 23.7 \text{ eV}$) and in the HOMO-1/-2 ($E_{\text{kin}} = 22.3 \text{ eV}$) suggests specific momentum patterns (top of Figure 4.14b), which should also be distinguishable in measured data (cf. calculated maps in Figure 4.14b and detail of intensity spectrum in Figure 4.15a).

Turning to experiment, we optically excite the S4 band of the C_{60} film with a pump energy of 3.6 eV. The resulting time resolved photoemission spectrum is shown in Figure 4.15b. Note, how we can see the beginning of the exciton cascade described above. Explicitly comparing energy distribution curves taken closely to the pump pulse (red curve in Figure 4.15c), we find indeed photoemission intensity rising at a kinetic energy of 23.6 and 22.2 eV. The energetic difference of 1.4 eV agrees well with the calculated difference of the GW quasiparticle levels HOMO and HOMO-1, giving us confidence that we have disentangled the different orbital contributions. Note that an almost simultaneous appearance of photoemission at $E_{\text{kin}} = 22.8 \text{ eV}$ suggests a fast relaxation of the S4 exciton to the S3 exciton with relaxation

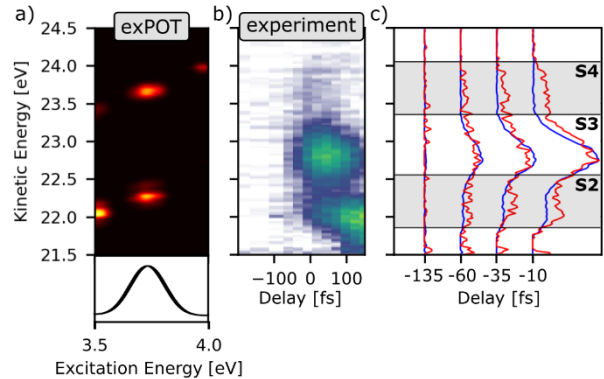


Figure 4.15: a) Detail of the Figure 4.14 showing the photoemission intensity stemming from the excitation S4 simulated with the exPOT method. b) Experimental time-resolved photoelectron spectrum of a multilayer C_{60} pumped with 3.6 eV. c) Energy distribution curves at early delays of time-resolved ARPES experiments pumping with 2.9 eV (blue) and 3.6 eV (red).

times below 25 fs (time resolution of experimental data). For reference, Figure 4.15c includes the energy distribution curves for the measurement with a pump-energy of 2.9 eV (blue curve), where we see intensity rising only at $E_{\text{kin}} = 22.8$ eV. Interestingly, it should also be mentioned that the photoemission signal of the S4 exciton is rather weak, i.e.: has a low signal to noise ratio, which is perhaps counterintuitive to its strong absorption probability. The explanation for this effect could be two-fold: First, the calculation following Equ. 4.48 predicts a fivefold weaker photoemission matrix element for the S4 compared to the other bands. Second, from an experimental perspective, the short lifetime of the state and unwanted space charge effects due to 2-photon photoemission processes further complicate the measurement. Unfortunately, even despite long integration times, it was not feasible to obtain clear angle-resolved data and, therefore, we could not unambiguously identify momentum maps for exPOT analysis.

THM: Employing the exPOT formalism on top of embedded GW+BSE calculations, we are able to explain the time-resolved photoemission spectra of a multilayer film of C_{60} assigning four excitation bands S1-S4. Interestingly, our simulations suggest that single-particle transitions with different hole positions contribute to the band S4, which should reflect in photoemission intensity at different kinetic energies. Pump-probe experiments of S4 confirm this prediction.

Charge Transfer Excitons in exPOT

In the following, we want to elucidate on some peculiarities of the charge transfer region S3, which may set it apart from the Frenkel-like S1, S2 and S4. Recalling the decompositions of the excitons into single particle contributions in Figure 4.12 (right), all three excitonic regions are dominated by $H \rightarrow L$ transitions. However, while the S1 and S2 is solely comprised of these transitions, a small percentage (5-10%) of also the $H \rightarrow L+1$ contributes to the S3. To identify the influence of the $H \rightarrow L+1$ contributions to the simulated S3 photoemission pattern, we evaluated the linear combination of the exciton wave function in Equ. 4.48 with and without the coefficients for the L+1 orbitals. The obtained momentum maps are shown in Figure 4.16 (left: without L+1, middle: full wave function). Excluding the L+1 component decreases the substructure of the momentum feature but does not fully recover the pronounced six lobes, which are characteristic for emission from the LUMO in the S1 and S2 map (and also S4). On

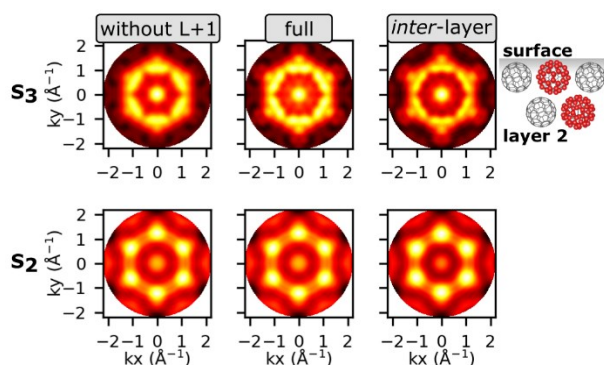


Figure 4.16: Influence of different settings on the momentum maps of S2 (bottom) and S3 (top). (left) Only LUMO coefficients are evaluated in Equ. 4.48. (middle) All coefficients are considered. (right) Dimers comprising of molecules in the first and second layer of the C_{60} film are added.

the one hand, this highlights the impact of supposedly small coefficients to the coherent sum of Equ. 4.48. On the other hand, and more importantly for our investigation, it suggests that simply the charge transfer character of the exciton affects its wave function in a way that is transferred to momentum space. As a reference, the bottom row in Figure 4.16 shows momentum maps of the S2 exciton region, which are composed up to 99% of $H \rightarrow L$. Coefficients smaller than 1% give no notable contribution to the exPOT pattern.

In order to further test the robustness of our theoretical predictions, it is important to recall that up to now, we have assumed that the excitons are located only in the topmost C_{60} layer. The restriction to such *intralayer* excitons arises from our choice of the C_{60} dimer as indicated in Figure 4.11c. While this is a reasonable approximation for Frenkel excitons, charge transfer excitons such as the S3 may not necessarily be confined to one layer. Instead, the charge separation can involve also a C_{60} molecule from the layer beneath, which in the closed-packed (111)-surface is at the same intermolecular distance as the in-plane molecules. As a consequence, the S3 exciton wave function can potentially be distributed by 60° out of the (111)-plane and, further, depends on the (arbitrary) orientation of the molecules in the second layer. To illustrate the influence, we have repeated our exPOT simulation for two *inter-layer* dimers of our embedded two-layer system and added them to the existing map (Figure 4.16 right). While the change is again minor, we do find a narrowing of the pattern, which, for instance, is not present in the momentum map of S2.

THM: Overall, we cannot fully explain the star shape feature of the measured S3 momentum map in our dimer model. However, the analysis of our simulation at least supports the presumption that the shape is a consequence of charge transfer excitons.

Limitations of Our Computational Approach

In the end, we want to address two approximations, which we had to make over the course of the C_{60} project, and their impact on exPOT analysis. The first simplification arises from modelling the periodically extended C_{60} film by a C_{60} dimer embedded into an appropriate dielectric surrounding. As a result, we cannot expect to capture all effects from molecular band dispersion responsible for a periodic substructure in ARPES features. In this regard, note that experiments find the hexagonal dispersion pattern of the C_{60} unit cell mainly in momentum maps of the ground state [290], while it is not apparent in our pump-probe data. Furthermore, the chosen cluster size determines the nature and spatial extent of the observed excitons, and therefore according to our investigation also the ARPES signatures. With these caveats in mind, we seek for a general assessment of the molecular states described by our dimer models in comparison with a periodic calculation. For this reason, we have simulated one layer of the C_{60} unit cell as a periodic monolayer and evaluated the photoemission intensity distribution of the molecular bands. Figure 4.17a compares the momentum maps of the HOMO-1/-2, HOMO and LUMO obtained from the localized Kohn-Sham orbitals of the dimer (top) to the ones from periodic boundary conditions (bottom). The maps of the dimer clusters are symmetrized to account for the possible orientations in the crystal. In the

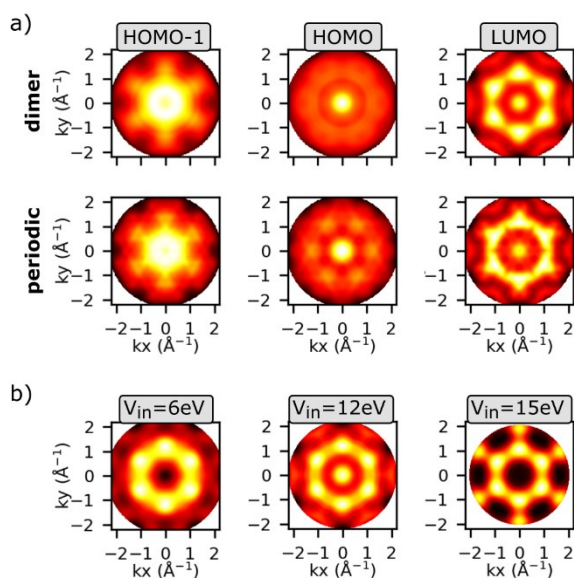


Figure 4.17: a) Momentum maps obtained as a superposition of dimer clusters compared with maps from a full periodic, ground state, calculation. b) Momentum maps of the S1 obtained with different inner potential values V_{in} .

periodic case, we average over the energy of the whole band with a suitable k -broadening to suppress dispersion. While the comparison admittedly concerns only ground state energy levels, the dimer models nicely recover the structures and k -values of the periodic maps, reassuring that they stem from similar states. It can also be noted that the LUMO of already a ground state calculation gives sufficient agreement with the experimentally observed maps.

As a second potential source of errors in our exPOT approach, we want to briefly touch upon the above-mentioned inner potential included in all photoemission simulations of C_{60} . Revisiting momentum conservation during the photoemission process, we have assumed that the momenta of the photoemitted electron parallel to the surface are conserved. However, we cannot assume the same about the momentum, k_z , normal to the surface. In fact, the component k_z has to compensate for a potential step, the so-called inner potential, which the electron experiences when leaving the material. Formally, photoemission experiments could not be simulated without the knowledge about this inner potential [258]. In practice, the photoemission intensity of planar, 2D materials (such as most of our organic molecules) shows little dependency along k_z and, thus, the resulting momentum maps are insensitive to the choice for the inner potential. For 3D molecules and bulk systems, the value is usually determined experimentally. The effect of the inner potential is illustrated in Figure 4.17b, where we show momentum maps of the exciton state S1 simulated with inner potential values of 6, 12.5 and 15 eV. Scanning through a range of inner potentials, the general, hexagonal shape of the ARPES feature does not change. However, the six distinct lobes observed experimentally can best be matched by including a potential of 12.5 eV. This value is in accordance with previous comparisons and fits to experimental C_{60} data [290,311].

4.4 Concluding Remarks

The main interest in this chapter has been the simulation of time-resolved photoemission experiments. Real-time TDDFT using the t-SURFF approach directly simulates the photoemission process of pump-probe experiments and naturally accounts for the pump/probe fields. On the downside, it is computationally very expensive and compromises in the description of *xc*-effects needs to be made, in practice this means, one is restricted to TD-LDA. In the newly introduced exPOT formalism, there is no such restriction regarding the treatment of *xc*-effects. In particular, electron-hole correlations can be accounted for in a very sophisticated way by employing, for instance, GW-BSE calculations. However, exPOT relies on the plane-wave approximation for the final state.

Benchmarking exPOT

In ref.[44], both approaches are shown to match if *xc*-effects are approximated on the *same* level of theory, namely by LDA. Here, we have assessed the sensitivity of the exPOT method towards *different* levels of theory of the underlying excited state calculation. Within exPOT, the photoemission intensity can mainly be related to the single-particle contributions of the exciton wave function, the description of which might be dependent on the level of theory. To this end, we have compared the absorption spectra of three molecules obtained within the framework of rt-TD-LDA and GW-BSE. Although the predicted excitation energies differ due to the different *xc*-description, we still find, in general, good agreement in the subsequently simulated photoemission between both approaches, exPOT and real-time TDDFT.

However, we also want to highlight that, for some excitons, LDA predicts different weights of the single-particle contributions or might simply describe an overall different exciton wavefunction than GW-BSE. Such effects should be kept in mind, when simulating pump-probe photoemission and comparing calculated to measured data. Once it becomes possible to reliably pump and probe intricate exciton structures similar to our examples, we acknowledge that experiments could be useful for benchmarking the excited state calculations.

Excited States in C₆₀ Aggregates

Applying exPOT to a practical example, we have focused on excited states in a multilayer film of C₆₀, relying on the many-body framework of GW+BSE. For computational feasibility, we have mimicked the periodic film as molecular dimers, which are embedded in two layers of the surrounding crystal described by a discrete polarizable model. First, we discuss the optical spectra of fullerene in the gas phase and the effect of the periodic arrangement on charge transfer and Frenkel-like excitons in C₆₀ aggregates. Especially for the former, embedding leads to a significant shift of 0.6 eV to lower excitation energies improving the agreement with experimental spectra.

Then, we combine our calculations with time resolved ARPES measurements to explore the excited state landscape of a real C₆₀ multilayer. Utilizing the exPOT approach of photoemission tomography, we connect the energy and k-resolved intensity distribution to the calculated absorption spectrum identifying four excitonic states. ExPOT analysis also suggests that the momentum image grants information about the spatial extent of the exciton wave function, i.e., its charge transfer character. Furthermore, the experimental data supports our theoretical

predictions that excitons with contributions from multiple holes lead to the appearance of multiple peaks in the photoemission spectrum.

5 Outlook

While each of the previous chapters concludes with a summary of my main computational results, this chapter provides more general conclusions as well as an outlook. First, several of our partners are continuing their work on metal-organic complexes and recently, also extended their ideas to 2D metal-organic networks on surfaces. To put this into context, such networks build the bridge between simple monolayer films of metal-organic complexes and full 3D metal-organic frameworks (MOFs). Hence, control and manipulation of spin and oxidation states of metal-centres and the simulation thereof will be an ongoing quest. Consequently, it will be helpful to deepen our understanding of how well the electronic structure of such systems can be represented with the computationally accessible GGA+U approach. In the investigations to follow, we should be aware of carefully evaluating the influence of the Hubbard parameter \tilde{U} , which depends on the system and the properties we are interested in, as we have seen in our study on gas adsorption. Related to this, we could improve our understanding of the interactions with external ligands by expanding our test set of ligands and conducting complementary experiments. Likewise, I would find it interesting to apply the discussed concepts of gas adsorption to the mentioned 2D networks. Finally, I want to mention that metal-tetrapyrroles are currently considered as attractive target systems for time-resolved pump-probe photoemission experiments. Thus, correctly simulating their ground state properties is a prerequisite for subsequent excited state calculations.

Intensifying our investigation of excited states, the framework of exPOT, which we have touched upon, provides access to the photoemission intensity distributions of all sorts of excitations. In contrast to, e.g., the t-SURFF approach in real-time TDDFT, its application is not restricted to the simulation of bright excitons. We can simulate photoemission for all excited states, which our theoretical level of choice predicts – including dark states. Therefore, the method may prove especially useful for the interpretation of exciton relaxation cascades. In this regard, I want to mention, that our current implementation of exPOT relies on quantum chemistry codes calculating the absorption of molecules in the gas phase. However, as most photoemission experiments target periodic interfaces, it would be a next logical step to also extend the theoretical formalism to a periodic description and simulate the excited states with periodic GW-BSE calculations. It would then, of course, be interesting to revisit our C₆₀ film and further investigate, for instance, the star shape in the momentum map of the charge transfer state and if it indeed originates from periodic effects.

6 List of Publications

- i. M.S. Sättele, A. Windischbacher, L. Egger, A. Haags, P. Hurdax, H. Kirschner, A. Gottwald, M. Richter, F.C. Bocquet, S. Soubatch, F.S. Tautz, H.F. Bettinger, H. Peisert, T. Chassé, M.G. Ramsey, P. Puschnig, G. Koller, Going beyond Pentacene: Photoemission Tomography of a Heptacene Monolayer on Ag(110), *The Journal of Physical Chemistry C*. 125 (2021) 2918–2925.
- ii. H.M. Sturmeit, I. Cojocariu, A. Windischbacher, C. Puschnig Peter and Piamonteze, M. Jugovac, A. Sala, C. Africh, A. Comelli Giovanni and Cossaro, A. Verdini, L. Floreano, M. Stredansky, E. Vesselli, C. Hohner, M. Kettner, J. Libuda, C.M. Schneider, G. Zamborlini, M. Cinchetti, V. Feyer, Room-Temperature On-Spin-Switching and Tuning in a Porphyrin-Based Multifunctional Interface, *Small*. 17 (2021) 2104779.
- iii. T.G. Boné, A. Windischbacher, M.S. Sättele, K. Greulich, L. Egger, T. Jauk, F. Lackner, H.F. Bettinger, H. Peisert, T. Chassé, M.G. Ramsey, M. Sterrer, G. Koller, P. Puschnig, Demonstrating the Impact of the Adsorbate Orientation on the Charge Transfer at Organic–Metal Interfaces, *The Journal of Physical Chemistry C*. 125 (2021) 9129–9137.
- iv. M.S. Sättele, A. Windischbacher, K. Greulich, L. Egger, A. Haags, H. Kirschner, R. Ovsyannikov, E. Giangrisostomi, A. Gottwald, M. Richter, S. Soubatch, F.S. Tautz, M.G. Ramsey, P. Puschnig, G. Koller, H.F. Bettinger, T. Chassé, H. Peisert, Hexacene on Cu(110) and Ag(110): Influence of the Substrate on Molecular Orientation and Interfacial Charge Transfer, *The Journal of Physical Chemistry C*. 126 (2022) 5036–5045.
- v. M. Stredansky, S. Moro, M. Corva, H. Sturmeit, V. Mischke, D. Janas, I. Cojocariu, M. Jugovac, A. Cossaro, A. Verdini, L. Floreano, Z. Feng, A. Sala, G. Comelli, A. Windischbacher, P. Puschnig, C. Hohner, M. Kettner, J. Libuda, M. Cinchetti, C.M. Schneider, V. Feyer, E. Vesselli, G. Zamborlini, Disproportionation of Nitric Oxide at a Surface-Bound Nickel Porphyrinoid, *Angewandte Chemie International Edition*. 61 (2022) e202201916.
- vi. I. Cojocariu, A. Windischbacher, D. Baranowski, M. Jugovac, R.C. de C. Ferreira, J. Doležal, M. Švec, J.M. Zamalloa-Serrano, M. Tormen, L. Schio, L. Floreano, J. Dreiser, P. Puschnig, V. Feyer, C.M. Schneider, Surface-Mediated Spin Locking and Thermal Unlocking in a 2D Molecular Array, *Advanced Science*. 10 (2023) 2300223.
- vii. T. Boné, A. Windischbacher, L. Scheucher, F. Presel, P. Schnabl, M.S. Wagner, H.F. Bettinger, H. Peisert, T. Chassé, P. Puschnig, M.G. Ramsey, M. Sterrer, G. Koller, Orientation, electronic decoupling and band dispersion of heptacene on modified and nanopatterned copper surfaces, *Journal of Physics: Condensed Matter*. 35 (2023) 475003.
- viii. C.S. Kern, A. Windischbacher, P. Puschnig, Photoemission orbital tomography for excitons in organic molecules, *Phys Rev B*. 108 (2023) 85132.

- ix. W. Bennecke, A. Windischbacher, D. Schmitt, J.P. Bange, R. Hemm, C.S. Kern, G. D`Avino, X. Blase, D. Steil, S. Steil, M. Aeschlimann, B. Stadtmueller, M. Reutzel, P. Puschnig, G.S.M. Jansen, S. Mathias, Multiorbital exciton formation in an organic semiconductor, *arXiv* (**2023**).
- x. D.M. Janas, A. Windischbacher, M.S. Arndt, M. Gutnikov, L. Sternemann, D. Gutnikov, T. Willershausen, J.E. Nitschke, K. Schiller, D. Baranowski, V. Feyer, I. Cojocariu, K. Dave, P. Puschnig, M. Stupar, S. Ponzoni, M. Cinchetti, G. Zamborlini, Metalloporphyrins on oxygen-passivated iron: Conformation and order beyond the first layer, *Inorganica Chim Acta*. 557 (**2023**) 121705.
- xi. A. Windischbacher, P. Puschnig, Computational study on the adsorption of small molecules to surface-supported Ni-porphyrins, *Inorganica Chim Acta*. 558 (**2023**) 121719.

7 Method Section

Longer Acenes on Coinage Metals (chapter 2.2)

All calculations were performed within the framework of density functional theory (DFT) using the Vienna Ab Initio Simulation Package (VASP) version 5.4.4. [312,313]. Exchange–correlation effects were described by the functional of Perdew–Burke–Ernzerhof (PBE) [53] and van der Waals contributions treated with the D3 dispersion correction [60]. We utilized the projector-augmented wave (PAW) method [314] together with an energy cutoff of 400 eV. The ionic positions of all structures were optimized until the remaining forces were below 0.01 eV/Å with Gaussian smearing of 0.01 eV. To model the experimental monolayer of 6A on Ag(110) and Cu(110), we adapted the experimentally determined unit cells from our LEED experiments. For the monolayer of 7A on Ag(110), the unit cell with the long axis of 7A along the [001] is based on the experimentally observed low-energy electron diffraction (LEED) structure of 5A on Ag(110) [85], while the unit cell in which 7A lies along the $[1\bar{1}0]$ direction was adapted from the experimental LEED structure of 4A on Ag(110) [102]. For the monolayer of heptacene on Cu(110), the unit cell along the $[1\bar{1}0]$ direction was derived from LEED and STM measurements. The model of heptacene in the [001] direction was constructed accordingly with the same intermolecular distances. All surfaces are simulated within the repeated slab approach using five metallic layers and a 30 Å vacuum layer. To avoid spurious electrical fields, a dipole layer is inserted in the vacuum region [315]. The structure is optimized on a Gamma-centred grid of $5 \times 2 \times 1$ grid of k-points constraining the coordinates of the two bottom Cu layers of the slab. The density of states of the total molecule–metal interface has been projected onto the molecular orbitals of the freestanding molecular layer in its distorted adsorption geometry, termed “molecular orbital projected DOS” (MOPDOS), following Lüftner et al. [316].

To simulate the POT momentum maps, we recalculated the Kohn–Sham energies and wave functions on a denser k-point mesh of $12 \times 5 \times 3$. The one-step model of photoemission [317] was utilized to simulate the angle-resolved photoemission momentum maps under assumption that the wave function of the final state can be described as a plane wave [85]. The simulations were corrected by an exponential damping factor ($\gamma = 0.5 \text{ \AA}^{-1}$ starting 1Å below the molecular monolayer), which takes the mean free path of the photoemitted electrons into account [316].

For the simulation of X-ray photoemission spectroscopy, we utilized the GPAW code (version 21.1.0) [318,319]. The XPS binding energies were calculated on the same level of theory using the delta Kohn–Sham total energy differences method, in which the energies of the C 1s core level excitations are determined as the total energy differences between the ground state and the first core ionized states [320]. For the ionized states, the core electrons of each target atom were modelled by a C 1s core-hole setup, while a charge was reintroduced at the Fermi level to ensure neutrality of the periodic unit cell. While the Kohn–Sham procedure should give consistent results for all atoms of the same kind, the absolute binding energies depend on the exchange–correlation functional. Therefore, the calculated energy scale was rigidly shifted to align with experiment.

Intermolecular Dispersion of Heptacene (chapter 2.3)

All calculations were performed within the framework of density functional theory (DFT) employing the Vienna Ab Initio Simulation Package (VASP) version 5.4.4 [312,313]. Exchange-correlation effects were approximated by the functional of Perdew-Burke-Ernzerhof (PBE) [53] and van der Waals contributions were treated with Grimme's D3 dispersion correction [60]. We used the projector-augmented wave (PAW) method [314] assuming an energy cutoff of 400 eV. The full monolayer of 7A on the (2x1)-O reconstructed Cu(110) surface was simulated in accordance with the experimental results with the 7A molecules oriented along the O rows. We utilize the repeated slab approach using five substrate layers and a 30 Å vacuum layer. To prevent disturbing spurious electrical fields, a dipole layer was placed in the vacuum region [315]. The ionic positions of the structure were optimized on a Gamma-centered grid of (2x8x1) k-points until the remaining forces were below 0.01 eV/Å. During the optimization, the two bottom Cu layers of the slab were constrained. To evaluate the molecular orbital-specific dispersion, we recalculated the electronic properties of a freestanding 7A monolayer on a denser k-mesh of 5x20x3 points. Based on this calculation, the angle-resolved photoemission intensity was simulated within the one-step model of photoemission [317] under the assumption that the wave function of the final state can be described as a plane wave [85].

Spin States in a NiPc Layer (chapter 3.2)

All calculations were performed within the framework of DFT+U[321], where the Ni d-orbitals were corrected with an effective Hubbard \tilde{U} of 3 eV. We optimized the structures utilizing the Vienna Ab Initio Simulation Package (VASP) [312,313] version 5.4.4. Exchange-correlation effects were approximated by the functional of Perdew-Burke-Ernzerhof (PBE) [53] and van der Waals contributions were treated with Grimme's D3 dispersion correction [60]. We used the projector-augmented wave (PAW) method [314], assuming an energy cutoff of 400 eV. As no predominant experimental unit cell was detected, we modelled three molecular arrangements covering the range from a very tightly packed monolayer to an isolated molecule on the surface. Depending on the size of the unit cell, the structures were calculated on a Gamma-centred grid of (6x6x1), (4x4x1) or (3x3x1) *k*-points. The surface was simulated within the repeated slab approach using four metallic layers and a 30 Å vacuum layer. To prevent disturbing spurious electrical fields, a dipole layer was placed in the vacuum region [315]. During the optimization, the two bottom Cu layers of the slab were constrained, and the ionic positions calculated until the remaining forces were below 0.01 eV/Å. Furthermore, the z-coordinate of the molecule was constrained during the evaluation of the distance dependence.

For the simulation of the XPS spectra, we utilized the GPAW code (version 21.1.0) [318,319]. The structures were recalculated at the same level of theory applying the delta Kohn-Sham total energy differences method (Δ KS). According to this scheme, the energies of the C 1s core level excitations are determined as the total energy differences between the ground state and the first core ionized states [320]. For the ionized states, the core electrons of each target atom were modelled by a C 1s core-hole setup, while a compensating homogeneous

background was introduced to ensure the neutrality of the periodic unit cells. While the Kohn–Sham procedure should give consistent results for all atoms of the same kind, the absolute binding energies depend on the exchange-correlation functional. Therefore, the calculated energy scale was rigidly shifted to align with experiment.

Adsorption of Small Gases at NiTPP (chapter 3.3)

For periodic systems, we employed the Vienna Ab Initio Simulation Package (VASP) version 5.4.4. [312,313]. Exchange-correlation effects were approximated by the functional of Perdew-Burke-Ernzerhof (PBE) [53]. Additionally, we included an effective Hubbard-U correction [321], $\tilde{U}=3\text{eV}$, to the Ni d-states to improve the treatment of on-site correlations at the metal centre of the NiTPP complex. Van der Waals contributions were treated with Grimme’s D3 dispersion correction [60]. We used the projector-augmented wave (PAW) method [314] assuming an energy cutoff of 400 eV. All calculations were spin-polarized, and the ionic positions optimized until forces were below 0.005 eV/Å. The surfaces (Cu and Cu-O) were simulated within the repeated slab approach using four substrate layers, two of which were held fix during optimization, and a 25 Å vacuum layer between the slabs. To avoid spurious electrical fields, a dipole layer was inserted in the vacuum region [315]. The Brillouin zone was sampled on a Gamma-centered grid of 4x4x1 k-points. For the (2x2) R45 O-Cu surface, we determined NiTPP with Ni on top of an O as the most favourable interface structure. The Cu-interface was modelled following one of our previous investigations with the Ni at the ”hollow” site of the (100) surface [236]. For the subsequent adsorption of the gas ligands to the Ni-centre, we report the most stable coordination modes from our structure search. For the pure Cu-surface, we also calculated the electronic structure of the optimized geometries using the range-separated hybrid functional HSE06 [116].

In addition, the isolated complexes in the gas phase were calculated with the quantum chemistry package ORCA version 5.0.1. [322,323]. Using the def2-TZVP basis set [324], molecular geometries were optimized with the hybrid functional B3LYP [54,325]. All systems were calculated as open-shell systems with the respective multiplicity. Dispersion was accounted for by Grimme’s D3 correction [60].

Application in Heterogeneous Catalysis (chapter 3.4)

For the calculation of the periodic systems, we utilized the Vienna Ab Initio Simulation Package (VASP) version 5.4.4 [312,313]. Exchange-correlation effects were described by the functional of Perdew-Burke-Ernzerhof [53], and van der Waals contributions treated with the D3 dispersion correction [60]. The projector augmented wave method [314] was used together with an energy cutoff of 400 eV. All calculations were spin-polarized and the ionic positions optimized until forces were below 0.01 eV/Å. The general structure search was conducted using standard DFT. The most stable structures of each step were optimized again treating the on-site correlation of the Ni d-states with a Hubbard parameter $\tilde{U}=3\text{eV}$ within the DFT+U approach [321]. The surfaces (Cu and Cu-O) were simulated within the repeated slab approach using four substrate layers, two of which were held fix during optimization, and a 25 Å vacuum layer between the slabs. To avoid spurious electrical fields, a dipole layer was inserted in the

vacuum region [315]. The periodic surface calculations were obtained on a Gamma-centered grid $4 \times 4 \times 1$ grid of k-points.

In addition, isolated molecules in the gas phase were calculated with the quantum chemistry package ORCA version 5.0.1.[322,323]. The molecular geometries were optimized employing PBE [53] and the hybrid functional B3LYP [54,325], both times in combination with the def2-TZVP basis set [324]. All systems were calculated as open-shell systems with the respective multiplicity. Dispersion was accounted for by Grimme's D3 correction [60].

Detecting Conformational Changes with ARPES (chapter 3.5)

The periodic calculations are performed with the Vienna Ab Initio Simulation Package (VASP) version 5.4.4. [312,313], to obtain the projected density of states for the composite interfaces. The arrangement of the molecules in the unit cell were taken from a previous STM study of Fratesi et al. [180]. Exchange-correlation effects were approximated by the functional of Perdew-Burke-Ernzerhof (PBE) [53]. Additionally, we included an effective Hubbard-U correction [321] to the metal d-states, $\tilde{U}=3\text{eV}$, to improve the treatment of on-site correlations at the metal center of the porphyrin complexes. Van der Waals contributions were treated with Grimme's D3 dispersion correction [60]. We used the projector-augmented wave (PAW) method [314] assuming an energy cutoff of 400 eV. All calculations were spin-polarized, and the ionic positions optimized until forces were below $0.01 \text{ eV}/\text{\AA}$. The interfaces were simulated within the repeated slab approach using six substrate layers, two of which were held fix during optimization, and a 25 \AA vacuum layer between the slabs. To avoid spurious electrical fields, a dipole layer was inserted in the vacuum region [315]. The Brillouin zone was sampled on a Gamma-centered grid of $3 \times 3 \times 1$ k-points. For our POT analysis, we extended our study with gas phase calculations using the quantum chemistry package ORCA version 5.0.1. [322,323]. Reducing the size of the systems seems reasonable, as the molecules are effectively electronically decoupled from the substrate. Furthermore, it enables the use of the more sophisticated hybrid-functional (B3LYP [54,325]) to describe the electronic structure of the porphyrins. The def2-TZVP basis set [324] was employed together with Grimme's D3 dispersion correction [60]. From the resulting Kohn-Sham orbitals, momentum maps are simulated by taking isokinetic cuts of the Fourier-transformed orbitals via the kMap software package [98].

Benchmarking exPOT (chapter 4.2)

The first part of our molecular calculations has been performed with the quantum chemistry package ORCA, version 5.0.1. [322,323]. Our calculations utilize the 6-311++G** basis set [326,327]. Exchange-correlation was described by the Perdew-Wang parameterization of the local density approximation (PWLDA) [328] as well as with the long-range separated hybrid functional CAM-B3LYP [58]. After optimizing the molecular structure, we calculated the excited state spectrum with linear-response TDDFT. Note that for convergence of the spectra computed with a localized-basis code like ORCA or Fiesta in comparison with OCTOPUS, it is important to include diffuse basis functions.

Based on the DFT Kohn-Sham orbitals and energies, we employ the Fiesta code [329] to self-consistently correct the molecular energy levels by quasi-particle self-energy calculations with the GW approximation. Building upon the GW energies, we compute neutral electron-hole excitations by solving the Bethe-Salpeter equation beyond the Tamm-Dancoff approximation (TDA).

The momentum maps were modelled within the exPOT formalism [44] with a photon energy of 35 eV.

Excited States in C₆₀ Aggregates (chapter 4.3)

The ab initio calculation of the exciton spectrum of the C₆₀ film was performed in two steps, using a GW +BSE approach. For the static electronic structure, we perform calculations for two unique C₆₀ dimers, which have been extracted from the suggested structure of the molecular film [306] (dimers 1-2 and 3-4 respectively). Starting from Kohn-Sham orbitals and energies of a ground state DFT calculation (6-311G*/PBE0+D3) [60,326,327,330] using ORCA 5.0.1 [322,323], we employ the Fiesta code [329] to self-consistently correct the molecular energy levels by quasi-particle self-energy calculations with the GW approximation. To account for polarization effects beyond the molecular dimer, we embed the dimer cluster in a discrete polarizable model using the MESCal program[331–333]. The reaction-field matrix was extrapolated from calculations with models spheres of 30Å (=65molecules) and 60Å (=250 molecules). Building upon the GW energies, we compute neutral electron-hole excitations by solving the Bethe-Salpeter equation beyond the Tamm-Dancoff approximation (TDA).

The photoemission spectra were simulated within the exPOT approach [44]. According to experiments, the momentum-dependent polarization factor $|A \cdot k|^2$ was modelled as p-polarized light incoming with 68° to the surface normal. To account for the symmetry of the C₆₀ film, the momentum maps were 3-fold rotated and mirrored. Finally, to arrive at the theoretical momentum maps, we sum up the photoelectron intensities of each contributing electron-hole transition in a kinetic energy range of 200 meV centred on the respective exciton band.

8 Appendix

Going beyond Pentacene

This section contains supplemental material for chapter 2.

Table 8.1: Epitaxial matrices with respect to substrate unit cell and molecular coverages of all adsorption structures used to calculate the adsorption energies of acenes on coinage metal surfaces in Figure 2.3.

Epitaxial matrix, molecular coverage [molecules/(nm) ²]					
6A/Ag(110)	Small coverage = i	Medium coverage = m	Full coverage with parallel order = f1	Full coverage with shifted order = f2	Experimental unit cell
[1 $\bar{1}$ 0] direction	$\begin{pmatrix} 4 & 0 \\ 0 & 9 \end{pmatrix}$, 0.24	$\begin{pmatrix} 3 & 0 \\ 0 & 8 \end{pmatrix}$, 0.36	$\begin{pmatrix} 2 & 0 \\ 0 & 7 \end{pmatrix}$, 0.62	$\begin{pmatrix} 2 & 2 \\ 0 & 7 \end{pmatrix}$, 0.62	$\begin{pmatrix} 2 & 1 \\ -1 & 6 \end{pmatrix}$, 0.66
[001] direction	$\begin{pmatrix} 7 & 0 \\ 0 & 5 \end{pmatrix}$, 0.25	$\begin{pmatrix} 6 & 0 \\ 0 & 4 \end{pmatrix}$, 0.36	$\begin{pmatrix} 5 & 0 \\ 0 & 3 \end{pmatrix}$, 0.58	$\begin{pmatrix} 5 & 0 \\ 1 & 3 \end{pmatrix}$, 0.58	$\begin{pmatrix} 5 & 1 \\ 1 & 3 \end{pmatrix}$, 0.62
7A/Ag(110)	Small coverage = i	Medium coverage = m	Full coverage with parallel order = f1	Full coverage with shifted order = f2	Experimental unit cell
[1 $\bar{1}$ 0] direction	$\begin{pmatrix} 4 & 0 \\ 0 & 10 \end{pmatrix}$, 0.22	$\begin{pmatrix} 3 & 0 \\ 0 & 9 \end{pmatrix}$, 0.32	$\begin{pmatrix} 2 & 0 \\ 0 & 8 \end{pmatrix}$, 0.54	$\begin{pmatrix} 2 & 2 \\ 0 & 8 \end{pmatrix}$, 0.54	$\begin{pmatrix} 2 & 1 \\ 0 & 8 \end{pmatrix}$, 0.54
[001] direction	$\begin{pmatrix} 8 & 0 \\ 0 & 5 \end{pmatrix}$, 0.22	$\begin{pmatrix} 7 & 0 \\ 0 & 4 \end{pmatrix}$, 0.31	$\begin{pmatrix} 6 & 0 \\ 0 & 3 \end{pmatrix}$, 0.48	$\begin{pmatrix} 6 & 0 \\ 1 & 3 \end{pmatrix}$, 0.48	$\begin{pmatrix} 6 & 1 \\ 1 & 3 \end{pmatrix}$, 0.51
6A/Cu(110)	Small coverage = i	Medium coverage = m	Full coverage with parallel order = f1	Full coverage with shifted order = f2	Experimental unit cell
[1 $\bar{1}$ 0] direction	$\begin{pmatrix} 4 & 0 \\ 0 & 10 \end{pmatrix}$, 0.28	$\begin{pmatrix} 3 & 0 \\ 0 & 9 \end{pmatrix}$, 0.42	$\begin{pmatrix} 2 & 0 \\ 0 & 8 \end{pmatrix}$, 0.70	$\begin{pmatrix} 2 & 2 \\ 0 & 8 \end{pmatrix}$, 0.70	$\begin{pmatrix} 2 & 0 \\ 0 & 9 \end{pmatrix}$, 0.62
[001] direction	$\begin{pmatrix} 7 & 0 \\ 0 & 5 \end{pmatrix}$, 0.32	$\begin{pmatrix} 6 & 0 \\ 0 & 4 \end{pmatrix}$, 0.47	$\begin{pmatrix} 6 & 0 \\ 0 & 3 \end{pmatrix}$, 0.62	$\begin{pmatrix} 6 & 0 \\ 1 & 3 \end{pmatrix}$, 0.62	-
7A/Cu(110)	Small coverage = i	Medium coverage = m	Full coverage with parallel order = f1	Full coverage with shifted order = f2	Experimental unit cell
[1 $\bar{1}$ 0] direction	$\begin{pmatrix} 4 & 0 \\ 0 & 11 \end{pmatrix}$, 0.26	$\begin{pmatrix} 3 & 0 \\ 0 & 10 \end{pmatrix}$, 0.37	$\begin{pmatrix} 2 & 0 \\ 0 & 9 \end{pmatrix}$, 0.62	$\begin{pmatrix} 2 & 3 \\ 0 & 9 \end{pmatrix}$, 0.62	$\begin{pmatrix} 2 & 0 \\ 1 & 9 \end{pmatrix}$, 0.62
[001] direction	$\begin{pmatrix} 8 & 0 \\ 0 & 5 \end{pmatrix}$, 0.28	$\begin{pmatrix} 7 & 0 \\ 0 & 4 \end{pmatrix}$, 0.40	$\begin{pmatrix} 6 & 0 \\ 0 & 3 \end{pmatrix}$, 0.62	$\begin{pmatrix} 6 & 0 \\ 2 & 3 \end{pmatrix}$, 0.62	$\begin{pmatrix} 6 & 1 \\ 0 & 3 \end{pmatrix}$, 0.62

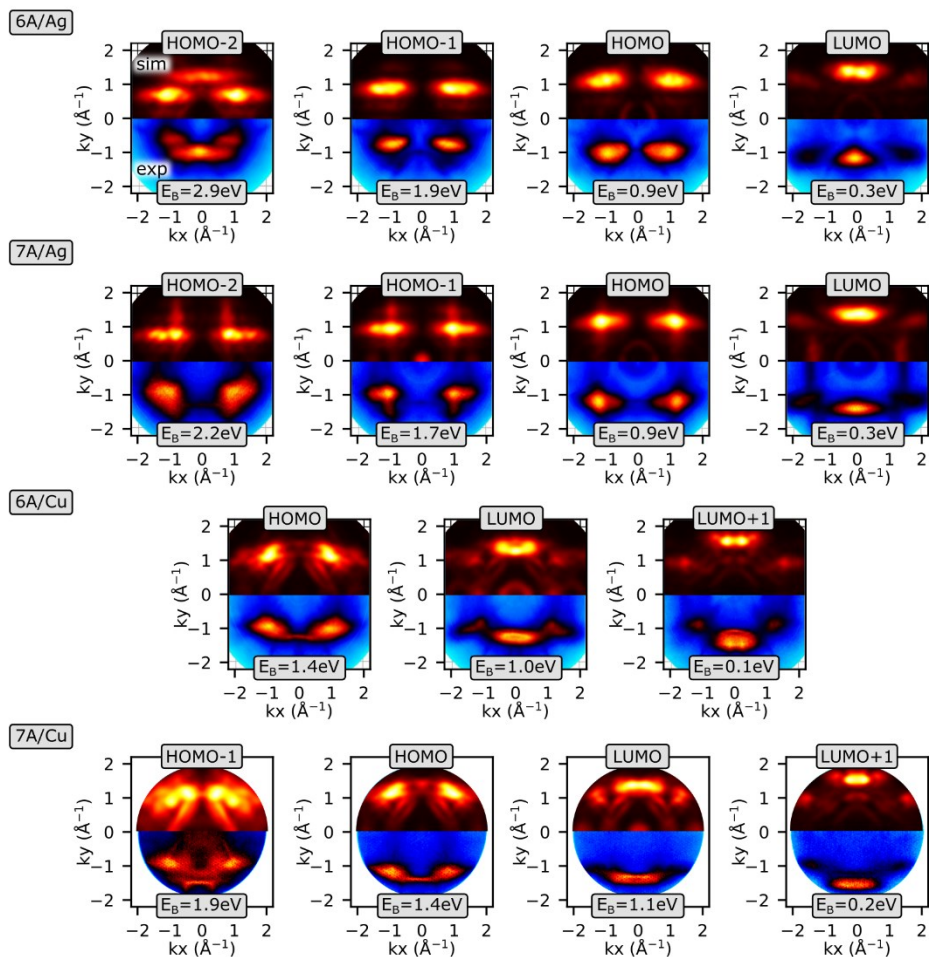


Figure 8.1: Comparison of experimental momentum maps (exp., bottom) to simulated maps (sim., top) of each acene/metal interface at specific binding energies. The simulated maps have been obtained from periodic calculations of the respective, experimentally determined unit cells. Note that for 7A/Ag, the maps of molecules along two perpendicular directions have been added.

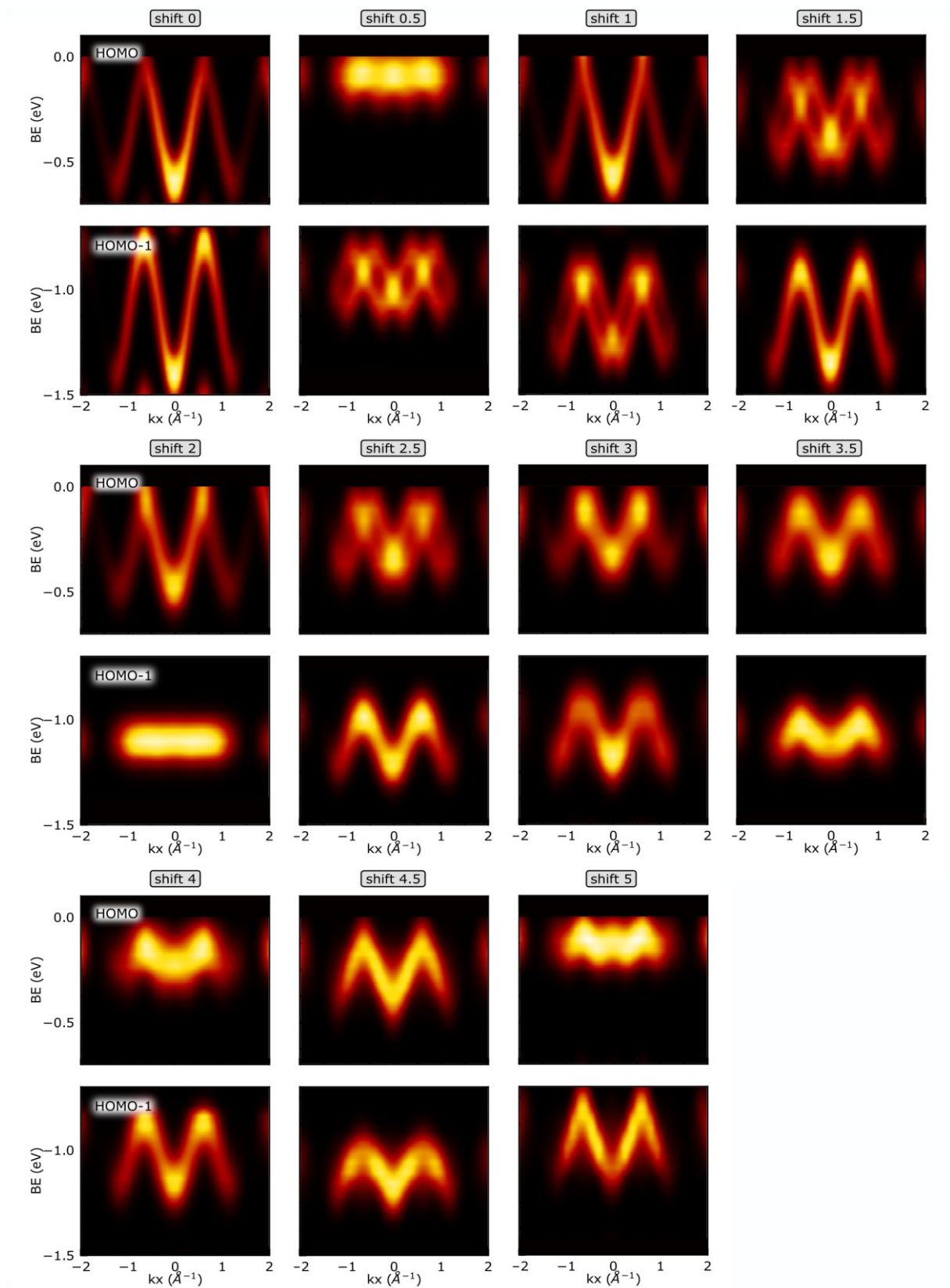


Figure 8.2: Symmetrized simulated ARPES dispersion of the HOMO and HOMO-1 of freestanding 7A monolayers with different lateral shifts given in units of benzene rings.

Controlling Spin at Interfaces

This section contains supplemental material for chapter 3.

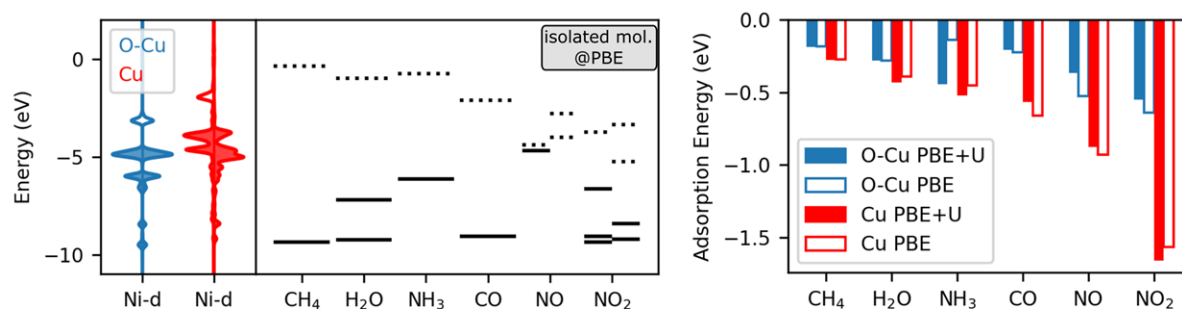


Figure 8.3: (left) Orbital energies of the separate subsystems (NiTPP and ligand molecules) before formation of a complex. Occupied orbitals are displayed as filled, solid lines, unoccupied orbitals as blank, dotted lines. For open shell systems, both spin channels are shown. All energies are calculated with PBE-D3 and in reference to the vacuum energy. (right) Adsorption energies on the pure (red) and passivated (blue) Cu-surface calculated with PBE-D3 and PBE+U-D3.

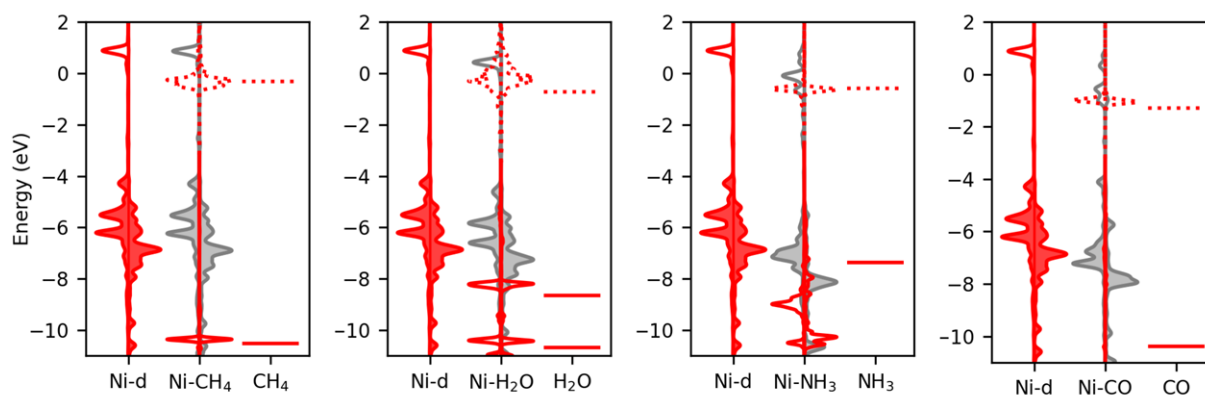


Figure 8.4 Molecular orbital diagrams for the adsorption of CH₄, H₂O, NH₃ and CO at NiTPP/Cu as obtained by single point HSE06.

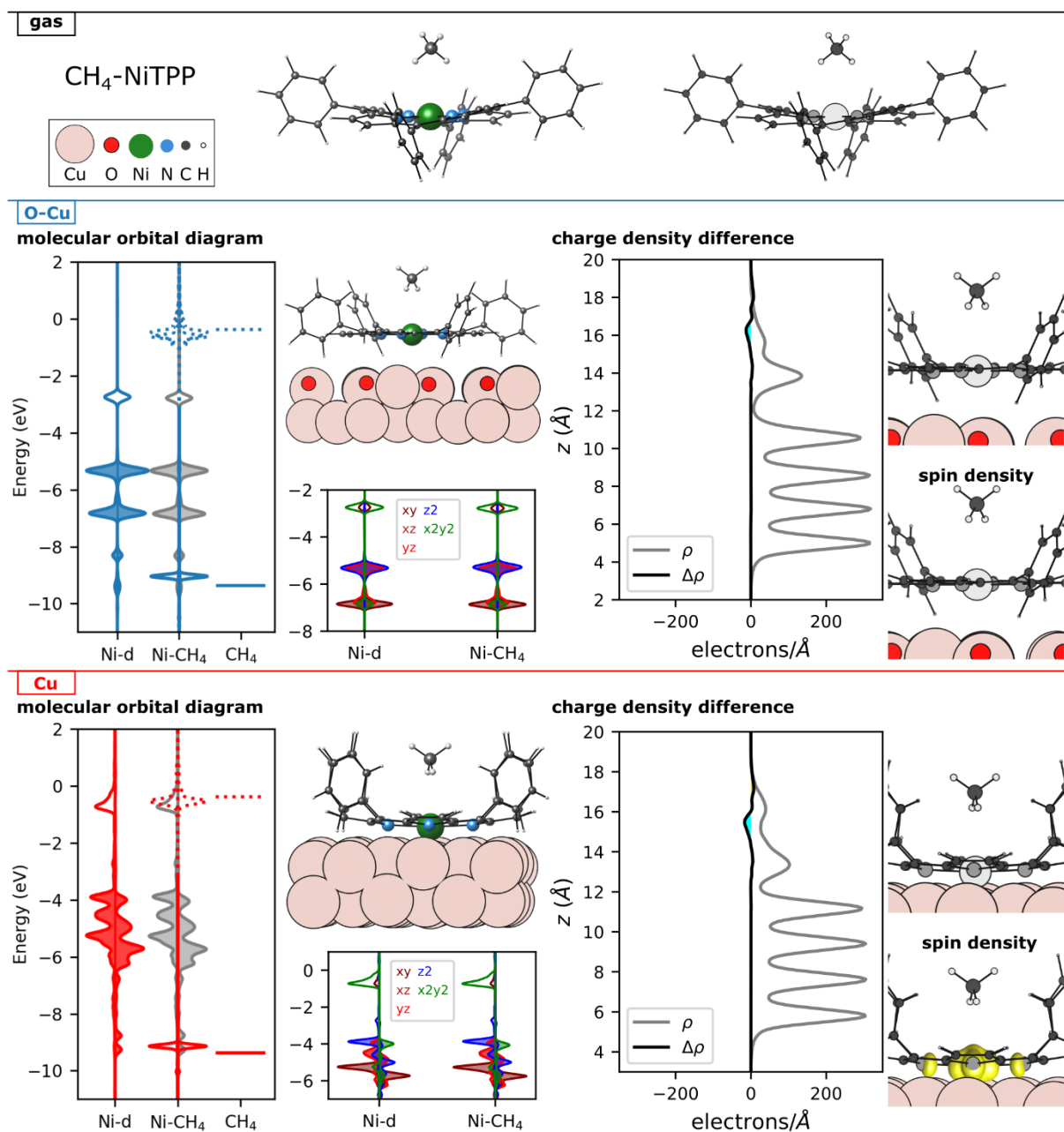


Figure 8.5: Structure, molecular orbital diagram and charge rearrangements upon adsorption of CH₄ at NiTPP in the gas phase (B3LYP-D3), on passivated Cu and on a pure Cu-surface (both PBE+U-D3). The "gas" section shows the optimized structure (left) and the isosurface of the charge density difference (right). The sections "O-Cu" and "Cu" summarize the analysis of the periodic calculations. The molecular orbital diagrams on the left are structured as follows: The left and right side of the panel shows the energy levels of the separate subsystems, i.e.: Ni d-states of the Ni-TPP/Cu interface and frontier molecular orbitals of the adsorbates. In the middle, the DOS of the full adsorbate-complex system projected onto the Ni d-states (grey line) and molecular orbitals (red line) is shown. The panel at the bottom middle then resolves the DOS of the NiTPP/surface with and without the adsorbate explicitly for the five d-states. Above, the optimized structure is illustrated (color code: Cu=rose, O=red, Ni=green, N=blue, C=black, H=white). The charge density difference of the periodic systems is shown plane-averaged along the z-coordinate of the unit cell (magnification factor=600) and as an 3D-isosurface (blue=electron loss, yellow=electron gain after adsorption). The last panel in the bottom right shows the spin density of the full adsorbate-complex system. All densities are plotted with an isovalue of 0.0025.

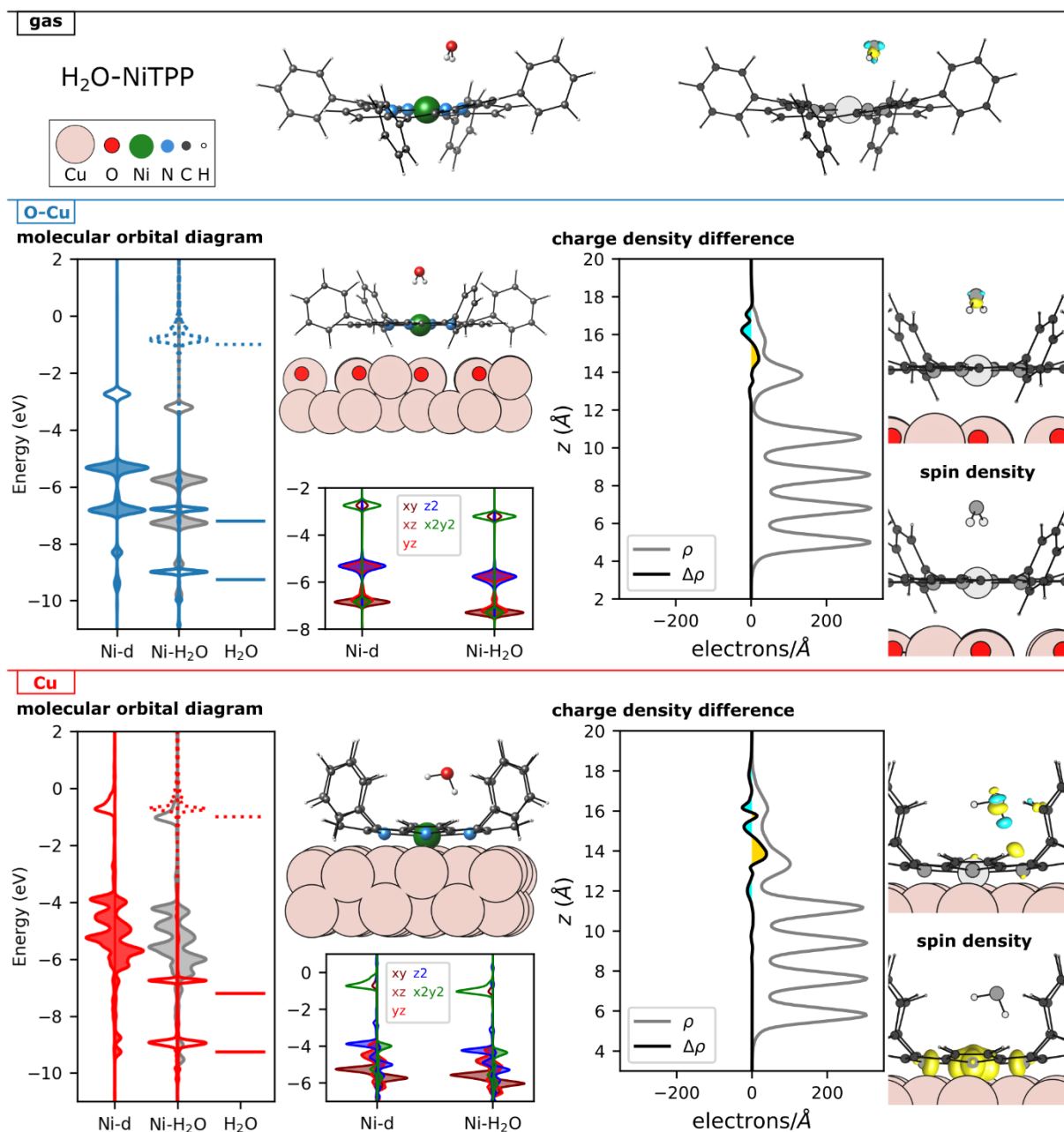


Figure 8.6: Structure, molecular orbital diagram and charge rearrangements upon adsorption of H₂O at NiTPP in the gas phase (B3LYP-D3), on passivated Cu and on a pure Cu-surface (both PBE+U-D3). The "gas" section shows the optimized structure (left) and the isosurface of the charge density difference (right). The sections "O-Cu" and "Cu" summarize the analysis of the periodic calculations. The molecular orbital diagrams on the left are structured as follows: The left and right side of the panel shows the energy levels of the separate subsystems, i.e.: Ni d-states of the Ni-TPP/Cu interface and frontier molecular orbitals of the adsorbates. In the middle, the DOS of the full adsorbate-complex system projected onto the Ni d-states (grey line) and molecular orbitals (red line) is shown. The panel at the bottom middle then resolves the DOS of the NiTPP/surface with and without the adsorbate explicitly for the five d-states. Above, the optimized structure is illustrated (color code: Cu=rose, O=red, Ni=green, N=blue, C=black, H=white). The charge density difference of the periodic systems is shown plane-averaged along the z-coordinate of the unit cell (magnification factor=600) and as a 3D-isosurface (blue=electron loss, yellow=electron gain after adsorption). The last panel in the bottom right shows the spin density of the full adsorbate-complex system. All densities are plotted with an isovalue of 0.0025.

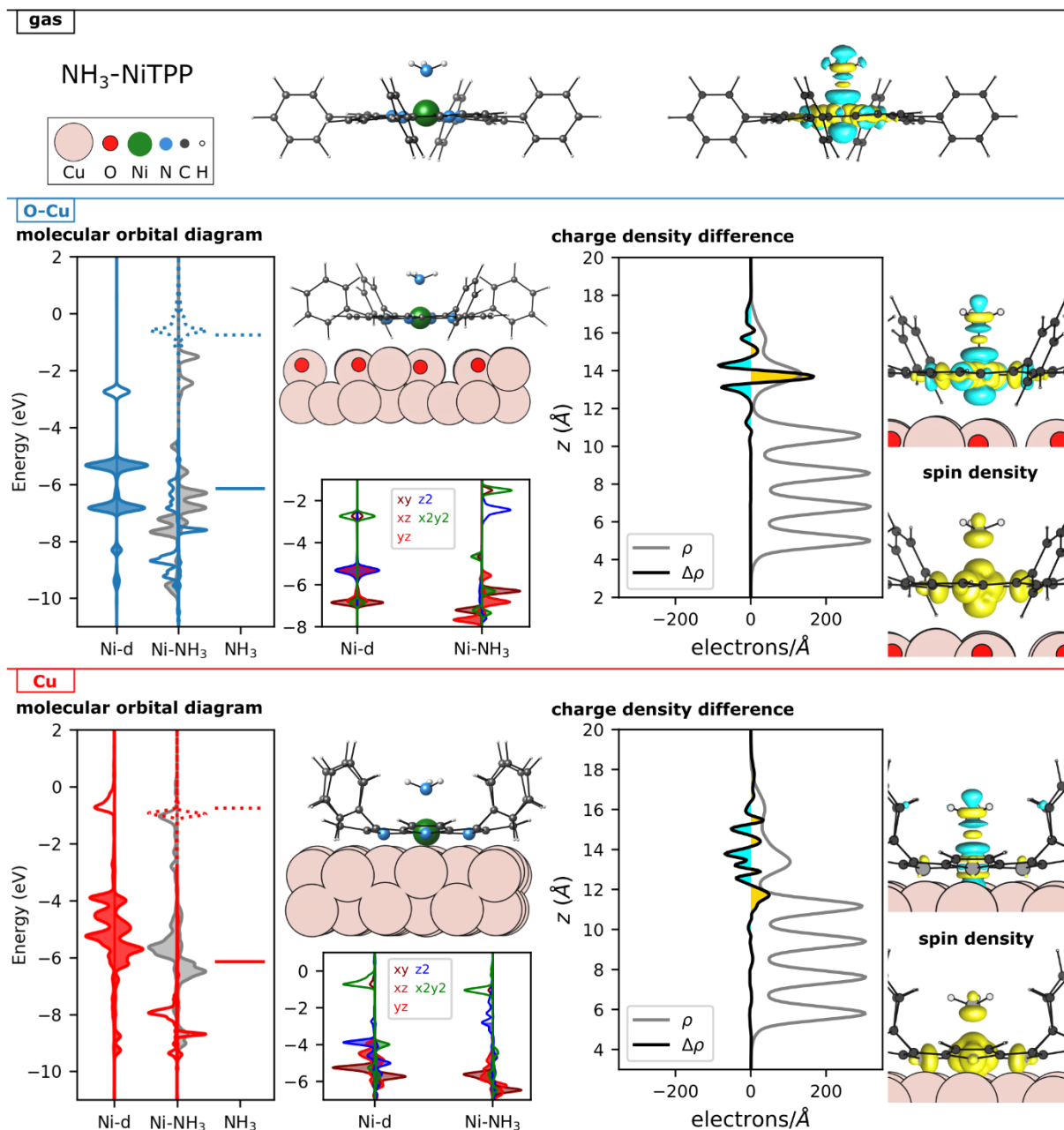


Figure 8.7.: Structure, molecular orbital diagram and charge rearrangements upon adsorption of NH₃ at NiTPP in the gas phase (B3LYP-D3), on passivated Cu and on a pure Cu-surface (both PBE+U-D3). The "gas" section shows the optimized structure (left) and the isosurface of the charge density difference (right). The sections "O-Cu" and "Cu" summarize the analysis of the periodic calculations. The molecular orbital diagrams on the left are structured as follows: The left and right side of the panel shows the energy levels of the separate subsystems, i.e.: Ni d-states of the Ni-TPP/Cu interface and frontier molecular orbitals of the adsorbates. In the middle, the DOS of the full adsorbate-complex system projected onto the Ni d-states (grey line) and molecular orbitals (red line) is shown. The panel at the bottom middle then resolves the DOS of the NiTPP/surface with and without the adsorbate explicitly for the five d-states. Above, the optimized structure is illustrated (color code: Cu=rose, O=red, Ni=green, N=blue, C=black, H=white). The charge density difference of the periodic systems is shown plane-averaged along the z-coordinate of the unit cell (magnification factor=600) and as an 3D-isosurface (blue=electron loss, yellow=electron gain after adsorption). The last panel in the bottom right shows the spin density of the full adsorbate-complex system. All densities are plotted with an isovalue of 0.0025.

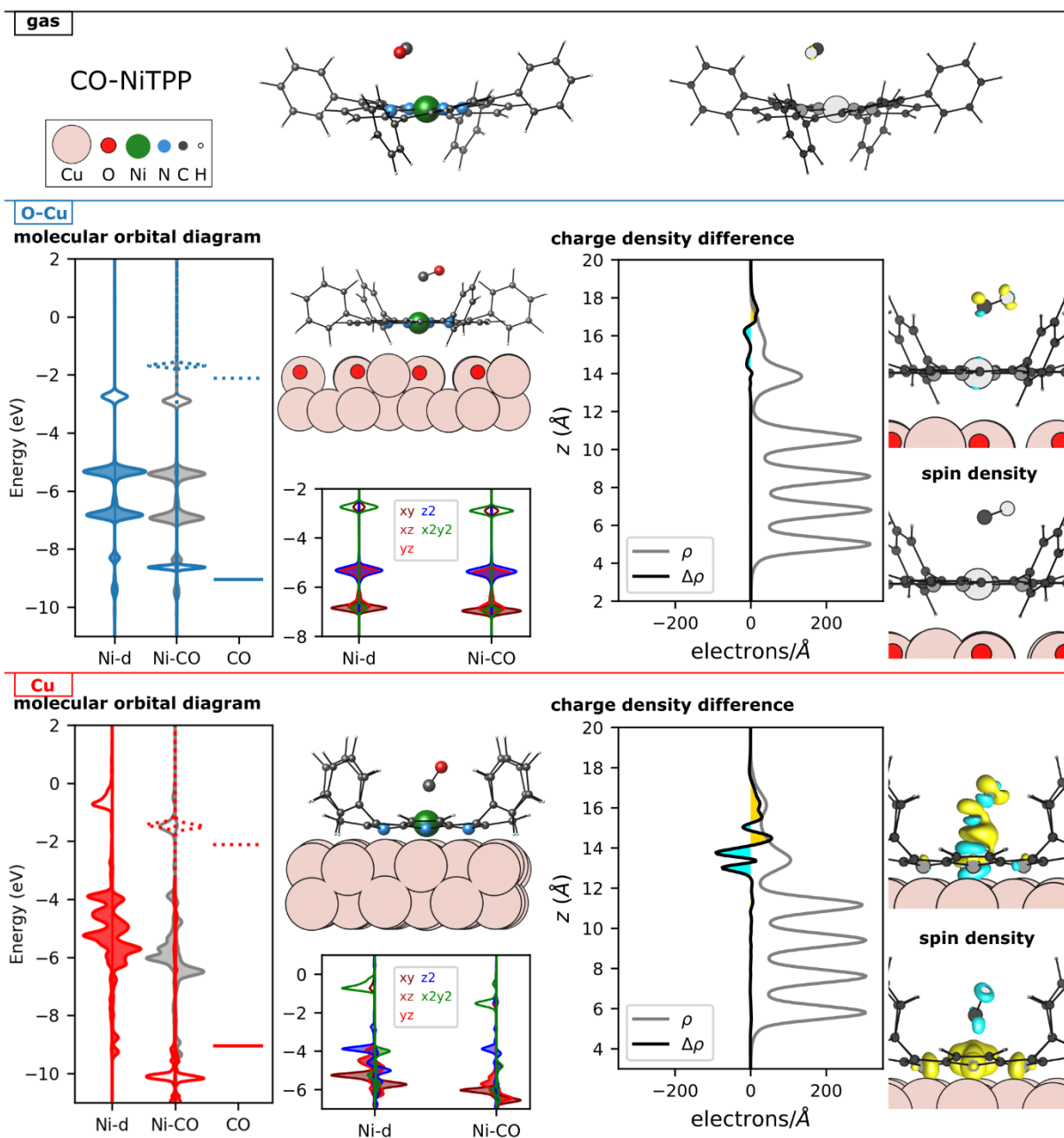


Figure 8.8: Structure, molecular orbital diagram and charge rearrangements upon adsorption of CO at NiTPP in the gas phase (B3LYP-D3), on passivated Cu and on a pure Cu-surface (both PBE+U-D3). The "gas" section shows the optimized structure (left) and the isosurface of the charge density difference (right). The sections "O-Cu" and "Cu" summarize the analysis of the periodic calculations. The molecular orbital diagrams on the left are structured as follows: The left and right side of the panel shows the energy levels of the separate subsystems, i.e.: Ni d-states of the Ni-TPP/Cu interface and frontier molecular orbitals of the adsorbates. In the middle, the DOS of the full adsorbate-complex system projected onto the Ni d-states (grey line) and molecular orbitals (red line) is shown. The panel at the bottom middle then resolves the DOS of the NiTPP/surface with and without the adsorbate explicitly for the five d-states. Above, the optimized structure is illustrated (color code: Cu=rose, O=red, Ni=green, N=blue, C=black, H=white). The charge density difference of the periodic systems is shown plane-averaged along the z-coordinate of the unit cell (magnification factor=600) and as a 3D-isosurface (blue=electron loss, yellow=electron gain after adsorption). The last panel in the bottom right shows the spin density of the full adsorbate-complex system. All densities are plotted with an isovalue of 0.0025.

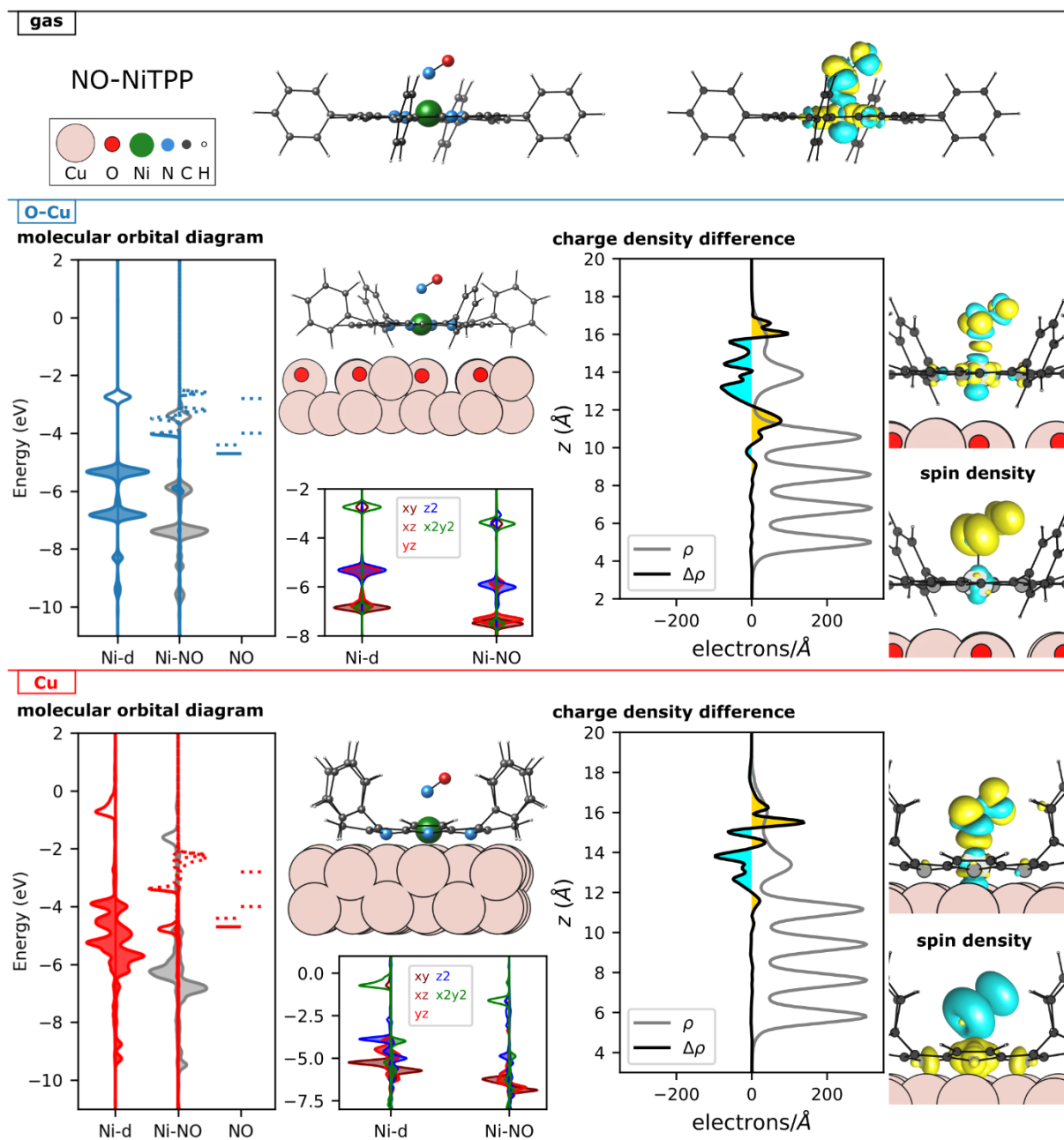


Figure 8.9: Structure, molecular orbital diagram and charge rearrangements upon adsorption of NO at NiTPP in the gas phase (B3LYP-D3), on passivated Cu and on a pure Cu-surface (both PBE+U-D3). The "gas" section shows the optimized structure (left) and the isosurface of the charge density difference (right). The sections "O-Cu" and "Cu" summarize the analysis of the periodic calculations. The molecular orbital diagrams on the left are structured as follows: The left and right side of the panel shows the energy levels of the separate subsystems, i.e.: Ni d-states of the Ni-TPP/Cu interface and frontier molecular orbitals of the adsorbates. In the middle, the DOS of the full adsorbate-complex system projected onto the Ni d-states (grey line) and molecular orbitals (red line) is shown. The panel at the bottom middle then resolves the DOS of the NiTPP/surface with and without the adsorbate explicitly for the five d-states. Above, the optimized structure is illustrated (color code: Cu=rose, O=red, Ni=green, N=blue, C=black, H=white). The charge density difference of the periodic systems is shown plane-averaged along the z-coordinate of the unit cell (magnification factor=600) and as an 3D-isosurface (blue=electron loss, yellow=electron gain after adsorption). The last panel in the bottom right shows the spin density of the full adsorbate-complex system. All densities are plotted with an isovalue of 0.0025. Note that the charge density difference for the passivated surface suggests strong charge rearrangements. This is (at least partially artificial) and stems from the different orientation of the two degenerate SOMO/SUMO π^* -orbitals in the molecular and interface calculations.

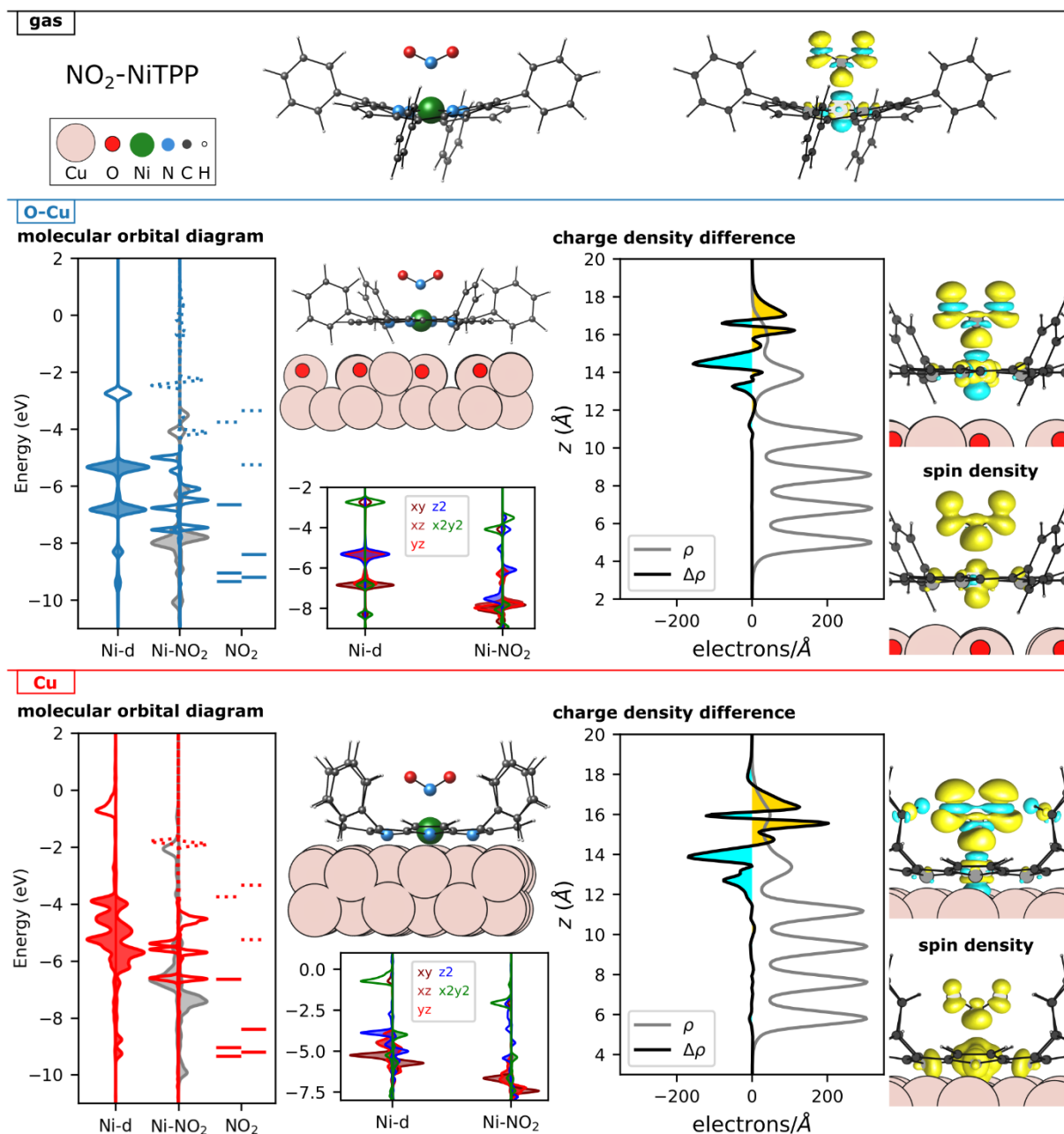


Figure 8.10: Structure, molecular orbital diagram and charge rearrangements upon adsorption of NO₂ at NiTPP in the gas phase (B3LYP-D3), on passivated Cu and on a pure Cu-surface (both PBE+U-D3). The "gas" section shows the optimized structure (left) and the isosurface of the charge density difference (right). The sections "O-Cu" and "Cu" summarize the analysis of the periodic calculations. The molecular orbital diagrams on the left are structured as follows: The left and right side of the panel shows the energy levels of the separate subsystems, i.e.: Ni d-states of the Ni-TPP/Cu interface and frontier molecular orbitals of the adsorbates. In the middle, the DOS of the full adsorbate-complex system projected onto the Ni d-states (grey line) and molecular orbitals (red line) is shown. The panel at the bottom middle then resolves the DOS of the NiTPP/surface with and without the adsorbate explicitly for the five d-states. Above, the optimized structure is illustrated (color code: Cu=rose, O=red, Ni=green, N=blue, C=black, H=white). The charge density difference of the periodic systems is shown plane-averaged along the z-coordinate of the unit cell (magnification factor=600) and as an 3D-isosurface (blue=electron loss, yellow=electron gain after adsorption). The last panel in the bottom right shows the spin density of the full adsorbate-complex system. All densities are plotted with an isovalue of 0.0025.

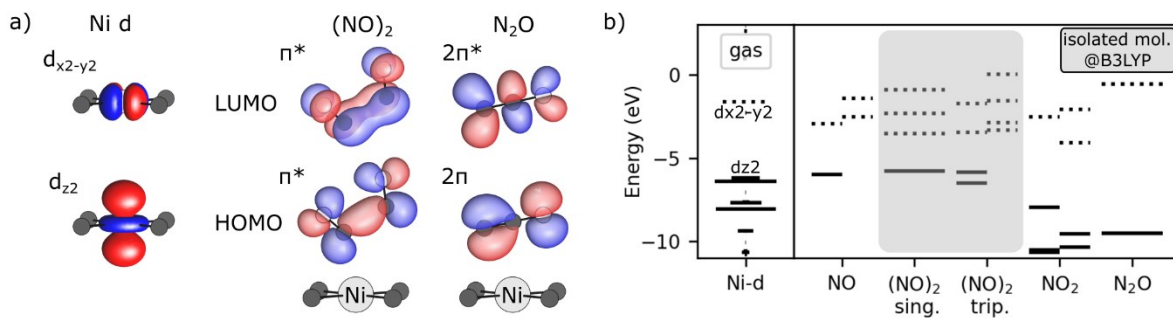


Figure 8.11: a) Highest occupied and lowest unoccupied d-orbital of the Ni-complex as well as molecular orbitals of NO-dimer and N₂O. b) Orbital energies of the separate subsystems (NiTPP and nitrogen oxides) in the gas phase before formation of a complex. Occupied orbitals are displayed as filled, solid lines, unoccupied orbitals as blank, dotted lines. For open shell systems, both spin channels are shown. All data is obtained with B3LYP-D3.

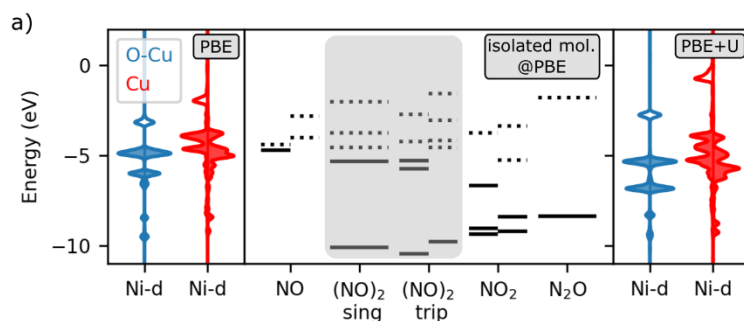


Figure 8.12: a) Orbital energies of the separate subsystems (NiTPP/surface and nitrogen oxides) before formation of a complex. The NiTPP interface was calculated with (right) and without Hubbard correction (left). Occupied orbitals are displayed as filled, solid lines, unoccupied orbitals as blank, dotted lines. For open shell systems, both spin channels are shown. All data is aligned relative to the vacuum energy.

9 Bibliography

- [1] Y. Yang, F. Wudl, Organic Electronics: From Materials to Devices, *Advanced Materials*. 21 (2009) 1401–1403. <https://doi.org/10.1002/adma.200900844>.
- [2] K.-J. Baeg, M. Binda, D. Natali, M. Caironi, Y.-Y. Noh, Organic Light Detectors: Photodiodes and Phototransistors, *Advanced Materials*. 25 (2013) 4267–4295. <https://doi.org/10.1002/adma.201204979>.
- [3] S.-J. Zou, Y. Shen, F.-M. Xie, J.-D. Chen, Y.-Q. Li, J.-X. Tang, Recent advances in organic light-emitting diodes: toward smart lighting and displays, *Mater Chem Front*. 4 (2020) 788–820. <https://doi.org/10.1039/C9QM00716D>.
- [4] H. Ren, J.-D. Chen, Y.-Q. Li, J.-X. Tang, Recent Progress in Organic Photodetectors and their Applications, *Advanced Science*. 8 (2021) 2002418. <https://doi.org/10.1002/advs.202002418>.
- [5] L.X. Chen, Organic Solar Cells: Recent Progress and Challenges, *ACS Energy Lett*. 4 (2019) 2537–2539. <https://doi.org/10.1021/acsenergylett.9b02071>.
- [6] E.K. Solak, E. Irmak, Advances in organic photovoltaic cells: a comprehensive review of materials, technologies, and performance, *RSC Adv*. 13 (2023) 12244–12269. <https://doi.org/10.1039/D3RA01454A>.
- [7] G. Horowitz, Organic Transistors, John Wiley & Sons, Hoboken, New Jersey, 2006.
- [8] E. Goiri, P. Borghetti, A. El-Sayed, J.E. Ortega, D.G. de Oteyza, Multi-Component Organic Layers on Metal Substrates, *Advanced Materials*. 28 (2016) 1340–1368. <https://doi.org/10.1002/adma.201503570>.
- [9] H. Ishii, K. Sugiyama, E. Ito, K. Seki, Energy Level Alignment and Interfacial Electronic Structures at Organic/Metal and Organic/Organic Interfaces, *Advanced Materials*. 11 (1999) 605–625. [https://doi.org/10.1002/\(SICI\)1521-4095\(199906\)11:8<605::AID-ADMA605>3.0.CO;2-Q](https://doi.org/10.1002/(SICI)1521-4095(199906)11:8<605::AID-ADMA605>3.0.CO;2-Q).
- [10] S. Braun, W.R. Salaneck, M. Fahlman, Energy-Level Alignment at Organic/Metal and Organic/Organic Interfaces, *Advanced Materials*. 21 (2009) 1450–1472. <https://doi.org/10.1002/adma.200802893>.
- [11] R. Otero, A.L. Vázquez de Parga, J.M. Gallego, Electronic, structural and chemical effects of charge-transfer at organic/inorganic interfaces, *Surf Sci Rep*. 72 (2017) 105–145. <https://doi.org/10.1016/j.surfrep.2017.03.001>.
- [12] R. Paolesse, S. Nardis, D. Monti, M. Stefanelli, C. Di Natale, Porphyrinoids for Chemical Sensor Applications, *Chem Rev*. 117 (2017) 2517–2583. <https://doi.org/10.1021/acs.chemrev.6b00361>.
- [13] F. Zaera, Molecular approaches to heterogeneous catalysis, *Coord Chem Rev*. 448 (2021) 214179. <https://doi.org/10.1016/j.ccr.2021.214179>.
- [14] C.A. Schoenbaum, D.K. Schwartz, J.W. Medlin, Controlling the Surface Environment of Heterogeneous Catalysts Using Self-Assembled Monolayers, *Acc Chem Res*. 47 (2014) 1438–1445. <https://doi.org/10.1021/ar500029y>.
- [15] J.N. Appaturi, R. Ratti, B.L. Phoon, S.M. Batagarawa, I.U. Din, M. Selvaraj, R.J. Ramalingam, A review of the recent progress on heterogeneous catalysts for Knoevenagel condensation, *Dalton Transactions*. 50 (2021) 4445–4469. <https://doi.org/10.1039/D1DT00456E>.
- [16] J.E. Anthony, Functionalized acenes and heteroacenes for organic electronics, *Chem Rev*. 106 (2006) 5028–5048. <https://doi.org/10.1021/cr050966z>.

- [17] J.E. Anthony, The larger acenes: Versatile organic semiconductors, *Angewandte Chemie - International Edition*. 47 (**2008**) 452–483. <https://doi.org/10.1002/anie.200604045>.
- [18] J.E. Anthony, J.S. Brooks, D.L. Eaton, S.R. Parkin, Functionalized Pentacene: Improved Electronic Properties from Control of Solid-State Order, *J Am Chem Soc*. 123 (**2001**) 9482–9483. <https://doi.org/10.1021/ja0162459>.
- [19] W.-Q. Deng, W.A. Goddard, Predictions of Hole Mobilities in Oligoacene Organic Semiconductors from Quantum Mechanical Calculations, *J Phys Chem B*. 108 (**2004**) 8614–8621. <https://doi.org/10.1021/jp0495848>.
- [20] Y.C. Cheng, R.J. Silbey, D.A. da Silva Filho, J.P. Calbert, J. Cornil, J.L. Brédas, Three-dimensional band structure and bandlike mobility in oligoacene single crystals: A theoretical investigation, *J Chem Phys*. 118 (**2003**) 3764–3774. <https://doi.org/10.1063/1.1539090>.
- [21] J.-L. Brédas, D. Beljonne, V. Coropceanu, J. Cornil, Charge-Transfer and Energy-Transfer Processes in π -Conjugated Oligomers and Polymers: A Molecular Picture, *Chem Rev*. 104 (**2004**) 4971–5004. <https://doi.org/10.1021/cr040084k>.
- [22] K.N. Houk, P.S. Lee, M. Nendel, Polyacene and cyclacene geometries and electronic structures: Bond equalization, vanishing band gaps, and triplet ground states contrast with polyacetylene, *Journal of Organic Chemistry*. 66 (**2001**) 5517–5521. <https://doi.org/10.1021/jo010391f>.
- [23] Y. Yang, E.R. Davidson, W. Yang, Nature of ground and electronic excited states of higher acenes, *Proceedings of the National Academy of Sciences*. 113 (**2016**) E5098–E5107. <https://doi.org/10.1073/pnas.1606021113>.
- [24] A.R. Reddy, M. Bendikov, Diels–Alder reaction of acenes with singlet and triplet oxygen – theoretical study of two-state reactivity, *Chemical Communications*. (**2006**) 1179–1181. <https://doi.org/10.1039/B513597D>.
- [25] S.S. Zade, M. Bendikov, Reactivity of acenes: mechanisms and dependence on acene length, *J Phys Org Chem*. 25 (**2012**) 452–461. <https://doi.org/10.1002/poc.1941>.
- [26] R. Mondal, R.M. Adhikari, B.K. Shah, D.C. Neckers, Revisiting the Stability of Hexacenes, *Org Lett*. 9 (**2007**) 2505–2508. <https://doi.org/10.1021/ol0709376>.
- [27] D. Biermann, W. Schmidt, Diels-Alder reactivity of polycyclic aromatic hydrocarbons. 1. Acenes and benzologs, *J Am Chem Soc*. 102 (**1980**) 3163–3173. <https://doi.org/10.1021/ja00529a046>.
- [28] P. von Ragué Schleyer, M. Manoharan, H. Jiao, F. Stahl, The Acenes: Is There a Relationship between Aromatic Stabilization and Reactivity?, *Org Lett*. 3 (**2001**) 3643–3646. <https://doi.org/10.1021/ol016553b>.
- [29] M.S. Sättele, A. Windischbacher, K. Greulich, L. Egger, A. Haags, H. Kirschner, R. Ovsyannikov, E. Giangrisostomi, A. Gottwald, M. Richter, S. Soubatch, F.S. Tautz, M.G. Ramsey, P. Puschnig, G. Koller, H.F. Bettinger, T. Chassé, H. Peisert, Hexacene on Cu(110) and Ag(110): Influence of the Substrate on Molecular Orientation and Interfacial Charge Transfer, *The Journal of Physical Chemistry C*. 126 (**2022**) 5036–5045. <https://doi.org/10.1021/acs.jpcc.2c00081>.
- [30] M.S. Sättele, A. Windischbacher, L. Egger, A. Haags, P. Hurdax, H. Kirschner, A. Gottwald, M. Richter, F.C. Bocquet, S. Soubatch, F.S. Tautz, H.F. Bettinger, H. Peisert, T. Chassé, M.G. Ramsey, P. Puschnig, G. Koller, Going beyond Pentacene: Photoemission Tomography of a Heptacene Monolayer on Ag(110), *The Journal of Physical Chemistry C*. 125 (**2021**) 2918–2925. <https://doi.org/10.1021/acs.jpcc.0c09062>.
- [31] T.G. Boné, A. Windischbacher, M.S. Sättele, K. Greulich, L. Egger, T. Jauk, F. Lackner, H.F. Bettinger, H. Peisert, T. Chassé, M.G. Ramsey, M. Sterrer, G. Koller, P. Puschnig, Demonstrating the Impact of the Adsorbate Orientation on the Charge Transfer at

- Organic–Metal Interfaces, *The Journal of Physical Chemistry C*. 125 (2021) 9129–9137. <https://doi.org/10.1021/acs.jpcc.1c01306>.
- [32] T. Boné, A. Windischbacher, L. Scheucher, F. Presel, P. Schnabl, M.S. Wagner, H.F. Bettinger, H. Peisert, T. Chassé, P. Puschnig, M.G. Ramsey, M. Sterrer, G. Koller, Orientation, electronic decoupling and band dispersion of heptacene on modified and nanopatterned copper surfaces, *Journal of Physics: Condensed Matter*. 35 (2023) 475003. <https://doi.org/10.1088/1361-648X/acf105>.
- [33] R.H. Crabtree, *The Organometallic Chemistry of the Transition Metals*, John Wiley & Sons, Ltd, Hoboken (New Jersey), 2014.
- [34] C.M. Drain, A. Varotto, I. Radivojevic, Self-Organized Porphyrinic Materials, *Chem Rev*. 109 (2009) 1630–1658. <https://doi.org/10.1021/cr8002483>.
- [35] J.M. Gottfried, Surface chemistry of porphyrins and phthalocyanines, *Surf Sci Rep*. 70 (2015) 259–379. <https://doi.org/10.1016/j.surfrep.2015.04.001>.
- [36] D.M. Lopes, J.C. Araujo-Chaves, L.R. Menezes, I.L. Nantes-Cardoso, Technological Applications of Porphyrins and Related Compounds: Spintronics and Micro-/Nanomotors, in: S. Sivasankaran, P.K. Nayak, E. Günay (Eds.), *Metastable, Spintronics Materials and Mechanics of Deformable Bodies*, IntechOpen, Rijeka, 2019. <https://doi.org/10.5772/intechopen.86206>.
- [37] A.R. Battersby, Tetrapyrroles: the pigments of life, *Nat Prod Rep*. 17 (2000) 507–526. <https://doi.org/10.1039/B002635M>.
- [38] I. Cojocariu, A. Windischbacher, D. Baranowski, M. Jugovac, R.C. de C. Ferreira, J. Doležal, M. Švec, J.M. Zamalloa-Serrano, M. Tormen, L. Schio, L. Floreano, J. Dreiser, P. Puschnig, V. Feyer, C.M. Schneider, Surface-Mediated Spin Locking and Thermal Unlocking in a 2D Molecular Array, *Advanced Science*. 10 (2023) 2300223. <https://doi.org/10.1002/advs.202300223>.
- [39] H.M. Sturmeit, I. Cojocariu, A. Windischbacher, C. Puschnig Peter and Piamonteze, M. Jugovac, A. Sala, C. Africh, A. Comelli Giovanni and Cossaro, A. Verdini, L. Floreano, M. Stredansky, E. Vesselli, C. Hohner, M. Kettner, J. Libuda, C.M. Schneider, G. Zamborlini, M. Cinchetti, V. Feyer, Room-Temperature On-Spin-Switching and Tuning in a Porphyrin-Based Multifunctional Interface, *Small*. 17 (2021) 2104779. <https://doi.org/10.1002/sml.202104779>.
- [40] M. Stredansky, S. Moro, M. Corva, H. Sturmeit, V. Mischke, D. Janas, I. Cojocariu, M. Jugovac, A. Cossaro, A. Verdini, L. Floreano, Z. Feng, A. Sala, G. Comelli, A. Windischbacher, P. Puschnig, C. Hohner, M. Kettner, J. Libuda, M. Cinchetti, C.M. Schneider, V. Feyer, E. Vesselli, G. Zamborlini, Disproportionation of Nitric Oxide at a Surface-Bound Nickel Porphyrinoid, *Angewandte Chemie International Edition*. 61 (2022) e202201916. <https://doi.org/10.1002/anie.202201916>.
- [41] A. Windischbacher, P. Puschnig, Computational study on the adsorption of small molecules to surface-supported Ni-porphyrins, *Inorganica Chim Acta*. 558 (2023) 121719. <https://doi.org/10.1016/j.ica.2023.121719>.
- [42] R. Wallauer, M. Raths, K. Stallberg, L. Münster, D. Brandstetter, X. Yang, J. Gütde, P. Puschnig, S. Soubatch, C. Kumpf, F.C. Bocquet, F.S. Tautz, U. Höfer, Tracing orbital images on ultrafast time scales, *Science (1979)*. 371 (2021) 1056–1059. <https://doi.org/10.1126/science.abf3286>.
- [43] A. Neef, S. Beaulieu, S. Hammer, S. Dong, J. Maklar, T. Pincelli, R.P. Xian, M. Wolf, L. Rettig, J. Pflaum, R. Ernstorfer, Orbital-resolved observation of singlet fission, *Nature*. 616 (2023) 275–279. <https://doi.org/10.1038/s41586-023-05814-1>.
- [44] C.S. Kern, A. Windischbacher, P. Puschnig, Photoemission orbital tomography for excitons in organic molecules, *Phys Rev B*. 108 (2023) 85132. <https://doi.org/10.1103/PhysRevB.108.085132>.
- [45] W. Bennecke, A. Windischbacher, D. Schmitt, J.P. Bange, R. Hemm, C.S. Kern, G. D`Avino, X. Blase, D. Steil, S. Steil, M. Aeschlimann, B. Stadtmueller, M. Reutzel, P.

- Puschnig, G.S.M. Jansen, S. Mathias, Multiorbital exciton formation in an organic semiconductor, (**2023**). <https://doi.org/10.48550/arXiv.2303.13904>.
- [46] P. Hohenberg, W. Kohn, Inhomogeneous Electron Gas, *Physical Review*. 136 (**1964**) B864–B871. <https://doi.org/10.1103/PhysRev.136.B864>.
- [47] W. Kohn, Nobel Lecture: Electronic structure of matter—wave functions and density functionals, *Rev Mod Phys*. 71 (**1999**) 1253–1266. <https://doi.org/10.1103/RevModPhys.71.1253>.
- [48] C.J. Cramer, Essentials of computational chemistry : theories and models, 2nd ed., Wiley, Chichester, West Sussex, England, **2004**.
- [49] K. Burke, The ABC of DFT, (**2007**) 92697.
- [50] F. Jensen, Introduction to Computational Chemistry, 3rd ed., John Wiley and Sons, Chichester, West Sussex, England, **2017**.
- [51] W. Koch, M.C. Holthausen, A Chemist's Guide to Density Functional Theory, John Wiley & Sons, Ltd, Hoboken, New Jersey, **2001**.
- [52] D.S. Sholl, J.A. Steckel, Density Functional Theory: A Practical Introduction, John Wiley & Sons, Ltd, Hoboken, New Jersey, **2009**.
- [53] J.P. Perdew, K. Burke, M. Ernzerhof, Generalized gradient approximation made simple, *Phys Rev Lett*. 77 (**1996**) 3865. <https://doi.org/10.1103/PhysRevLett.77.3865>.
- [54] A.D. Becke, Density-functional thermochemistry. III. The role of exact exchange, *J Chem Phys*. 98 (**1993**) 5648–5652. <https://doi.org/10.1063/1.464913>.
- [55] S. Kümmel, L. Kronik, Orbital-dependent density functionals: Theory and applications, *Rev Mod Phys*. 80 (**2008**) 3–60. <https://doi.org/10.1103/RevModPhys.80.3>.
- [56] A. Savin, H.-J. Flad, Density functionals for the Yukawa electron-electron interaction, *Int J Quantum Chem*. 56 (**1995**) 327–332. <https://doi.org/10.1002/qua.560560417>.
- [57] T. Leininger, H. Stoll, H.-J. Werner, A. Savin, Combining long-range configuration interaction with short-range density functionals, *Chem Phys Lett*. 275 (**1997**) 151–160. [https://doi.org/10.1016/S0009-2614\(97\)00758-6](https://doi.org/10.1016/S0009-2614(97)00758-6).
- [58] T. Yanai, D.P. Tew, N.C. Handy, A new hybrid exchange–correlation functional using the Coulomb-attenuating method (CAM-B3LYP), *Chem Phys Lett*. 393 (**2004**) 51–57. <https://doi.org/10.1016/j.cplett.2004.06.011>.
- [59] A. Tkatchenko, M. Scheffler, Accurate molecular van der Waals interactions from ground-state electron density and free-atom reference data, *Phys Rev Lett*. 102 (**2009**) 6–9. <https://doi.org/10.1103/PhysRevLett.102.073005>.
- [60] S. Grimme, J. Antony, S. Ehrlich, H. Krieg, A consistent and accurate ab initio parametrization of density functional dispersion correction (DFT-D) for the 94 elements H-Pu, *J Chem Phys*. 132 (**2010**) 154104. <https://doi.org/10.1063/1.3382344>.
- [61] M. Dauth, M. Wiessner, V. Feyer, A. Schöll, P. Puschnig, F. Reinert, S. Kümmel, Angle resolved photoemission from organic semiconductors: Orbital imaging beyond the molecular orbital interpretation, *New J Phys*. 16 (**2014**). <https://doi.org/10.1088/1367-2630/16/10/103005>.
- [62] C.D. Dimitrakopoulos, P.R.L. Malenfant, Organic Thin Film Transistors for Large Area Electronics, *Advanced Materials*. 14 (**2002**) 99–117. [https://doi.org/10.1002/1521-4095\(20020116\)14:2<99::AID-ADMA99>3.0.CO;2-9](https://doi.org/10.1002/1521-4095(20020116)14:2<99::AID-ADMA99>3.0.CO;2-9).
- [63] N. Koch, Organic Electronic Devices and Their Functional Interfaces, *ChemPhysChem*. 8 (**2007**) 1438–1455. <https://doi.org/10.1002/cphc.200700177>.

- [64] C. Hetzer, D.M. Guldi, R.R. Tykwinski, Pentacene Dimers as a Critical Tool for the Investigation of Intramolecular Singlet Fission, *Chemistry – A European Journal*. 24 (2018) 8245–8257. <https://doi.org/10.1002/chem.201705355>.
- [65] A.F. Paterson, S. Singh, K.J. Fallon, T. Hodsden, Y. Han, B.C. Schroeder, H. Bronstein, M. Heeney, I. McCulloch, T.D. Anthopoulos, Recent Progress in High-Mobility Organic Transistors: A Reality Check, *Advanced Materials*. 30 (2018) 1–33. <https://doi.org/10.1002/adma.201801079>.
- [66] R.R. Tykwinski, Synthesis of Unsymmetrical Derivatives of Pentacene for Materials Applications, *Acc Chem Res*. 52 (2019) 2056–2069. <https://doi.org/10.1021/acs.accounts.9b00216>.
- [67] M. Bendikov, F. Wudl, D.F. Perepichka, Tetrathiafulvalenes, Oligoacenenenes, and Their Buckminsterfullerene Derivatives: The Brick and Mortar of Organic Electronics, *Chem Rev*. 104 (2004) 4891–4946. <https://doi.org/10.1021/cr030666m>.
- [68] N. V Korovina, N.F. Pompetti, J.C. Johnson, Lessons from intramolecular singlet fission with covalently bound chromophores, *J Chem Phys*. 152 (2020) 040904. <https://doi.org/10.1063/1.5135307>.
- [69] W. Fudickar, T. Linker, Why Triple Bonds Protect Acenes from Oxidation and Decomposition, *J Am Chem Soc*. 134 (2012) 15071–15082. <https://doi.org/10.1021/ja306056x>.
- [70] S.S. Zade, N. Zamoshchik, A.R. Reddy, G. Fridman-Marueli, D. Sheberla, M. Bendikov, Products and mechanism of acene dimerization. A computational study, *J Am Chem Soc*. 133 (2011) 10803–10816. <https://doi.org/10.1021/ja106594v>.
- [71] J.I. Urgel, S. Mishra, H. Hayashi, J. Wilhelm, C.A. Pignedoli, M. Di Giovannantonio, R. Widmer, M. Yamashita, N. Hieda, P. Ruffieux, H. Yamada, R. Fasel, On-surface light-induced generation of higher acenes and elucidation of their open-shell character, *Nat Commun*. 10 (2019) 1–9. <https://doi.org/10.1038/s41467-019-08650-y>.
- [72] M. Zugermeier, M. Gruber, M. Schmid, B.P. Klein, L. Ruppenthal, P. Müller, R. Einholz, W. Hieringer, R. Berndt, H.F. Bettinger, J.M. Gottfried, On-surface synthesis of heptacene and its interaction with a metal surface, *Nanoscale*. 9 (2017) 12461–12469. <https://doi.org/10.1039/c7nr04157h>.
- [73] J. Krüger, F. García, F. Eisenhut, D. Skidin, J.M. Alonso, E. Guitián, D. Pérez, G. Cuniberti, F. Moresco, D. Peña, Decacene: On-Surface Generation, *Angewandte Chemie - International Edition*. 56 (2017) 11945–11948. <https://doi.org/10.1002/anie.201706156>.
- [74] R. Zuzak, R. Dorel, M. Kolmer, M. Szymonski, S. Godlewski, A.M. Echavarren, Higher Acenes by On-Surface Dehydrogenation: From Heptacene to Undecacene, *Angewandte Chemie - International Edition*. 57 (2018) 10500–10505. <https://doi.org/10.1002/anie.201802040>.
- [75] R. Zuzak, R. Dorel, M. Krawiec, B. Such, M. Kolmer, M. Szymonski, A.M. Echavarren, S. Godlewski, Nonacene Generated by On-Surface Dehydrogenation, *ACS Nano*. 11 (2017) 9321–9329. <https://doi.org/10.1021/acsnano.7b04728>.
- [76] L. Colazzo, M.S.G. Mohammed, R. Dorel, P. Nita, C. García Fernández, P. Abufager, N. Lorente, A.M. Echavarren, D.G. De Oteyza, On-surface synthesis of heptacene on Ag(001) from brominated and non-brominated tetrahydroheptacene precursors, *Chemical Communications*. 54 (2018) 10260–10263. <https://doi.org/10.1039/C8CC04402C>.
- [77] F. Eisenhut, T. Kühne, F. García, S. Fernández, E. Guitián, D. Pérez, G. Trinquier, G. Cuniberti, C. Joachim, D. Peña, F. Moresco, Dodecacene Generated on Surface: Reopening of the Energy Gap, *ACS Nano*. 14 (2020) 1011–1017. <https://doi.org/10.1021/acsnano.9b08456>.

- [78] C. Tönshoff, H.F. Bettinger, Pushing the Limits of Acene Chemistry: The Recent Surge of Large Acenes, *Chemistry – A European Journal*. 27 (2021) 3193–3212. <https://doi.org/10.1002/chem.202003112>.
- [79] J. Krüger, F. Eisenhut, D. Skidin, T. Lehmann, D.A. Ryndyk, G. Cuniberti, F. García, J.M. Alonso, E. Guitián, D. Pérez, D. Peña, G. Trinquier, J.-P. Malrieu, F. Moresco, C. Joachim, Electronic Resonances and Gap Stabilization of Higher Acenes on a Gold Surface, *ACS Nano*. 12 (2018) 8506–8511. <https://doi.org/10.1021/acsnano.8b04046>.
- [80] P. Grüninger, M. Polek, M. Ivanović, D. Balle, R. Karstens, P. Nagel, M. Merz, S. Schuppler, R. Ovsyannikov, H.F. Bettinger, H. Peisert, T. Chassé, Electronic Structure of Hexacene and Interface Properties on Au(110), *The Journal of Physical Chemistry C*. 122 (2018) 19491–19498. <https://doi.org/10.1021/acs.jpcc.8b04274>.
- [81] P. Grüninger, K. Greulich, R. Karstens, A. Belser, R. Ovsyannikov, E. Giangrisostomi, H.F. Bettinger, D. Batchelor, H. Peisert, T. Chassé, Highly Oriented Hexacene Molecules Grown in Thin Films on Cu(110)–(2 × 1)O, *The Journal of Physical Chemistry C*. 123 (2019) 27672–27680. <https://doi.org/10.1021/acs.jpcc.9b08837>.
- [82] A. Ferretti, C. Baldacchini, A. Calzolari, R. Di Felice, A. Ruini, E. Molinari, M.G. Betti, Mixing of Electronic States in Pentacene Adsorption on Copper, *Phys Rev Lett*. 99 (2007) 46802. <https://doi.org/10.1103/PhysRevLett.99.046802>.
- [83] C. Baldacchini, F. Allegretti, R. Gunnella, M.G. Betti, Molecule–metal interaction of pentacene on copper vicinal surfaces, *Surf Sci*. 601 (2007) 2603–2606. <https://doi.org/10.1016/j.susc.2006.12.016>.
- [84] N. Koch, A. Gerlach, S. Duhm, H. Glowatzki, G. Heimel, A. Vollmer, Y. Sakamoto, T. Suzuki, J. Zegenhagen, J.P. Rabe, F. Schreiber, Adsorption-Induced Intramolecular Dipole: Correlating Molecular Conformation and Interface Electronic Structure, *J Am Chem Soc*. 130 (2008) 7300–7304. <https://doi.org/10.1021/ja800286k>.
- [85] T. Ules, D. Lüftner, E.M. Reinisch, G. Koller, P. Puschnig, M.G. Ramsey, Orbital tomography of hybridized and dispersing molecular overlayers, *Phys Rev B Condens Matter Mater Phys*. 90 (2014) 1–8. <https://doi.org/10.1103/PhysRevB.90.155430>.
- [86] X. Yang, L. Egger, J. Fuchsberger, M. Unzog, D. Lüftner, F. Hajek, P. Hurdax, M. Jugovac, G. Zamborlini, V. Feyer, G. Koller, P. Puschnig, F.S. Tautz, M.G. Ramsey, S. Soubatch, Coexisting Charge States in a Unary Organic Monolayer Film on a Metal, *J Phys Chem Lett*. 10 (2019) 6438–6445. <https://doi.org/10.1021/acs.jpcclett.9b02231>.
- [87] M.S. Wagner, Untersuchung der elektronischen Struktur von längeren Acenen an der Grenzfläche zum Metall, im Film und in der Gasphase, Doctoral Thesis, Eberhard Karls Universität Tübingen, 2023. <http://dx.doi.org/10.15496/publikation-83629> (accessed September 17, 2023).
- [88] L. Egger, Photoemission tomography of oriented molecular films, Doctoral Thesis, University of Graz, 2020. <https://doi.org/urn:nbn:at:at-ubg:1-161958>.
- [89] F. Maass, M. Ajdari, F.C. Kabeer, M. Vogtland, A. Tkatchenko, P. Tegeder, Nonadditivity of the Adsorption Energies of Linear Acenes on Au(111): Molecular Anisotropy and Many-Body Effects, *Journal of Physical Chemistry Letters*. 10 (2019) 1000–1004. <https://doi.org/10.1021/acs.jpcclett.9b00265>.
- [90] Y. Jiang, S. Yang, S. Li, W. Liu, Aromatic molecules on low-index coinage metal surfaces: Many-body dispersion effects, *Sci Rep*. 6 (2016) 1–8. <https://doi.org/10.1038/srep39529>.
- [91] S.J. Carey, W. Zhao, C.T. Campbell, Energetics of adsorbed benzene on Ni(111) and Pt(111) by calorimetry, *Surf Sci*. 676 (2018) 9–16. <https://doi.org/10.1016/j.susc.2018.02.014>.
- [92] H. Ihm, H.M. Ajo, J.M. Gottfried, P. Bera, C.T. Campbell, Calorimetric Measurement of the Heat of Adsorption of Benzene on Pt(111), *J Phys Chem B*. 108 (2004) 14627–14633. <https://doi.org/10.1021/jp040159o>.

- [93] C. Morin, D. Simon, P. Sautet, Chemisorption of Benzene on Pt(111), Pd(111), and Rh(111) Metal Surfaces: A Structural and Vibrational Comparison from First Principles, *J Phys Chem B*. 108 (2004) 5653–5665. <https://doi.org/10.1021/jp0373503>.
- [94] J.M. Gottfried, E.K. Vestergaard, P. Bera, C.T. Campbell, Heat of Adsorption of Naphthalene on Pt(111) Measured by Adsorption Calorimetry, *J Phys Chem B*. 110 (2006) 17539–17545. <https://doi.org/10.1021/jp062659i>.
- [95] T.L. Silbaugh, C.T. Campbell, Energies of Formation Reactions Measured for Adsorbates on Late Transition Metal Surfaces, *The Journal of Physical Chemistry C*. 120 (2016) 25161–25172. <https://doi.org/10.1021/acs.jpcc.6b06154>.
- [96] X. Crispin, V. Geskin, A. Crispin, J. Cornil, R. Lazzaroni, W.R. Salaneck, J.-L. Brédas, Characterization of the Interface Dipole at Organic/ Metal Interfaces, *J Am Chem Soc*. 124 (2002) 8131–8141. <https://doi.org/10.1021/ja025673r>.
- [97] G. Henkelman, A. Arnaldsson, H. Jónsson, A fast and robust algorithm for Bader decomposition of charge density, *Comput Mater Sci*. 36 (2006) 354–360. <https://doi.org/10.1016/j.commatsci.2005.04.010>.
- [98] D. Brandstetter, X. Yang, D. Lüftner, F.S. Tautz, P. Puschnig, kMap.py: A Python program for simulation and data analysis in photoemission tomography, *Comput Phys Commun*. 263 (2021) 107905. <https://doi.org/10.1016/j.cpc.2021.107905>.
- [99] D. Lüftner, M. Milko, S. Huppmann, M. Scholz, N. Ngyuen, M. Wießner, A. Schöll, F. Reinert, P. Puschnig, CuPc/Au(110): Determination of the azimuthal alignment by a combination of angle-resolved photoemission and density functional theory, *J Electron Spectros Relat Phenomena*. 195 (2014) 293–300. <https://doi.org/10.1016/j.elspec.2014.06.002>.
- [100] B. Stadtmüller, M. Willenbockel, E.M. Reinisch, T. Ules, F.C. Bocquet, S. Soubatch, P. Puschnig, G. Koller, M.G. Ramsey, F.S. Tautz, C. Kumpf, Orbital tomography for highly symmetric adsorbate systems, *Europhys Lett*. 100 (2012) 26008. <https://doi.org/10.1209/0295-5075/100/26008>.
- [101] P. Kliuiev, G. Zamborlini, M. Jugovac, Y. Gurdal, K. von Arx, K. Waltar, S. Schnidrig, R. Alberto, M. Iannuzzi, V. Feyrer, M. Hengsberger, J. Osterwalder, L. Castiglioni, Combined orbital tomography study of multi-configurational molecular adsorbate systems, *Nat Commun*. 10 (2019) 5255. <https://doi.org/10.1038/s41467-019-13254-7>.
- [102] K. Takasugi, T. Yokoyama, Coverage induced structural transformations of tetracene on Ag(110), *J Chem Phys*. 144 (2016) 104702. <https://doi.org/10.1063/1.4943576>.
- [103] R. Einholz, T. Fang, R. Berger, P. Grüninger, A. Früh, T. Chassé, R.F. Fink, H.F. Bettinger, Heptacene: Characterization in Solution, in the Solid State, and in Films, *J Am Chem Soc*. 139 (2017) 4435–4442. <https://doi.org/10.1021/jacs.6b13212>.
- [104] M. Alagia, C. Baldacchini, M.G. Betti, F. Bussoletti, V. Carravetta, U. Ekström, C. Mariani, S. Stranges, Core-shell photoabsorption and photoelectron spectra of gas-phase pentacene: Experiment and theory, *J Chem Phys*. 122 (2005) 124305. <https://doi.org/10.1063/1.1864852>.
- [105] G. Kaindl, T.-C. Chiang, D.E. Eastman, F.J. Himpsel, Distance-Dependent Relaxation Shifts of Photoemission and Auger Energies for Xe on Pd(001), *Phys Rev Lett*. 45 (1980) 1808–1811. <https://doi.org/10.1103/PhysRevLett.45.1808>.
- [106] H. Peisert, D. Kolacyak, T. Chassé, Site-Specific Charge-Transfer Screening at Organic/Metal Interfaces, *The Journal of Physical Chemistry C*. 113 (2009) 19244–19250. <https://doi.org/10.1021/jp9057548>.
- [107] I. Cojocariu, H.M. Sturmeit, G. Zamborlini, A. Cossaro, A. Verdini, L. Floreano, E. D’Incecco, M. Stredansky, E. Vesselli, M. Jugovac, M. Cinchetti, V. Feyrer, C.M. Schneider, Evaluation of molecular orbital symmetry via oxygen-induced charge

- transfer quenching at a metal-organic interface, *Appl Surf Sci.* 504 (2020) 144343. <https://doi.org/10.1016/j.apsusc.2019.144343>.
- [108] M. Koini, T. Haber, O. Werzer, S. Berkebile, G. Koller, M. Oehzelt, M.G. Ramsey, R. Resel, Epitaxial order of pentacene on Cu(110)-(2×1)O: One dimensional alignment induced by surface corrugation, *Thin Solid Films.* 517 (2008) 483–487. <https://doi.org/10.1016/j.tsf.2008.06.053>.
- [109] M. Koini, T. Haber, S. Berkebile, G. Koller, M.G. Ramsey, R. Resel, M. Oehzelt, Growth of sexithiophene crystals on Cu(110) and Cu(110)-(2×1)O stripe phase—The influence of surface corrugation, *J Cryst Growth.* 311 (2009) 1364–1369. <https://doi.org/10.1016/j.jcrysro.2009.01.018>.
- [110] M. Oehzelt, L. Grill, S. Berkebile, G. Koller, F.P. Netzer, M.G. Ramsey, The Molecular Orientation of para-Sexiphenyl on Cu(110) and Cu(110) p(2×1)O, *ChemPhysChem.* 8 (2007) 1707–1712. <https://doi.org/10.1002/cphc.200700357>.
- [111] V. Coropceanu, J. Cornil, D.A. da Silva Filho, Y. Olivier, R. Silbey, J.-L. Brédas, Charge Transport in Organic Semiconductors, *Chem Rev.* 107 (2007) 926–952. <https://doi.org/10.1021/cr050140x>.
- [112] H. Yoshida, N. Sato, Crystallographic and electronic structures of three different polymorphs of pentacene, *Phys Rev B.* 77 (2008) 235205. <https://doi.org/10.1103/PhysRevB.77.235205>.
- [113] S. Berkebile, G. Koller, P. Puschnig, C. Ambrosch-Draxl, F.P. Netzer, M.G. Ramsey, Angle-resolved photoemission of chain-like molecules: the electronic band structure of sexithiophene and sexiphenyl, *Applied Physics A.* 95 (2009) 101–105. <https://doi.org/10.1007/s00339-008-5034-9>.
- [114] F. Bussolotti, Y. Yamada-Takamura, Y. Wang, R. Friedlein, Structure-dependent band dispersion in epitaxial anthracene films, *J Chem Phys.* 135 (2011) 124709. <https://doi.org/10.1063/1.3643717>.
- [115] J. Klimeš, D.R. Bowler, A. Michaelides, Chemical accuracy for the van der Waals density functional, *Journal of Physics: Condensed Matter.* 22 (2010) 022201. <https://doi.org/10.1088/0953-8984/22/2/022201>.
- [116] A. V Krukau, O.A. Vydrov, A.F. Izmaylov, G.E. Scuseria, Influence of the exchange screening parameter on the performance of screened hybrid functionals, *J Chem Phys.* 125 (2006) 224106. <https://doi.org/10.1063/1.2404663>.
- [117] T. Körzdörfer, S. Kümmel, N. Marom, L. Kronik, When to trust photoelectron spectra from Kohn-Sham eigenvalues: The case of organic semiconductors, *Phys Rev B.* 79 (2009) 201205. <https://doi.org/10.1103/PhysRevB.79.201205>.
- [118] D. Lüftner, S. Refaely-Abramson, M. Pachler, R. Resel, M.G. Ramsey, L. Kronik, P. Puschnig, Experimental and theoretical electronic structure of quinacridone, *Phys Rev B.* 90 (2014) 75204. <https://doi.org/10.1103/PhysRevB.90.075204>.
- [119] L. Kronik, S. Kümmel, Piecewise linearity, freedom from self-interaction, and a Coulomb asymptotic potential: three related yet inequivalent properties of the exact density functional, *Physical Chemistry Chemical Physics.* 22 (2020) 16467–16481. <https://doi.org/10.1039/D0CP02564J>.
- [120] S. Refaely-Abramson, S. Sharifzadeh, N. Govind, J. Autschbach, J.B. Neaton, R. Baer, L. Kronik, Quasiparticle Spectra from a Nonempirical Optimally Tuned Range-Separated Hybrid Density Functional, *Phys Rev Lett.* 109 (2012) 226405. <https://doi.org/10.1103/PhysRevLett.109.226405>.
- [121] N. Dori, M. Menon, L. Kilian, M. Sokolowski, L. Kronik, E. Umbach, Valence electronic structure of gas-phase 3,4,9,10-perylene tetracarboxylic acid dianhydride: Experiment and theory, *Phys Rev B.* 73 (2006) 195208. <https://doi.org/10.1103/PhysRevB.73.195208>.

- [122] P. Mori-Sánchez, A.J. Cohen, W. Yang, Many-electron self-interaction error in approximate density functionals, *J Chem Phys.* 125 (2006) 201102. <https://doi.org/10.1063/1.2403848>.
- [123] J.P. Perdew, R.G. Parr, M. Levy, J.L. Balduz, Density-Functional Theory for Fractional Particle Number: Derivative Discontinuities of the Energy, *Phys Rev Lett.* 49 (1982) 1691–1694. <https://doi.org/10.1103/PhysRevLett.49.1691>.
- [124] B. Himmetoglu, A. Floris, S. de Gironcoli, M. Cococcioni, Hubbard-corrected DFT energy functionals: The LDA+U description of correlated systems, *Int J Quantum Chem.* 114 (2014) 14–49. <https://doi.org/10.1002/qua.24521>.
- [125] H.J. Kulik, Perspective: Treating electron over-delocalization with the DFT+U method, *J Chem Phys.* 142 (2015) 240901. <https://doi.org/10.1063/1.4922693>.
- [126] J.P. Janet, Q. Zhao, E.I. Ioannidis, H.J. Kulik, Density functional theory for modelling large molecular adsorbate–surface interactions: a mini-review and worked example, *Mol Simul.* 43 (2017) 327–345. <https://doi.org/10.1080/08927022.2016.1258465>.
- [127] V.I. Anisimov, J. Zaanen, O.K. Andersen, Band theory and Mott insulators: Hubbard U instead of Stoner I, *Phys Rev B.* 44 (1991) 943–954. <https://doi.org/10.1103/PhysRevB.44.943>.
- [128] A.I. Liechtenstein, V.I. Anisimov, J. Zaanen, Density-functional theory and strong interactions: Orbital ordering in Mott-Hubbard insulators, *Phys Rev B.* 52 (1995) R5467–R5470. <https://doi.org/10.1103/PhysRevB.52.R5467>.
- [129] S.L. Dudarev, G.A. Botton, S.Y. Savrasov, C.J. Humphreys, A.P. Sutton, Electron-energy-loss spectra and the structural stability of nickel oxide: An LSDA+U study, *Phys Rev B.* 57 (1998) 1505–1509. <https://doi.org/10.1103/PhysRevB.57.1505>.
- [130] T.G. Gopakumar, F. Matino, H. Naggert, A. Bannwarth, F. Tuczek, R. Berndt, Electron-Induced Spin Crossover of Single Molecules in a Bilayer on Gold, *Angewandte Chemie International Edition.* 51 (2012) 6262–6266. <https://doi.org/10.1002/anie.201201203>.
- [131] S. Bhandary, B. Brena, P.M. Panchmatia, I. Brumboiu, M. Bernien, C. Weis, B. Krumme, C. Etz, W. Kuch, H. Wende, O. Eriksson, B. Sanyal, Manipulation of spin state of iron porphyrin by chemisorption on magnetic substrates, *Phys. Rev. B.* 88 (2013) 24401. <https://doi.org/10.1103/PhysRevB.88.024401>.
- [132] I. Cojocariu, S. Carlotto, H.M. Sturmeit, G. Zamborlini, M. Cinchetti, A. Cossaro, A. Verdini, L. Floreano, M. Jugovac, P. Puschnig, C. Piamonteze, M. Casarin, V. Feyrer, C.M. Schneider, Ferrous to Ferric Transition in Fe-Phthalocyanine Driven by NO₂ Exposure, *Chemistry – A European Journal.* 27 (2021) 3526–3535. <https://doi.org/10.1002/chem.202004932>.
- [133] A. Köbke, F. Gutzeit, F. Röhricht, A. Schlimm, J. Grunwald, F. Tuczek, M. Studniarek, D. Longo, F. Choueikani, E. Otero, P. Ohresser, S. Rohlf, S. Johannsen, F. Diekmann, K. Rossnagel, A. Weismann, T. Jasper-Toennies, C. Näther, R. Herges, R. Berndt, M. Gruber, Reversible coordination-induced spin-state switching in complexes on metal surfaces, *Nat Nanotechnol.* 15 (2020) 18–21. <https://doi.org/10.1038/s41565-019-0594-8>.
- [134] T. Komeda, H. Isshiki, J. Liu, Y.-F. Zhang, N. Lorente, K. Katoh, B.K. Breedlove, M. Yamashita, Observation and electric current control of a local spin in a single-molecule magnet, *Nat Commun.* 2 (2011) 217. <https://doi.org/10.1038/ncomms1210>.
- [135] T. Miyamachi, M. Gruber, V. Davesne, M. Bowen, S. Boukari, L. Joly, F. Scheurer, G. Rogez, T.K. Yamada, P. Ohresser, E. Beaurepaire, W. Wulfhekel, Robust spin crossover and memristance across a single molecule, *Nat Commun.* 3 (2012) 938. <https://doi.org/10.1038/ncomms1940>.
- [136] P. Atkins, J. Paula, Physical Chemistry, 9th ed., W. H. Freeman Co., New York, 2010.

- [137] I.E. Brumboiu, S. Haldar, J. Lüder, O. Eriksson, H.C. Herper, B. Brena, B. Sanyal, Influence of Electron Correlation on the Electronic Structure and Magnetism of Transition-Metal Phthalocyanines, *J Chem Theory Comput.* 12 (2016) 1772–1785. <https://doi.org/10.1021/acs.jctc.6b00091>.
- [138] I.E. Brumboiu, S. Haldar, J. Lüder, O. Eriksson, H.C. Herper, B. Brena, B. Sanyal, Ligand Effects on the Linear Response Hubbard U: The Case of Transition Metal Phthalocyanines, *J Phys Chem A.* 123 (2019) 3214–3222. <https://doi.org/10.1021/acs.jpca.8b11940>.
- [139] L. Ottaviano, S. Di Nardo, L. Lozzi, M. Passacantando, P. Picozzi, S. Santucci, Thin and ultra-thin films of nickel phthalocyanine grown on highly oriented pyrolytic graphite: an XPS, UHV-AFM and air tapping-mode AFM study, *Surf Sci.* 373 (1997) 318–332. [https://doi.org/10.1016/S0039-6028\(96\)01179-X](https://doi.org/10.1016/S0039-6028(96)01179-X).
- [140] F. Petraki, V. Papaefthimiou, S. Kennou, The electronic structure of Ni-phthalocyanine/metal interfaces studied by X-ray and ultraviolet photoelectron spectroscopy, *Org Electron.* 8 (2007) 522–528. <https://doi.org/10.1016/j.orgel.2007.03.006>.
- [141] A. Casotto, G. Drera, D. Perilli, S. Freddi, S. Pagliara, M. Zanotti, L. Schio, A. Verdini, L. Floreano, C. Di Valentin, L. Sangaletti, π -Orbital mediated charge transfer channels in a monolayer Gr–NiPc heterointerface unveiled by soft X-ray electron spectroscopies and DFT calculations, *Nanoscale.* 14 (2022) 13166–13177. <https://doi.org/10.1039/D2NR02647C>.
- [142] H.M. Sturmeit, I. Cojocariu, M. Jugovac, A. Cossaro Albano and Verdini, L. Floreano, A. Sala, G. Comelli, S. Moro, M. Stredansky, M. Corva, E. Vesselli, P. Puschnig, C.M. Schneider, V. Feyer, G. Zamborlini, M. Cinchetti, Molecular anchoring stabilizes low valence Ni(i)TPP on copper against thermally induced chemical changes, *J Mater Chem C Mater.* 8 (2020) 8876–8886. <https://doi.org/10.1039/D0TC00946F>.
- [143] L.M. Arruda, Md.E. Ali, M. Bernien, F. Nickel, J. Kopprasch, C. Czekelius, P.M. Oppeneer, W. Kuch, Modifying the Magnetic Anisotropy of an Iron Porphyrin Molecule by an on-Surface Ring-Closure Reaction, *The Journal of Physical Chemistry C.* 123 (2019) 14547–14555. <https://doi.org/10.1021/acs.jpcc.9b03126>.
- [144] S. Thies, H. Sell, C. Schütt, C. Bornholdt, C. Näther, F. Tuzek, R. Herges, Light-Induced Spin Change by Photodissociable External Ligands: A New Principle for Magnetic Switching of Molecules, *J Am Chem Soc.* 133 (2011) 16243–16250. <https://doi.org/10.1021/ja206812f>.
- [145] S. Al Shehimi, O. Baydoun, S. Denis-Quanquin, J.-C. Mulatier, L. Khrouz, D. Frath, É. Dumont, M. Murugesu, F. Chevallier, C. Bucher, Ni-Centered Coordination-Induced Spin-State Switching Triggered by Electrical Stimulation, *J Am Chem Soc.* 144 (2022) 17955–17965. <https://doi.org/10.1021/jacs.2c07196>.
- [146] M.F. Perutz, Stereochemistry of Cooperative Effects in Haemoglobin: Haem–Haem Interaction and the Problem of Allostery, *Nature.* 228 (1970) 726–734. <https://doi.org/10.1038/228726a0>.
- [147] M.F. Perutz, A.J. Wilkinson, M. Paoli, G.G. Dodson, THE STEREOCHEMICAL MECHANISM OF THE COOPERATIVE EFFECTS IN HEMOGLOBIN REVISITED, *Annu Rev Biophys Biomol Struct.* 27 (1998) 1–34. <https://doi.org/10.1146/annurev.biophys.27.1.1>.
- [148] R.N. Pittman, Regulation of Tissue Oxygenation, Morgan & Claypool Life Sciences, San Rafael (CA), 2011.
- [149] K. Seufert, W. Auwärter, J. V Barth, Discriminative Response of Surface-Confined Metalloporphyrin Molecules to Carbon and Nitrogen Monoxide, *J Am Chem Soc.* 132 (2010) 18141–18146. <https://doi.org/10.1021/ja1054884>.

- [150] C. Wäckerlin, D. Chylarecka, A. Kleibert, K. Müller, C. Iacovita, F. Nolting, T.A. Jung, N. Ballav, Controlling spins in adsorbed molecules by a chemical switch, *Nat Commun.* 1 (2010) 61. <https://doi.org/10.1038/ncomms1057>.
- [151] J. Miguel, C.F. Hermanns, M. Bernien, A. Krüger, W. Kuch, Reversible Manipulation of the Magnetic Coupling of Single Molecular Spins in Fe-Porphyrins to a Ferromagnetic Substrate, *J Phys Chem Lett.* 2 (2011) 1455–1459. <https://doi.org/10.1021/jz200489y>.
- [152] C. Wäckerlin, K. Tarafder, D. Siewert, J. Girovsky, T. Hählen, C. Iacovita, A. Kleibert, F. Nolting, P.M. Jung Thomas A. and Oppeneer, N. Ballav, On-surface coordination chemistry of planar molecular spin systems: novel magnetochemical effects induced by axial ligands, *Chem Sci.* 3 (2012) 3154–3160. <https://doi.org/10.1039/C2SC20828H>.
- [153] C. Wäckerlin, K. Tarafder, J. Girovsky, J. Nowakowski, T. Hählen, A. Shchyrba, D. Siewert, A. Kleibert, P.M. Nolting Frithjof and Oppeneer, T.A. Jung, N. Ballav, Ammonia Coordination Introducing a Magnetic Moment in an On-Surface Low-Spin Porphyrin, *Angewandte Chemie International Edition.* 52 (2013) 4568–4571. <https://doi.org/10.1002/anie.201208028>.
- [154] M.H. Chang, N.-Y. Kim, Y.H. Chang, Y. Lee, U.S. Jeon, H. Kim, Y.-H. Kim, S.-J. Kahng, O₂, NO₂ and NH₃ coordination to Co-porphyrin studied with scanning tunneling microscopy on Au(111), *Nanoscale.* 11 (2019) 8510–8517. <https://doi.org/10.1039/C9NR00843H>.
- [155] I. Cojocariu, S. Carlotto, G. Zamborlini, M. Jugovac, L. Schio, L. Floreano, M. Casarin, V. Feyrer, C.M. Schneider, Reversible redox reactions in metal-supported porphyrin: the role of spin and oxidation state, *J Mater Chem C Mater.* 9 (2021) 12559–12565. <https://doi.org/10.1039/D1TC02222A>.
- [156] J.B. Neaton, M.S. Hybertsen, S.G. Louie, Renormalization of Molecular Electronic Levels at Metal-Molecule Interfaces, *Phys. Rev. Lett.* 97 (2006) 216405. <https://doi.org/10.1103/PhysRevLett.97.216405>.
- [157] A. Stroppa, G. Kresse, The shortcomings of semi-local and hybrid functionals: what we can learn from surface science studies, *New J Phys.* 10 (2008) 63020. <https://doi.org/10.1088/1367-2630/10/6/063020>.
- [158] J.M. Garcia-Lastra, C. Rostgaard, A. Rubio, K.S. Thygesen, Polarization-induced renormalization of molecular levels at metallic and semiconducting surfaces, *Phys. Rev. B.* 80 (2009) 245427. <https://doi.org/10.1103/PhysRevB.80.245427>.
- [159] N. Gerrits, E.W.F. Smeets, S. Vuckovic, A.D. Powell, K. Doblhoff-Dier, G.-J. Kroes, Density Functional Theory for Molecule–Metal Surface Reactions: When Does the Generalized Gradient Approximation Get It Right, and What to Do If It Does Not, *J Phys Chem Lett.* 11 (2020) 10552–10560. <https://doi.org/10.1021/acs.jpcclett.0c02452>.
- [160] H. Tang, N. Tarrat, V. Langlais, Y. Wang, Adsorption of iron tetraphenylporphyrin on (111) surfaces of coinage metals: a density functional theory study, *Beilstein Journal of Nanotechnology.* 8 (2017) 2484–2491. <https://doi.org/10.3762/bjnano.8.248>.
- [161] B. Chilukuri, U. Mazur, K.W. Hipps, Structure, Properties, and Reactivity of Porphyrins on Surfaces and Nanostructures with Periodic DFT Calculations, 10 (2020). <https://doi.org/10.3390/app10030740>.
- [162] S. Ninova, O.B. Malçoğlu, P. Auburger, M. Franke, O. Lytken, H.-P. Steinrück, M. Bockstedte, Morphology dependent interaction between Co(ii)-tetraphenylporphyrin and the MgO(100) surface, *Physical Chemistry Chemical Physics.* 23 (2021) 2105–2116. <https://doi.org/10.1039/D0CP04859C>.
- [163] L. Schio, D. Forrer, M. Casarin, A. Goldoni, C. Rogero, A. Vittadini, L. Floreano, On surface chemical reactions of free-base and titanyl porphyrins with r-TiO₂(110): a unified picture, *Physical Chemistry Chemical Physics.* 24 (2022) 12719–12744. <https://doi.org/10.1039/D2CP01073A>.

- [164] W. Hieringer, K. Flechtner, A. Kretschmann, K. Seufert, W. Auwärter, J. V Barth, A. Görling, J.M. Steinrück Hans-Peter and Gottfried, The Surface Trans Effect: Influence of Axial Ligands on the Surface Chemical Bonds of Adsorbed Metalloporphyrins, *J Am Chem Soc.* 133 (2011) 6206–6222. <https://doi.org/10.1021/ja1093502>.
- [165] S. Carlotto, I. Cojocariu, V. Feyer, L. Floreano, M. Casarin, The Magnetic Behaviour of CoTPP Supported on Coinage Metal Surfaces in the Presence of Small Molecules: A Molecular Cluster Study of the Surface trans-Effect, 12 (2022). <https://doi.org/10.3390/nano12020218>.
- [166] G. Zamborlini, M. Jugovac, A. Cossaro, A. Verdini, L. Floreano, D. Lüftner, P. Puschnig, V. Feyer, C.M. Schneider, On-surface nickel porphyrin mimics the reactive center of an enzyme cofactor, *Chemical Communications.* 54 (2018) 13423–13426. <https://doi.org/10.1039/C8CC06739B>.
- [167] S. Thies, C. Bornholdt, F. Köhler, F.D. Sönnichsen, C. Näther, F. Tuczek, R. Herges, Coordination-Induced Spin Crossover (CISCO) through Axial Bonding of Substituted Pyridines to Nickel–Porphyrins: σ -Donor versus π -Acceptor Effects, *Chemistry – A European Journal.* 16 (2010) 10074–10083. <https://doi.org/10.1002/chem.201000603>.
- [168] L.J. Sham, M. Schlüter, Density-Functional Theory of the Energy Gap, *Phys. Rev. Lett.* 51 (1983) 1888–1891. <https://doi.org/10.1103/PhysRevLett.51.1888>.
- [169] P. Mori-Sánchez, A.J. Cohen, W. Yang, Localization and Delocalization Errors in Density Functional Theory and Implications for Band-Gap Prediction, *Phys. Rev. Lett.* 100 (2008) 146401. <https://doi.org/10.1103/PhysRevLett.100.146401>.
- [170] A.J.R. Hensley, K. Ghale, C. Rieg, T. Dang, F. Anderst Emily and Studt, C.T. Campbell, J.-S. McEwen, Y. Xu, DFT-Based Method for More Accurate Adsorption Energies: An Adaptive Sum of Energies from RPBE and vdW Density Functionals, *The Journal of Physical Chemistry C.* 121 (2017) 4937–4945. <https://doi.org/10.1021/acs.jpcc.6b10187>.
- [171] B.X. Shi, V. Kapil, A. Zen, J. Chen, A. Alavi, A. Michaelides, General embedded cluster protocol for accurate modeling of oxygen vacancies in metal-oxides, *J Chem Phys.* 156 (2022) 124704. <https://doi.org/10.1063/5.0087031>.
- [172] R.B. Araujo, G.L.S. Rodrigues, E.C. dos Santos, L.G.M. Pettersson, Adsorption energies on transition metal surfaces: towards an accurate and balanced description, *Nat Commun.* 13 (2022) 6853. <https://doi.org/10.1038/s41467-022-34507-y>.
- [173] E.M. Christlmaier, D. Kats, A. Alavi, D. Usvyat, Full configuration interaction quantum Monte Carlo treatment of fragments embedded in a periodic mean field, *J Chem Phys.* 156 (2022) 154107. <https://doi.org/10.1063/5.0084040>.
- [174] T. Mullan, L. Maschio, P. Saalfrank, D. Usvyat, Reaction barriers on non-conducting surfaces beyond periodic local MP2: Diffusion of hydrogen on α -Al₂O₃(0001) as a test case, *J Chem Phys.* 156 (2022) 74109. <https://doi.org/10.1063/5.0082805>.
- [175] P.M. Oppeneer, P.M. Panchmatia, B. Sanyal, O. Eriksson, Md.E. Ali, Nature of the magnetic interaction between Fe-porphyrin molecules and ferromagnetic surfaces, *Prog Surf Sci.* 84 (2009) 18–29. <https://doi.org/10.1016/j.progsurf.2008.12.001>.
- [176] Md.E. Ali, B. Sanyal, P.M. Oppeneer, Electronic Structure, Spin-States, and Spin-Crossover Reaction of Heme-Related Fe-Porphyrins: A Theoretical Perspective, *J Phys Chem B.* 116 (2012) 5849–5859. <https://doi.org/10.1021/jp3021563>.
- [177] A. Mugarza, R. Robles, C. Krull, R. Korytár, N. Lorente, P. Gambardella, Electronic and magnetic properties of molecule-metal interfaces: Transition-metal phthalocyanines adsorbed on Ag(100), *Phys. Rev. B.* 85 (2012) 155437. <https://doi.org/10.1103/PhysRevB.85.155437>.
- [178] C. Wäckerlin, P. Maldonado, L. Arnold, J. Shchyrba Aneliia and Girovsky, J. Nowakowski, Md.E. Ali, T. Hählen, M. Baljovic, D. Siewert, A. Kleibert, K. Müllen, T.A. Oppeneer Peter M. and Jung, N. Ballav, Magnetic exchange coupling of a synthetic

- Co(ii)-complex to a ferromagnetic Ni substrate, *Chemical Communications*. 49 (2013) 10736–10738. <https://doi.org/10.1039/C3CC45401K>.
- [179] A. Calloni, M.S. Jagadeesh, G. Bussetti, G. Fratesi, S. Achilli, A. Picone, A. Lodesani, A. Brambilla, C. Goletti, F. Ciccacci, L. Duò, M. Finazzi, A. Goldoni, A. Verdini, L. Floreano, Cobalt atoms drive the anchoring of Co-TPP molecules to the oxygen-passivated Fe(001) surface, *Appl Surf Sci*. 505 (2020) 144213. <https://doi.org/10.1016/j.apsusc.2019.144213>.
- [180] G. Fratesi, S. Achilli, A. Ugolotti, A. Lodesani, A. Picone, A. Brambilla, L. Floreano, A. Calloni, G. Bussetti, Nontrivial central-atom dependence in the adsorption of M-TPP molecules (M = Co, Ni, Zn) on Fe(001)-p(11)O, *Appl Surf Sci*. 530 (2020) 147085. <https://doi.org/10.1016/j.apsusc.2020.147085>.
- [181] P.J. Feibelman, B. Hammer, J.K. Nørskov, F. Wagner, M. Scheffler, R. Stumpf, R. Watwe, J. Dumesic, The CO/Pt(111) Puzzle, *J Phys Chem B*. 105 (2001) 4018–4025. <https://doi.org/10.1021/jp002302t>.
- [182] P.S. Deimel, R.M. Bababrik, B. Wang, P.J. Blowey, L.A. Rochford, P.K. Thakur, T.-L. Lee, M.-L. Bocquet, J. V Barth, D.P. Woodruff, D.A. Duncan, F. Allegretti, Direct quantitative identification of the “surface trans-effect”, *Chem Sci*. 7 (2016) 5647–5656. <https://doi.org/10.1039/C6SC01677D>.
- [183] H. Duval, V. Bulach, J. Fischer, R. Weiss, Four-Coordinate, Low-Spin (S = 0) and Six-Coordinate, High-Spin (S = 1) Nickel(II) Complexes of Tetraphenylporphyrins with β -Pyrrole Electron-Withdrawing Substituents: Porphyrin-Core Expansion and Conformation, *Inorg Chem*. 38 (1999) 5495–5501. <https://doi.org/10.1021/ic990231a>.
- [184] S. Venkataramani, U. Jana, M. Dommaschk, F.D. Sönnichsen, F. Tuczek, R. Herges, Magnetic Bistability of Molecules in Homogeneous Solution at Room Temperature, *Science (1979)*. 331 (2011) 445–448. <https://doi.org/10.1126/science.1201180>.
- [185] U. Ermler, W. Grabarse, S. Shima, M. Goubeaud, R.K. Thauer, Crystal Structure of Methyl-Coenzyme M Reductase: The Key Enzyme of Biological Methane Formation, *Science (1979)*. 278 (1997) 1457–1462. <https://doi.org/10.1126/science.278.5342.1457>.
- [186] T. Hino, Y. Matsumoto, S. Nagano, H. Sugimoto, Y. Fukumori, T. Murata, S. Iwata, Y. Shiro, Structural Basis of Biological N₂O Generation by Bacterial Nitric Oxide Reductase, *Science (1979)*. 330 (2010) 1666–1670. <https://doi.org/10.1126/science.1195591>.
- [187] S. Rendic, F.P. Guengerich, Survey of Human Oxidoreductases and Cytochrome P450 Enzymes Involved in the Metabolism of Xenobiotic and Natural Chemicals, *Chem Res Toxicol*. 28 (2015) 38–42. <https://doi.org/10.1021/tx500444e>.
- [188] B. Meunier, Metalloporphyrins as versatile catalysts for oxidation reactions and oxidative DNA cleavage, *Chem Rev*. 92 (1992) 1411–1456. <https://doi.org/10.1021/cr00014a008>.
- [189] M.C. Feiters, A.E. Rowan, R.J.M. Nolte, From simple to supramolecular cytochrome P450 mimics, *Chem Soc Rev*. 29 (2000) 375–384. <https://doi.org/10.1039/A804252G>.
- [190] M.M. Pereira, L.D. Dias, M.J.F. Calvete, Metalloporphyrins: Bioinspired Oxidation Catalysts, *ACS Catal*. 8 (2018) 10784–10808. <https://doi.org/10.1021/acscatal.8b01871>.
- [191] P. Gotico, Z. Halime, A. Aukauloo, Recent advances in metalloporphyrin-based catalyst design towards carbon dioxide reduction: from bio-inspired second coordination sphere modifications to hierarchical architectures, *Dalton Transactions*. 49 (2020) 2381–2396. <https://doi.org/10.1039/C9DT04709C>.
- [192] Z. Lyu, N. Shao, T. Akinyemi, W.B. Whitman, Methanogenesis, *Current Biology*. 28 (2018) R727–R732. <https://doi.org/10.1016/j.cub.2018.05.021>.

- [193] S.P.J. Albracht, D. Ankel-Fuchs, R. Böcher, J. Ellermann, J. Moll, J.W. van der Zwaan, R.K. Thauer, Five new EPR signals assigned to nickel in methyl-coenzyme M reductase from *Methanobacterium thermoautotrophicum*, strain Marburg, *Biochimica et Biophysica Acta (BBA) - Protein Structure and Molecular Enzymology*. 955 (1988) 86–102. [https://doi.org/10.1016/0167-4838\(88\)90182-3](https://doi.org/10.1016/0167-4838(88)90182-3).
- [194] U. Ermler, On the mechanism of methyl-coenzyme M reductase, *Dalton Transactions*. (2005) 3451–3458. <https://doi.org/10.1039/B506697B>.
- [195] N. Sheppard, C. De La Cruz, A systematic review of the application of vibrational spectroscopy to the determination of the structures of NO adsorbed on single-crystal metal surfaces, *Physical Chemistry Chemical Physics*. 12 (2010) 2275–2284. <https://doi.org/10.1039/B914016F>.
- [196] M. Minissale, G. Fedoseev, E. Congiu, S. Ioppolo, F. Dulieu, H. Linnartz, Solid state chemistry of nitrogen oxides – Part I: surface consumption of NO, *Physical Chemistry Chemical Physics*. 16 (2014) 8257–8269. <https://doi.org/10.1039/C3CP54917H>.
- [197] B. Ruscic, R.E. Pinzon, M.L. Morton, N.K. Srinivasan, M.-C. Su, J.W. Sutherland, J. V Michael, Active Thermochemical Tables: Accurate Enthalpy of Formation of Hydroperoxyl Radical, HO₂, *J Phys Chem A*. 110 (2006) 6592–6601. <https://doi.org/10.1021/jp056311j>.
- [198] L.V. Gurvich, I. V Veyts, C.B. Alcock, Thermodynamic Properties of Individual Substances, 4th ed., Hemisphere Pub. Co., New York, 1989.
- [199] H. Tsukahara, T. Ishida, Y. Todoroki, M. Hiraoka, M. Mayumi, Gas-phase Disproportionation of Nitric Oxide at Elevated Pressures, *Free Radic Res*. 37 (2003) 171–177. <https://doi.org/10.1080/1071576021000036489>.
- [200] C. Sun, L. Yang, M.A. Ortuño, A.M. Wright, T. Chen, A.R. Head, N. López, M. Dincă, Spectroscopic Evidence of Hyponitrite Radical Intermediate in NO Disproportionation at a MOF-Supported Mononuclear Copper Site, *Angewandte Chemie International Edition*. 60 (2021) 7845–7850. <https://doi.org/10.1002/anie.202015359>.
- [201] C.K. Brozek, J.T. Miller, S.A. Stoian, M. Dincă, NO Disproportionation at a Mononuclear Site-Isolated Fe²⁺ Center in Fe²⁺-MOF-5, *J Am Chem Soc*. 137 (2015) 7495–7501. <https://doi.org/10.1021/jacs.5b03761>.
- [202] J. Gwak, S. Ahn, M.-H. Baik, Y. Lee, One metal is enough: a nickel complex reduces nitrate anions to nitrogen gas, *Chem Sci*. 10 (2019) 4767–4774. <https://doi.org/10.1039/C9SC00717B>.
- [203] D. Denysenko, D. Volkmer, Cyclic gas-phase heterogeneous process in a metal–organic framework involving a nickel nitrosyl complex, *Faraday Discuss*. 201 (2017) 101–112. <https://doi.org/10.1039/C7FD00034K>.
- [204] S. Metz, N₂O Formation via Reductive Disproportionation of NO by Mononuclear Copper Complexes: A Mechanistic DFT Study, *Inorg Chem*. 56 (2017) 3820–3833. <https://doi.org/10.1021/acs.inorgchem.6b02551>.
- [205] M.D. Brookes, A.R.W. McKellar, T. Amano, Millimeter-Wave Spectrum of the NO Dimer, *J Mol Spectrosc*. 185 (1997) 153–157. <https://doi.org/10.1006/jmsp.1997.7357>.
- [206] E.A. Wade, J.I. Cline, K.T. Lorenz, C. Hayden, D.W. Chandler, Direct measurement of the binding energy of the NO dimer, *J Chem Phys*. 116 (2002) 4755–4757. <https://doi.org/10.1063/1.1459702>.
- [207] H.A. Duarte, E. Proynov, D.R. Salahub, Density functional study of the NO dimer using GGA and LAP functionals, *J Chem Phys*. 109 (1998) 26–35. <https://doi.org/10.1063/1.476561>.
- [208] Y.-L. Zhao, M.D. Bartberger, K. Goto, K. Shimada, T. Kawashima, K.N. Houk, Theoretical Evidence for Enhanced NO Dimerization in Aromatic Hosts: Implications

- for the Role of the Electrophile (NO)₂ in Nitric Oxide Chemistry, *J Am Chem Soc.* 127 (2005) 7964–7965. <https://doi.org/10.1021/ja042247s>.
- [209] A. Snis, I. Panas, N₂O₂, N₂O₂⁻ and N₂O₂²⁻: structures, energetics and N□N bonding, *Chem Phys.* 221 (1997) 1–10. [https://doi.org/https://doi.org/10.1016/S0301-0104\(97\)00165-1](https://doi.org/https://doi.org/10.1016/S0301-0104(97)00165-1).
- [210] R. Sayós, R. Valero, J.M. Anglada, M. González, Theoretical investigation of the eight low-lying electronic states of the cis- and trans-nitric oxide dimers and its isomerization using multiconfigurational second-order perturbation theory (CASPT2), *J Chem Phys.* 112 (2000) 6608–6624. <https://doi.org/10.1063/1.481234>.
- [211] M. Tobita, S.A. Perera, M. Musial, R.J. Bartlett, M. Nooijen, J.S. Lee, Critical comparison of single-reference and multireference coupled-cluster methods: Geometry, harmonic frequencies, and excitation energies of N₂O₂, *J Chem Phys.* 119 (2003) 10713–10723. <https://doi.org/10.1063/1.1619952>.
- [212] J. Ivanic, M.W. Schmidt, B. Luke, High-level theoretical study of the NO dimer and tetramer: Has the tetramer been observed?, *J Chem Phys.* 137 (2012) 214316. <https://doi.org/10.1063/1.4769226>.
- [213] V. Menoux, R. Le Doucen, C. Haeusler, J.C. Deroche, Etude à basse température dans l'infrarouge proche du dimère (NO)₂, *Can J Phys.* 62 (1984) 322–329. <https://doi.org/10.1139/p84-048>.
- [214] M.P. Casassa, J.C. Stephenson, D.S. King, Time- and state-resolved measurements of nitric oxide dimer infrared photodissociation, *J Chem Phys.* 89 (1988) 1966–1976. <https://doi.org/10.1063/1.455694>.
- [215] J.R. Hetzler, M.P. Casassa, D.S. King, Product energy correlations in the dissociation of overtone excited nitric oxide dimer, *J Phys Chem.* 95 (1991) 8086–8095. <https://doi.org/10.1021/j100174a017>.
- [216] B.J. Howard, A.R.W. McKellar, The ν_1 band of (NO)₂, *Mol Phys.* 78 (1993) 55–72. <https://doi.org/10.1080/00268979300100061>.
- [217] A. Dkhissi, P. Soulard, A. Perrin, N. Lacombe, The NO Dimer, *J Mol Spectrosc.* 183 (1997) 12–17. <https://doi.org/https://doi.org/10.1006/jmsp.1996.7249>.
- [218] L.M. Sverdlov, M.A. Kovner, E.P. Krainov, *Vibrational Spectra of Polyatomic Molecules*, New York, 1974.
- [219] J. Zúñiga, A. Bastida, A. Requena, Theoretical calculations of vibrational frequencies and rotational constants of the N₂O isotopomers, *J Mol Spectrosc.* 217 (2003) 43–58. [https://doi.org/10.1016/S0022-2852\(02\)00014-0](https://doi.org/10.1016/S0022-2852(02)00014-0).
- [220] K.K. Irikura, *Experimental Vibrational Zero-Point Energies: Diatomic Molecules*, *J Phys Chem Ref Data.* 36 (2007) 389–397. <https://doi.org/10.1063/1.2436891>.
- [221] D. Awasabisah, G.B. Richter-Addo, Chapter One - NO_x Linkage Isomerization in Metal Complexes, in: R. van Eldik, J.A. Olabe (Eds.), *Adv Inorg Chem*, Academic Press, 2015: pp. 1–86. <https://doi.org/10.1016/bs.adioch.2014.11.003>.
- [222] A.M. Wright, T.W. Hayton, Understanding the Role of Hyponitrite in Nitric Oxide Reduction, *Inorg Chem.* 54 (2015) 9330–9341. <https://doi.org/10.1021/acs.inorgchem.5b00516>.
- [223] J. Jover, C.K. Brozek, M. Dincă, N. López, Computational Exploration of NO Single-Site Disproportionation on Fe-MOF-5, *Chemistry of Materials.* 31 (2019) 8875–8885. <https://doi.org/10.1021/acs.chemmater.9b02910>.
- [224] M.D. Fryzuk, N₂ coordination, *Chemical Communications.* 49 (2013) 4866–4868. <https://doi.org/10.1039/C3CC42001A>.

- [225] Y. Tanabe, Y. Nishibayashi, Recent advances in catalytic silylation of dinitrogen using transition metal complexes, *Coord Chem Rev.* 389 (2019) 73–93. <https://doi.org/10.1016/j.ccr.2019.03.004>.
- [226] K.M. Kadish, K.M. Smith, R. Guilard, eds., *The Porphyrin Handbook*, Academic Press, London, 2000.
- [227] C.J. Kingsbury, M.O. Senge, The shape of porphyrins, *Coord Chem Rev.* 431 (2021) 213760. <https://doi.org/10.1016/j.ccr.2020.213760>.
- [228] M.O. Senge, S.A. MacGowan, J.M. O'Brien, Conformational control of cofactors in nature – the influence of protein-induced macrocycle distortion on the biological function of tetrapyrroles, *Chemical Communications.* 51 (2015) 17031–17063. <https://doi.org/10.1039/C5CC06254C>.
- [229] P. Ochsenbein, K. Ayougou, D. Mandon, J. Fischer, R. Weiss, R.N. Austin, K. Jayaraj, A. Gold, J. Turner, J. Fajer, Conformational Effects on the Redox Potentials of Tetraarylporphyrins Halogenated at the β -Pyrrole Positions, *Angewandte Chemie International Edition in English.* 33 (1994) 348–350. <https://doi.org/10.1002/anie.199403481>.
- [230] K.M. Kadish, F. D'Souza, A. Villard, M. Autret, E. Van Caemelbecke, P. Bianco, A. Antonini, P. Tagliatesta, Effect of Porphyrin Ring Distortion on Redox Potentials of β -Brominated-Pyrrole Iron(III) Tetraphenylporphyrins, *Inorg Chem.* 33 (1994) 5169–5170. <https://doi.org/10.1021/ic00101a005>.
- [231] K.M. Kadish, J. Li, E. Van Caemelbecke, Z. Ou, N. Guo, M. Autret, F. D'Souza, P. Tagliatesta, Electrooxidation of Cobalt(II) β -Brominated-Pyrrole Tetraphenylporphyrins in CH₂Cl₂ under an N₂ or a CO Atmosphere, *Inorg Chem.* 36 (1997) 6292–6298. <https://doi.org/10.1021/ic970789n>.
- [232] K.M. Barkigia, L. Chantranupong, K.M. Smith, J. Fajer, Structural and theoretical models of photosynthetic chromophores. Implications for redox, light-absorption properties and vectorial electron flow, *J Am Chem Soc.* 110 (1988) 7566–7567. <https://doi.org/10.1021/ja00230a063>.
- [233] R.E. Haddad, S. Gazeau, J. Pécaut, J.-C. Marchon, C.J. Medforth, J.A. Shelnutt, Origin of the Red Shifts in the Optical Absorption Bands of Nonplanar Tetraalkylporphyrins, *J Am Chem Soc.* 125 (2003) 1253–1268. <https://doi.org/10.1021/ja0280933>.
- [234] S. Gentemann, C.J. Medforth, T.P. Forsyth, D.J. Nurco, K.M. Smith, J. Fajer, D. Holten, Photophysical Properties of Conformationally Distorted Metal-Free Porphyrins. Investigation into the Deactivation Mechanisms of the Lowest Excited Singlet State, *J Am Chem Soc.* 116 (1994) 7363–7368. <https://doi.org/10.1021/ja00095a046>.
- [235] B. Röder, M. Büchner, I. Rückmann, M.O. Senge, Correlation of photophysical parameters with macrocycle distortion in porphyrins with graded degree of saddle distortion, *Photochemical & Photobiological Sciences.* 9 (2010) 1152–1158. <https://doi.org/10.1039/C0PP00107D>.
- [236] G. Zamborlini, D. Lüftner, Z. Feng, B. Kollmann, P. Puschnig, C. Dri, M. Panighel, Di Santo Giovanni, A. Goldoni, G. Comelli, M. Jugovac, V. Feyer, C.M. Schneider, Multi-orbital charge transfer at highly oriented organic/metal interfaces, *Nat Commun.* 8 (2017) 335. <https://doi.org/10.1038/s41467-017-00402-0>.
- [237] K. Seufert, M.-L. Bocquet, W. Auwärter, A. Weber-Bargioni, J. Reichert, N. Lorente, J. V Barth, Cis-dicarbonyl binding at cobalt and iron porphyrins with saddle-shape conformation, *Nat Chem.* 3 (2011) 114–119. <https://doi.org/10.1038/nchem.956>.
- [238] P. Knecht, J. Reichert, P.S. Deimel, P. Feulner, F. Haag, F. Allegretti, M. Garnica, M. Schwarz, W. Auwärter, P.T.P. Ryan, T.-L. Lee, D.A. Duncan, A.P. Seitsonen, J. V Barth, A.C. Papageorgiou, Conformational Control of Chemical Reactivity for Surface-Confining Ru-Porphyrins, *Angewandte Chemie International Edition.* 60 (2021) 16561–16567. <https://doi.org/10.1002/anie.202104075>.

- [239] P. Hurdax, C.S. Kern, T.G. Boné, A. Haags, M. Hollerer, L. Egger, X. Yang, H. Kirschner, A. Gottwald, M. Richter, F.C. Bocquet, S. Soubatch, G. Koller, F.S. Tautz, M. Sterrer, P. Puschnig, M.G. Ramsey, Large Distortion of Fused Aromatics on Dielectric Interlayers Quantified by Photoemission Orbital Tomography, *ACS Nano*. 16 (2022) 17435–17443. <https://doi.org/10.1021/acsnano.2c08631>.
- [240] D.M. Janas, A. Windischbacher, M.S. Arndt, M. Gutnikov, L. Sternemann, D. Gutnikov, T. Willershausen, J.E. Nitschke, K. Schiller, D. Baranowski, V. Feyer, I. Cojocariu, K. Dave, P. Puschnig, M. Stupar, S. Ponzoni, M. Cinchetti, G. Zamborlini, Metalloporphyrins on oxygen-passivated iron: Conformation and order beyond the first layer, *Inorganica Chim Acta*. 557 (2023) 121705. <https://doi.org/10.1016/j.ica.2023.121705>.
- [241] A. Picone, D. Giannotti, A. Brambilla, G. Bussetti, A. Calloni, R. Yivlialin, M. Finazzi, L. Duò, F. Ciccacci, A. Goldoni, A. Verdini, L. Floreano, Local structure and morphological evolution of ZnTPP molecules grown on Fe(001)-p(11)O studied by STM and NEXAFS, *Appl Surf Sci*. 435 (2018) 841–847. <https://doi.org/10.1016/j.apsusc.2017.11.128>.
- [242] I. Majumdar, F. Goto, A. Calloni, G. Albani, L. Duò, M. Finazzi, F. Ciccacci, G. Bussetti, Porphyrin central metal ion driven self-assembling in heterogeneous ZnTPP – CoTPP films grown on Fe(001)-p(1 1)O, *Appl Surf Sci*. 636 (2023) 157807. <https://doi.org/10.1016/j.apsusc.2023.157807>.
- [243] G. Albani, A. Calloni, A. Picone, A. Brambilla, M. Capra, A. Lodesani, L. Duò, M. Finazzi, F. Ciccacci, G. Bussetti, An In-Depth Assessment of the Electronic and Magnetic Properties of a Highly Ordered Hybrid Interface: The Case of Nickel Tetra-Phenyl-Porphyrins on Fe(001)-p(1 × 1)O, *Micromachines (Basel)*. 12 (2021). <https://doi.org/10.3390/mi12020191>.
- [244] M.O. Senge, Exercises in molecular gymnastics—bending, stretching and twisting porphyrins, *Chemical Communications*. (2006) 243–256. <https://doi.org/10.1039/B511389J>.
- [245] J. Barbee, A.E. Kuznetsov, Revealing substituent effects on the electronic structure and planarity of Ni-porphyrins, *Comput Theor Chem*. 981 (2012) 73–85. <https://doi.org/10.1016/j.comptc.2011.11.049>.
- [246] T.S. Rush, P.M. Kozłowski, C.A. Piffat, R. Kumble, M.Z. Zgierski, T.G. Spiro, Computational Modeling of Metalloporphyrin Structure and Vibrational Spectra: Porphyrin Ruffling in NiTPP, *J Phys Chem B*. 104 (2000) 5020–5034. <https://doi.org/10.1021/jp000266s>.
- [247] Q. Zhang, X. Zheng, G. Kuang, W. Wang, L. Zhu, R. Pang, X. Shi, X. Shang, X. Huang, P.N. Liu, N. Lin, Single-Molecule Investigations of Conformation Adaptation of Porphyrins on Surfaces, *J Phys Chem Lett*. 8 (2017) 1241–1247. <https://doi.org/10.1021/acs.jpcclett.7b00007>.
- [248] A.E. Pogonin, A.A. Otlyotov, Y. Minenkov, A.S. Semeikin, Y.A. Zhabanov, S.A. Shlykov, G. V Girichev, Molecular Structure of Nickel Octamethylporphyrin—Rare Experimental Evidence of a Ruffling Effect in Gas Phase, *Int J Mol Sci*. 23 (2022). <https://doi.org/10.3390/ijms23010320>.
- [249] C. Ullrich, Time-Dependent Density-Functional Theory: Concepts and Applications, Oxford University Press, OUP , 2012.
- [250] M.E. Casida, Time-Dependent Density Functional Response Theory for Molecules, in: Recent Advances in Density Functional Methods, WORLD SCIENTIFIC, 1995: pp. 155–192. https://doi.org/10.1142/9789812830586_0005.
- [251] M.E. Casida, M. Huix-Rotllant, Progress in Time-Dependent Density-Functional Theory, *Annu Rev Phys Chem*. 63 (2012) 287–323. <https://doi.org/10.1146/annurev-physchem-032511-143803>.

- [252] M. Rohlfing, S.G. Louie, Electron-hole excitations and optical spectra from first principles, *Phys Rev B*. 62 (**2000**) 4927–4944. <https://doi.org/10.1103/PhysRevB.62.4927>.
- [253] G. Onida, L. Reining, A. Rubio, Electronic excitations: density-functional versus many-body Green's-function approaches, *Rev Mod Phys*. 74 (**2002**) 601–659. <https://doi.org/10.1103/RevModPhys.74.601>.
- [254] X. Blase, I. Duchemin, D. Jacquemin, P.-F. Loos, The Bethe–Salpeter Equation Formalism: From Physics to Chemistry, *J Phys Chem Lett*. 11 (**2020**) 7371–7382. <https://doi.org/10.1021/acs.jpcclett.0c01875>.
- [255] L. Hedin, New Method for Calculating the One-Particle Green's Function with Application to the Electron-Gas Problem, *Physical Review*. 139 (**1965**) A796–A823. <https://doi.org/10.1103/PhysRev.139.A796>.
- [256] M. van Schilfgaarde, T. Kotani, S. Faleev, Quasiparticle Self-Consistent \$GW\$ Theory, *Phys Rev Lett*. 96 (**2006**) 226402. <https://doi.org/10.1103/PhysRevLett.96.226402>.
- [257] C. Faber, P. Boulanger, C. Attaccalite, I. Duchemin, X. Blase, Excited states properties of organic molecules: from density functional theory to the GW and Bethe–Salpeter Green's function formalisms, *Philosophical Transactions of the Royal Society A: Mathematical, Physical and Engineering Sciences*. 372 (**2014**) 20130271. <https://doi.org/10.1098/rsta.2013.0271>.
- [258] A.M. Bradshaw, D.P. Woodruff, Molecular orbital tomography for adsorbed molecules: is a correct description of the final state really unimportant?, *New J Phys*. 17 (**2015**) 013033. <https://doi.org/10.1088/1367-2630/17/1/013033>.
- [259] A. Damascelli, Z. Hussain, Z.-X. Shen, Angle-resolved photoemission studies of the cuprate superconductors, *Rev Mod Phys*. 75 (**2003**) 473–541. <https://doi.org/10.1103/RevModPhys.75.473>.
- [260] F. Da Pieve, P. Krüger, Real-space Green's function approach to angle-resolved resonant photoemission: Spin polarization and circular dichroism in itinerant magnets, *Phys Rev B*. 88 (**2013**) 115121. <https://doi.org/10.1103/PhysRevB.88.115121>.
- [261] C.H. Li, A.R. Lubinsky, S.Y. Tong, Multiple-scattering approach to angle-resolved photoemission, *Phys Rev B*. 17 (**1978**) 3128–3142. <https://doi.org/10.1103/PhysRevB.17.3128>.
- [262] P. Wopperer, U. De Giovannini, A. Rubio, Efficient and accurate modeling of electron photoemission in nanostructures with TDDFT, *Eur Phys J B*. 90 (**2017**) 51. <https://doi.org/10.1140/epjb/e2017-70548-3>.
- [263] U. De Giovannini, H. Hübener, A. Rubio, A First-Principles Time-Dependent Density Functional Theory Framework for Spin and Time-Resolved Angular-Resolved Photoelectron Spectroscopy in Periodic Systems, *J Chem Theory Comput*. 13 (**2017**) 265–273. <https://doi.org/10.1021/acs.jctc.6b00897>.
- [264] M. Dauth, S. Kümmel, Predicting photoemission intensities and angular distributions with real-time density-functional theory, *Phys Rev A (Coll Park)*. 93 (**2016**) 22502. <https://doi.org/10.1103/PhysRevA.93.022502>.
- [265] U. De Giovannini, Pump-Probe Photoelectron Spectra, in: W. Andreoni, S. Yip (Eds.), *Handbook of Materials Modeling : Methods: Theory and Modeling*, Springer International Publishing, Cham, **2018**: pp. 1–19. https://doi.org/10.1007/978-3-319-42913-7_5-1.
- [266] U. De Giovannini, G. Brunetto, A. Castro, J. Walkenhorst, A. Rubio, Simulating Pump–Probe Photoelectron and Absorption Spectroscopy on the Attosecond Timescale with Time-Dependent Density Functional Theory, *ChemPhysChem*. 14 (**2013**) 1363–1376. <https://doi.org/https://doi.org/10.1002/cphc.201201007>.

- [267] S. Hammon, S. Kümmel, Pump-probe photoemission simulated in real time: Revealing many-particle signatures, *Phys Rev A (Coll Park)*. 104 (2021) 12815. <https://doi.org/10.1103/PhysRevA.104.012815>.
- [268] C.S. Kern, Exploring the Frontiers of Photoemission Orbital Tomography, Doctoral Thesis, University of Graz, 2023. https://static.uni-graz.at/fileadmin/_Persoenliche_Webseite/puschnig_peter/unigrazform/Theses/Dissertation_Kern_2023.pdf (accessed October 8, 2023).
- [269] I. Ikemoto, K. Samizo, T. Fujikawa, K. Ishii, T. Ohta, H. Kuroda, Photoelectron Spectra of Tetracyanoethylene(TCNE) and Tetracyanoquinodimethane(TCNQ), *Chem Lett.* 3 (1974) 785–790. <https://doi.org/10.1246/cl.1974.785>.
- [270] G.-Z. Zhu, L.-S. Wang, Communication: Vibrationally resolved photoelectron spectroscopy of the tetracyanoquinodimethane (TCNQ) anion and accurate determination of the electron affinity of TCNQ, *J Chem Phys*. 143 (2015) 221102. <https://doi.org/10.1063/1.4937761>.
- [271] S.R. Forrest, D.D.C. Bradley, M.E. Thompson, Measuring the Efficiency of Organic Light-Emitting Devices, *Advanced Materials*. 15 (2003) 1043–1048. <https://doi.org/10.1002/adma.200302151>.
- [272] A. Wadsworth, M. Moser, A. Marks, M.S. Little, N. Gasparini, C.J. Brabec, D. Baran, I. McCulloch, Critical review of the molecular design progress in non-fullerene electron acceptors towards commercially viable organic solar cells, *Chem Soc Rev.* 48 (2019) 1596–1625. <https://doi.org/10.1039/c7cs00892a>.
- [273] D.M. DeLongchamp, Organic Photovoltaics, in: W. and B.R.N. Paranthaman M. Parans and Wong-Ng (Ed.), *Semiconductor Materials for Solar Photovoltaic Cells*, Springer International Publishing, Cham, 2016: pp. 169–196. https://doi.org/10.1007/978-3-319-20331-7_6.
- [274] A. Buckley, R. Ragni, A. Operamolla, G.M. Farinola, Z. Wang, M.G. Helander, Z.-H. Lu, L.F. Gildea, J.A. Gareth Williams, Z. Dechun, B. D'Andrade, B. Lüsse, M. Furno, K. Leo, H. Bässler, A. Köhler, M. Gerken, A. V Tishchenko, M. Cocchi, N. Danz, M. Flämlich, D. Deganello, A.C. Grimsdale, J.-H. Jou, S. Kumar, Y.-C. Jou, A. Lääperi, A. Buckley, C. Yates, J. Meyer, P. Görrn, T. Riedl, S. Prasad, J. Woon Park, C. Kristukat, T. Gerloff, M. Hoffmann, K. Diekmann, *Organic Light-Emitting Diodes (OLEDs)*, Woodhead Publishing, 2013. <https://doi.org/10.1016/B978-0-85709-425-4.50023-3>.
- [275] A.A. Bakulin, A. Rao, V.G. Pavelyev, P.H.M. van Loosdrecht, M.S. Pshenichnikov, D. Niedzialek, J. Cornil, D. Beljonne, R.H. Friend, The Role of Driving Energy and Delocalized States for Charge Separation in Organic Semiconductors, *Science (1979)*. 335 (2012) 1340–1344. <https://doi.org/10.1126/science.1217745>.
- [276] M.A. Baldo, D.F. O'Brien, Y. You, A. Shoustikov, S. Sibley, M.E. Thompson, S.R. Forrest, Highly efficient phosphorescent emission from organic electroluminescent devices, *Nature*. 395 (1998) 151–154. <https://doi.org/10.1038/25954>.
- [277] K. Baumgärtner, M. Reuner, C. Metzger, D. Kutnyakhov, M. Heber, F. Pressacco, C.-H. Min, T.R.F. Peixoto, M. Reiser, C. Kim, W. Lu, R. Shayduk, M. Izquierdo, G. Brenner, F. Roth, A. Schöll, S. Molodtsov, W. Wurth, F. Reinert, A. Madsen, D. Popova-Gorelova, M. Scholz, Ultrafast orbital tomography of a pentacene film using time-resolved momentum microscopy at a FEL, *Nat Commun*. 13 (2022) 2741. <https://doi.org/10.1038/s41467-022-30404-6>.
- [278] S. Kazaoui, N. Minami, Y. Tanabe, H.J. Byrne, A. Eilmes, P. Petelenz, Comprehensive analysis of intermolecular charge-transfer excited states in C60 and C70 films, *Phys Rev B*. 58 (1998) 7689–7700. <https://doi.org/10.1103/PhysRevB.58.7689>.
- [279] V. Capozzi, G. Casamassima, G.F. Lorusso, A. Minafra, R. Piccolo, T. Trovato, A. Valentini, Optical characterization of fullerite C60 thin films, *Synth Met*. 77 (1996) 3–5. [https://doi.org/https://doi.org/10.1016/0379-6779\(96\)80045-2](https://doi.org/https://doi.org/10.1016/0379-6779(96)80045-2).

- [280] M.C. Fravventura, J. Hwang, J.W.A. Suijkerbuijk, P. Erk, L.D.A. Siebbeles, T.J. Savenije, Determination of Singlet Exciton Diffusion Length in Thin Evaporated C60 Films for Photovoltaics, *J Phys Chem Lett.* 3 (2012) 2367–2373. <https://doi.org/10.1021/jz300820n>.
- [281] H. Kobayashi, S. Hattori, R. Shirasawa, S. Tomiya, Wannier-Like Delocalized Exciton Generation in C60 Fullerene Clusters: A Density Functional Theory Study, *The Journal of Physical Chemistry C.* 124 (2020) 2379–2387. <https://doi.org/10.1021/acs.jpcc.9b10703>.
- [282] M. Zhang, H. Wang, H. Tian, Y. Geng, Ching.W. Tang, Bulk Heterojunction Photovoltaic Cells with Low Donor Concentration, *Advanced Materials.* 23 (2011) 4960–4964. <https://doi.org/https://doi.org/10.1002/adma.201102173>.
- [283] Y. Zou, R.J. Holmes, The Role of Exciton Ionization Processes in Bulk Heterojunction Organic Photovoltaic Cells, *Adv Energy Mater.* 5 (2015) 1500019. <https://doi.org/https://doi.org/10.1002/aenm.201500019>.
- [284] R. Bauernschmitt, R. Ahlrichs, F.H. Hennrich, M.M. Kappes, Experiment versus Time Dependent Density Functional Theory Prediction of Fullerene Electronic Absorption, *J Am Chem Soc.* 120 (1998) 5052–5059. <https://doi.org/10.1021/ja9730167>.
- [285] C. Chakravarty, H. Aksu, B. Maiti, B.D. Dunietz, Electronic Spectra of C60 Films Using Screened Range Separated Hybrid Functionals, *J Phys Chem A.* 125 (2021) 7625–7632. <https://doi.org/10.1021/acs.jpca.1c04908>.
- [286] M.S. Dresselhaus, G. Dresselhaus, P.C. Eklund, Science of Fullerenes and Carbon Nanotubes, 1st ed., Academic Press, San Diego, 1996.
- [287] L. Piela, Appendix C - Group Theory in Spectroscopy, in: L. Piela (Ed.), Ideas of Quantum Chemistry (Second Edition), Elsevier, Oxford, 2014: pp. e17–e64. <https://doi.org/10.1016/B978-0-444-59436-5.00023-4>.
- [288] S. Refaely-Abramson, S. Sharifzadeh, M. Jain, R. Baer, J.B. Neaton, L. Kronik, Gap renormalization of molecular crystals from density-functional theory, *Phys Rev B.* 88 (2013) 81204. <https://doi.org/10.1103/PhysRevB.88.081204>.
- [289] D Muigg, P Scheier, K Becker, T D Märk, Measured appearance energies of fragment ions produced by electron impact on, *Journal of Physics B: Atomic, Molecular and Optical Physics.* 29 (1996) 5193. <https://doi.org/10.1088/0953-4075/29/21/029>.
- [290] N. Haag, D. Lüftner, F. Haag, J. Seidel, L.L. Kelly, G. Zamborlini, M. Jugovac, V. Feyer, M. Aeschlimann, P. Puschnig, M. Cinchetti, B. Stadtmüller, Signatures of an atomic crystal in the band structure of a C60 thin film, *Phys Rev B.* 101 (2020) 165422. <https://doi.org/10.1103/PhysRevB.101.165422>.
- [291] B. Stadtmüller, S. Emmerich, D. Jungkenn, N. Haag, M. Rollinger, S. Eich, M. Maniraj, M. Aeschlimann, M. Cinchetti, S. Mathias, Strong modification of the transport level alignment in organic materials after optical excitation, *Nat Commun.* 10 (2019) 1470. <https://doi.org/10.1038/s41467-019-09136-7>.
- [292] S. Emmerich, S. Hedwig, B. Arnoldi, J. Stöckl, F. Haag, R. Hemm, M. Cinchetti, S. Mathias, B. Stadtmüller, M. Aeschlimann, Ultrafast Charge-Transfer Exciton Dynamics in C60 Thin Films, *The Journal of Physical Chemistry C.* 124 (2020) 23579–23587. <https://doi.org/10.1021/acs.jpcc.0c08011>.
- [293] S. Saito, A. Oshiyama, Cohesive mechanism and energy bands of solid C60, *Phys Rev Lett.* 66 (1991) 2637–2640. <https://doi.org/10.1103/PhysRevLett.66.2637>.
- [294] E. Westin, A. Rosén, Evaluation of the dispersion of the third order optical nonlinearity of C60, *Zeitschrift Für Physik D Atoms, Molecules and Clusters.* 26 (1993) 273–275. <https://doi.org/10.1007/BF01425688>.
- [295] E. Westin, A. Rosén, Analysis of the absorption spectra of C60 and KC60, *Zeitschrift Für Physik D Atoms, Molecules and Clusters.* 26 (1993) 276–278. <https://doi.org/10.1007/BF01425689>.

- [296] A.L. Montero-Alejo, E. Menéndez-Proupin, M.E. Fuentes, A. Delgado, F.-P. Montforts, L.A. Montero-Cabrera, J.M. García de la Vega, Electronic excitations of C60 aggregates, *Physical Chemistry Chemical Physics*. 14 (2012) 13058–13066. <https://doi.org/10.1039/C2CP41979C>.
- [297] S. Leach, M. Vervloet, A. Desprès, E. Bréheret, J.P. Hare, D.T. John, H.W. Kroto, R. Taylor, D.R.M. Walton, Electronic spectra and transitions of the fullerene C60, *Chem Phys*. 160 (1992) 451–466. [https://doi.org/10.1016/0301-0104\(92\)80012-K](https://doi.org/10.1016/0301-0104(92)80012-K).
- [298] A. Sassara, G. Zerza, M. Chergui, S. Leach, Absorption Wavelengths and Bandwidths for Interstellar Searches of C₆₀ in the 2400–4100 Å Region, *Astrophys J Suppl Ser*. 135 (2001) 263–273. <https://doi.org/10.1086/323533>.
- [299] R.E. Haufler, Y. Chai, L.P.F. Chibante, M.R. Fraelich, R.B. Weisman, R.F. Curl, R.E. Smalley, Cold molecular beam electronic spectrum of C6 and C7, *J Chem Phys*. 95 (1991) 2197–2199. <https://doi.org/10.1063/1.460968>.
- [300] H. Yasumatsu, T. Kondow, H. Kitagawa, K. Tabayashi, K. Shobatake, Absorption spectrum of C60 in the gas phase: Autoionization via core-excited Rydberg states, *J Chem Phys*. 104 (1996) 899–902. <https://doi.org/10.1063/1.470813>.
- [301] Q. Gong, Y. Sun, Z. Huang, X. Zhou, Z. Gu, D. Qiang, Optical and thermodynamic properties of isolated fullerene molecules, *Journal of Physics B: Atomic, Molecular and Optical Physics*. 29 (1996) 4981. <https://doi.org/10.1088/0953-4075/29/21/012>.
- [302] J.H. Morkath, Delocalized exciton formation in C60 linear molecular aggregates, *Physical Chemistry Chemical Physics*. 23 (2021) 21901–21912. <https://doi.org/10.1039/D1CP02430B>.
- [303] M.M. Muhammed, J.H. Morkath, A.J. Chamkha, Impact of packing arrangement on the optical properties of C60 cluster aggregates, *Physical Chemistry Chemical Physics*. 24 (2022) 5946–5955. <https://doi.org/10.1039/D1CP04128B>.
- [304] J. Li, G. D'Avino, I. Duchemin, D. Beljonne, X. Blase, Accurate description of charged excitations in molecular solids from embedded many-body perturbation theory, *Phys Rev B*. 97 (2018) 35108. <https://doi.org/10.1103/PhysRevB.97.035108>.
- [305] A.R. Kshirsagar, C. Attacalite, X. Blase, J. Li, R. Poloni, Bethe–Salpeter Study of the Optical Absorption of trans and cis Azobenzene-Functionalized Metal–Organic Frameworks Using Molecular and Periodic Models, *The Journal of Physical Chemistry C*. 125 (2021) 7401–7412. <https://doi.org/10.1021/acs.jpcc.1c00367>.
- [306] W. I. F. David, R. M. Ibberson, T. J. S. Dennis, J. P. Hare, K. Prassides, Structural Phase Transitions in the Fullerene C60, *Europhys Lett*. 18 (1992) 219. <https://doi.org/10.1209/0295-5075/18/3/006>.
- [307] H. Wang, C. Zeng, B. Wang, J.G. Hou, Q. Li, J. Yang, Orientational configurations of the C60 molecules in the (2x2) superlattice on a solid C60 (111) surface at low temperature, *Phys Rev B*. 63 (2001) 85417. <https://doi.org/10.1103/PhysRevB.63.085417>.
- [308] F. Rossel, M. Pivetta, F. Patthey, E. Čavar, A.P. Seitsonen, W.-D. Schneider, Growth and characterization of fullerene nanocrystals on NaCl/Au(111), *Phys Rev B*. 84 (2011) 75426. <https://doi.org/10.1103/PhysRevB.84.075426>.
- [309] P. Merino, C. Große, A. Rosławska, K. Kuhnke, K. Kern, Exciton dynamics of C60-based single-photon emitters explored by Hanbury Brown–Twiss scanning tunnelling microscopy, *Nat Commun*. 6 (2015) 8461. <https://doi.org/10.1038/ncomms9461>.
- [310] J. Leaf, A. Stannard, S.P. Jarvis, P. Moriarty, J.L. Dunn, A Combined Monte Carlo and Hückel Theory Simulation of Orientational Ordering in C60 Assemblies, *The Journal of Physical Chemistry C*. 120 (2016) 8139–8147. <https://doi.org/10.1021/acs.jpcc.6b00638>.

- [311] S. Hasegawa, T. Miyamae, K. Yakushi, H. Inokuchi, K. Seki, N. Ueno, Comparison between calculated and measured photoemission spectra of C60 thin films, *J Electron Spectros Relat Phenomena*. 88–91 (**1998**) 891–895. [https://doi.org/10.1016/S0368-2048\(97\)00208-9](https://doi.org/10.1016/S0368-2048(97)00208-9).
- [312] G. Kresse, J. Hafner, Ab initio molecular dynamics for liquid metals, *Phys Rev B*. 47 (**1993**) 558. <https://doi.org/10.1103/PhysRevB.47.558>.
- [313] G. Kresse, D. Joubert, From ultrasoft pseudopotentials to the projector augmented-wave method, *Phys Rev B*. 59 (**1999**) 1758. <https://doi.org/10.1103/PhysRevB.59.1758>.
- [314] P.E. Blöchl, Projector augmented-wave method, *Phys Rev B*. 50 (**1994**) 17953. <https://doi.org/10.1103/PhysRevB.50.17953>.
- [315] J. Neugebauer, M. Scheffler, Adsorbate-substrate and adsorbate-adsorbate interactions of Na and K adlayers on Al (111), *Phys Rev B*. 46 (**1992**) 16067. <https://doi.org/10.1103/PhysRevB.46.16067>.
- [316] D. Lüftner, S. Weiß, X. Yang, P. Hurdax, V. Feyer, A. Gottwald, G. Koller, S. Soubatch, P. Puschnig, M.G. Ramsey, F.S. Tautz, Understanding the photoemission distribution of strongly interacting two-dimensional overlayers, *Phys Rev B*. 96 (**2017**) 125402. <https://doi.org/10.1103/PhysRevB.96.125402>.
- [317] P.J. Feibelman, D.E. Eastman, Photoemission spectroscopy---Correspondence between quantum theory and experimental phenomenology, *Phys Rev B*. 10 (**1974**) 4932–4947. <https://doi.org/10.1103/PhysRevB.10.4932>.
- [318] J.J. Mortensen, L.B. Hansen, K.W. Jacobsen, Real-space grid implementation of the projector augmented wave method, *Phys Rev B*. 71 (**2005**) 35109. <https://doi.org/10.1103/PhysRevB.71.035109>.
- [319] J. Enkovaara, C. Rostgaard, J.J. Mortensen, J. Chen, M. Dułak, L. Ferrighi, J. Gavnholt, C. Glinsvad, V. Haikola, H.A. Hansen, H.H. Kristoffersen, M. Kuisma, A.H. Larsen, L. Lehtovaara, M. Ljungberg, O. Lopez-Acevedo, P.G. Moses, J. Ojanen, T. Olsen, V. Petzold, N.A. Romero, J. Stausholm-Møller, M. Strange, G.A. Tritsarlis, M. Vanin, M. Walter, B. Hammer, H. Häkkinen, G.K.H. Madsen, R.M. Nieminen, J.K. Nørskov, M. Puska, T.T. Rantala, J. Schiøtz, K.S. Thygesen, K.W. Jacobsen, Electronic structure calculations with GPAW: a real-space implementation of the projector augmented-wave method, *Journal of Physics: Condensed Matter*. 22 (**2010**) 253202. <https://doi.org/10.1088/0953-8984/22/25/253202>.
- [320] M.P. Ljungberg, J.J. Mortensen, L.G.M. Pettersson, An implementation of core level spectroscopies in a real space Projector Augmented Wave density functional theory code, *J Electron Spectros Relat Phenomena*. 184 (**2011**) 427–439. <https://doi.org/10.1016/j.elspec.2011.05.004>.
- [321] S.L. Dudarev, G.A. Botton, S.Y. Savrasov, C.J. Humphreys, A.P. Sutton, Electron-energy-loss spectra and the structural stability of nickel oxide: An LSDA+U study, *Phys Rev B*. 57 (**1998**) 1505–1509. <https://doi.org/10.1103/PhysRevB.57.1505>.
- [322] F. Neese, The ORCA program system, *Wiley Interdiscip Rev Comput Mol Sci*. 2 (**2012**) 73–78. <https://doi.org/10.1002/wcms.81>.
- [323] F. Neese, Software update: The ORCA program system—Version 5.0, *WIREs Computational Molecular Science*. 12 (**2022**) e1606. <https://doi.org/10.1002/wcms.1606>.
- [324] F. Weigend, R. Ahlrichs, Balanced basis sets of split valence, triple zeta valence and quadruple zeta valence quality for H to Rn: Design and assessment of accuracy, *Physical Chemistry Chemical Physics*. 7 (**2005**) 3297–3305. <https://doi.org/10.1039/b508541a>.
- [325] P.J. Stephens, F.J. Devlin, C.F. Chabalowski, M.J. Frisch, Ab Initio Calculation of Vibrational Absorption and Circular Dichroism Spectra Using Density Functional

- Force Fields, *J Phys Chem.* 98 (1994) 11623–11627.
<https://doi.org/10.1021/j100096a001>.
- [326] R. Krishnan, J.S. Binkley, R. Seeger, J.A. Pople, Self-consistent molecular orbital methods. XX. A basis set for correlated wave functions, *J Chem Phys.* 72 (2008) 650–654. <https://doi.org/10.1063/1.438955>.
- [327] M.J. Frisch, J.A. Pople, J.S. Binkley, Self-consistent molecular orbital methods 25. Supplementary functions for Gaussian basis sets, *J Chem Phys.* 80 (1984) 3265–3269. <https://doi.org/10.1063/1.447079>.
- [328] J.P. Perdew, Y. Wang, Accurate and simple analytic representation of the electron-gas correlation energy, *Phys Rev B.* 45 (1992) 13244–13249.
<https://doi.org/10.1103/PhysRevB.45.13244>.
- [329] D. Jacquemin, I. Duchemin, X. Blase, Is the Bethe–Salpeter Formalism Accurate for Excitation Energies? Comparisons with TD-DFT, CASPT2, and EOM-CCSD, *J Phys Chem Lett.* 8 (2017) 1524–1529. <https://doi.org/10.1021/acs.jpcclett.7b00381>.
- [330] C. Adamo, V. Barone, Toward reliable density functional methods without adjustable parameters: The PBE0 model, *Journal of Chemical Physics.* 110 (1999) 6158–6170.
<https://doi.org/10.1063/1.478522>.
- [331] G. D’Avino, L. Muccioli, C. Zannoni, D. Beljonne, Z.G. Soos, Electronic Polarization in Organic Crystals: A Comparative Study of Induced Dipoles and Intramolecular Charge Redistribution Schemes, *J Chem Theory Comput.* 10 (2014) 4959–4971.
<https://doi.org/10.1021/ct500618w>.
- [332] J. Li, G. D’Avino, I. Duchemin, D. Beljonne, X. Blase, Combining the Many-Body GW Formalism with Classical Polarizable Models: Insights on the Electronic Structure of Molecular Solids, *J Phys Chem Lett.* 7 (2016) 2814–2820.
<https://doi.org/10.1021/acs.jpcclett.6b01302>.
- [333] J. Li, G. D’Avino, A. Pershin, D. Jacquemin, I. Duchemin, D. Beljonne, X. Blase, Correlated electron-hole mechanism for molecular doping in organic semiconductors, *Phys Rev Mater.* 1 (2017) 25602.
<https://doi.org/10.1103/PhysRevMaterials.1.025602>.